Probing the quark-gluon plasma at the LHC : study of charmonia with the ALICE detector and thermal dileptons phenomenology

Maurice Coquet

université PARIS-SACLAY

Probing the quark-gluon plasma at the LHC: study of charmonia with the ALICE detector and thermal dileptons phenomenology

Sonder le plasma de quarks et de gluons au LHC : étude des charmonia avec le détecteur ALICE et phénoménologie de dileptons thermiques

Thèse de doctorat de l'université Paris-Saclay

École doctorale n° 576, Particules, Hadrons, Energie, Noyau, Instrumentation, Imagerie, Cosmos et Simulation (PHENIICS)
Spécialité de doctorat: Physique nucléaire
Graduate School : Physique, Référent : Faculté des sciences d'Orsay

Thèse préparée au **Département de Physique Nucléaire** (Université Paris-Saclay, CEA), sous la direction de **Stefano PANEBIANCO**, Directeur de recherche, le co-encadrement de **Andry RAKOTOZAFINDRABE**, Cadre scientifique, et le co-encadrement de **Michael WINN**, Cadre scientifique

Thèse soutenue à Paris-Saclay, le 12 octobre 2023, par

Maurice COQUET

Composition du jury

Membres du jury avec voix délibérative

Frédéric FLEURET Directeur de recherche, LLR, Institut Polytechnique de Paris	Président
Andrea DAINESE Directeur de recherche, INFN, Section de Padoue	Rapporteur & Examinateur
Marlene NAHRGANG Enseignante-Chercheuse (HDR), Subatech, IMT Atlantique	Rapporteure & Examinatrice
Zaida CONESA DEL VALLE Chargée de recherche (HDR), IJCLab, Université Paris-Saclay	Examinatrice
Tetyana GALATYUK Professeure, Institut de Physique Nucléaire, Univérsité de Darmstadt	Examinatrice

THESE DE DOCTORAT

NNT : 2023UPASP123

université PARIS-SACLAY

ÉCOLE DOCTORALE
Particules, hadrons, énergie et noyau : instrumentation, imagerie, cosmos et simulation (PHENIICS)

Titre: Sonder le plasma de quarks et de gluons au LHC : étude des charmonia avec le détecteur ALICE et phénoménologie des dileptons thermiques

Mots clés: Collisions d'ions lourds, Plasma de quarks et de gluons (PQG), Charmonium, Pré-équilibre

Résumé: Les collisions ultrarelativistes d'ions lourds permettent d'étudier le comportement de la matière en interaction forte à haute température. Dans ces conditions, les quarks et les gluons ne sont plus confinés dans des hadrons, mais forment un plasma de quarks et de gluons (QGP). Les charmonia, états liés de quarks et antiquarks de saveur charm, sont des sondes importantes de la formation d'un tel état de la matière. En particulier, la production et le transport du charmonium J/ψ dans les collisions d'ions lourds sont influencés par l'interaction des quarks charm avec le QGP.

En 2021, l'expérience ALICE s'enrichit d'un nouveau détecteur appelé Muon Forward Tracker (MFT). Celui-ci permet désormais de séparer les J/ψ non prompts, issus de la désintégration des hadrons composés de quarks beauty, de ceux produits directement lors des collisions, dits prompts, dans la région de rapidité à l'avant de l'expérience ALICE. Cette séparation permet de mieux évaluer l'effet de l'interaction des quarks lourds avec le QGP. Des études préliminaires présentées dans cette thèse montrent que cette séparation est effectivement réalisable dans les collisions proton-proton à l'aide du MFT, ce qui ouvre la voie à la poursuite de cette analyse dans les données d'ions lourds.

Au côté des charmonia, les dileptons thermiques, paires électron-positron ou muon-anti-muon émises par le QGP, constituent une autre sonde remarquable du milieu produit dans les collisions d'ions lourds et de son évolution. Ils sont particulièrement sensibles aux premiers instants de ces collisions et donnent des clés pour comprendre dans quelle mesure l'équilibre thermique peut y être atteint. Dans une étude phénoménologique, nous calculons la production de dileptons thermiques en prenant en compte la contribution des premiers instants de la formation du QGP, et nous montrons que leurs distributions de masse invariante, de masse transverse et de polarisation peuvent donner un accès direct au temps de thermalisation et aux propriétés du QGP lors de ses premiers instants.

Title: Probing the quark-gluon plasma at the LHC: study of charmonia with the ALICE detector and thermal dileptons phenomenology
Keywords: Heavy-ion collisions, Quark-Gluon Plasma (QGP), Charmonium, Pre-equilibrium

Abstract: Ultrarelativistic heavy-ion collisions allow to study the behavior of strongly interacting matter at high temperature. In such conditions, the quarks and gluons are no longer confined into hadrons, but form a quark-gluon plasma (QGP). Charmonia, bound states of charm and anti-charm quarks, are important probes of the formation of such a state of matter. In particular, the production and transport of J/ψ particles in heavy-ion collisions are impacted by the interaction of the charm quarks with the QGP.

In 2021, a new secondary vertexing detector called the Muon Forward Tracker (MFT) was installed in the ALICE experiment. It now allows to separate non-prompt J/ψ, originating from the decay of hadrons containing beauty quarks, from those produced promptly in the collisions, in the forward rapidity region of this experiment. This separation allows to further assess the effect of heavy quarks interaction with the QGP. First preliminary studies presented in this thesis show that this separation is indeed achievable in proton-proton collisions using the MFT, opening the door to pursue this analysis in heavy-ion data.

Beside charmonia, another significant probe of the medium produced in heavy-ion collisions are thermal dileptons, pairs of electron-positron or muon-anti-muon radiated by the QGP. In particular, dileptons can be used to gain insight into the first instants of heavy-ion collisions and give keys to understand to what extent thermalization can be achieved in such collision. In a phenomenology study, we compute the dilepton production including the contribution from the early stages of the QGP, and show that their invariant mass, transverse mass and polarization distributions can give direct access to the thermalization time and early-time properties of the QGP.

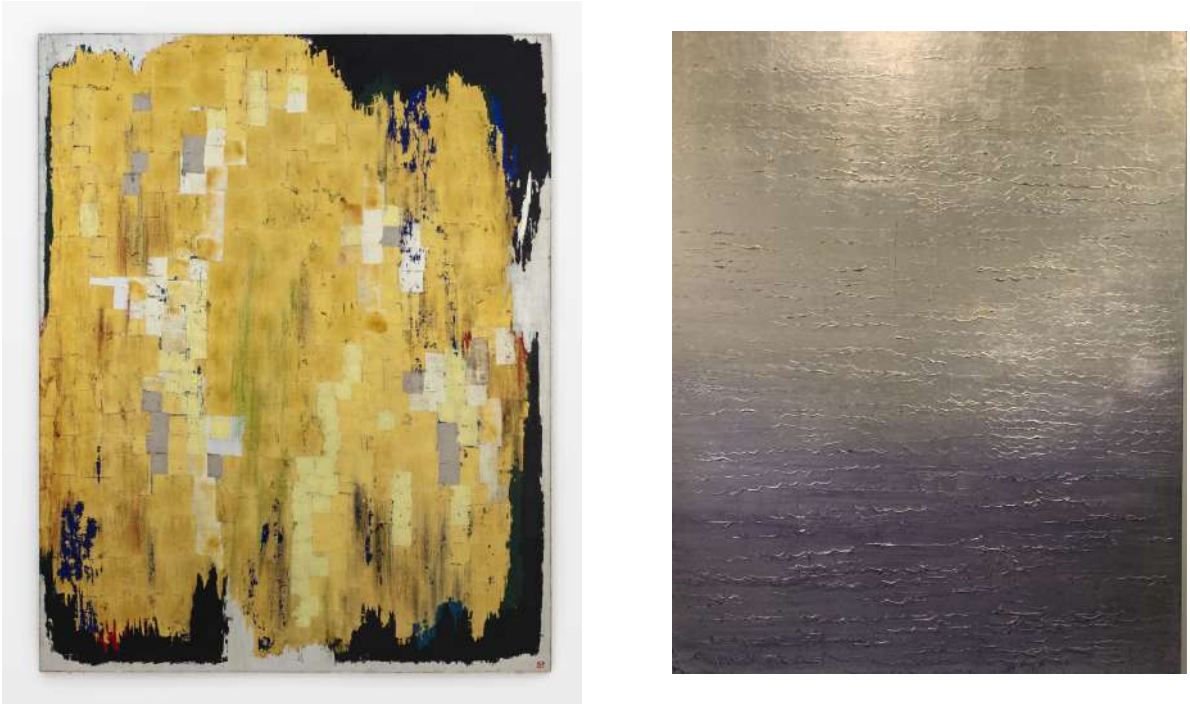

Figure 1: Anna-Eva Bergman, (Left) N°26 Feu (1962), (Right) N° 67 Grand Océan (1966)

Figure 2: Anna-Eva Bergman, N°63 Grand univers aux petits carrés (1961)

Anna-Eva Bergman (1909-1987) was a Norwegian-French artist. After first seeing her depictions of "Fire" and the "Big ocean", her representation of the "Big universe" reminded me of a liquid fireball.

Acknowledgements

I would first like to express my gratitude to the members of the jury, Marlene, Tetyana, Zaida, Andrea, and Frédéric, for their availability, kindness, and the very interesting discussions we had during my defense. I would also like to thank all the wonderful people at DPhN whom I had the chance to meet over these three years. In particular, I thank Isabelle and all the members of LQGP for welcoming me into the department. Working with all of you has been a great pleasure, and I hope with all my heart that this collaboration will continue.

Of course, I especially thank my supervisors, Andry, Michael and Stefano. I now realize how tremendously lucky I was to have been supported by such kind, patient, pleasant people (each in their own way!), who are also brilliant experts in their fields. I am very grateful to them for entrusting me with this work and for being such outstanding teachers. I have learned a great deal from them, both scientifically and humanely. I also extend my thanks to all the other collaborators I met during these years, as well as all the wonderful people I encountered at CERN and at P2, including Charlotte, Sarah, Shreyasi, Rafael, Guillaume, Tomas, the DQ colleagues, Laure, Fiorella, Maxime, Luca, and many others. In addition, I had the privilege to exchange with great people during our phenomenology studies, Xiaojian, Sören and especially Jean-Yves, who I thank dearly for all his help and advice. I feel honoured to have been a part of this collaboration.

I am equally grateful for the friendships I forged along the way. My sincere thanks go out to all my fellow (current and former) PhD students from the lab, including Aude, Chi, Gabriel, Robin, and Sébastien, and those outside the lab such as Lida, Fabian, and many others. I am deeply grateful to Carolina, who was not only a great friend but also a great support, allowing us to share our "états d'âme" during these challenging times. I owe special thanks to Batoul, without whom I could not have conducted the analysis part of my work and who also assisted me significantly with my manuscript; she was like a fourth supervisor. To all my friends outside the field, I express my gratitude for the wonderful times we shared. I also want to acknowledge Cécîle for her support and for being very courageous in putting up with me during all these years. I apologize for all the time I spent working instead of being with you.

Finally, I thank my entire family for their constant and loving support. My parents and my sister, in particular, have always been there for me, and I owe everything in my life to them. In closing, I would like to dedicate this work to you and to Yvette, Marie-France, Léonce and Patrice. My only hope is to make you proud.

Contents

General introduction

The study of particle physics in collider facilities has proven to be highly successful in understanding the fundamental nature of matter and the universe. It is based on the Standard Model of particle physics, which aims to classify all observed particles and their interactions within a single framework. One of these interactions, the strong nuclear force, is responsible for holding the nucleus together, and is described by quantum chromodynamics. This interaction exhibits remarkable characteristics compared to other forces in the Standard Model, such as confinement and asymptotic freedom. These features do not only make the dynamics of the strong force more complex than electrodynamics for example, but also make its study very rich in many aspects. In particular, the strong force exhibits a non-trivial behavior at high temperatures. When nuclear matter is heated to temperatures exceeding $10^{12}\,\mathrm{K}$, a new state of matter called quark-gluon plasma can form. The experimental investigations have revealed that it is the most perfect fluid ever observed. The study of this state of matter raises numerous questions, such as whether thermal equilibrium can be reached in systems as small as a nucleus, the strength of the strong force at high temperatures, and the applicability limits of hydrodynamics.

Ultrarelativistic heavy-ion collision facilities, such as the ALICE experiment at the LHC, provide valuable laboratories for studying strongly interacting matter under extreme conditions and attempting to address these questions. In these facilities, heavy nuclei are accelerated and collided to produce a quark-gluon plasma for an extremely short period of approximately $10^{-23}\,\mathrm{s}$, in a volume of a few $10^{-13}\,\mathrm{m}^3$. These conditions pose significant challenges in learning about the state of matter produced in such collisions. One must carefully select probes, that are produced alongside the plasma and are sensitive to the relevant properties to address the desired problem. In this thesis, our focus centers on two such observables: charmonia and thermal dileptons.

Charmonia are bound states of quarks and anti-quarks of a specific flavor known as charm. Hence, they are composed of two colored objects, which means they interact via the strong force. In addition, due to their large mass, it is largely assumed that charmonia are predominantly produced during the initial moments of heavy-ion collisions. Thus, according to the standard picture of heavy-ion collisions, they interact with the produced plasma throughout its entire lifetime.

In contrast, dileptons are pairs of electron-positron or muon-anti-muon. They are not composed of colored objects and therefore do not interact via the strong force but rather electromagnetically. They can be produced in the quark-gluon plasma as some of its constituents, namely quarks, carry electric charge and can emit electromagnetic radiation

such as thermal dileptons. Unlike charmonia, thermal dileptons hardly interact with the strongly interacting plasma once they are produced. Consequently, they only probe the state of matter present at the time of their production. However, they can be produced throughout the entire lifetime of the medium.

Therefore, charmonia and dileptons can be considered complementary observables of the medium produced in heavy-ion collisions, probing either the overall heavy-quark-plasma interaction or different stages of the collision, respectively. Both observables present distinct challenges. To evaluate how the quark-gluon plasma affects the charmonium formation, it is necessary to disentangle different production sources, such as the decay of other particles. This distinction can be achieved using secondary vertexing detectors, which allow for the separation of non-prompt charmonia, produced by the decay of beauty hadrons, from prompt charmonia produced by hard collisions in the initial stages of the collision. The measurement of the thermal dilepton spectrum poses a significant challenge that requires the rejection of substantial background sources.

The first chapter of this thesis serves as an introduction to the quark-gluon plasma in ultrarelativistic heavy-ion collisions and explores charmonia as probes of such collisions. In the second chapter, we present the Large Hadron Collider and the ALICE experiment, which is specifically dedicated to study heavy-ion collisions. The third chapter focuses on a new detector, the Muon Forward Tracker, added to the ALICE experiment for the third data-taking period of the LHC, known as Run 3. This detector enables the disentanglement of prompt and non-prompt J/ψ, a charmonium state, at forward rapidities in the dimuon decay channel. In the ALICE experiment, this separation was previously only achievable in the central barrel, at midrapidity. The fourth chapter comprises a preliminary analysis of this prompt-to-non-prompt separation using the Muon Forward Tracker with Run 3 proton-proton data. Finally, the fifth chapter introduces the concept of the pre-equilibrium stage of heavy-ion collisions. We present a phenomenological calculation of thermal dilepton production, including the contribution from the pre-equilibrium stage. We demonstrate that the dilepton distribution provides access to unique features of the early stages of heavy-ion collisions, such as equilibration time or momentum space anisotropy. While current experimental facilities do not yet permit such dilepton measurements, they will become feasible with future upgrades.

Chapter 1

Introduction

1.1 The strong interaction

There are four known fundamental forces in Nature: the gravitational, weak, electromagnetic, and strong interactions. Gravity is described by the theory of general relativity, while the other three are depicted in the Standard Model of particle physics. The weak force, which has a short range ($\sim 0.01\,\mathrm{fm}$, where $1\,\mathrm{fm} = 10^{-15}\,\mathrm{m}$), is responsible for some forms of radioactivity, namely beta decays. The electromagnetic force describes the interaction between electrically charged particles, as well as electromagnetic fields. At a quantum scale, it is described by a quantum field theory: quantum electrodynamics (QED). Finally, the strong force holds the protons and neutrons of a nucleus together and governs the internal structure and interactions of many other particles, which form a category known as "hadrons". They make up most of the visible matter in the universe, and are described as combinations of fundamental constituents: quarks and gluons [1]. The strong interaction is described by the quantum field theory of quantum chromodynamics (QCD) [2]. It is based on the Yang-Mills theory with the $SU(3)$ gauge group (describing gauge fields i.e. gluons) combined with fermionic fields described by the Dirac equations (i.e. quarks) [3]. The $SU(3)$ group associates an internal degree of freedom, known as "color", to all particles affected by the strong force, namely quarks and gluons. Color is a quantum state which can take different values, which we label as red (R), green (G) and blue (B), or their opposite state, an "anti-color", which can be anti-red ($\bar{R}$), anti-green ($\bar{G}$) or anti-blue ($\bar{B}$). Quarks carry color and anti-quark carry anti-color; they form what is known as a fundamental representation of the $SU(3)$ symmetry group. In addition, they can be classified into three different generations. In the Standard Model, we count 6 different flavors of quarks, each with a finite mass. These are the up and down quarks, and the much heavier charm, strange, top, and bottom quarks. Each of them exists in the three different color states. These quarks and gluons are illustrated in Fig. 1.1. In addition, this figure also classifies the other fundamental particles of the Standard Model. Leptons which comprise electrons, muons, tau particles and their associated neutrinos, are fermions that are not sensitive to the strong interactions. Next are photons and the Z/W$^{\pm}$ bosons, which are the carriers of the electroweak force. Finally, the Higgs boson, discovered at the LHC in 2012, is a massive scalar field, with neither electric nor color charge. The masses of all elementary particles are related to their coupling constants with this field.

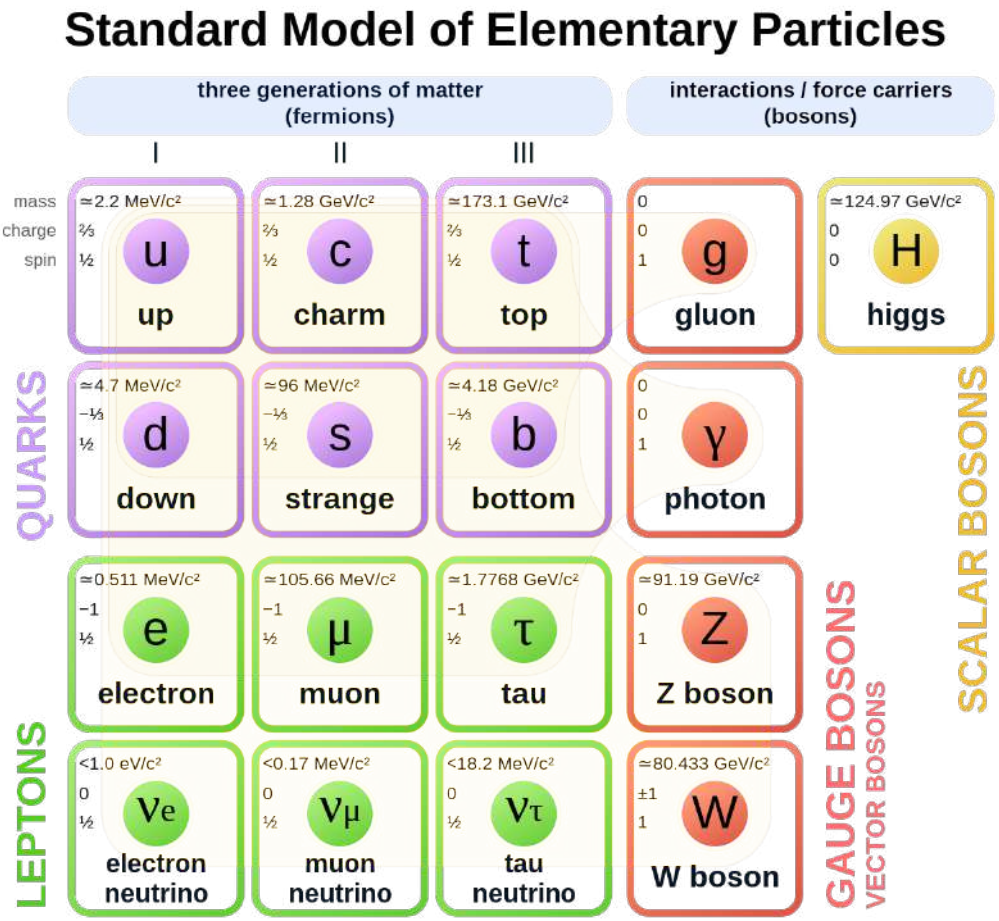

Figure 1.1: Illustration of the fundamental particles of the Standard Model of particle physics [4].

These quarks interact between themselves by the exchange of gauge fields: the gluons. Each gluon carries a color as well as an anti-color. They form an adjoint representation of the SU(3) group and are thus of 8 types [5]:

$$
\begin{aligned}
g_1 &= R\bar{G} \quad g_2 = R\bar{B} \quad g_3 = G\bar{R} \\
g_4 &= G\bar{B} \quad g_5 = B\bar{R} \quad g_6 = B\bar{G} \\
g_7 &= \frac{1}{\sqrt{2}}(R\bar{R} - G\bar{G}) \\
g_8 &= \frac{1}{\sqrt{6}}(R\bar{R} + G\bar{G} - 2B\bar{B})
\end{aligned}
$$

with one remaining adjoint $SU(3)$ combination:

$$
g_0 = \frac{1}{\sqrt{3}}(R\bar{R} + G\bar{G} + B\bar{B})
$$

which couples equally to all colors and thus does not participate in the strong force. Such state is known as a color singlet.

The possible interactions allowed between quarks and gluons are given by the different terms of the Lagrangian of QCD. The general structure is fixed by the requirement of

Lorentz invariance and can be written [6]:

$$\mathcal{L} = \sum_{q=1}^{N_f} \bar{\psi}_{q,a} \left(i\gamma^\mu \partial_\mu \delta_{ab} - g\gamma^\mu t^C_{ab} A^C_\mu - m_q \delta_{ab} \right) \psi_{q,b} - \frac{1}{4} G^C_{\mu\nu} G^{C,\mu\nu} \tag{1.1}$$

where $\psi_{q,a}$ are the quark fields with flavor q, a color-index $a = \{r, g, b\}$, and with a mass m_q. A^C_μ represent gluon fields (with C running from 1 to 8, for each possible color configuration), γ^μ are the Dirac matrices, t^C are 3×3 matrices which are the generators of the $SU(3)$ group, and G^C is the gluon field strength tensor. The quantity g is the QCD coupling constant. It is a parameter which quantifies the interaction strength between the different QCD fields. In order to satisfy the local gauge invariance given by the color $SU(3)$ group, the gluon field strength tensor is constructed as:

$$G^A_{\mu\nu} = \partial_\mu A^A_\nu - \partial_\nu A^A_\mu - g f_{ABC} A^B_\mu A^C_\nu \tag{1.2}$$

where f_{ABC} is a constant known as the structure constant of QCD. In the mathematical description of QED, the electromagnetic field strength has a similar expression but the structure constant is zero. This is because the gauge group on which the theory of QED relies, the $U(1)$ group, is an abelian group, meaning all its elements commute with each other. This is not the case for the $SU(3)$ group of QCD, which is non-abelian, meaning that the elements of the group do not commute. This means that the commutator $\left[t^A, t^B\right] = i f_{ABC} t^C$ is non-zero, and hence the structure constant f_{ABC} is non-zero.

Each term in the Lagrangian which involves the coupling constant g can be associated to a corresponding Feynman diagram describing the interaction between quarks and gluons, as illustrated in Fig. 1.2. The $g(\bar{\psi}\gamma^\mu A_\mu \psi)$ term in Eq. 1.1 describes the interaction between a quark, an anti-quark and a gluon field. The $g(f\partial_\mu A_\nu A^\mu A^\nu)$ terms describe the interaction between three gluon fields. Finally, the $g^2(f^2 A_\mu A_\nu A^\mu A^\nu)$ term describes the interaction between four gluons. From these last two terms, we see that gluons interact with other gluons due to the non-abelian nature of QCD (the structure constant f is non-zero). As a consequence, the Yang-Mills equations are intrinsically non-linear. They can be viewed as a non-linear generalization of Maxwell's equations of electrodynamics.

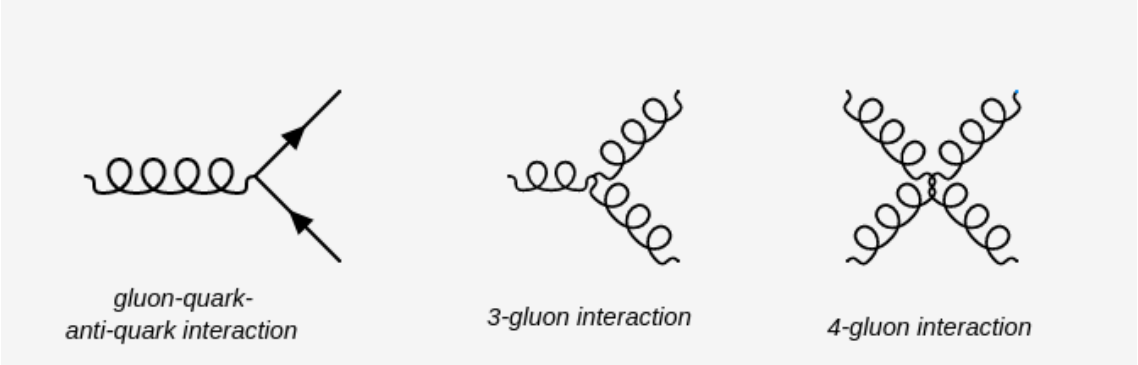

Figure 1.2: Representation of the different field interactions allowed by the QCD Lagrangian.

The non-linearity of QCD interactions between gluons leads to important implications, in particular regarding the coupling constant g. As we saw, this number characterizes the strength of the strong interaction. It is common in the literature to introduce it in another form, by defining a number $\alpha_s \equiv \frac{g^2}{4\pi}$, to which we will refer when talking about the QCD coupling in the rest of this thesis.

In all quantum field theories of the Standard Model, the coupling strength varies according to the probed scale: at short distances (or large momentum exchange), the strength of the interaction will be different than at large distances (or small momentum exchange). This is due to quantum effects, namely the inclusion of loop diagrams, which are included in the calculation of the coupling strength through a procedure known as "renormalization" [7]. In the case of QCD, this procedure results, at leading-order in perturbation theory, in the following expression of α_s, which is scale-dependent [8]:

$$\alpha_s(Q^2) = \frac{4\pi N_C}{(11N_C - 2N_f)\ln(\frac{Q^2}{\Lambda^2_{QCD}})} \tag{1.3}$$

where Q^2 is the four-momentum transfer scale under consideration, Λ_{QCD} is the characteristic energy scale of QCD ($\Lambda_{QCD} \approx 200\,\mathrm{MeV}$), N_C is the number of color degrees of freedom and N_f is the number of quark flavors (so that $N_C = 3$ and $N_f = 6$). Since $11N_C > 2N_f$, the denominator of Eq. 1.3 is positive, and thus α_s decreases with increasing Q^2.

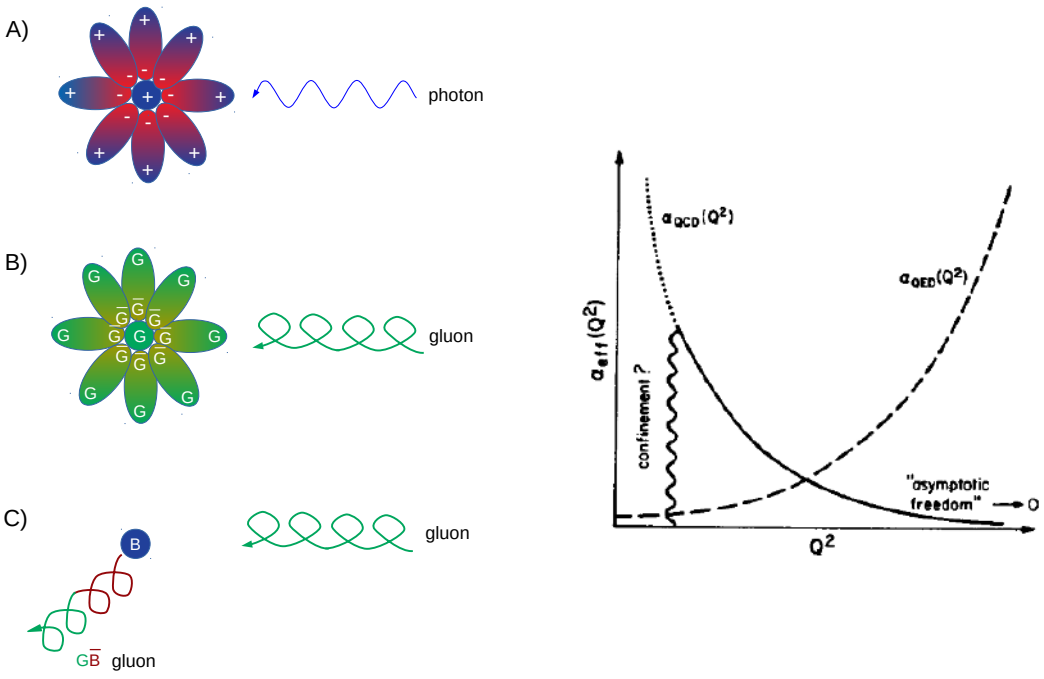

Figure 1.3: (Left) (a) Illustration of how vacuum polarization in QED shields a bare charge. (b) Same as (a) but for a green charge in QCD. (c) Shows how in QCD a charge can radiate away its color via gluon radiation, adapted from [5]. (Right) Illustration of the behavior of the QED and QCD coupling constants as a function of Q^2 [5].

This dependence is opposite to the coupling in QED. Indeed, in QED, as we increase the probed energy scale Q^2, the electromagnetic coupling $\alpha_{\text{EM}}\left(Q^2\right)$ increases. At asymptotically high Q^2, $\alpha_{\text{EM}}\left(Q^2\right)$ becomes infinite, see Fig. 1.3 (right). At low Q^2, $\alpha_{\text{EM}}\left(Q^2\right)$ is small: $\alpha_{\text{EM}}(m_e^2) \approx 1/137$, where $m_e = 511\,\text{keV}$ is the electron mass.

The physical reason for the rising coupling with increased Q^2 is illustrated in Fig. 1.3 (left, a). We consider the interaction between a virtual photon with virtuality Q^2, which sets the scale for the momentum exchange. If Q^2 is small then the photon cannot resolve small distances and "sees" a point charge shielded by the vacuum polarization, i.e. by many electron-positron pairs fluctuating from vacuum. As Q^2 increases, the photon "sees" a smaller and smaller spatial area and the shielding effect is weaker.

In QCD, the behavior of the effective coupling constant is different. The reason for this difference is that the gluons interact with each other. As illustrated in Fig. 1.3 (left, b,c), quark-anti-quark vacuum polarization shields the color charge as in QED. However, since the source can radiate color (e.g. change from red to blue by emitting a red-anti-blue gluon), the color is no longer located at a definite place in space. It is diffusely spread out due to gluon emission and absorption. As one increases the Q^2 of the incoming gluon probe, thereby looking at smaller and smaller spatial distances, it becomes less likely to find the "bare" color (green in Fig. 1.3 (left)). This effect is known as "anti-screening" and is due to the non-abelian nature of QCD [5].

As one can deduce from the running coupling in Eq. 1.3, as long as $11N_C > 2N_f$, the anti-screening prevails in comparison to the screening property. This means that the interactions between quarks and gluons become weaker as the scale Q^2 increases. This is known as "asymptotic freedom" [9, 10]. Measured values of α_s for different values of Q are shown on Fig. 1.4.

Another important feature of QCD is the phenomenon of color confinement: neither quarks nor gluons are observed as free particles in nature, and the only free states that seem to exist are color neutral, made for instance from red+green+blue colors or color+anti-color combinations. These are known as color singlets. This can be interpreted as the fact that for energy scales smaller than Λ_{QCD} (i.e. at large distances), quarks must form colorless objects known as hadrons by forming color-singlet combinations of quarks, anti-quarks and gluons. The hadrons are classified in two types, the quark-anti-quark pairs $(q\bar{q})$ called mesons, and the three quark states (qqq) called baryons[1]. These two families are illustrated on Fig. 1.5. This grouping of colored particles into colorless composite objects is known as hadronization. It is intrinsically a low-energy mechanism that cannot be described with perturbative techniques, as the QCD coupling is large at low scales. Confinement is not directly linked to extrapolating the asymptotic freedom towards large α_s: it can exist without a divergence of the coupling.

The last important feature of QCD that we will mention is chiral symmetry breaking [11]. It is related to the symmetry between the left- and right-handed parts of the quarks. A quark is right-handed when the direction of its spin is the same as the direction of its

[1]Configurations with more than 3 quarks are also allowed to form what are known as exotic hadrons such as tetraquarks, made up of four quarks, or pentaquarks, made up of five quarks and measured by the LHCb collaboration in 2015. These are outside the scope of this thesis.

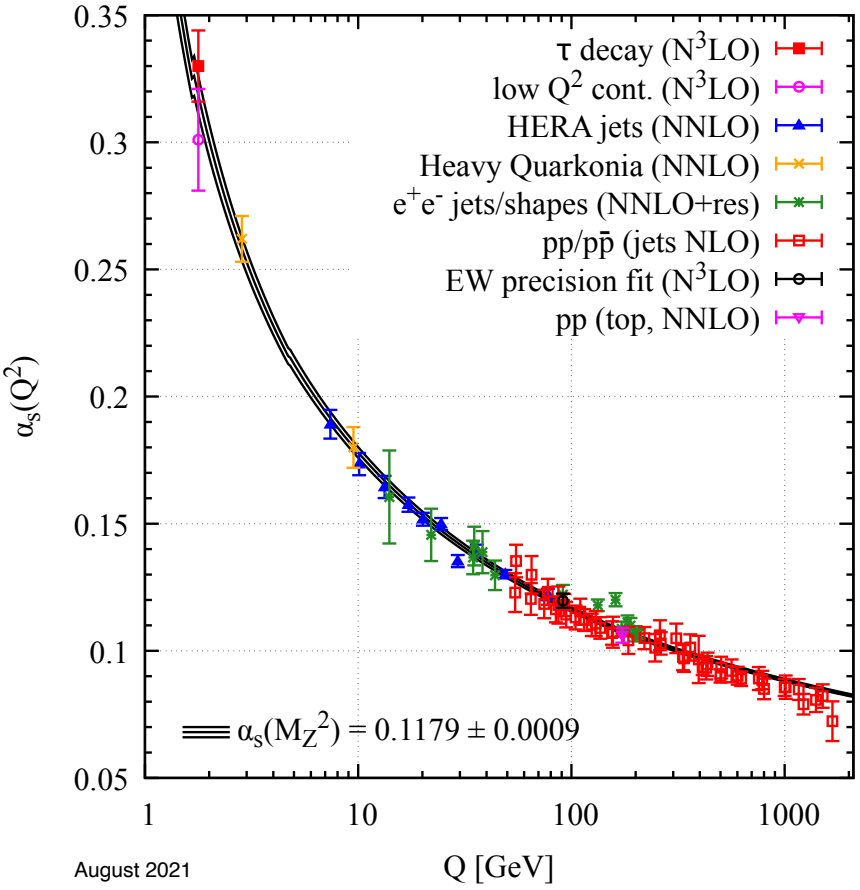

Figure 1.4: Summary of α_s measurements as a function of the energy scale Q [6]. The respective degree of QCD perturbation theory used in the extraction of α_s is indicated in brackets (NLO: next-to-leading order; NNLO: next-to-next-to-leading order; NNLO+res.: NNLO matched to a resummed calculation; $\mathrm{N^3LO}$: next-to-NNLO).

motion, while it is left-handed when the directions of spin and motion are opposite. In the limit of vanishing quark masses $(m_q \approx 0)$ the QCD Lagrangian Eq. 1.1 shows no interactions between left- and right-handed quarks and thus preserves chiral symmetry, i.e. the two states do not mix with each other. In addition, in the vacuum, the chiral symmetry is also spontaneously broken by the chiral condensate $\langle\bar{\psi}\psi\rangle = \langle\bar{\psi}_L\psi_R + \psi_L\bar{\psi}_R\rangle$ populating the QCD vacuum, which can spontaneously annihilate with a left-handed quark for right-handed one and vice-versa.

The non-abelian nature of QCD, confinement, and breaking of symmetry, make any direct QCD calculation very complicated. However, at high momentum scale $Q^2 \gg \Lambda_{\mathrm{QCD}}$ (or short distances), the QCD coupling α_s becomes sufficiently small ($\alpha_s(10\,\mathrm{GeV}) \sim 0.2$) so that perturbation theory can be applied; quantities such as cross sections can be written as expansions in powers of α_s, and truncated to a given order to get an approximate estimate of the solution. In the context of QCD, such techniques are known as perturbative QCD (pQCD) [12]. In addition, a well-established computational approach is lattice QCD

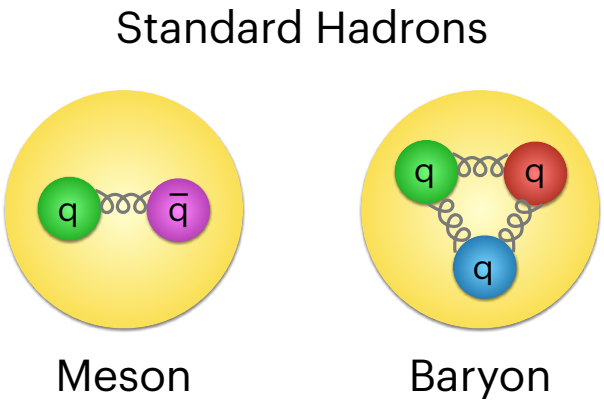

Figure 1.5: Illustration of the two families of known standard hadrons: mesons and baryons. Made by Batoul Diab.

(lQCD) [13], in which a gauge theory is formulated on discretized space and (imaginary) time, formed by a lattice of points. The QCD solutions are recovered when the lattice spacing is reduced to zero and the lattice size grows to infinity.

1.2 The Quark-Gluon plasma

At the densities and temperatures present in most of the current universe, the quarks and gluons are confined into hadrons. However, the properties outlined in Sec. 1.1 suggest that QCD matter has non-trivial thermodynamic properties. Indeed, at high temperature, nuclear matter contains a population of thermally excited hadrons, mostly pions [14]. Their typical momentum scale is set by the temperature T. At very high temperature, $p \sim T >> \Lambda_{\mathrm{QCD}}$, such that the scattering between the thermally excited hadrons probe very short distances, according to asymptotic freedom. Thus, these scatterings probe their quark and gluon content. In addition, the density of thermally excited particles scales like $n \propto T^3$. Hence, at high temperatures, the hadronic wave functions will overlap and nuclear matter can no longer be described in terms of hadronic degrees of freedom, but rather in terms of interactions between quarks and gluons. In other words, as temperature grows, this simple idea suggests that there is a transition from a confined state of hadronic matter to a new deconfined state. This particular state of matter is known as the Quark-Gluon Plasma (QGP).

In cold nuclear matter, a similar transition is expected to arise at high net baryonic density. This density is defined as $n_B = (n_q - n_{\bar{q}})/3$ where n_q is the quark density and $n_{\bar{q}}$ is the anti-quark density. In ordinary nuclear matter, the density of nucleons is such that $n_B \sim 0.16\,\mathrm{fm}^{-3}$ [15]. This corresponds to a so-called "baryon chemical potential" $\mu_B \sim 924\,\mathrm{MeV}$. At very large densities ($n_B \geq 0.5\,\mathrm{fm}^{-3}$), the wave functions of hadrons will start to overlap and, similarly to the high temperature case above, the relevant degrees of freedom to describe this state of matter will be quarks and gluons [16]. Such a mechanism predicts that a QGP-like state of matter at high density could constitute the core of neutron stars [17].

From these considerations, one can draw a picture of a phase diagram of QCD matter like the one shown on Fig. 1.6: for baryon chemical potentials μ which are on the order of $900\,\mathrm{MeV}$ or smaller, and for temperatures $T < \Lambda_{\mathrm{QCD}} \sim 200\,\mathrm{MeV}$, nuclear matter is made of hadrons. On the other hand, for $T, \mu \gg \Lambda_{\mathrm{QCD}}$, nuclear matter is described by quark and gluon degrees of freedom. The natural question which emerges is whether the "hadron phase" and the "quark-gluon phase" (the QGP) are separated by a phase transition in the thermodynamic sense. The determination of the nature of this phase transition would in addition have a strong impact on other fields, especially in cosmology [18, 19, 20].

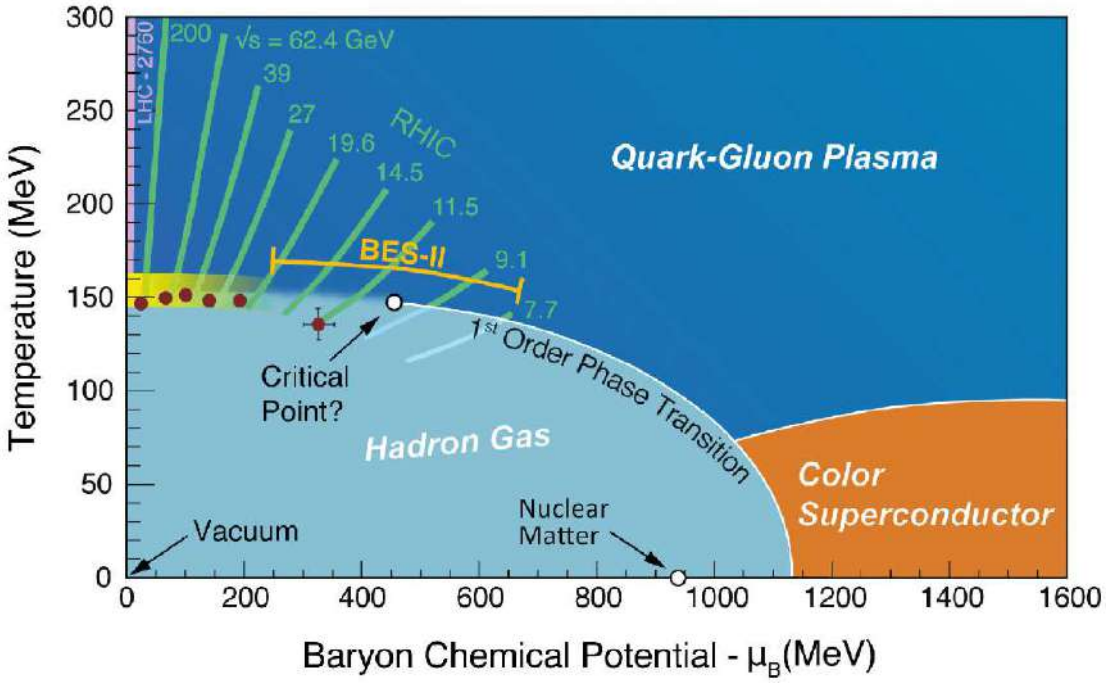

Figure 1.6: The QCD phase diagram as a function of baryon chemical potential and temperature [21].

The investigation of the nature of the phase transition requires the study of order parameters that indicate the degree of regularity in the transition from one state of matter to another. In the limit of no dynamical quarks (e.g. quarks with infinite mass and only free gluons), the order parameter of the QGP-hadron transition is the so-called Polyakov loop $\langle L(\mathbf{x})\rangle$ [16]. In QCD, this parameter can be expressed as $\langle L(\mathbf{x})\rangle \propto e^{-F_Q/T}$, where F_Q is the free energy of a sole quark in the medium [22]. For the hadronic phase, quarks are confined and it takes an infinite amount of energy to isolate a quark, hence $F \sim \infty$, so $\langle L(\mathbf{x})\rangle = 0$. If this order parameter is non-zero, this implies that the free energy of a quark is finite. This indicates the liberation of colored degrees of freedom, i.e. deconfinement.

Another order parameter that can be studied, now in the limit of vanishing quark masses, is the restoration of chiral symmetry. Indeed, as mentioned in Sec. 1.1, the QCD Lagrangian is symmetric under the exchange of left- and right-handed quarks. This leads to a theory

which has chiral symmetry and massless pions. The small explicit breaking of the symmetry by the quark masses gives a non-zero mass to pions. But the large mass difference between mesons, for instance the ρ ($\sim 776\,\mathrm{MeV}$) and $a1$ ($\sim 1230\,\mathrm{MeV}$), indicates that this symmetry is dynamically broken by vacuum chiral condensates. However, the thermal dependence of the meson masses and of the condensate expectation value can be computed through chiral perturbation theory [11]. It shows that the breaking of symmetry no longer holds at high temperatures. Thus, all the meson masses would become degenerate at sufficiently high temperature, and chiral symmetry would be restored.

These two parameters are important to understand the nature of the phase transition between hadrons and the QGP, as well as to understand the properties of QCD at finite temperature.

For realistic quark masses and zero net-baryon density, and via the study of these two order parameters, lattice QCD calculations (see e.g. [23]) indicate that hadronic matter indeed undergoes a transition from a confined to a deconfined state at high temperatures. However, there is no actual phase transition, but rather a cross-over around a pseudo-critical temperature T_c, which can be computed by locating the maximum of the susceptibility of an order parameter, i.e. identifying the point at which fluctuations of the parameters are the largest. Remarkably, for the two considered order parameters, Polyakov loop and chiral condensate expectation value, lQCD calculations show very similar pseudo-critical temperatures around $T_c \sim 155\,\mathrm{MeV}$ [14].

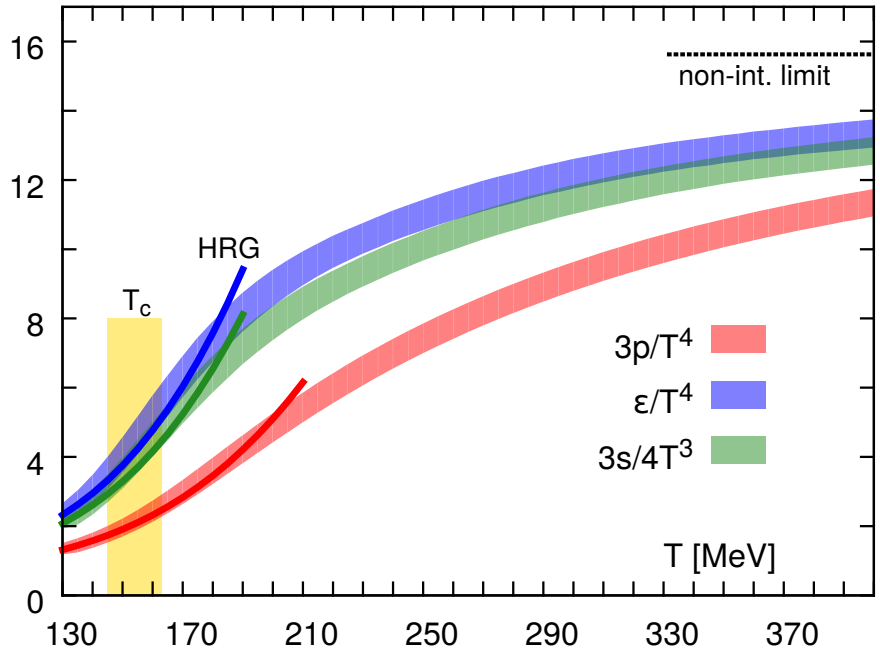

Figure 1.7: Equation of state of QCD with 2+1 flavors. This shows the normalized pressure, energy entropy density as a function of the temperature. The red band corresponds to the equation of state for pressure, the blue band corresponds to the one for energy density, and the green one is for entropy density. The vertical band at $T_c = (154 \pm 9)\mathrm{MeV}$ indicates the critical temperature [24].

Another remarkable feature of lQCD computations, is that they can provide estimates for the evolution of energy and entropy density in a QCD medium at finite temperature [24, 25], displayed on Fig. 1.7. Although we clearly see a transition from a hadron gas to another state of matter with different degrees of freedom, even at very high temperatures $T \gg T_c \sim 155\,\mathrm{MeV}$, these degrees of freedom are still far below in value than the limit of non-interacting quarks and gluons. Thus, contrary to what one might have naively assumed from asymptotic freedom, even at high temperature, QCD does not behave as a gas of free roaming quarks and gluons, with no inter-particle interactions, but rather as a strongly interacting fluid [2]. This finding confirmed that the equation of hydrodynamics could be used to model this deconfined medium, as was observed before at the Relativistic Heavy Ion Collider [26, 27, 28, 29] In addition, due to its strongly interacting properties, one can associate a very low viscosity to this fluid. We will come back to this consideration in the following chapters.

1.3 Ultrarelativistic heavy-ion collisions

Lattice QCD calculations have established the existence of this phase of strongly interacting QGP at temperatures larger than the pseudo-critical temperature $T_c \sim 155\,\mathrm{MeV}$ [23]. This corresponds to a critical energy density of the order of $1\,\mathrm{GeV\,fm^{-3}}$ [30]. In order to reach this high initial energy density, heavy-ions are accelerated to ultrarelativistic velocities and collided at the interaction points of dedicated facilities. The term “ultrarelativistic” signifies that the kinetic energy of the nucleons being collided is far greater than their rest energy ($p \gg m$). Ultrarelativistic heavy-ion collision (HIC) experiments aim at understanding the behavior of nuclear matter at these high energies. It can give us access to the dynamics of the fundamental constituents of hadrons in extreme conditions and thus enable us to learn more about the structure of matter and the behavior of QCD at different scales.

They are also interesting because of their capability to generate large interacting systems ($\sim 10\,\mathrm{fm}$ being the typical length scale) as well as large numbers of quarks and gluons through the collisions. Therefore, the system is large enough to be described by thermodynamic ensembles and reaches the required high energy densities while maintaining a near zero net-baryon density. As such, HIC experiments are the only accessible way to generate QGP in the laboratory.

HIC experiments started in the mid-1970s. Nowadays, there are mainly two laboratories which study matter using ultrarelativistic heavy-ion collisions: the Relativistic Heavy Ion Collider (RHIC) at Brookhaven National Laboratory and the Large Hadron Collider (LHC) at CERN. In such experiments, in a first step towards the collision of heavy nuclei, the chosen element (Pb, Au, U ...) is heated up to vaporize. Then, thanks to their passage through several accelerating rings with increasing size and power, they get ultrarelativistic speed.

[2] This terminology can be a source of confusion, as, since the QGP is expanding into vacuum, it experiences a compressible flow. The term "ideal fluid" can sometimes be understood as being reserved for incompressible flow, whereas one could talk about "gas dynamics" in the context of compressible fluids. In the following, gas-like behavior refers to no inter-particle interactions, whereas ideal (or perfect) fluid will mainly be used as a synonym of inviscid fluid, i.e. with large Reynolds number, which can be the case for both compressible and incompressible fluids.

At the LHC, lead ($^{208}\,\mathrm{Pb}$) is mainly used, and three main types of collisions are achieved to study hadronic matter: proton-proton collisions (pp collisions), proton-lead (pPb) and lead-lead (Pb–Pb). This allows to study the evolution of the QGP and to investigate other important questions such as the nature of the different QCD phase transitions, or the hadronic structure.

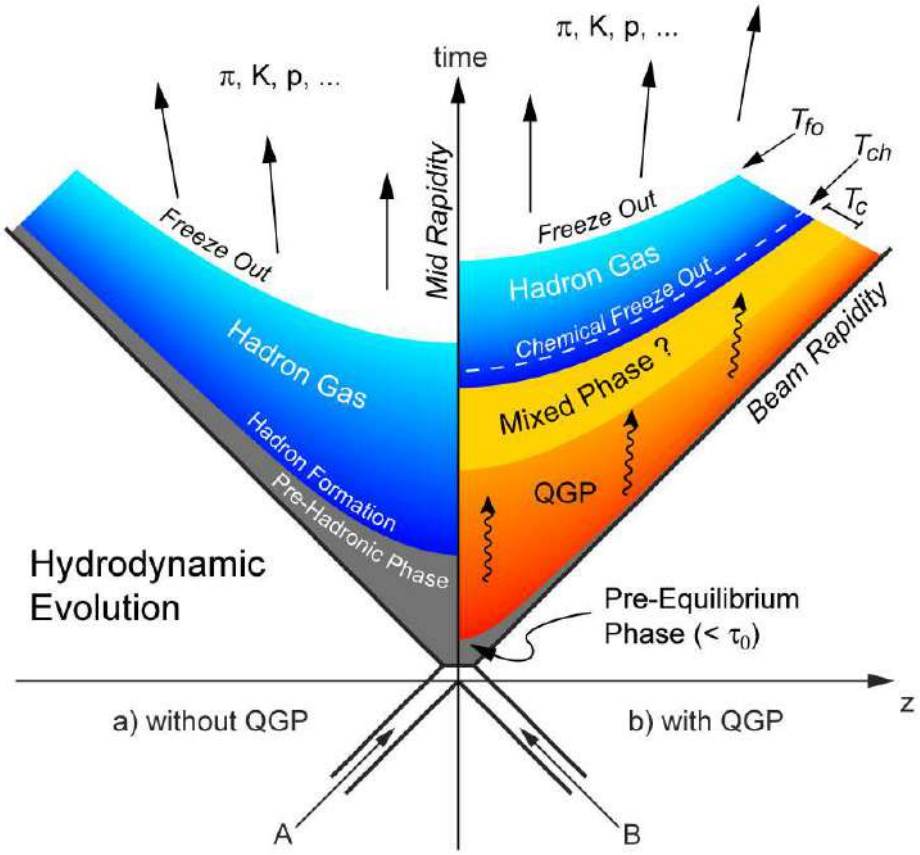

Figure 1.8: Illustration of the Bjorken scenario of heavy-ion collisions, with or without QGP formation [31].

Due to the ultrarelativistic speed, the colliding nuclei in a HIC are highly Lorentz contracted along the longitudinal beam direction by a factor γ. As a result, they appear like flattened disks. For Pb–Pb collisions at $\sqrt{s_{NN}} = 5\,\mathrm{TeV}$, each Pb beam has an energy of $2.5\,\mathrm{TeV}$ per nucleon, equal to $m_N\,c^2(\gamma - 1)$. Thus $\gamma \sim 2500$. The nucleus longitudinal extent is then $L_z = 2R/\gamma \sim 8 \times 10^{-3}\,\mathrm{fm}$, where $R \sim 10\,\mathrm{fm}$ is the Pb nucleus radius.

After the crossing of these two "pancakes", the deposited energy goes through different stages, as illustrated on Fig. 1.8, ending up with an ensemble of particles flying freely to the detector. We now give a schematic summary of the current understanding of these different phases for Pb–Pb collisions at the LHC as a function of proper time τ:

- At the very beginning of the collision ($\tau \sim 0\,\mathrm{fm}/c$), energy deposition and hard scatterings occur between quarks and gluons from the two colliding nuclei. These

scatterings include the production of particles with high transverse momentum, as well as heavy quarks (i.e. charm or bottom quarks). At this stage, most of the constituents of the colliding nuclei, quarks and gluons, form a dense phase far from equilibrium.

- Next comes the pre-equilibrium stage. At the end of this evolution, the system thermalizes[3] at time $\tau \sim 1 - 2\,\mathrm{fm}/c$: the bulk of the non-equilibrium medium comes to a state of thermal equilibrium. Experiments suggest a fast thermalization process [32] but this is not fully understood theoretically yet. This stage will be our main focus in the last chapter of this thesis.

- The QGP in equilibrium evolves approximately in the time interval $2 \leq \tau \leq 10\,\mathrm{fm}/c$. At this stage, the matter behaves as an almost perfect fluid, which can be described by hydrodynamics [33, 34]. During its evolution, the QGP expands and its local temperature falls. When it gets below a certain limit ($T \sim 150 - 170\,\mathrm{MeV}$), quarks become confined within color-neutral hadrons and the system forms an interacting gas of hot hadrons. This step, called hadronization, takes place in the interval $10 \leq \tau \leq 20\,\mathrm{fm}/c$. The subsequent hadronic state after hadronization is well-described as a gas of hadrons and hadronic resonances.

- Finally, at time $\tau \longrightarrow \infty$, the system reaches freeze-out, i.e. the equilibrium breaks down. At this stage, hadrons stop interacting strongly and colliding inelastically: they undergo chemical freeze-out, so the particles' number stay conserved [14]. Chemical freeze-out is then followed by kinetic freeze-out where the hadrons stop having elastic collisions as well. The resulting hadrons then fly freely to the detector.

We now give definitions of some kinematic variables which are extensively used to describe such experiments. From now on and to the end of this report, to simplify the expressions, we will use the natural units in which $\hbar = c = k_B = 1$.

In HICs, one often refers to the energy of the collision by the invariant mass of two colliding nucleons, each belonging to a different nucleus, which is noted $\sqrt{s_{NN}}$. In what follows, we will often refer to collisions at energies of $5\,\mathrm{TeV}$, meaning $\sqrt{s_{NN}} = 5\,\mathrm{TeV}$.

Another important variable is transverse momentum p_T. A HIC experiment consists of two colliding beams, each following an axis named the beam axis. We can define a system of coordinates with respect to this axis. We call the direction of the beam axis the longitudinal direction and the plane orthogonal to it, the transverse plane. We can decompose each momentum vector into its longitudinal and its transverse components: $\vec{p} = \vec{p_L} + \vec{p_\mathrm{T}}$. The transverse component is particularly important as it is invariant under longitudinal boosts; if we consider a detector which is not located right above the collision point but further down the beam axis (this is called forward geometry), a particle will need to have some longitudinal boost to hit this detector. In this case, the transverse momentum will be the same wherever we put the detector on the axis.

[3] As we will explain in later chapters, with thermalization we imply the applicability of hydrodynamics rather than local thermal equilibrium that may be reached only later.

Let us now define the rapidity and the pseudo-rapidity of a particle. The rapidity y is given by the formula $y = \frac{1}{2}\ln(\frac{E+p_L}{E-p_L})$ where E is the energy and p_L is the longitudinal momentum of the particle. It is a generalization of the longitudinal velocity $\beta_L = \frac{p_L}{E}$ and is additive with respect to longitudinal boosts; if a particle in a frame S' has rapidity y' and the frame S' has rapidity y'' with respect to another frame S, then the particle will have a rapidity $y = y' + y''$ in the frame S. So the rapidity of a particle gives us information about its longitudinal boost.

The pseudo-rapidity η is a related quantity but of more convenient use in experimental setups. It is defined as : $\eta = -\ln(\tan(\frac{\theta}{2}))$ where θ is the angle between the beam axis and the particle's trajectory. We have the relation $y \simeq \eta$ when $p \gg m$.

A historical, as well as practical, picture to describe the early times of the collision right after this crossing is known as Bjorken flow, see Bjorken's paper [35], or a more pedagogical approach in [36]. First, it is assumed that, since the motion of the two colliding nuclei is longitudinal, the motion of all produced particles is also close to the longitudinal direction: $p_x = p_y = 0$. In addition, all particles at a given position z have the same longitudinal velocity $v_z = z/t$. In a hydrodynamic approach, the produced particles are collectively modeled as a fluid, and the particle velocity v_z is also the fluid velocity. This prescription is boost invariant, in the following sense: if one does a Lorentz transformation along the z axis, all three quantities v_z, z, t are transformed, but $v_z = z/t$ still holds in the new frame. This is illustrated in Fig. 1.9. This variable v_z is related to the fluid rapidity y by $v_z = \tan y$. With the Bjorken prescription $v_z = z/t$, y is equal to the space-time rapidity which is defined as $y_s \equiv \operatorname{atanh}\left(\frac{z}{t}\right)$. This boost invariance is the basis of Bjorken flow, and is supported by initial state and early time models such as Color Glass Condensate and Glasma [37, 38, 39]. We see that this model describes a 1-dimensional expansion, along the longitudinal direction. It is expected to be valid at early times, in a stage where radial and elliptic flow have not yet developed.

1.4 Initial state and pre-equilibrium

It was established in the late 60's and 70's that the proton is not a point-like particle but is a composite structure of elementary particles [40]. This was first discovered at SLAC by probing the structure of the proton with virtual photons emitted by high-energy electrons, in so-called deep inelastic scattering (DIS) measurements. Such measurements later culminated at facilities such as the HERA experiments at DESY.

These scattering experiments allowed to measure the structure functions of the proton as a function of the momentum exchanged Q^2 between the electron and the proton, which is the virtuality of the exchanged photon, i.e. $Q^2 = -q^2$ where q is the four-momentum of the photon. These were incompatible with a point-like proton and rather suggested that it is made up of a collection of smaller particles, named partons [41]. The starting point of this "parton model" is to assume that in the infinite-momentum frame, where the incoming proton and outgoing state have opposite momentum, the time scale of the interactions between the constituents of the proton is very large compared to the

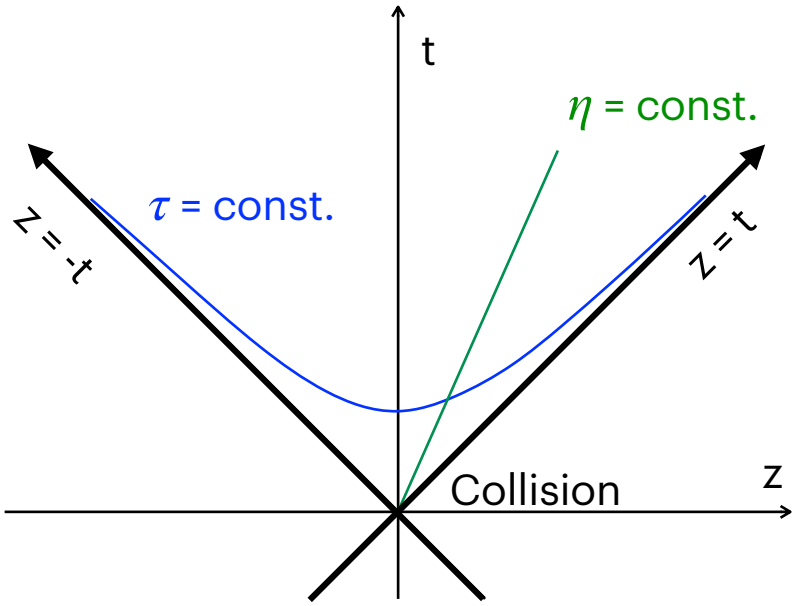

Figure 1.9: Nucleus-nucleus collision in the (z, t) plane, where z is the longitudinal position along the beam axis and t is time in the laboratory frame of reference. The thick lines are the trajectories of the colliding nuclei. The lines of constant proper time τ and space-time rapidity η are also shown. Adapted by Batoul Diab from [36].

time scale of the interaction with the virtual photon. In this frame, one can define the so-called Bjorken-x variable, which is the longitudinal momentum fraction of the probed parton in the nucleon. Then, the probed proton appears as a collection of approximately non-interacting partons [42]. Today, these partons are understood to be the quarks and gluons of QCD which make up all hadrons.

DIS experiments allowed to extract the parton distribution functions (PDFs), which measure the probability of finding a parton of a given nature[4], at a given longitudinal momentum fraction x, when the proton is probed at a scale Q^2. The PDFs are non-perturbative functions that cannot be determined from first principles, but they are, however, universal objects. This means that for instance, the extraction of PDFs from DIS experiments allows to predict cross-sections for other processes, such as Drell-Yan production in proton-proton scatterings. Sets of PDFs are extracted from global fits to the available data by various groups, probing the proton content at multiple scales. In addition, pQCD calculations manage to predict the Q^2 dependence of these extracted PDFs [43, 44, 45]. Various theoretical collaborations perform these fits with subtle differences. A depiction of the PDFs of the proton is presented on Fig. 1.10.

We see that the probability of finding valence quarks (the constituent quarks in the quark model of QCD) peaks at x values of $0.1 - 0.2$, and is higher for the u than the d quark, as we would expect from the quark model stating that protons are made of uud

[4]Gluon or quarks of different flavors.

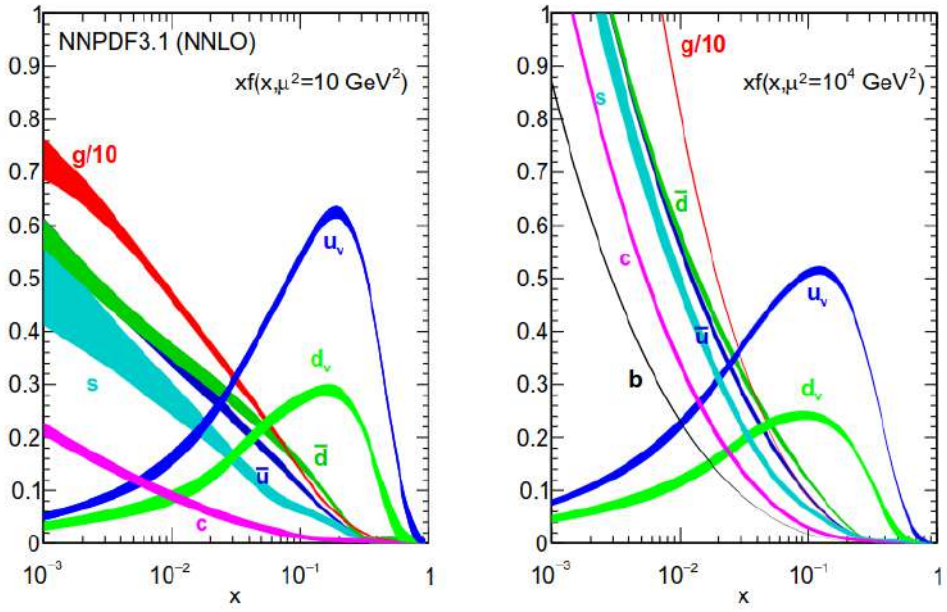

Figure 1.10: Parton distribution functions versus their momentum fraction x in the proton, at two different probing scales corresponding to typical energies of the final states of 3 or $100\,\mathrm{GeV}$ [46].

constituent quarks. However, we also see that there are other quarks created by the various interactions among partons in the proton, called "sea quarks". And the probability density of these sea quarks rises with decreasing x. Finally, the gluons are the most numerous partons at low x.

Indeed, a parton with momentum p can emit and reabsorb a gluon with transverse momentum k_T, in the form of fluctuations. The lifetime of such a fluctuation can be estimated as $\Delta t \sim \frac{2x(1-x)p}{k_T^2}$. For high enough energy, $xp \gg k_T^2$, these fluctuations become long-lived. The emitted parton carries a fraction x of the total momentum of the nucleon even smaller than the one of its parent parton. In addition, since the daughter parton is long-lived, it can further fluctuate into additional partons with even smaller x. Hence, the probed nucleon becomes populated by parton with smaller and smaller x. Hence, increasing the collision energy, which corresponds to smaller probed values of x, allows to probe smaller and smaller values of x and thus probe larger gluon phase-space density. As a consequence, processes which kinematically favor low-x partons will be dominated by gluon-initiated reactions; this is the case for instance for heavy-quark production which is dominated by gluon fusion processes [47]. We also see that the proton is a far more complicated object than the naive quark model that QCD suggested.

The parton distributions of the proton are known with good precision over a broad range of Bjorken-x down to about 10^{-4} based on data from HERA and electroweak boson measurements [48].

Let us now elaborate on what happens during the first instants of a proton-proton collision, in particular the hard particles produced during the initial scatterings between the

partons making up the protons. The production cross-section of these hard particles can be calculated by assuming a separation of scales between the non-perturbative processes determining which partons from the protons will interact, and the hard scattering of partons which is calculated pertubatively. This is known as factorization [8]. In particular, in collinear factorization, the production cross-section of a particle is expressed as a convolution of the PDFs in the initial state and a cross section associated with the hard partonic process. Hence, the cross-section for a given process in the collision of hadron h_1 with hadron h_2 can be written as [49]:

$$\sigma_{\mathrm{pp}\to HX}\left(s,Q^2\right)=\sum_{i,j}\int \mathrm{d}x_1\,\mathrm{d}x_2 f_{i/h_1}\left(x_1,\mu_F^2\right) f_{j/h_2}\left(x_2,\mu_F^2\right)\sum_{n=0}^{\infty}\alpha_S^n\left(\mu_R^2\right)\hat{\sigma}^n_{i,j\to H}\left(\hat{s},\mu_R^2,\mu_F^2\right), \tag{1.4}$$

where HX is the produced final state, x_1 and x_2 are the momentum fractions of the interacting partons, and $f_{i/k}\left(x_k,Q\right)$ is the PDF for a parton of type i to be found with momentum fraction x_k in the proton k. The sum over n runs over powers of the coupling constant α_S and represents the perturbative series which can be cut at a given order. Then, $\hat{\sigma}^n$ is the cross section of the partonic hard scattering at energy $\hat{s}=x_1x_2s$ at order n in the perturbative α_S expansion and it is further controlled by two parameters, which are artefacts of the perturbative expansion, the renormalization scale μ_R and the factorization scale μ_F [49]. A common choice is to set both the factorization and renormalization scale to the external hard scale Q^2, or to vary this choice to assess the impact of higher order corrections in the perturbative expansion.

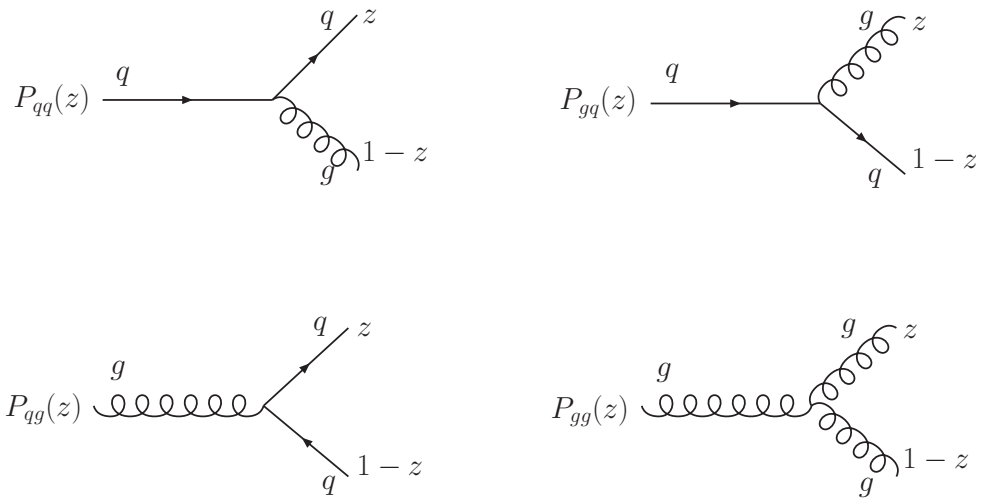

Figure 1.11: Illustration of the splitting processes associated with the splitting kernels which intervene in the DGLAP equations which describe the scale evolution of parton distribution functions [50].

The non-perturbative PDFs depend logarithmically on the scale μ at which it is evaluated, due to the splitting of partons. This dependence is given by the Dokshitzer-Gribov-Lipatov-Altarelli-Parisi (DGLAP) evolution equations [43, 44, 45], which allow to determine

the PDFs $f_i\left(x, Q^2\right)$ at all scales μ when it is known at some scale μ_0:

$$\frac{\mathrm{d}f_i\left(x,\mu\right)}{\mathrm{d}\log\mu^2} = \sum_j \int_x^1 \frac{dz}{z}\frac{\alpha_s}{2\pi} P_{ij}(z) f_j\left(\frac{x}{z},\mu\right) \tag{1.5}$$

where $P_{ij}(z)$ is the splitting kernel that determines the probability for a parton of type i to split into a final state containing a parton of type j, as illustrated in Fig. 1.11. These splitting functions are also at the core of parton showers, meaning that a parton produced in a hard processe splits multiple times until the daughter partons reach the hadronization scale forming a spray of collimated hadrons observed in the experiments, known as a jet[5].

This collinear-factorization formalism is widely used in high-energy physics to calculate production cross sections of jets, heavy quarkonia[6] (further discussed in a specific section), weak-gauge bosons and the Higgs particle [49].

Nuclei cannot be viewed as bags of independent nucleons and cannot be described as a mere superposition of proton and neutron PDFs, because interactions between protons and neutrons affect the momentum and density distributions of their constituent partons. The actual measured distribution of partons in nuclei, known as nuclear PDFs (nPDFs), show modifications from the free proton and neutron PDFs, as can be seen on Fig. 1.12.

Depending on the nPDF being depleted or enhanced with respect to the free PDF, one can notice different regions:

- the shadowing region for $x < 10^{-2}$
- the antishadowing region around $x = 10^{-1}$
- the EMC-effect region around $x = 5 \cdot 10^{-1}$

Although there is no definite theoretical description of these modification effects, some phenomenological interpretations exist. Shadowing is usually attributed to multiple scattering [51] or consequences of gluon saturation [52]. Antishadowing can be understood as a consequence of sum rules and quantum number balancing the modifications at lower x due to shadowing. The EMC-effect is often associated with short-range correlations or Fermi-motion at high-x [53]. These nuclear modifications are often assumed to follow the same Q^2 dependence as the proton PDFs, i.e. following the DGLAP evolution equations.

[5]The main difference is that the partons splittings in PDF evolution is time-like, whereas the parton shower in the fragmentation of jets is space-like.

[6]Other approaches exist, in particular in the context of semi-inclusive observables, where the focus is on the production of heavy quarkonium with very low transverse momentum $p_{\mathrm{T}} \ll m_{\mathrm{Q\bar{Q}}}$ in Semi-Inclusive-Deep-Inelastic scattering (SIDIS). For this type of observable, the transverse momentum of the produced quarkonium is low enough so that it can be produced by the transverse momentum of the partons inside the proton. This low transverse momentum is non-perturbative and, as in collinear factorization, can be produced by the non-perturbative evolution of the parton distributions. In this approach, parton distribution functions which are convoluted with the hard scattering cross section are now allowed to have a associated transverse momentum k_{T}.This is known as the Transverse-Momentum-Dependent factorization (TMD factorization) framework.

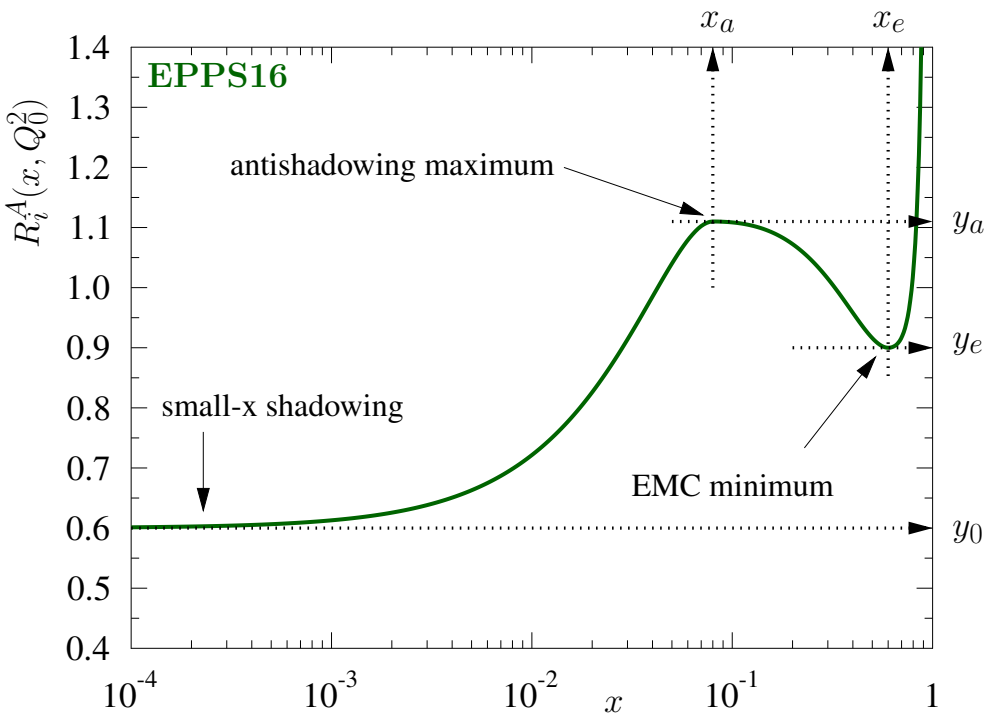

Figure 1.12: Illustration of the EPPS16 $R_i^A\left(x, Q_0^2\right)$, which is the ratio of the nPDF, within a nucleus of mass number A, by the free proton PDF for the parton of type i [54].

Since heavy ions are extended objects with transverse size of order $\sim 10\,\mathrm{fm}$, at high energy, each collision between two of them has a specific geometry characterized by quantities such as the impact parameter b between the colliding nuclei, the number of participating nucleons N_{part}, and the number of binary nucleon-nucleon collisions N_{coll}.

The Glauber Model [55] is a tool to infer these event-by-event quantities using geometric considerations. In this model, the collision of two nuclei is seen as the superposition of individual interactions of the constituent nucleons. The number of participating nucleons, N_{part} , represents the total number of nucleons which undergo at least one inelastic nucleon-nucleon collision (the nucleons which do not participate in collisions are usually referred to as spectators). N_{coll} is the total number of binary nucleon-nucleon collisions (each nucleon with different nucleons). The numbers N_{part} and N_{coll} are both important quantities that cannot be determined directly from measured cross-sections but can be computed with this model.

The Glauber Model depends on inputs that can be determined experimentally, such as nuclear density or the nucleon-nucleon cross section. An important use of this model is the inference of the geometry of a given collision from the measured number of charged particles (this is known as the "charged-particle multiplicity" and is usually given per unit of pseudo-rapidity $dN_{\mathrm{ch}}/d\eta$). Indeed, as illustrated on Fig. 1.14, this model gives a relation between N_{part}, the impact parameter b, and the total charged-particle multiplicity N_{ch}. Hence, the multiplicity of a given collision gives access to its impact parameter. More precisely, the collisions are sorted into different bins of multiplicity, known as "centrality classes". The 0-10% centrality class corresponds to the top decile of collisions in the mul-

tiplicity distribution, while the 90-100% centrality class corresponds to the last decile. The 0-10% or 0-5% centrality classes have an associated impact parameter b which is close to zero. This means that these collisions are almost head-on, and are known as "central" collisions. On the other hand, collisions in the lower centrality classes are "peripheral" collisions and correspond to large impact parameters between the colliding nuclei.

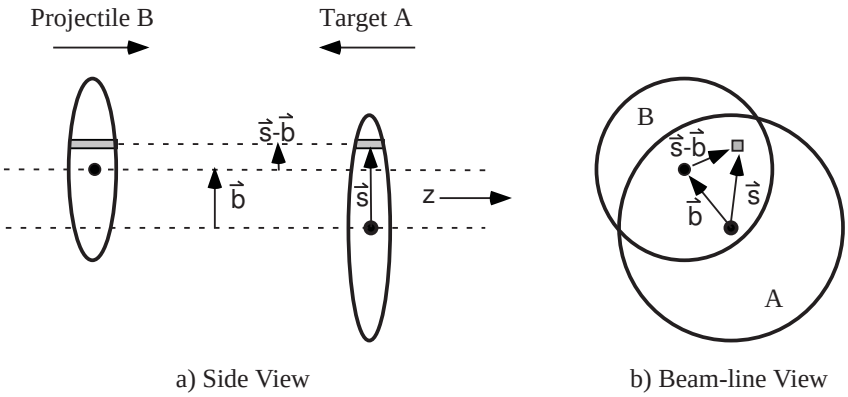

Figure 1.13: Schematic representation of the Optical Glauber Model geometry, with transverse (a) and longitudinal (b) views [55].

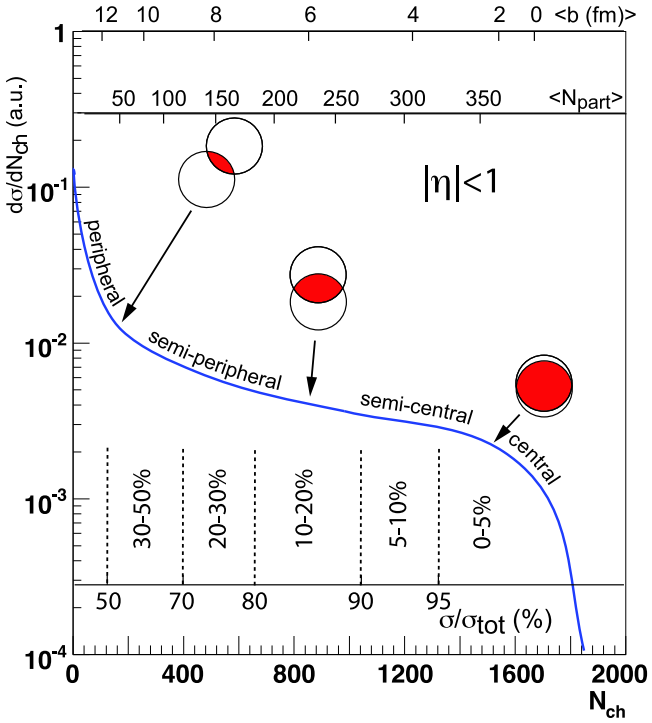

Figure 1.14: Illustration of the correlation of between charged-particle multiplicity N_{ch}, number of participant N_{part} and impact parameter b. The division in different centrality classes is also shown [55].

1.5 Probing the QGP

As we saw in Sec. 1.2, lattice QCD calculations predict that the experimental conditions achieved in heavy-ion collisions, almost zero μ_B and high temperature $T > T_c$, are such that the strongly interacting matter undergoes a transition to a deconfined medium, with restored chiral symmetry, known as the QGP. This transition occurs when a sufficient energy density is reached.

The midrapidity region corresponds to $\eta \sim 0$, i.e. particles produced at an angle from the beam pipe of about $\sim 90°$. Let us estimate the early energy density in this region in heavy-ion collisions. As it is well known in relativistic statistical physics, entropy and particle multiplicity are both extensive quantities which have the same scaling with temperature $\propto T^3$. Hence, the final entropy per unit rapidity dS/dy can be related to the number of charged particles per unit rapidity $dN_{\rm ch}/dy$ by a simple factor S/N. As we will see in a later chapter, it has been estimated to be about $S/N \sim 6.7$. In a Pb–Pb collision at the LHC at $\sqrt{s_{NN}} \sim 5\,\mathrm{TeV}$collision energy, the typical charged-particle multiplicity is $dN_{\rm ch}/dy|_{y=0} \sim 1900$ in the midrapidity region [56]. Thus $dS/dy|_{y=0} \sim 12700$. We now assume that after its creation and equilibration, the evolution of the QGP is isentropic, so that its total entropy is the same in the final state and right after its equilibration. This assumption is an approximation, since there is some entropy production in particular at the hadronization stage. Then the entropy density varies uniquely according to the expansion of the QGP 4-volume. We can then access the initial entropy density:

$$s\left(\tau_0\right) = \frac{1}{A\tau_0}\frac{\mathrm{d}S}{\mathrm{d}y}\bigg|_{y=0}.$$

where τ_0 is the formation time and A is the transverse surface. We use $\tau_0 \sim 1\,\mathrm{fm}/c$. For central Pb-Pb collisions, $A \sim 110\,\mathrm{fm}^2$. Then $s\left(\tau_0\right) \sim 115\,\mathrm{fm}^{-3} = 0.88\,\mathrm{GeV}^3$. Lattice QCD calculation gives an estimate of the relation between entropy density and temperature: $s(T) \sim 14\,T^3$. Then we get an initial temperature at the formation of the QGP of $T_0 = 397\,\mathrm{MeV}$, which is well above the pseudo-critical temperature determined by lattice QCD calculation $T_{ps} \sim 155\,\mathrm{MeV}$. This indeed confirms the idea of the formation of a hot deconfined medium with high entropy density.

Using a similar calculation, we can estimate the time at which the produced medium has cooled down enough to reach the pseudo-critical temperature; we get $\tau_{ps} \sim 17\,\mathrm{fm}/c$. We see that the lifetime of this deconfined medium is incredibly short, and the characteristics of the QGP can only be probed through the study of indirect observables. The currently exploited probes to access these observables can be put in different categories, explained hereafter.

Soft probes: Most of the particles produced in a typical heavy-ion collision are known as soft, meaning that their energy and momentum are $\lesssim \Lambda_{\rm QCD}$. These particles are in majority pions, kaons and protons. The soft physics explored with the study of these particles gives access to the late stages of the medium evolution. In particular, they are relevant to inquire hydrodynamic properties of the QGP, through the measurement of collective

behaviors between detected particles. These are known as "flow" observables. An example of such an observable is the elliptic flow [57]: in non-central heavy-ion collisions, the overlap region between the two colliding nuclei has an "almond-like" shape. This shape causes an azimuthal anisotropy of the produced medium in coordinate space. Due to the hydrodynamical behavior of the QGP, this anisotropy in space will cause a difference in pressure gradients between the long and short axis of the almond-shaped deposited energy region. This difference in gradients of pressure then generates, according to the equations of hydrodynamics, an anisotropy in momentum space: particles will tend to be produced with a momentum larger in the direction of the short axis of the almond than in the orthogonal direction. This is illustrated in Fig. 1.15. This azimuthal anisotropy of particle production is one of the clearest experimental signatures of the so-called "collective flow" in heavy-ion collisions.

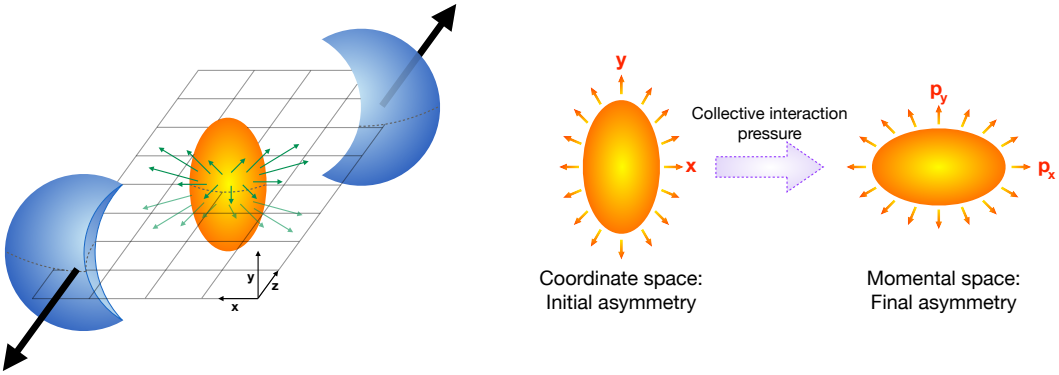

Figure 1.15: Illustration of a non-central collision: the almond-shaped interaction volume leads initial pressure gradients which produce a momentum anisotropy, known as elliptic flow. Adapted by Batoul Diab from [58].

Hard probes: These probes are created by initial hard scatterings and carry a large momentum and/or mass compared to $\Lambda_{QCD} \sim 200\,\mathrm{MeV}$. They are particularly noteworthy because their production can be computed using perturbative QCD. The idea is to see how the traversed medium affects these hard probes, compared to the in-vaccum production and propagation, then to deduce the properties of the medium. Among these probes are jets. These are collimated bundles of particles produced by the parton shower process of a highly energetic parton, followed by the hadronization of all the produced particles in this shower. In heavy-ion collisions, jets can be produced in the center of the produced medium and thus have to propagate through the QGP medium before hitting the detector. During this propagation, the interaction of the jet constituents with the hot medium can cause the jet to lose energy. This phenomenon is commonly referred to as "jet-quenching" [59]. Heavy flavor hadrons (D and B mesons, baryons containing a heavy-quark c or b) are another category of hard probes. Similarly to jets, heavy quarks can propagate through the medium of soft deconfined partons and loose energy. This energy loss can occur both by collisions with partons (this is known as collisional energy loss) or by radiating soft gluons (this is known as radiative energy loss). The comparison of

the p_{T} spectrum of these mesons in proton-proton and heavy-ion collisions can be used to assess the level of this energy loss of heavy quarks in the medium.

Initial-state probes: Particles which do not carry any color charge do not interact via the strong force, and thus will experience a fairly transparent QGP medium, owing to small interaction cross sections with the QGP. This is notably the case for the electroweak bosons : Z^0, $W^{\pm}$ and photons. Whereas the strong coupling is of order $\alpha_s(M_{Z^0}) \approx 0.11$ at the pole mass of the Z^0 boson, the electromagnetic coupling is only $\alpha_{\mathrm{EM}} \approx 1/128$. In particular, the weak bosons are created by initial hard collisions and can be used to study and constrain nPDFs. On the other hand, electromagnetic probes (real or virtual photons) can be produced during the entire history of the medium. Therefore they can be used to study different stages of the collision.

The following section will be devoted to the last kind of QGP probe that we will mention is this thesis, namely the heavy quarkonia.

1.6 Heavy quarkonia in proton-proton and heavy-ion collisions

Quarkonia are mesons which contain a quark bound to its own anti-particle. The most interesting states are heavy quarkonia, among which are charmonia (bound states of $c\bar{c}$ pairs, such as J/ψ, $\psi(2S)$, ...), and bottomonia (bound states of $b\bar{b}$ pairs, such as $\Upsilon(\mathrm{n}S)$).

Heavy quarkonia are particularly interesting objects since they provide a natural separation of scales. Indeed, the large mass of heavy quarks $m_{\mathrm{Q}} \gg \Lambda_{QCD}$ implies that the relative velocity v between the two heavy quarks is small: the charm quark mass is about $1.3\,\mathrm{GeV}/c^2$, while the beauty quark mass is $4.7\,\mathrm{GeV}/c^2$. We hence have a hierarchy of energy scales: $m_{\mathrm{Q}} \gg m_{\mathrm{Q}}v \gg m_{\mathrm{Q}}v^2$, where $m_{\mathrm{Q}}v$ is of the order of the relative momentum between the two quarks and $m_{\mathrm{Q}}v^2$ is of the order of the binding energy, due to the Virial theorem. This small binding energy and relative momentum compared to the mass of the quarks (and hence of the quarkonium), allows for a non-relativistic treatment of this object, and can thus be regarded as the "hydrogen atom of QCD" [60].

The interaction of the two quarks can then be described by an effective potential, obtained after integrating out the momentum scales above m_{Q}, which can then be used in Schrödinger-like non-relativistic equations. This procedure is the core of so-called non-relativistic QCD (NRQCD), which is an effective field theory and is thus a simplification of the full underlying QCD theory [61].

Quarkonia can be classified according to their total angular momentum $\vec{J} = \vec{L} + \vec{S}$, where S is the spin of the state and L is the angular momentum. The parity $\left(P = (-1)^{L+1}\right)$ and charge conjugate parity $\left(C = (-1)^{L+S}\right)$ of quarkonium states, are both conserved quantities in the strong and electromagnetic decays. This classification is shown in Fig. 1.16.

These $Q\bar{Q}$ resonances are not stable particles and will decay with a characteristic proper time inversely proportional to their width, as $\tau_d \approx 1/\Gamma$. In particular, for J/ψ, this width is about $92.6 \pm 1.7\mathrm{keV}$, which corresponds to a mean lifetime of $(2.13 \pm 0.04) \times$

$10^3\,\mathrm{fm}/c = (7.09 \pm 0.12) \times 10^{-21}\,\mathrm{s}$. For $\psi(2S)$, the decay width is about $286 \pm 16\,\mathrm{keV}$, which corresponds to a mean lifetime $(6.89 \pm 0.36) \times 10^2\,\mathrm{fm}/c = (2.29 \pm 0.12) \times 10^{-21}\,\mathrm{s}$ [6].

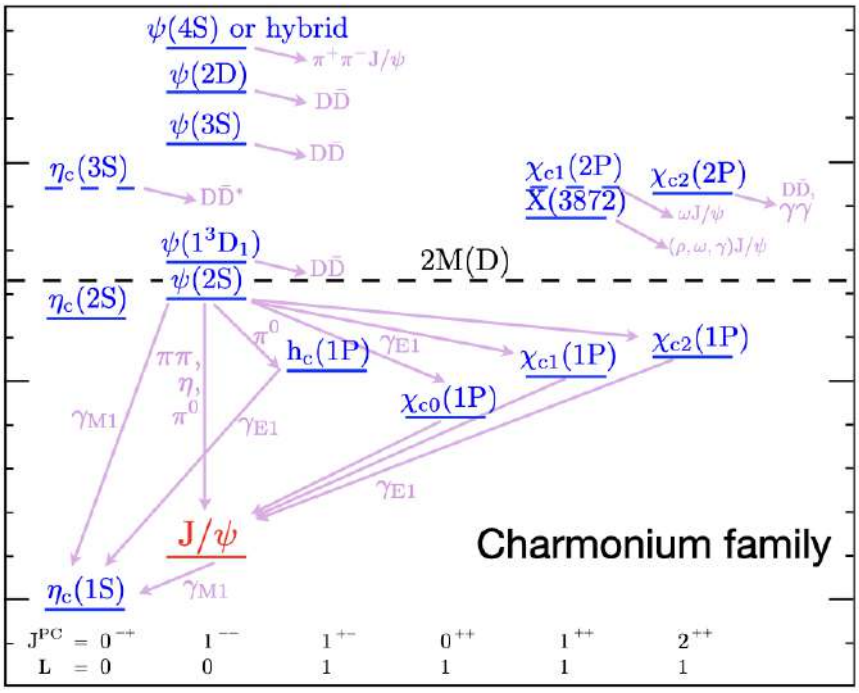

Figure 1.16: Level scheme of the charmonium family. Adapted by Batoul Diab from [6].

The J/ψ has a rest mass of $3096.900 \pm 0.006\,\mathrm{GeV}/c^2$ and a spin of 1. It was discovered in 1974 simultaneously at the Brookhaven National Lab (BNL) [62] and at the Stanford Linear Accelerator Center (SLAC) [63]. It was the first observation of the charm quark, as a bound state of charm and anti-charm quarks. This particle is among the most studied quarkonium state in particle physics, in particular because it is abundantly produced, and because it is a vector state ($L = 0$ and $S = 1$). Such states have a significant decay probability to a dilepton channel, meaning a decay into an electron-positron pair or a muon-anti-muon pair. In hadron collisions, these channels have the advantage of being much cleaner to study experimentally compared to hadronic ones. For instance, for J/ψ the branching ratios to dileptons are [6]:

Decay channel	branching ratio (%)
$\mu^+\mu^-$	5.961 ± 0.033
$\mathrm{e^+e^-}$	5.971 ± 0.032
hadrons	87.7 ± 0.5

This relatively large decay branching ratio of vector particles to the dilepton channels is a consequence of the Landau-Yang theorem [64, 65], stating that a vector particle (J=1) cannot couple to two massless spin 1 particles. This means that it cannot decay into only two

gluons but must decay in at least three gluons. Hence, the decay channel into hadrons, through the decay into three gluons, is power-suppressed by an additional power of α_s compared to pseudo-scalar states ($J = 0$) such as the η_c which can decay into two gluons. In the particular case of the J/ψ, the decay into only two gluons is also forbidden by parity conservation. In addition, the decay width of J/ψ via a virtual photon contributes to about 25% to the total decay width, i.e. the same order of magnitude as the decay via 3 gluons. This explains the (comparatively) long lifetime of the J/ψ state of about $\tau_{J/\psi} = (2.13 \pm 0.04) \times 10^3\,\mathrm{fm}/c$, which is much longer than the QGP lifetime $\tau_{J/\psi} \gg \tau_{\mathrm{QGP}} \sim 10\,\mathrm{fm}/c$ at LHC energy.

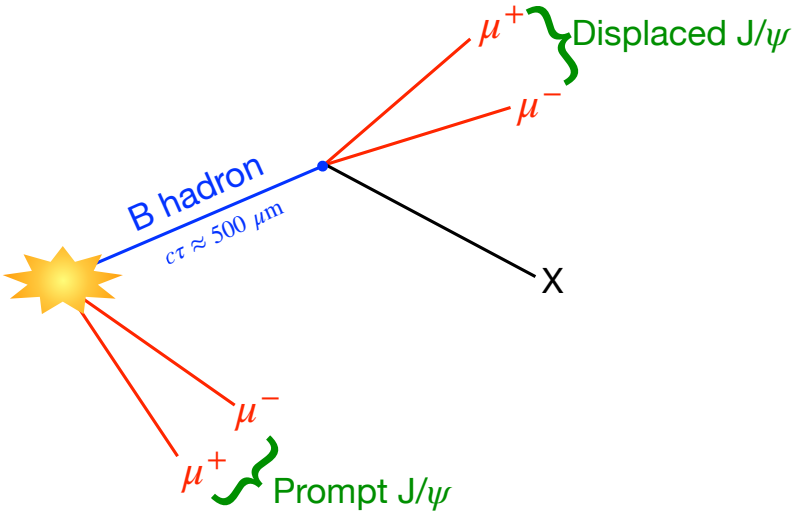

Figure 1.17: Illustration of the production of a prompt and a non-prompt J/ψ decaying into dimuons. The prompt J/ψ is reconstructed at the collision point while the reconstructed vertex of the non-prompt J/ψ is displaced. Adapted by Batoul Diab from [66].

We distinguish two contributions to the inclusive J/ψ production in hadronic collisions, which are both illustrated in Fig. 1.17:

- The *prompt* production encompasses J/ψs from a $c\bar{c}$-pair produced by the strong interaction at the primary vertex[7], and hadronizing either directly into a J/ψ (direct J/ψ) or into an excited charmonium resonance later decaying into a J/ψ (feed-down from a higher charmonium state).
- The *non-prompt* production originates from weak decays of hadrons containing a b valence quark (b-hadron). For this contribution, a secondary displaced vertex corresponding to the decay of b-hadrons (mostly B mesons, with a typical lifetime of $c\tau_B \sim 500\mu\mathrm{m}$) can be identified with silicon vertex detectors.

[7]The decay products of prompt production originate from the primary vertex within the experimental resolutions at experimentally accessible momenta.

The prompt J/ψ cross section, both differential or integrated over transverse momentum, has been measured by all LHC experiments in proton-proton (pp) collisions in different kinematic regimes at collision energies $2.76,\ 7,\ 8$ and $13\,\mathrm{TeV}$, and in Pb–Pb collisions at $5.02\,\mathrm{TeV}$ [67]. From these measurements, the fraction of the J/ψ produced from b-hadron decays has been estimated to be about 10% at low transverse momentum and increases as a function of p_{T}. In addition, Fig. 1.18 illustrates the fact that prompt J/ψ can also be produced by the feed-down decay of higher resonance states. For instance, the χ_c feed-down to the prompt J/ψ is about $12\% - 30\%$ at high p_{T}. The feed-down contribution of $\psi(2S)$ to prompt J/ψ production is about 10%.

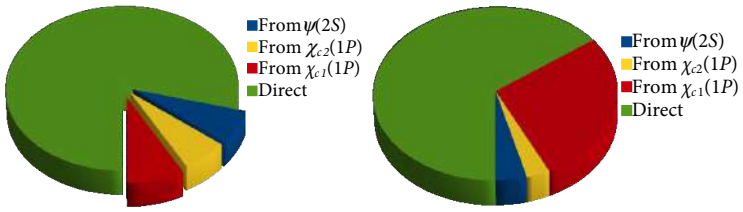

Figure 1.18: Typical sources of hadroproduced J/ψ at low and high p_{T} [68].

1.6.1 Charmonia in pp

The mass spectrum of the charmonium states can be derived from a non-relativistic Schrödinger equation [69] and by using a Cornell-type potential [70]:

$$V(r) \propto -\frac{4}{3}\frac{\alpha_{\mathrm{eff}}}{r} + k \cdot r \tag{1.6}$$

The variable r denotes the radial distance between the two color charges, α_{eff} is an effective coupling constant and k is a nonperturbative long-distance parameter which is equivalent to a "string tension". It is a confining potential. A typical value of k is about $0.2\,\mathrm{GeV}^2$ [71]. One can view this confining force in a naive string picture, where both quarks are linked together with a string characterised by a given tension. This tension prevents the release of the free quarks when additional energy is transferred to the bound state.

A more precise form of the potential between two static color charges can be derived from lattice QCD and follows approximately this Cornell shape [72]. Using this potential, similarly to the Bohr model, one can infer the radius of the ground state of quarkonia. For J/ψ, the computed value is $r_{J/\psi} \sim 0.5\,\mathrm{fm}$, while for $\Upsilon(1S)$, $r_{\Upsilon(1S)} \sim 0.3\,\mathrm{fm}$.

The mass splittings between the two lowest lying vector states in terms of radial excitation (J/ψ and $\psi(2S)$ for charmonium, $\Upsilon(1S)$ and $\Upsilon(2S)$ for bottomonium) are approximately $600\,\mathrm{MeV}$. By attributing this mass splitting to the average kinetic energy $m_{\mathrm{Q}}v^2$, one gets the relative velocity between quarks in quarkonium states: $v_c^2 \sim 0.3$ for charmonium and $v_b^2 \sim 0.1$ for bottomonium [47, 73]. These estimates confirm the hierarchy of scales assumed above.

During a hadronic collision, the charm quarks are expected to be produced mainly during the initial hard scatterings between participating nucleons. This means that, in order to conserve flavor number, they are always produced in $c\bar{c}$ pairs. In addition, since the strong interaction is the dominant one in hadronic collisions, the total number of charm and anti-charm quarks is conserved throughout the history of the collision. The mass of the $c\bar{c}$-quark pair amounts to $\sim 3\,\mathrm{GeV}/c^2$. Hence, $m_{c\bar{c}} \gg \Lambda_{\mathrm{QCD}}$, and perturbative QCD can be employed in conjunction with the collinear factorization to compute J/ψ production cross sections. In addition, Fig. 1.19 shows the kinematic coverage of different experiments. Q^2 refers to the hard scale of the process, e.g. invariant mass or transverse momentum, while Bjorken-x of incoming partons is computed as $x = (Q/\sqrt{s})e^{\pm y}$, where y is the rapidity. Some observables accessible at the LHC are indicated in blue. In particular, J/ψ production probes the Bjorken-x range between $10^{-2} - 10^{-5}$. In this low-x range, the PDFs a largely dominated by gluons, so that charmonium production is dominated by gluon fusion at LHC energies.

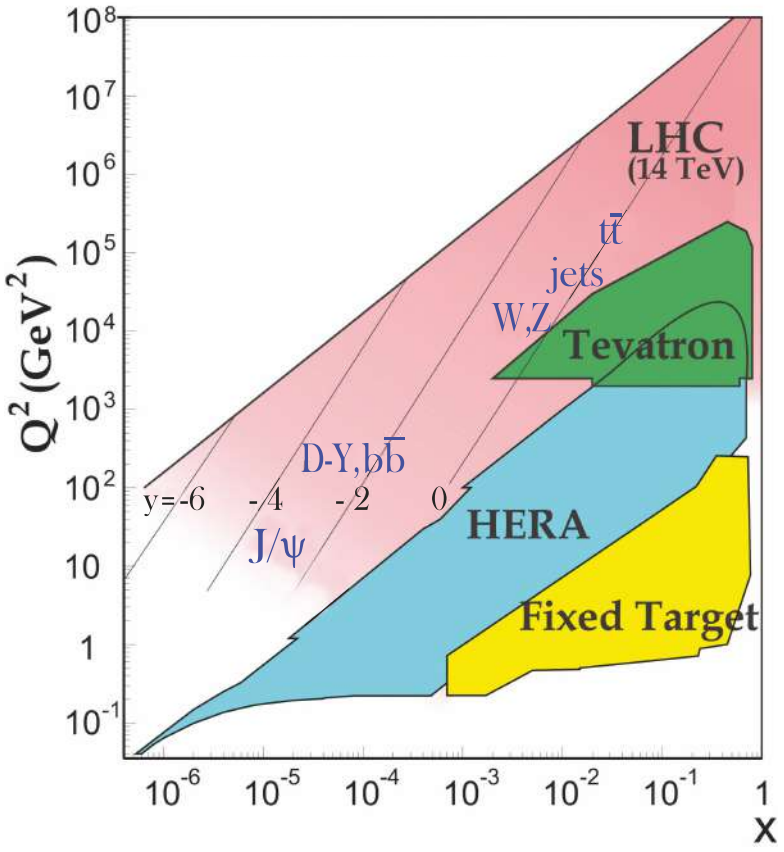

Figure 1.19: Illustration of the kinematic coverage of different facilities as a function of Q^2 and x [6].

According to the collinear-factorization framework mentioned earlier, the prompt production of charmonium is separated into non-perturbative parton distributions in the colliding hadrons, which collide and produce a $c\bar{c}$ pair. The partonic production cross section can be calculated with perturbative QCD. The main additional challenge to the factorization formula presented in Eq. 1.4 is the fact that the produced $c\bar{c}$ pair must finally

hadronize into a physical quarkonium. Hence, there is a non-perturbative transition of the $c\bar{c}$-quark pair to the corresponding charmonium bound state, which must be modeled separately.

The prompt charmonium production can also be calculated in the high energy limit using a framework known as Color Glass Condensate (CGC), on which we will give more details later on. It has the advantage of taking into account the so-called "next-to-leading twist" diagrams, where a large number of partons can interact in the partonic scattering cross section, instead of a simple 2-to-2 scattering as in the naive parton model.

Concerning the transition between the $c\bar{c}$-pair and the bound states, the Color Singlet Model (CSM), the non-relativistic QCD (NRQCD) and the Color Evaporation Model (CEM) are used for the calculations.

- The CSM [74, 75] assumes that the quark pair is produced with the same quantum numbers as the physical quarkonium, including the color, and thus the quantum state does not evolve between its production and its hadronization. This means that the $c\bar{c}$-pair must be produced as a color singlet. The hadronic cross section can then be computed in the collinear framework. In this approach, NLO and NNLO contributions are significantly larger than the LO contributions at mid and large p_{T} [68].

- NRQCD [61] is an effective theory based on the hierarchy of scales outlined above, driven by the large quark mass and small relative velocity. Unlike CSM, the quark pair is not required to be produced in a color singlet state, but also includes color octet states. The nonperturbative hadronization process of the $c\bar{c}$ into a J/ψ is encapsulated in long-distance matrix elements (LDMEs) that are, in the model, assumed to be process-independent and can be constrained by fitting experimental data. However, a still-standing difficulty for NRQCD is to describe both the p_{T} spectrum and the close-to-null polarisation of J/ψ mesons.

- In the CEM [76, 77], the probability of forming a quarkonium state is assumed to be independent of the color or spin state of the produced $c\bar{c}$ pairs. Every produced pair below the open-heavy flavor threshold contributes to the production of every quarkonium state. After its production, the pair is free to evolve by non-perturbative gluon emissions. The color and spin are integrated over so that the color of the state is said to "evaporate" away without changing the kinematics of the pair.

These models do not manage to reproduce simultaneously the prompt J/ψ cross section and the polarization measurements. In particular, NRQCD is successful in describing many charmonium observables, including the J/ψ production cross sections at different LHC energies, but predicts a transverse polarisation with increasing p_{T} [78], while NLO CSM predicts an increasingly longitudinal yield with p_{T} [68]. None of these predictions correctly describes the measured polarization parameter and its p_{T} trend. This lack of understanding is a motivation for precision multi-differential cross section and polarisation measurements in pp collisions. In addition, pp data are reference measurements

for heavy-ion collision data. Thus, the production of charmonium in pp collisions is an important topic to test pQCD calculations and probe non-perturbative physics.

The non-prompt J/ψ are produced from the decays of the b hadrons, containing a b quark. The process of b quark production can be computed using the collinear factorisation approach, in which the hard parton-parton scattering cross section is computed perturbatively. In addition, the hadronization process describing the non-perturbative evolution of a b quark into a b hadron is described by introducing fragmentation functions in the factorization formula Eq. 1.4. These fragmentation functions are non-perturbative objects which are usually extracted from e^-e^+ experimental data. The last step for non-prompt production is the weak decay function from B-hadron to charmonium state.

The perturbative b quark production cross section can be evaluated by the Fixed Order Next-to-Leading-Logarithm (FONLL) calculations [79]. These calculations are implemented at NLO with an all-order resummation to next-to-leading $\log$ (NLL) accuracy in the limit where the p_{T} of the heavy quark is much larger than its mass. These computations, although they have large theoretical uncertainties, describe the production cross sections of open heavy-flavour hadrons measured in pp and pPb collisions in different kinematic domains at centre-of-mass energies ranging from 0.2 to $13\,\mathrm{TeV}$ [67, 80, 81]. FONLL calculations predict a harder p_{T} spectrum of non-prompt J/ψ than for prompt J/ψ and thus the fraction of non-prompt contribution to the inclusive J/ψ yield is expected to increase with p_{T}.

Non-prompt J/ψ production can be used to estimate open beauty-hadron production after an extrapolation (see e.g. [82]). The measurement of beauty production in pp collisions provides a reference for the beauty-hadron production measurements in proton-nucleus and nucleus-nucleus collisions, and is thus crucial for studying the impact of b quark interaction with the QGP.

1.6.2 Charmonia in heavy-ion collisions

In heavy-ion collisions, the suppression of J/ψ production has been proposed by Matsui and Satz as a signature of deconfinement in nucleus-nucleus collisions in 1986 [83]. Their model raised great interest in both experiment and theory communities and since then, many developments in the understanding of charmonium production took place. Their idea was based on an analogy between QCD and QED plasma. Indeed, in both cases, mobile charge carriers (electrons for electromagnetic plasma and partons for QGP) can screen Coulomb fields. In the case of QCD, the non-relativistic potential between two static color charges in Eq. 1.6 is then damped at large distances according to:

$$V(r) \propto -\alpha_{\mathrm{eff}} \frac{e^{-m_D r}}{r} \tag{1.7}$$

where m_D is the Debye mass. This means the attracting potential between two quarks at distance r decreases rapidly when $r > \frac{1}{m_D} \equiv r_D$, the Debye radius. In an electromagnetic plasma, mobile electrons screen the electric fields at distances larger than the Debye

radius [84]:

$$r_D = \sqrt{\frac{T}{ne^2}} \tag{1.8}$$

where T is the temperature of the plasma, e is the electron charge, and n is the number density of electrons.

Similarly, in the QGP, the free partons screen the color potential between heavy quarks with larger separation than r_D. A quarkonium of large-enough size thus dissociates into two open flavor mesons in the QGP, making their production directly suppressed compared to quarkonium production in the vacuum. Such a high-temperature relativistic medium is populated by thermally excited particles, so that the color charge density scales with temperature as $n \propto T^3$. Hence, the Debye radius for a deconfined QCD medium is [85]:

$$r_D = \frac{1}{m_D} \propto \frac{1}{g_s T} \tag{1.9}$$

where g_s is the strong coupling. Therefore, when the temperature of the medium rises, the Debye radius decreases, and states of smaller size start to dissociate. In this picture, one can associate to each quarkonium state a "melting temperature" T_{melt} which is the temperature at which the Debye radius is equal to the in-vacuum radius of the state. From the definition of the Debye radius in Eq. 1.9, one gets that $T_{\mathrm{melt}} \propto c_n m_{\mathrm{Q}} g_s$, where m_{Q} is the heavy quark mass and c_n is a parameter depending on the considered state, which decreases for increasing radius. Hence, different quarkonium species are associated with different melting temperatures and the study of the relative abundances of these different species can be used as tools to access the QGP temperature. This is known as "sequential melting" of quarkonia [86].

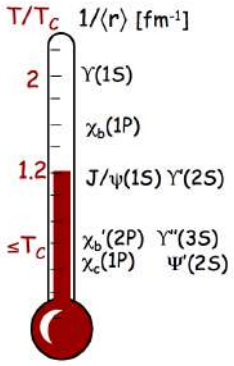

Figure 1.20: Illustration of the "sequential metling", where different quarkonium species with different radii r correpond to different melting temperatures T [87].

This melting of quarkonium states should be reflected in a suppression of their production yields in collisions where we expect the formation of QGP (A-A) compared to collisions where no such phenomenon should occur (pp). This relative suppression is quantified in experiments by the nuclear modification factor R_{AA}. It is used to compare the production

rate of a probe, such as quarkonium, in A-A collisions with its production in pp collisions, scaled with appropriate factors. It is defined as:

$$R_{\mathrm{AA}}(p_{\mathrm{T}}, y) = \frac{1}{\langle N_{\mathrm{coll}} \rangle} \frac{\mathrm{d}^2 N_{\mathrm{AA}}/\mathrm{d}p_{\mathrm{T}}\mathrm{d}y}{\mathrm{d}^2 N_{\mathrm{pp}}/\mathrm{d}p_{\mathrm{T}}\mathrm{d}y} \tag{1.10}$$

$$= \frac{1}{\langle T_{AA} \rangle} \frac{\mathrm{d}^2 N_{\mathrm{AA}}/\mathrm{d}p_{\mathrm{T}}\mathrm{d}y}{\mathrm{d}^2 \sigma_{\mathrm{pp}}/\mathrm{d}p_{\mathrm{T}}\mathrm{d}y} \tag{1.11}$$

Here, $\mathrm{d}^2 N_{\mathrm{AA}}/\mathrm{d}p_{\mathrm{T}}\mathrm{d}y$ denotes the yield, i.e. the number of quarkonia normalized by the number of events, in a rapidity and transverse momentum bin in the corresponding collision system. $\mathrm{d}^2\sigma_{\mathrm{pp}}/\mathrm{d}p_{\mathrm{T}}\mathrm{d}y$ is the corresponding cross section. $\langle N_{\mathrm{coll}} \rangle$ is the mean number of binary nucleon-nucleon collisions, and $\langle \mathrm{T_{AA}} \rangle$ is the average effective nucleon-nucleon luminosity delivered by a single heavy ion collision for a given centrality class. They are both extracted from the Glauber model mentioned in Sec. 1.4. In the absence of any nuclear effects, the nuclear modification factor R_{AA} equals unity, up to small isospin effects.

However, this simplistic idea is missing a few important features. In particular, it assumes that thermalization takes place instantaneously, whereas hydrodynamic modeling of the QGP evolution indicates that it takes $\sim 1\,\mathrm{fm}/c$ to build up. In addition, it misses possible dissociation processes. For instance, for J/ψ, processes such as gluo-dissociation $J/\psi + g \rightarrow c + \bar{c}$ or dissociation by inelastic parton scattering [88], can break up the bound state. This allowed dissociative phase space corresponds to an enlarged resonance width, which can be encoded by adding an imaginary part of the non-relativistic potential of the bound state [89]. This imaginary part corresponds to a decay width representing a dissolution of the charmonium state. This is in addition to the bound-state spectrum modification due to the change of the real part of the potential, attributed to Debye screening. The decay rate of these bound states can also be computed in lattice QCD [90, 91].

This point of view where a bound state is broken by partonic interactions opened the door to alternative, dynamical descriptions of a moving $c\bar{c}$ pair in a non-static medium. These models rely on the assumption that the number of charm and anti-charm quarks is approximately conserved throughout the evolution of the system after the creation of the charm quarks. However, a fraction of the heavy quarks can be produced later than the initial hard scatterings, during the fragmentation of parton showers. CMS observed J/ψ mesons generated in jets, suggesting an important role of jet fragmentation in the production of J/ψ [92].

In addition, these dynamical pictures of the evolution of charmonium in A–A collisions require the distinction between different important time scales. The $c\bar{c}$-quark pairs are mostly produced at time scales $1/m_{\mathrm{Q}}$ (where $\mathrm{Q} = m_{\mathrm{b}} \sim 5\,\mathrm{GeV}$ or $m_{\mathrm{c}} \sim 1.5\,\mathrm{GeV}$). Hence the formation time of the pair is $\tau_{\mathrm{Q\bar{Q}}} \sim 0.05 - 0.1\,\mathrm{fm}/c$. The description of the bulk properties with hydrodynamic simulations requires the assumption of thermalization $\tau_{\mathrm{th}} \sim 0.2 - 1\,\mathrm{fm}/c$.

After the initial production, the quarks in the $c\bar{c}$ pair travel extremely close to each other. To form a $c\bar{c}$ resonance, they need to expand up to the characteristic size of the

corresponding bound state. This formation time can be approximated using the formula

$$\tau_\psi \approx \frac{2E}{m_\psi^2}.$$

The time needed for the $c\bar{c}$ pair to form a J/ψ is around $2\,\mathrm{fm}/c$ at $E = 10\,\mathrm{GeV}$. It increases with E which is proportional to the particle momentum. Thus, at $30\,\mathrm{GeV}$, this formation time goes up to $6\,\mathrm{fm}/c$.

Finally, we get the following ordering of time scales at the LHC :

$$\tau_{\mathrm{Q\bar{Q}}} < \tau_{\mathrm{th}} < \tau_\psi < \tau_{\mathrm{QGP}}$$

where $\tau_{\mathrm{QGP}} \sim 10\,\mathrm{fm}/c$ is the QGP lifetime. Therefore, the time when the $c\bar{c}$ pair is expected to bound can occur during the QGP phase itself. This time ordering suggests a more complex picture than the sequential melting of quarkonia. The medium must influence the formation process of the bound states, and we can not simply consider the dissociation of already formed resonances statically standing in a thermal bath. A thorough description is rather one where the charmonium formation may be accomplished as a result of a dynamic process, arising from in-medium interactions with deconfined charm quarks as we mentioned above.

1.6.3 Regeneration and dynamical models

At high collision energy, there is a significant number of initially produced heavy quarks: a central Pb–Pb collision at the LHC produces around $\sim 200\ c\bar{c}$ pairs and $10\ b\bar{b}$ pairs [79]. In a dynamic picture of the charmonium formation, the deconfined medium allows charm quarks to move freely in the medium. Even if they originated from different hard scatterings, the charm and anti-charm quarks in the medium which come close enough in phase space could form charmonium states. J/ψ mesons could thus be produced from the recombination of initially uncorrelated charm quarks. This recombination or regeneration mechanism should be most effective for low-p_{T} charm quarks, as they are more numerous and can get closer to each other in phase space.

For the same centrality, A–A collisions at LHC energies allow to reach a much hotter QGP than at RHIC. Therefore, in the absence of any regeneration, the charmonium suppression by melting alone would have been even more dramatic at LHC, and would have resulted in a significantly smaller R_{AA} at LHC than at RHIC. On the other hand, at LHC energies, the number of $c\bar{c}$ pairs initially produced in the hard scatterings is considerably larger than at lower energies (e.g. at RHIC or SPS), which can lead to an important population of recombined J/ψ, able to compensate the increased melting. Hence, recombination is the common understanding of the R_{AA} of inclusive J/ψ mesons measured with ALICE in central collisions at LHC, where the R_{AA} is higher than the one measured by the PHENIX experiment at lower RHIC energy, as shown on Fig. 1.21. This R_{AA} enhancement in Fig. 1.21 is mostly located at low p_{T}, suggesting that it is consistent with a charm recombination mechanism.

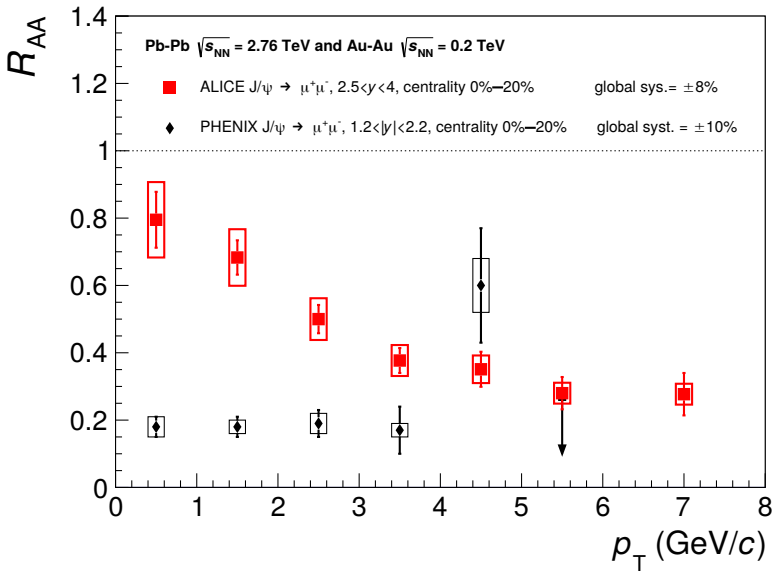

Figure 1.21: Transverse momentum dependence of J/ψ R_{AA} in 0–20% most central collisions measured by ALICE in Pb–Pb collisions at $\sqrt{s_{NN}} = 2.76\,\mathrm{TeV}$ and compared to PHENIX results in Au-Au collisions at $\sqrt{s_{NN}} = 0.2\,\mathrm{TeV}$ [94].

Another indication of the relevance of this regeneration mechanism is the non-zero J/ψ elliptic flow, or v_2, measured at LHC [93]. It is positive at low p_{T}, where regeneration is expected to be most effective. This observation could mean that the J/ψ inherits its anisotropic flow from the charm quarks interacting with the medium during the expansion. In this picture, the charm quarks must be at least partially kinetically thermalized, meaning that they have undergone an important number of interactions with the constituents of the thermal medium. Primordial J/ψs could also interact with medium constituents and thermalize. However, the J/ψ is a compact object and one expects it to interact feebly once it is produced. At high p_{T}, most of the J/ψ mesons are considered to originate from primordial production.

In 2000, two different models were developed accounting for charmonium production in A–A collisions, based on different dynamical pictures: the transport model [95] and the statistical hadronization model [96]. They both include regeneration contributions to the inclusive cross section, although the underlying mechanisms of these contributions are different.

In the statistical hadronization model (illustrated in Fig. 1.22), no bound states are formed during the lifetime of the deconfined medium, for light or heavy flavor hadrons. In particular, charmonia are all generated at freeze-out from initially produced charm quarks with thermal statistical distributions between the different states, depending on the medium temperature and the QGP volume at freeze-out. More generally, this model describes very well the abundance of different light particle species through statistical distributions [97]. Contrarily to the light quarks that are in chemical equilibrium in the medium, charm quarks are too heavy to be significantly produced thermally, and a significant fu-

gacity factor $g_c \sim 30$ is necessary for the model to describe charmonium production, assuming a full kinetic thermalization of the charm quarks. In this model, all memory is lost regarding the initial correlation between the charm quarks produced in the initial hard scatterings.

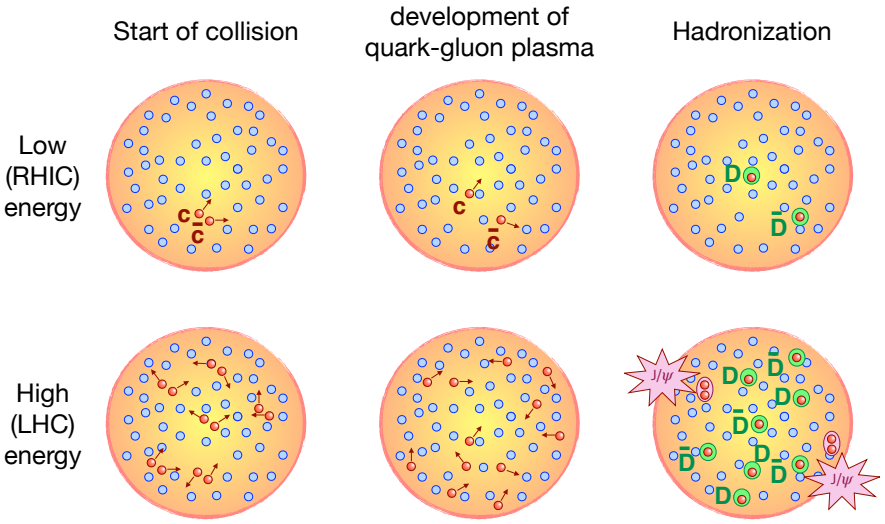

Figure 1.22: Illustration of the statistical hadronization model: (Top) In low energy collisions, $c\bar{c}$ pairs interact with the medium constituents and form D mesons at hadronization. (Bottom) At high energies, many $c\bar{c}$ pairs are produced. At hadronization, charm and anti-charm quarks from different original pairs may combine to form charmonium. Adapted by Batoul Diab from [98].

In the transport approach (see Fig. 1.23), there is a continuous formation and dissociation of the bound states during the whole lifetime of the QGP. This picture has been further developed in different models with different assumptions and different levels of sophistication for the description of the medium. Most recent transport models are based on Boltzmann or on Langevin equations. A simple form of the time-dependent kinetic rate is:

$$\frac{\mathrm{d}N_\psi}{\mathrm{d}\tau} = -\Gamma_\psi(T)\left[N_\psi - N_\psi^{\mathrm{eq}}(T)\right]$$

where $N_\psi^{\mathrm{eq}}(T)$ is the equilibrium limit of the number of charmonium, from a population of partially thermalized charm quarks, and $\Gamma_\psi(T)$ is the dissociation/formation rate. This basic form can be elaborated in a number of ways, e.g. by considering a space and momentum dependent charm density. In addition, the underlying physics taken into account in Γ can be more or less sophisticated in the various available transport models, such as

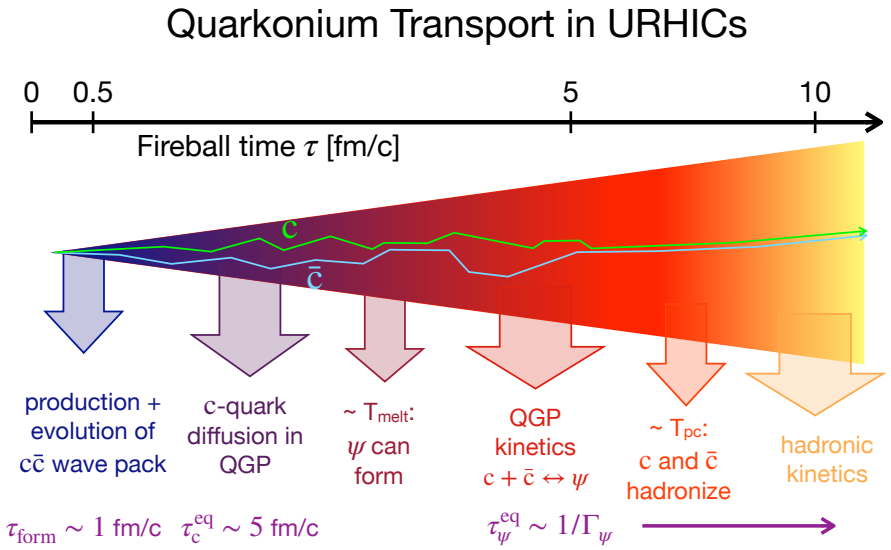

Figure 1.23: Illustration of time evolution of a $c\bar{c}$ pair in a HIC, with time scales which are relevant in transport models. Adapted by Batoul Diab from [99].

TAMU [101] or the Zhuang *et al.* model [102]. Let us note that these approaches best fit the data when an important fraction of the measured J/ψ is primordial, i.e. did not undergo any dissociation in the medium.

Modern approaches, based on Open-Quantum Systems, aim at a more realistic description of the quantum nature of the evolution and formation of heavy-quark bound states [47]. In particular, they take into account quantum coherence between different quarkonium states at early times, which is important in order to correctly capture the dissociation rates.

The J/ψ R_{AA} measurements by ALICE in Pb–Pb collisions at $\sqrt{s_{NN}} = 5.02\,\mathrm{TeV}$ are shown on Fig. 1.24. The centrality dependence of R_{AA} (left) is well described by both the statistical hadronization model and transport approaches. Figure 1.24 (right) shows the p_{T} dependent R_{AA}. We see that the suppression of J/ψ is reduced at low p_{T} and the R_{AA} is compatible with unity below $3\,\mathrm{GeV}/c$. This is in line with the expectations of the regeneration mechanism. This p_{T} dependence is also in agreement with the transport models, while the statistical hadronization model predicts more suppression than is actually measured for $p_{\mathrm{T}} > 5\,\mathrm{GeV}/c$.

A measurement of the J/ψ elliptic flow, or v_2, made by ALICE is shown in Fig. 1.25. It shows a non-zero elliptic flow over a large p_{T} range and is compatible with the transport model of [103], which includes recombination effects.

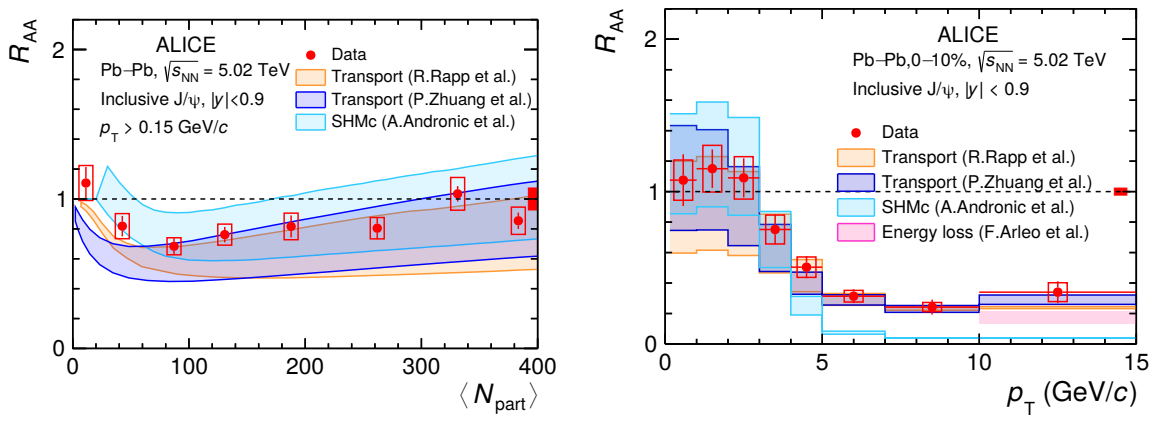

Figure 1.24: (Left) Inclusive J/ψ R_{AA} at midrapidity, integrated over p_{T}, as a function of $\langle N_{\mathrm{part}} \rangle$ in Pb–Pb collisions at $\sqrt{s_{NN}} = 5.02\,\mathrm{TeV}$ and compared to models (Right) Transverse-momentum dependence of the J/ψ R_{AA} in Pb–Pb collisions at midrapidity in the 0–10% centrality intervals [100].

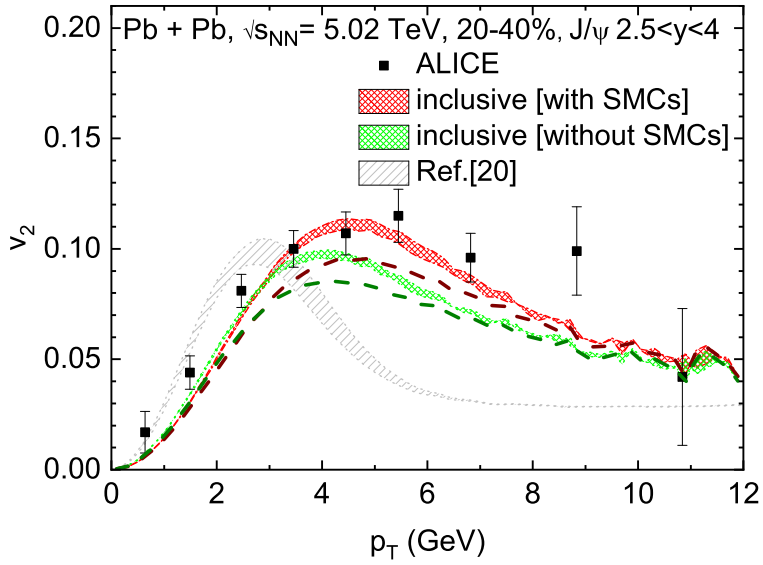

Figure 1.25: v_2 of inclusive J/ψ production in $5.02\,\mathrm{TeV}$ Pb–Pb collisions at the LHC computed in the transport model approach, compared to ALICE data [103].

In Fig. 1.26, the R_{AA} of inclusive J/ψ, measured by ALICE, is compared to the one of $\psi(2S)$ as a function of centrality, at forward rapidity in Pb–Pb collisions at $5.02\,\mathrm{TeV}$. One can see that the $\psi(2S)$ is more suppressed than the J/ψ. In addition, a comparison with the statistical hadronization model and transport models is shown. The latter is in good agreement with both the J/ψ and $\psi(2S)$ data over the whole $\langle N_{\mathrm{part}} \rangle$ range, whereas the statistical model underestimates the $\psi(2S)$ R_{AA} for the most central collisions. Fig. 1.27 shows the ratio of the $\psi(2S)$ and J/ψ cross sections as a function of $\langle N_{\mathrm{part}} \rangle$. The transport model is in good agreement with the ALICE data, whereas the statistical hadronization model underestimates the $\psi(2S)$-to-J/ψ ratio in the most central collisions. One should note that the $\psi(2S)$ is expected to have a longer formation time than the J/ψ, and in addition, transport models with the primordial component, i.e. not dissociated by medium interaction, are mandatory to reproduce the data.

Finally, as we will elaborate in the next chapters, during Run 1 and 2, ALICE only had vertexing capabilities at midrapidity. This allowed to separate prompt and non-prompt contributions to J/ψ production. Fig. 1.28 shows the R_{AA} of prompt J/ψ at midrapidity in $5.02\,\mathrm{TeV}$ Pb–Pb collisions for different centrality classes [104]. An enhancement for the more central collisions is seen at low p_{T}, where more regeneration is expected. However, the measurements do not reach zero p_{T}, where the effect of regeneration should be the most important. Fig. 1.29 shows the non-prompt J/ψ fraction, f_{B}, measured by ALICE and CMS, as a function of p_{T}. The two experiments seem to be in good agreement in the overlapping p_{T} bin. Moreover, as can be seen on the figure, f_{B} ranges from $\sim 10\%$ at $p_{\mathrm{T}} = 2\,\mathrm{GeV}/c$ to $\sim 60\%$ at $p_{\mathrm{T}} = 30\,\mathrm{GeV}/c$.

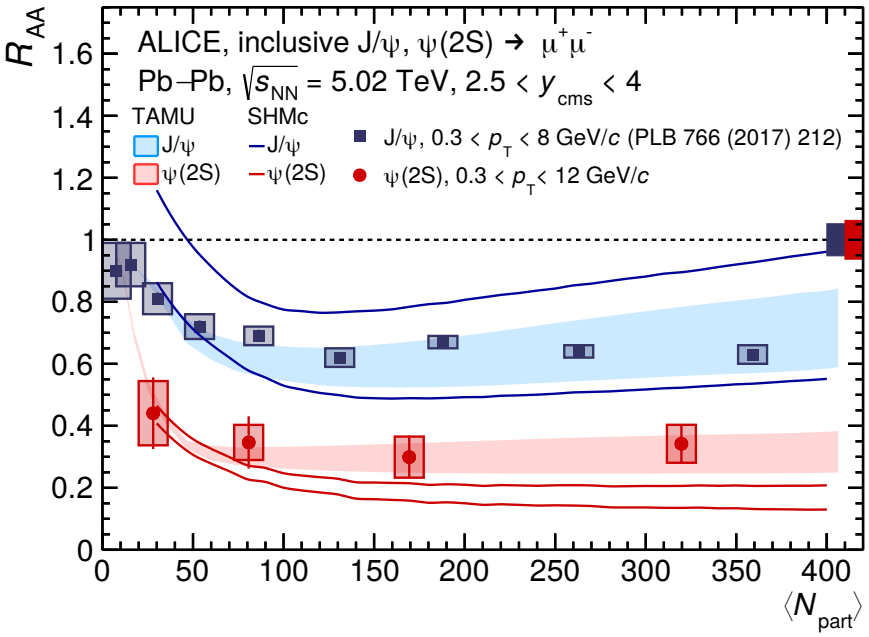

Figure 1.26: R_{AA} for $\psi(2S)$ and J/ψ as a function of $\langle N_{\mathrm{part}} \rangle$ [105]. Comparisons with theory models are also shown.

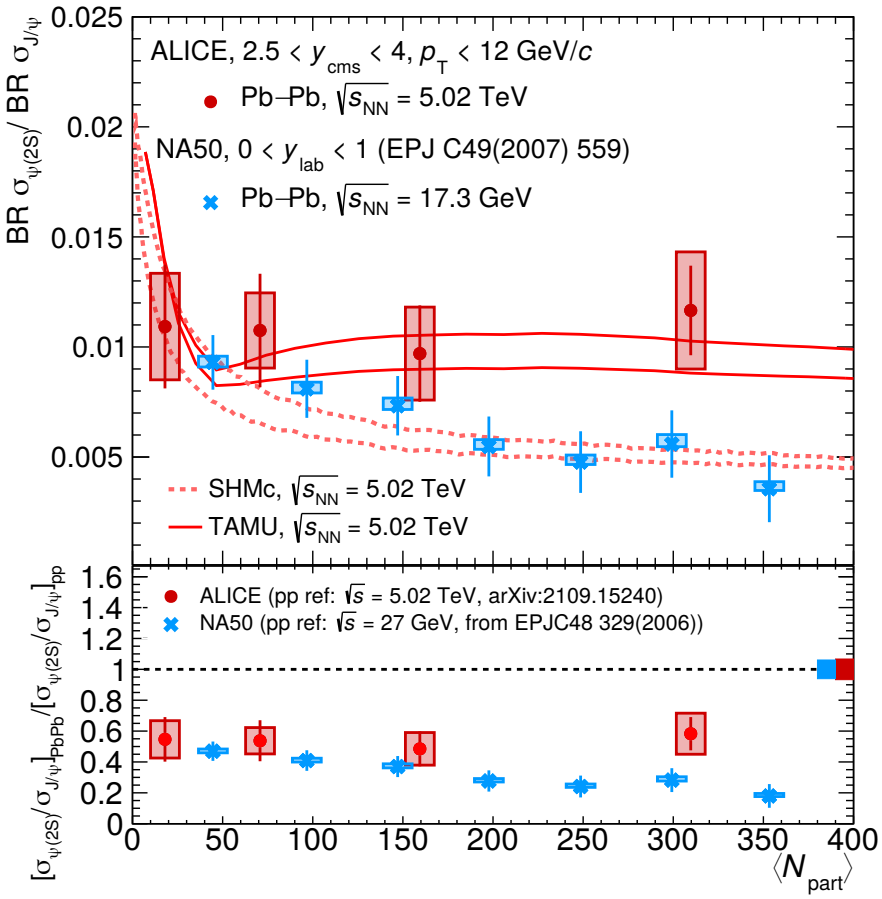

Figure 1.27: Ratio of the $\psi(2S)$ and J/ψ cross sections as a function of $\langle N_{\rm part} \rangle$. In the lower panel the ratios are normalized to the corresponding pp value (double ratio). Data are compared to predictions of the TAMU and SHMc models and to results of the SPS NA50 experiment [105].

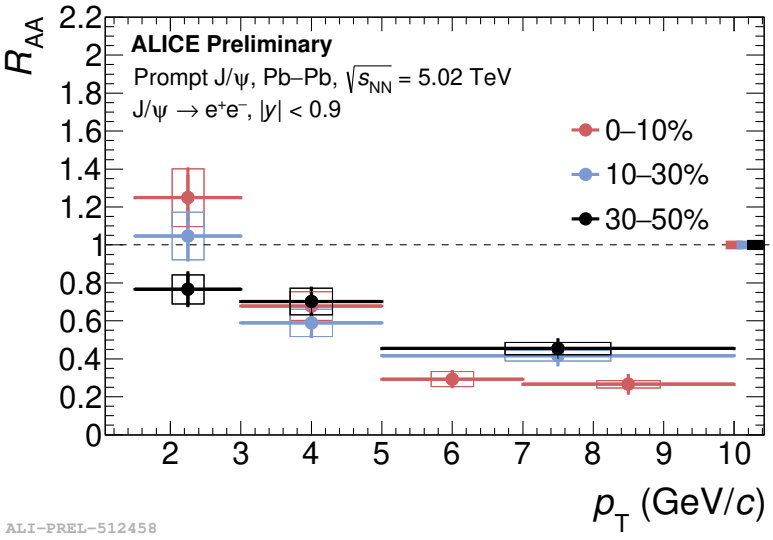

Figure 1.28: Nuclear modification factor (R_{AA}) of prompt J/ψ as a function of the transverse momentum p_{T} in 0–10%, 10–30% and 30–50% Pb–Pb collisions at $\sqrt{s_{NN}} = 5.02\,\mathrm{TeV}$.

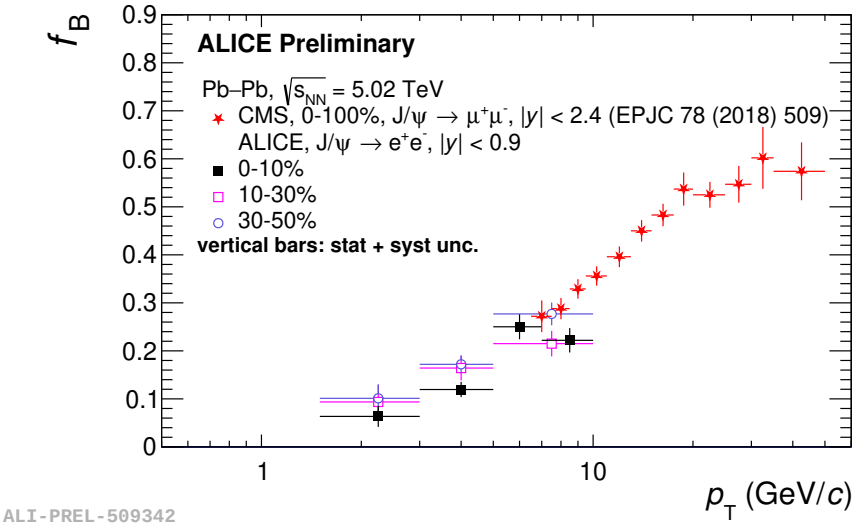

Figure 1.29: Non-prompt J/ψ fraction, f_{B}, as a function of the transverse momentum p_{T}, using ALICE full run 2 statistics, in central (0–10%), semicentral (10–30%) and 30–50% collisions, comparing with CMS measurements at centrality range of 0–100%.

1.6.4 Nuclear effects

In addition to the dissociation by hot medium interactions, the J/ψ meson is also affected by the so-called Cold Nuclear Matter (CNM) effects [8]. They can also modify the quarkonium yields, and they do not depend on whether a deconfined QGP is formed or not in the collisions. These effects are independently studied in p–A collisions where no QGP effects are expected. It is of prime importance to correctly capture these effects, as they can significantly impact the relative role of hot medium suppression of quarkonium yields and change our interpretation of the underlying models. Let us quote some of the most important CNM effects:

- Nuclear absorption: in p–A or A–A collisions, the produced $c\bar{c}$ might scatter with spectator nucleons during their propagation. This interaction can break the bound states and thus produce a suppression of the charmonium yield. However, at the LHC, the crossing time of the two colliding hadrons is much shorter than the formation time of charmonia, so this effect is not expected to play a major role. It can however be important at lower energies [106].

- Energy loss: Partons can lose energy while propagating through the nuclear medium by radiating gluons. This can affect the p_{T} spectra in p–A or A–A collisions compared to pp. In addition, colored objects such as $c\bar{c}$ pairs could undergo coherent energy loss where gluons emitted from the initial and final state interfere coherently [107]. This type of energy loss might represent an important nuclear effect, especially for nPDF fits to p–A data.

- Gluon shadowing: As mentioned in Sec. 1.4, nuclear PDFs exhibit non-trivial behaviors as a function of x compared to regular PDFs. The most important effect for charmonium production at the LHC is gluon shadowing [108]. This is due to the low-x region probed by their production at the considered energies. The shadowing is a relative suppression of the nuclear gluon PDF at low x which can lead to a suppression of charmonium production. Fits of nPDFs indicate a strong shadowing, as well as ultra-peripheric collision data, where no energy loss is expected.

[8] It was pointed out to me by a colleague that this nomenclature is not the most appropriate, since, similarly to the HRE which was, according to Voltaire, "neither Holy, nor Roman, nor an Empire", CNM effects are neither cold, nor nuclear nor related to matter.

1.7 Summary

The study of the QGP presents a large range of interests, from the fundamental properties of the theory of the strong interaction, to the applicability of hydrodynamics. This state of matter is produced in ultra-relativistic heavy-ion collisions by procuring a high enough energy density to reach the pseudo-critical temperature calculated by lattice QCD computations, which predict a cross-over transition from confined color-singlet hadrons, to a strongly interacting fluid made of free color charges. Contrary to proton-proton collisions in high energy physics, heavy-ion collisions have the remarkable feature of having well defined time scales which allow to distinguish different stages of the collision. Different probes can be used to study these stages; for instance, particles which are produced during the early stages of the collision and have a sufficiently long lifetime can propagate through the QGP and probe some of its properties. This is the case for the charmonium, such as J/ψ, which is created at the beginning of the collision. The suppression or enhancement of the latter, depending on the collision energy, is observed in heavy-ion collisions compared to proton-proton collisions. However, the J/ψ production can either be prompt or non-prompt. The prompt J/ψ are produced directly as a result of hard processes or following the feed-down of excited charmonium states. The non-prompt J/ψ are produced as a result of the weak-decays of b hadrons. To understand to which the extent this modification can be a sign of QGP formation, the so-called CNM effects must be controlled, and the contribution of prompt and non-prompt components to J/ψ production must be estimated. In addition, the non-prompt J/ψ by itself can be a very good proxy to study the production of b-hadrons and their modification in heavy-ion collisions. Measurements of prompt and non-prompt J/ψ were carried out in the central barrel of ALICE, as well as in other LHC experiments. At forward rapidities, only inclusive measurements were possible before Run 3, due to design limitations. In the following chapters, I will present my work on a new detector in ALICE at forward rapidities, that makes the separation between prompt and non-prompt components possible down to low transverse momentum in pp collisions. This is an important step towards future analysis using this detector and similar method for Pb–Pb collisions.

Chapter 2

Experimental setup

2.1 The Large Hadron Collider

The Large Hadron Collider (LHC) is a hadron accelerator and collider of $26.7\,\mathrm{km}$ in circumference [109]. It was constructed by the European Organization for Nuclear Research (CERN) $100\,\mathrm{m}$ underground on the border between France and Switzerland between 1998 and 2008. It is currently the largest and highest-energy particle accelerator in the world.

In the LHC, two beams of particles travel in opposite directions in two separate rings. They are guided by superconducting dipole magnets, powered by currents as high as $12\,\mathrm{kA}$ circulate, and cooled down using liquid helium down to $1.9\,\mathrm{K}$. They produce a magnetic field of $8.3\,\mathrm{T}$. In addition, quadrupoles allow to focus the beams of particles, to maximize the probability of collision at the interaction point.

Using older accelerators as injectors, highly energetic hadron beams are pre-accelerated by a series of systems (see Fig. 2.1) that successively increase the beam energy. These hadrons can either be protons or heavy nuclei.

In the case of protons, H^- ions are first accelerated in the linear accelerator LINAC4 [110], using radiofrequency (RF) cavities. These accelerated ions go through a stripping foil that removes part of the ions' electrons. After the foil, dipole magnets deviate the H^- and H^0 which are then dumped. The remaining protons enter the next accelerator at an energy of $160\,\mathrm{MeV}$ and circle back to the stripping foil where they meet the H^- beam from LINAC4 again, gradually increasing the density of protons in the beam. The next accelerator is the Proton Synchrotron Booster (PSB) [111], where the protons are accelerated up to $1.4\,\mathrm{GeV}$, and are grouped into bunches. The beam is then injected into the Proton Synchrotron (PS) where it is further accelerated to $25\,\mathrm{GeV}$. In addition, the proton bunches of the beam are separated in time by $25\,\mathrm{ns}$, before they are injected into the Super Proton Synchrotron (SPS). Gradually increasing in energy, the SPS brings proton beams to $450\,\mathrm{GeV}$, and bunch trains are created. Finally, they are transferred to the LHC where they are then accelerated up to nominal energy of $7\,\mathrm{TeV}$, which takes approximately 20 minutes.

In the ion case, lead nuclei come from a sample of solid and isotopically pure $^{208}\mathrm{Pb}$. The source is placed in an ECR (Electron Cyclotron Resonance) chamber where a magnetic field

oscillating at $14.5\,\mathrm{GHz}$ heats electrons and creates Pb^{29+} ions [112]. The resulting ions are then accelerated to $4.2\,\mathrm{MeV}$ per nucleon in the linear accelerator LINAC3 and sent through a thin carbon target to strip another 25 electrons. In the Low Energy Ion Ring (LEIR), the ions are then accumulated, cooled, and further accelerated to $72\,\mathrm{MeV}$ per nucleon. The beam is also segmented into bunches. The resulting bunches are then fully stripped of their electrons in the transfer line to the SPS with an aluminium foil.

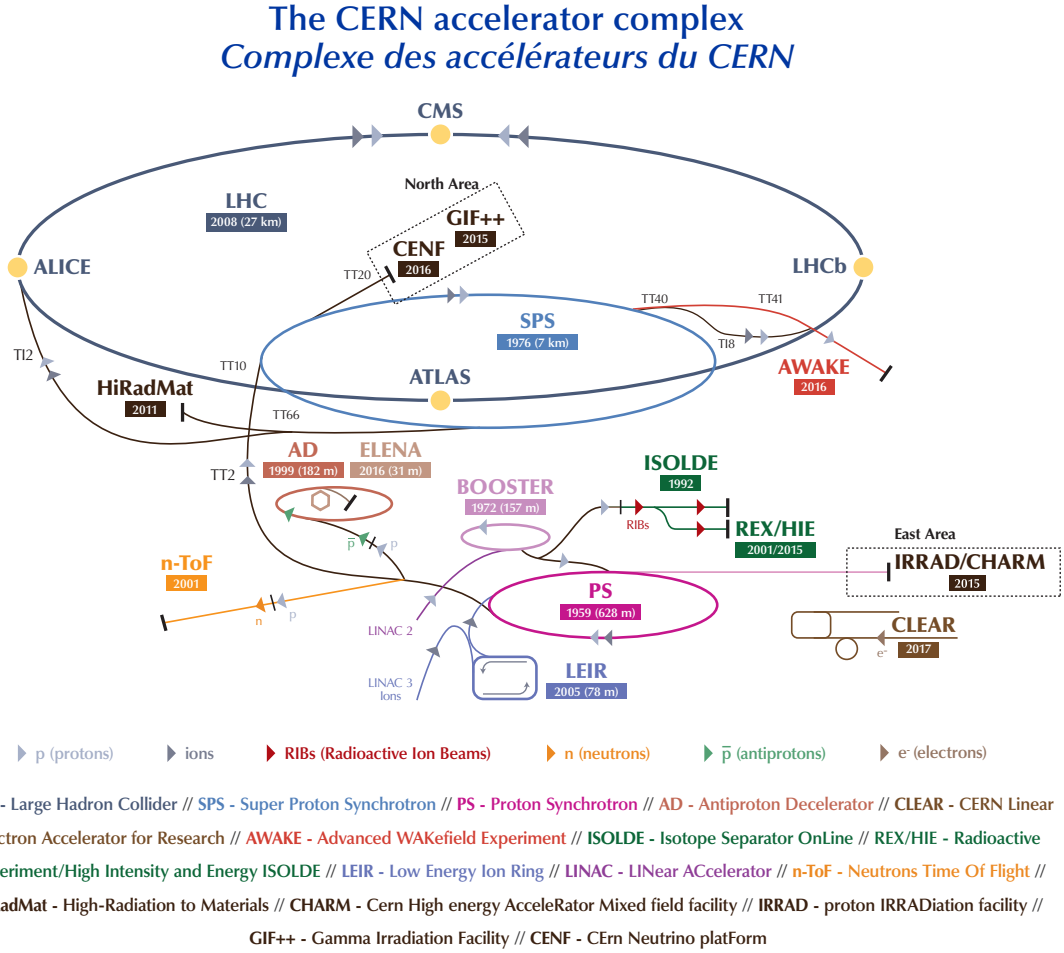

Figure 2.1: The CERN detailed accelerator structure [113].

For both proton and ion beams, the SPS accelerates the batches and then alternately injects them into the two LHC beam pipes, in opposite directions. Alongside accelerating the beams in the LHC, the size and trajectory are controlled by the dipole and quadrupole magnets. The beams cross at four interaction points that host the four largest CERN experiments. The energies at play at the LHC are the highest ever seen in a collider.

The filling of the LHC ring with proton or Pb ion bunches for physics measurements is known as an LHC fill. The sequence of operations that take place to achieve a physics fill

defines a LHC cycle. During a LHC cycle, the proton or ion bunches prepared by the SPS accelerator are injected in a precise time ordering, called a filling scheme. Since consecutive bunches are separated by a time interval of $25\,\mathrm{ns}$, the LHC ring which has an orbit of $89.1\,\mu\mathrm{s}$ can be divided into 3564 radio-frequency slots (named buckets) which can be filled or not with a bunch. The filling scheme is a map of the slots that are occupied by the bunches (1 bunch per bucket). The main stages involved in an LHC cycle (Fig. 2.2) are the following [114]:

- Injection: protons or ion beams are injected into the LHC. The beams are delivered by the smaller pre-accelerators mentioned above.
- Ramp-up: once the beams are injected into the LHC, they undergo a gradual increase in energy, by progressively raising their speed and energy level (the flat top). At the end of this stage, the LHC machine can be seen as storing energy in the radio-frequency cavities, the dipole and quadrupole magnets and in the beam itself.
- Squeeze and Adjust: the beam intensity is adjusted, the beams' focus (transverse size) and their horizontal and vertical separations are optimized to reach the targeted probability of interactions requested by each interaction point by the LHC experiments.
- Stable beam: once the beams reach the desired energy and focus, they are brought into collision at the interaction points surrounded by the detectors of the LHC experiments. During the stable beam, the beam intensity decreases with time, since the accumulation of collisions is reducing at an exponential rate the population of protons or ions per colliding bunch. Beam losses at various points of the ring also contribute to this reduction.
- Beam dump: when the population per colliding bunch is too low, a decision is taken to end the on-going fill. During this procedure, the remaining beam particles are dumped on purpose into dedicated areas.
- Ramp-down: once the beam dump is achieved, the process of ramping down the LHC magnets begins. The stored energy is dissipated. At the end of this step, the LHC is ready for a new fill.

Around the LHC ring, several experiments are installed at the interaction points, where the beams can collide. They are designed for different purposes. The four main experiments are:

- A Large Ion Collider Experiment (ALICE): It specializes in heavy-ion collisions and QGP studies. This experiment will be further detailed in the next section.
- A Toroidal LHC ApparatuS (ATLAS) [115]: The largest detector of the LHC. It is a multi-purpose detector, designed to study the Higgs boson and explore beyond SM physics thanks to high luminosity pp collisions. It also contributes to QGP studies. ATLAS has the shape of a cylinder containing a toroidal magnetic system generating a field of $2\,\mathrm{T}$. The acceptance in pseudorapidity of this detector is $|\eta| < 2.5$.

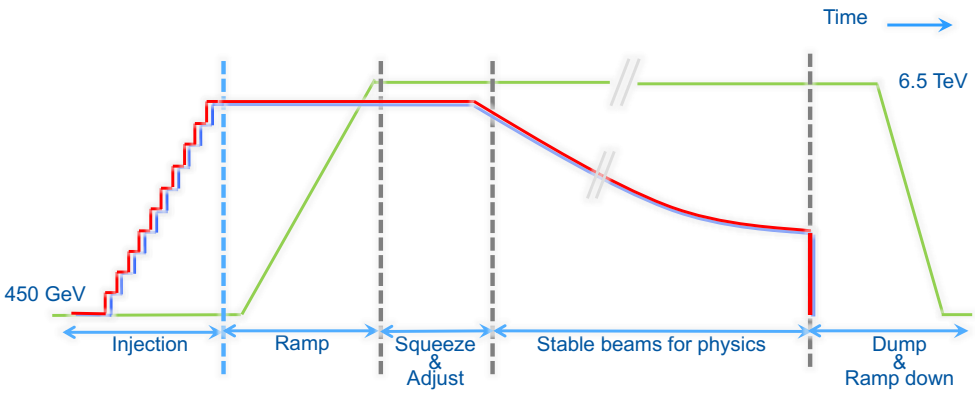

Figure 2.2: Illustration of the different steps of an LHC fill cycle [114]. The blue and red curves represent the intensity in the two colliding beams, while the green curve represents the beam energy.

- Compact Muon Solenoid (CMS) [116]: Similar to ATLAS, CMS is a multi-purpose detector, allowing a complementary cross-check between the two collaborations working independently. The detector is constructed around a large solenoid magnet, generating a field of $4\,\mathrm{T}$. The pseudorapidity region of this detector is $|\eta| < 2.5$, with the minimum transverse momentum for muon measurements going from 1.2 to $3.5\,\mathrm{GeV}/c$.

- LHC beauty (LHCb) [117]: The main goal of the LHCb collaboration is to study the b quark, as well as matter-anti-matter asymmetry. The detector is a forward spectrometer designed to precisely measure the decays of b-hadrons. It is comprised of a dipole magnet with a bending power of $4\,\mathrm{T\,m}$, and covers an acceptance of $2 < \eta < 5$. In addition to the pp and heavy-ion runs, LHCb can operate in fixed-target mode by injecting noble gas (He, Ne, Ar) into the LHC beam pipe at their interaction point.

Experiments at the LHC involve probabilistic processes which occur in the crossing of the colliding objects. The probability of occurrence of a given interaction is quantified by the cross section σ. This quantity is a universal property of the studied physical process. It has units of inverse squared length, and at low energies can be viewed in a classical approach as the transverse section of the overlap region between the two objects, similar to the interaction between two hard spheres.

Furthermore, LHC experiments deal with rare events with a small production cross-section σ. Thus, an important number of events is necessary to study these processes using statistical methods. The number of inelastic collisions per unit of time occurring at a given interaction point at the LHC is noted dR/dt and is known as the collision rate. During Run 3, this rate increased compared to Run 2 to gather more events which will help in the study of rare candidates, and will reach up to $50\,\mathrm{kHz}$ for Pb–Pb collisions. The instantaneous luminosity $\mathcal{L}$ is then defined such that, when multiplied with the interaction

cross section of the colliding objects, it gives the collision rate:

$$\frac{dR}{dt} = \mathcal{L} \cdot \sigma \tag{2.1}$$

where σ is here the inelastic collision cross section. Thus $\mathcal{L}$ has units of $\mathrm{cm}^{-2}\,\mathrm{s}^{-1}$. This luminosity is one of the main characteristics of accelerators such as the LHC. It measures the ability of the particle accelerator to produce a large number of interactions, or collisions.

One can also define the integrated luminosity L_{int} which quantifies the number of events observed during a given data-taking period:

$$L_{\text{int}} = \int \mathcal{L} dt = \int \frac{1}{\sigma} \times \frac{dR}{dt} dt \tag{2.2}$$

In the case of circular accelerators the luminosity can be estimated with the basic expression [6]:

$$\mathcal{L} = f_{\text{coll}} \frac{N_1 N_2}{4\pi \sigma_x^* \sigma_y^*} \mathcal{F} \tag{2.3}$$

where N_1 and N_2 are the number of particles per bunch in the two beams, σ_x^* and σ_y^* characterize the transverse size of the colliding beams at the interaction point, and $\mathcal{F}$ is a factor of order 1 , that takes into account inefficient geometric overlapping of the beams due to a crossing angle between the colliding beams, finite bunch length and beam focus. f_{coll} is the frequency of bunch crossings, which is linked to the number of bunches per beam n_{b} by $f_{\text{coll}} = n_{\text{b}} f_0$ where f_0 the revolution frequency of the LHC which is $11.223\,\mathrm{kHz}$. To achieve a high luminosity, one has to maximize the number of colliding bunches, collide them at high frequencies and optimize the geometric overlapping of the beams at the interaction point.

During Run 3, the LHC instantaneous luminosity is expected to reach $2 \times 10^{34} \mathrm{cm}^{-2}\,\mathrm{s}^{-1}$. The so-called High Luminosity LHC upgrade (HL-LHC) [118] aims at increasing the instantaneous luminosity at the LHC up to $5 \times 10^{34}\ \mathrm{cm}^{-2}\,\mathrm{s}^{-1}$, for the ATLAS and CMS experiments, while the collimation and focusing magnets are not adpated in ALICE and LHCb to accomodate such luminosity due to specific needs of these experiments. This would represent an integrated luminosity of $250\,\mathrm{fb}^{-1}$ per year[1]. This project will be put into place during Long Shutdown 3 at the end of the 2020s.

2.2 A Large Ion Collider Experiment

ALICE is the only LHC experiment dedicated to the study of heavy-ion collisions and the quark gluon plasma [119]. In particular, the experiment is designed to handle the large charged particle multiplicity produced in Pb–Pb collisions, which can attain 2000 per unit of rapidity. In addition, the particles are tracked and identified down to a few MeV/c on transverse momentum. These characteristics make ALICE unique among the LHC experiments. During LS2 (2018-2021), the LHC upgrade increased the instantaneous Pb–Pb luminosity $\mathcal{L}_{\mathrm{Pb-Pb}} = 6 \times 10^{27} \mathrm{cm}^{-2}\,\mathrm{s}^{-1}$.

[1] 1 barn = $10^{-24} \mathrm{cm}^{-2}$

ALICE is made up of different sub-detectors (Fig. 2.3) with different purposes which we will detail below. Global detectors, located around the interaction point, provide measurements of quantities such as the collision time and particle multiplicity. The central barrel detectors allow to identify and track the charged particles at midrapidity. It also provides photon detection capabilities. The Muon spectrometer covers the forward rapidity region $-4.0 < \eta < -2.5$ and is intended for muon measurements.

The ALICE coordinate system is a Cartesian system where the z-axis coincides with the beam pipe direction. The positive z is oriented towards the ATLAS experiment, known as the A-side. The C-side is in the opposite orientation, pointing towards the CMS experiment. The x-axis is in the horizontal plane, pointing to the center of the LHC. The y-axis points upward.

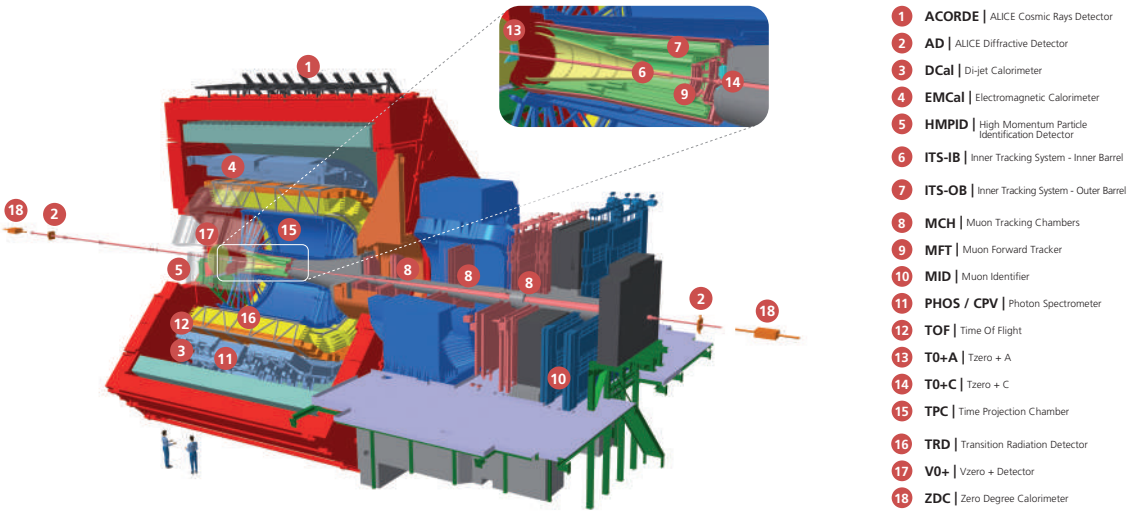

Figure 2.3: The Run 3 ALICE detector structure [120].

The Inner Tracking System 2 (ITS2) [121]: it allows for the determination of primary vertex position of collisions and the secondary vertices of heavy hadron decays at midrapidity. It also provides tracking down to low p_{T} and improves the momentum and angular resolution for the TPC. It is made up of seven silicon layers around the interaction point (Fig. 2.4), with the pseudorapidity region $|\eta| \leq 1.3$ and full azimuthal coverage. It is based on ALPIDE chips, which will be discussed in the next chapter. The total surface of active silicon is $10\,\mathrm{m}^2$. It provides a good impact parameter resolution of $\sim 25\,\mu\mathrm{m}$ in both $r\phi$ and z dimensions [121]. This is mainly due to the location of the ITS2 $21\,\mathrm{mm}$ away from the interaction region, a small pixel size and a light material budget for the inner barrel (from $1.14\%\mathrm{X}_0$ to $0.35\%\ \mathrm{X}_0$).

The Time Projection Chamber (TPC) [122]: it is a $90\,\mathrm{m}^3$ cylinder (Fig. 2.5) filled with $\mathrm{Ne}-\mathrm{CO}_2-\mathrm{N}_2$ gas, with the acceptance $|\eta| \leq 0.9$ and full azimuthal coverage. When a charged particle passes through the detector, it will ionize the gas. An electric field will make the produced secondary electrons drift towards the TPC end-plates, based on Gas Electron

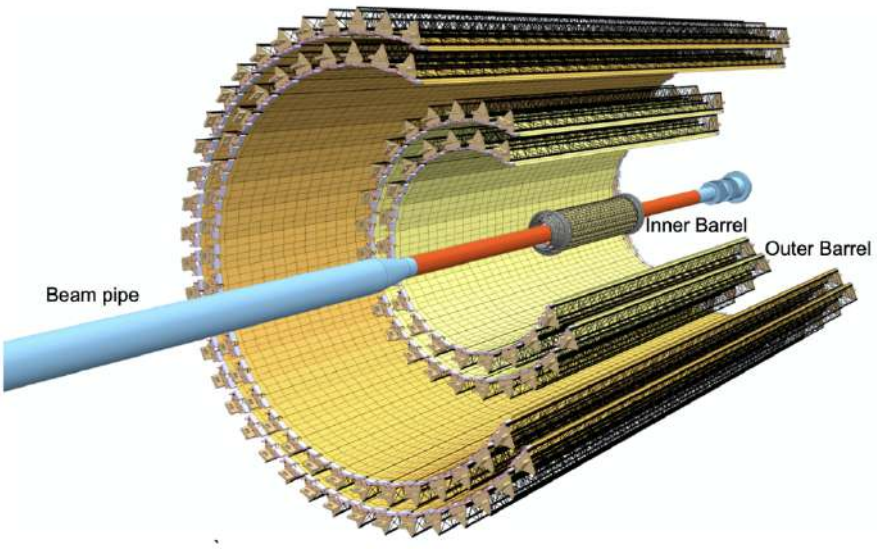

Figure 2.4: Illustration of the ITS2 layout [121].

Multipliers (GEM). The information provided by these end-plates allows for particle identification, tracking and momentum measurements of the charged particle.

The Time Of Flight detector (TOF) [123]: it is composed of a cylindrical array located radially $3.7\,\mathrm{m}$ from the interaction point. It is divided into 18 sectors based on Multigap Resistive Plate Chambers. The acceptance of the detector is $|\eta| \leq 0.9$, with full azimuthal coverage. TOF measures the time at which the particle crossed the detector, with a resolution better than $50\,\mathrm{ps}$. This measurement allows to determine the velocity of particles passing through the detector, and identify protons with $p < 4\,\mathrm{GeV}/c$, pions and kaons with $p < 2.5\,\mathrm{GeV}/c$.

The Transition Radiation Detector (TRD) [124]: it consists of a cylinder around the TPC with a diameter of $7\,\mathrm{m}$ and covers the pseudorapidity region of $|\eta| \leq 0.84$, with full azimuthal coverage. It is composed of 6 chambers of MWPC with an amplification and a drift region. It distinguishes between electron-pion particles with $p_\mathrm{T} \geq 1\,\mathrm{GeV/c}$, and provides tracking information to complement the other central barrel detectors.

The ElectroMagnetic Calorimeter (EMCal) [125]: it covers the azimuthal region of $\Delta\phi = 110^\circ$ and the pseudorapidity region $|\eta| < 0.7$. It is a layered Pb-scintillator sampling calorimeter. It allows for the identification of particles as photons and neutral mesons via their photonic decay channel.

The PHOton Spectrometer (PHOS) [126]: it covers the azimuthal range of $\Delta\phi = 70^\circ$, in the pseudorapidity region $|\eta| < 0.12$. It consists of an electromagnetic calorimeter, and measures photons and neutral mesons via their photonic decay channel.

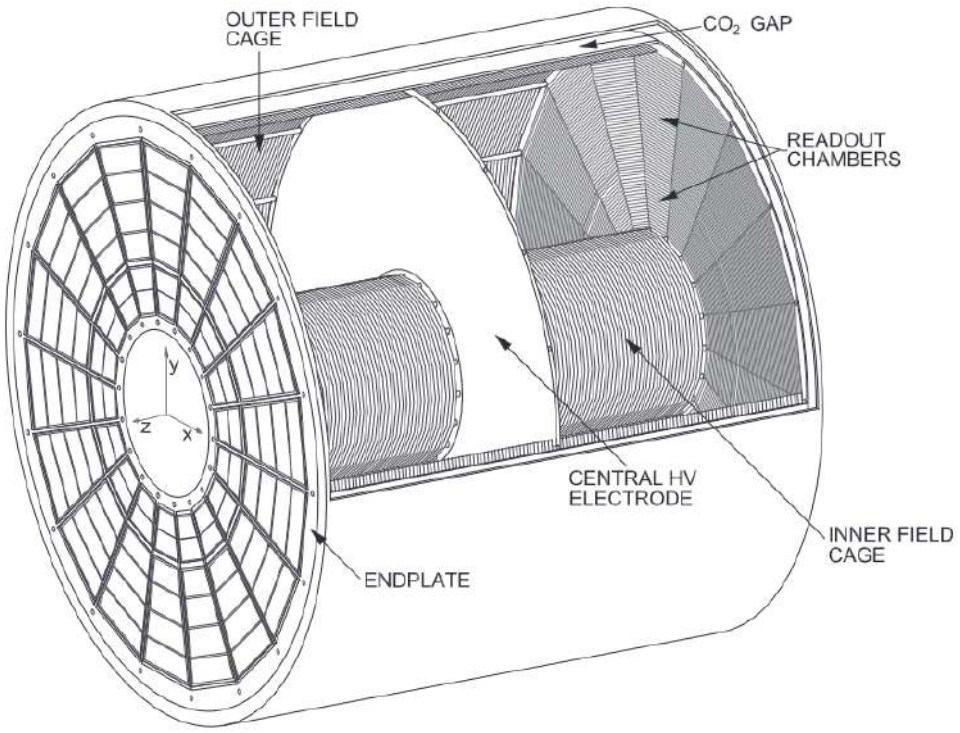

Figure 2.5: Illustration of the TPC layout [122].

The High Momentum Particle Identification Detector (HMPID) [127]: it covers the azimuthal range $\Delta\phi = 58°$ within the pseudorapidity region $|\eta| \leq 0.6$. It is based on the Ring Imaging CHerenkov (RICH) technology. It provides additional identification information for kaons, pions and proton separation.

The Fast Interaction Trigger detector (FIT) [128]: it is composed of three detectors (Fig. 2.6), located at positions along the beam pipe between $-19.5\,\mathrm{m}$ and $17\,\mathrm{m}$ from the interaction point (IP):

- The FT-zero (FT0) detector: it consists of two detectors, FT0A and FT0C, located on opposite sides of the interaction point, each composed of 12 Cherenkov counters. This detector determines a vertex position for the collisions, and provides a precise collision time with $25\,\mathrm{ps}$ resolution, giving a start-time for the TOF detector.

- The FV-zero (FV0) detector: it is a large, segmented scintillator disk, divided into five concentric rings of equal pseudorapidity coverage. The outer diameter of the largest ring is $144\,\mathrm{cm}$ and the inner diameter of the smallest is $8\,\mathrm{cm}$. This segmentation, combined with the information from the other forward detectors, is sufficient to yield the required centrality and event plane resolution. Together with FT0, FV0 provides the needed input to generate minimum bias and multiplicity triggers.

- The Forward Diffractive Detector (FDD): it is composed of two subdetectors placed on opposite sides of the IP. Each array consists of eight rectangular scintillator pads.

The FDD provides measurement of centrality based on the charged-particle multiplicity, and contributes to the selection of ultra-peripheral collisions as well as measurements of diffractive cross section.

The Zero Degree Calorimeter (ZDC) [129]: it is a detector made up of two electromagnetic calorimeters (ZEM), two hadronic calorimeters for the detection of protons (ZP) and two for the detection of neutrons (ZN). Each of these calorimeters is a Cherenkov detector, composed of quartz fibers, read out by photomultipliers. The Cherenkov light, produced by the charged particles passing through the quartz at a speed higher than the speed of light within this material, is collected and amplified. The two hadronic calorimeters are located at $\mathrm{z} = \pm 112.5\,\mathrm{m}$ from the nominal interaction point, and detect spectator nucleons that emerge at 0° from the collisions. The electromagnetic calorimeters are both placed in the forward region of the experiment, at $7\,\mathrm{m}$ from the interaction point. They measure the energy deposited by photons at forward rapidity. The ZDC is mainly used to remove the parasitic beam-gas background events, and to determine the centrality in pPb and Pb–Pb collisions by measuring the energy deposited by the spectator nucleons.

2.2.1 The Muon spectrometer

The Muon spectrometer [130] is the main detector which will be used in the analysis presented in the following chapters. Its purpose is to study quarkonia $(J/\psi, \psi(2S), \Upsilon, \Upsilon', \Upsilon'')$, as well as the low mass vector mesons (ρ, ω, ϕ), open heavy flavor (D and B mesons), and gauge bosons $\left(Z^0, W^{\pm}\right)$ at forward rapidities $-4 < \eta < -2.5$ via their muonic decay channel, in pp, pPb and Pb–Pb collisions. The spectrometer covers the full azimuthal angle. As can be seen on Fig. 2.7, it is composed of a dipole magnet, muon tracking and muon identifier stations separated by an iron wall, front and rear absorbers, and an inner beam shielding. Due to the location of the front absorber between the spectrometer and the interaction point, tracks extrapolated to the IP undergo multiple scattering resulting notably in a resolution degradation. Thus, limitations are imposed on the exploitable physics program, in particular the inability to separate open charm and beauty contributions. To overcome these limitations for Run 3, the Muon Forward Tracker (MFT) was added in front of the muon spectrometer, between the interaction point and the front absorber. This new detector will be the topic of the next chapter.

The absorbers: the front absorber is designed to reduce the contamination of primary hadrons and of low momentum muons coming from pion and kaon decays. It is $4.13\,\mathrm{m}$ long ($\sim 10\,\lambda_{\mathrm{int}}$, $\sim 60\,X_0$) and located inside the solenoid at $90\,\mathrm{cm}$ from the interaction point. It is engineered to limit the multiple scatterings and thus limit the degradation of momentum and quarkonia invariant mass resolution. To reduce the multiple scatterings, the closest region to the IP is made of low-Z material, carbon, followed by concrete. Furthermore, materials with high-Z are used on the absorber's end side, such as Pb and Tungsten. The goal is to stop photons at low energies, along with the secondaries created in the absorber. Additionally, in order to protect the spectrometer from beam-gas interactions and secondaries produced at high rapidities, the low angle absorber is located around the beam pipe and is made of dense material such as Pb, Tungsten, and steel. Besides, an iron wall, measuring $1.2\,\mathrm{m}$ long ($\sim 7.2\,\lambda_{\mathrm{int}}$), is present between the tracking

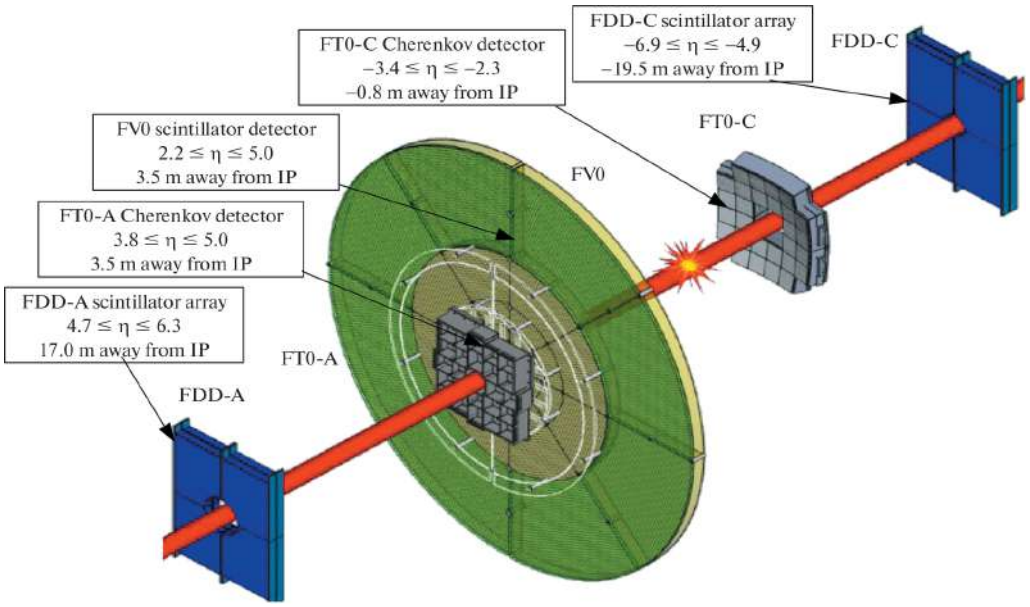

Figure 2.6: Illustration of the FIT layout [131].

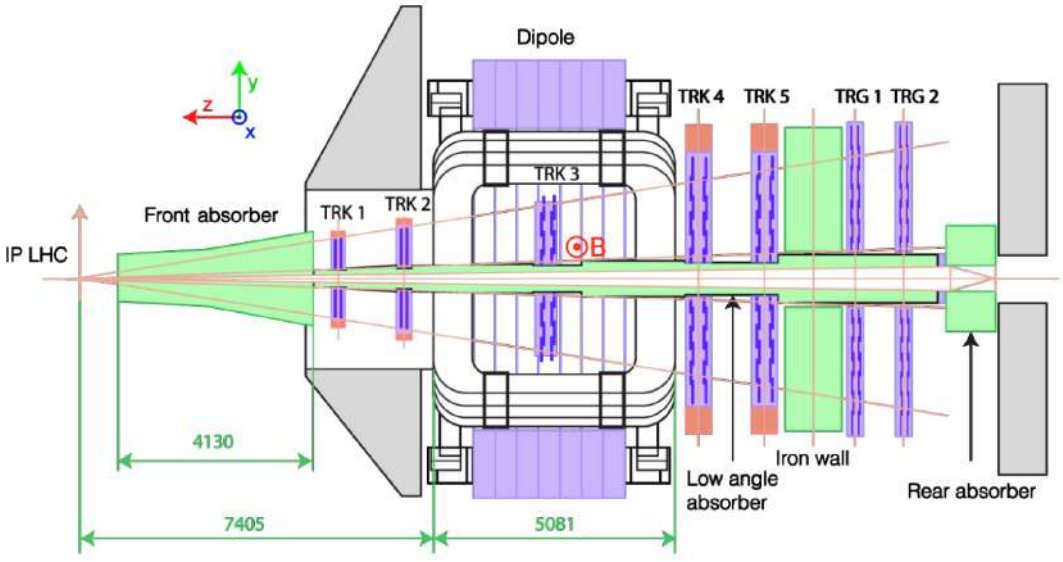

Figure 2.7: Schematic of the ALICE Muon Spectrometer [132].

and trigger chambers, with the objective of filtering muons, thus stopping the energetic hadronic background. The combined effect of the front absorber and the iron wall implies a minimum momentum for a muon to reach the muon identifier chambers to be $4\,\mathrm{GeV}/c$.

The dipole magnet: it is $5\,\mathrm{m}$ in length, $6.6\,\mathrm{m}$ wide, and $8.6\,\mathrm{m}$ in height, and it is located at $7\,\mathrm{m}$ from the IP. It creates a magnetic field with bending power of $3\,\mathrm{T\,m}$. The plane perpendicular to the magnetic field is known as the bending plane, and is the (yz) plane in the ALICE coordinate system. It bends energetic particles passing through, allowing the measurement of their curvature, and thus of their momentum and electric charge.

The Muon CHambers (MCH): they form the tracking system of the Muon spectrometer, with 5 stations, each composed of 2 chambers, located between $5.2\,\mathrm{m}$ and $14.4\,\mathrm{m}$ from the IP. Their design was optimized to minimize the scatterings that can take place when the muons are going through; they are composed of low-Z materials, such as carbon fibers. They consist of cathode pad chambers with a high granularity ($\sim 2\%$ occupancy in central Pb–Pb collisions at $\sqrt{s_{\mathrm{NN}}} = 2.76\,\mathrm{TeV}$ [133]), each composed of a central anode wire situated between two cathode planes. The chambers are filled with a gas mixture of Argon (80%), and $\mathrm{CO}_2(20\%)$. Thus, a particle passing through will ionize the volume, liberating electrons that will drift to a nearby cathode, generating a signal.

The Muon IDentification (MID): it is located $16\,\mathrm{m}$ away from the IP, behind the iron wall filter. It is composed of 2 stations, each made of two planes of resistive plate. These plates are composed of electrodes separated by a gap of $2\,\mathrm{mm}$ filled with gas. The crossing of charged particles produces an avalanche of secondary electrons. The time of response when a muon passes through these chambers is around $2\,\mathrm{ns}$. However, as will be mentioned later, the readout frame of this detector is longer: about $25\,\mathrm{ns}$.

2.2.2 Continuous readout and Online-Offline processing

During the Long Shutdown 2 (from 2018 to late 2021) preceding Run 3, the detector electronics were improved to allow for an operative mode known as "continuous readout" [134]. This means that the detectors are continuously read during the full duration of the physics fill. This is in contrast with the prior mode of operation used in Run 1 and Run 2, which was based on start-of-readout signals delivered by dedicated hardware, known as triggers, when various types of signals indicating valuable events are detected. To ensure synchronisation, all detectors working in the continuous mode receive a clock signal propagated[2] from the LHC radio-frequency cavities (the "beam" clock), allowing each piece of readout data to be timestamped with the precision of a LHC bunch crossing of $\sim 25\,\mathrm{ns}$.

The data stream from the detector front-end electronics is distributed to the data acquisition system, which is comprised of Local Trigger Units connected to Common Readout Units (CRUs). It is then directed to the processing farms, equipped with the new Online-Offline (O^2) software environment, where the First Level Processors (FLPs) receive the

[2]The distribution of this timing signal to all subdetectors is handled by the Central Trigger System of ALICE [134]. The distribution units are the Local Trigger Units (LTUs).

raw detector data from the CRUs and send them after some local treatment to the Event Processing Nodes (EPNs)[3] This processing chain handles the continuous data stream by dividing it into chunks named time frames (TFs). Indeed, this architecture is designed to run the reconstruction over the duration of one such time chunk, and process independent ones in parallel (one TF per EPN) to speed-up the data treatment, while also running algorithms to compress and skim the data. The detector front-end electronics generate as much raw data as $\sim 3.4\,\mathrm{TB\,s^{-1}}$. The data are compressed to $900\,\mathrm{GB\,s^{-1}}$ by the FLPs. The output of the EPN farm amounts to $\sim 130\,\mathrm{GB\,s^{-1}}$ at the end of the intermediate step of the reconstruction (i.e. the synchronous or online part) [134]. This continuous readout and the data reduction lead to an efficient use of the enhanced luminosity to be delivered by the LHC in Run 3 and thus significantly increase in statistics and performance for the study of rare events, such as heavy-flavours, which is one of the objectives of Run 3.

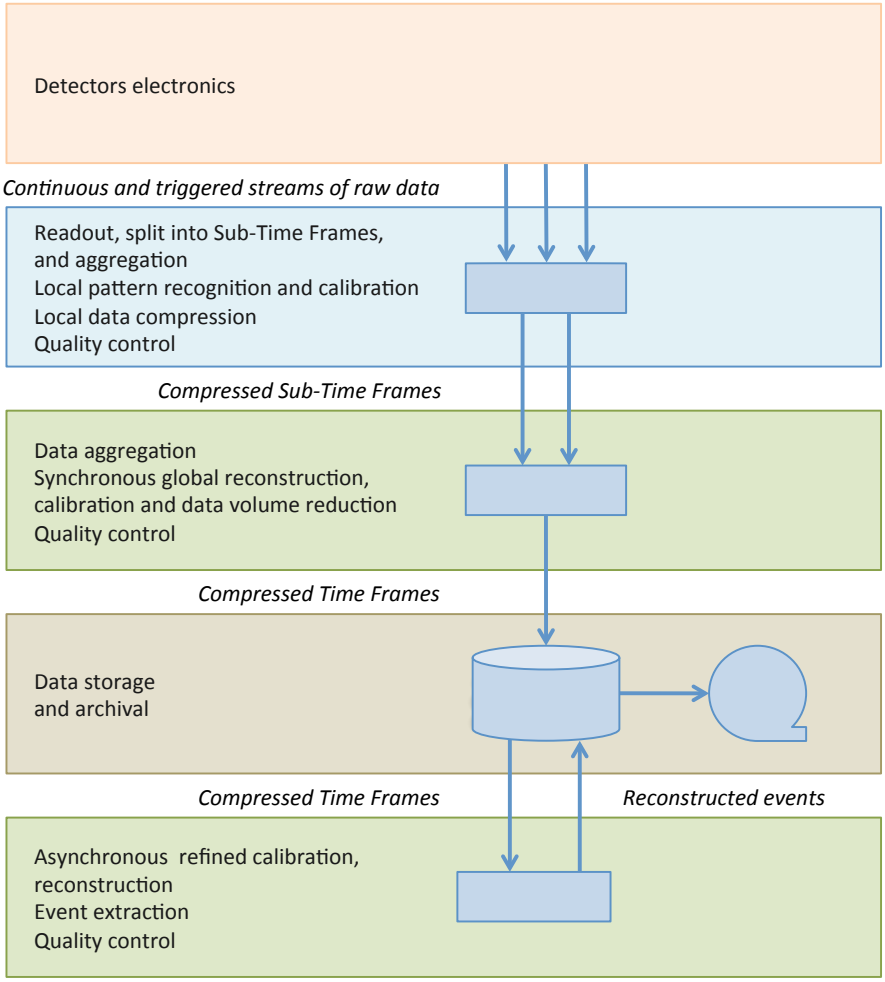

Figure 2.8: A full scheme of the online-offline computing system [135].

The duration of a TF is defined arbitrarily by ALICE as a given number of LHC orbits. One LHC orbit is completed into $\sim 89\,\mu\mathrm{s}$ or 3564 bunch crossings (BC). During the commission-

[3]The first level farm is composed of 198 FLPs and 474 CRUs. The EPN farm consists of 280 servers hosting 8 GPUs and 64 CPU cores each [134].

ing in 2021 and the regular data taking period in 2022, 1 TF = 128 LHC orbits, equivalent to $11.3825\,\mathrm{ms}$. At $50\,\mathrm{kHz}$ interaction rate, it contains on average 569 Pb–Pb collisions [134]. In 2023, to fluidify the synchronous processing, it was reduced such that 1 TF = 32 LHC orbits.

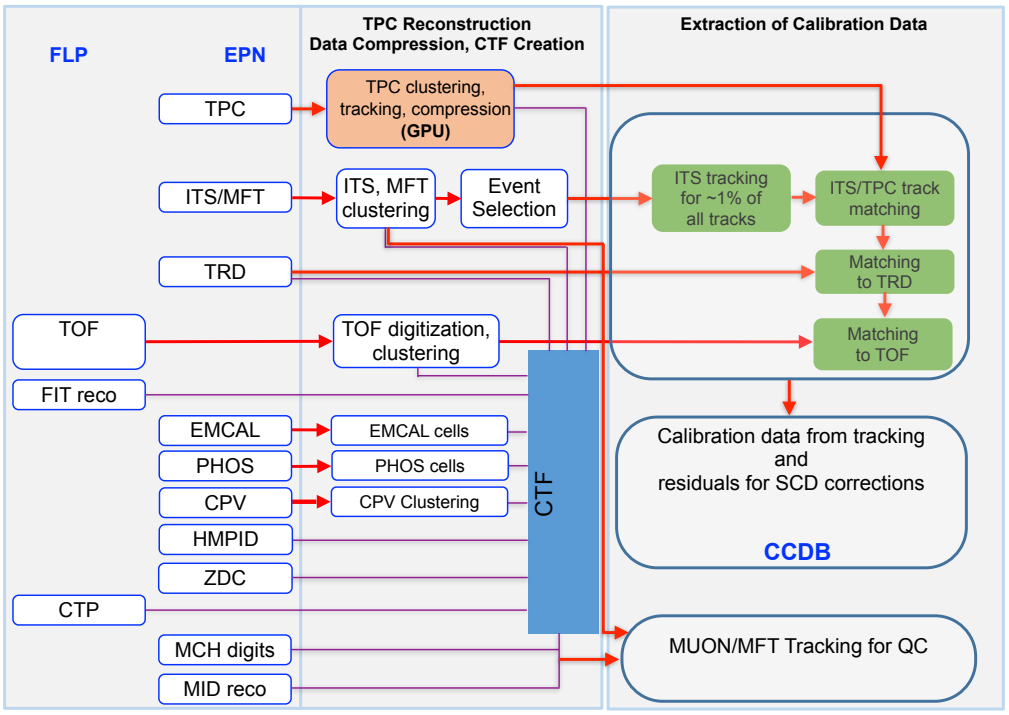

Figure 2.9: Illustration of the different processes of synchronous reconstruction workflow [134].

Going into the details of the synchronous and asynchronous processing sketched on Fig. 2.8 and Fig. 2.9:

- Each TF is further subdivided into sub-time frames (STFs). An STF corresponds to the data from a sub-part of the ALICE detector during a LHC orbit. The STFs follow parallelized synchronous (online) processing on the FLPs. One can note that FLPs can also perform calibration tasks, depending on the detector, and a dedicated FLP is used to collect and process data from the Detector Control System (DCS). It processes and stores detector-related conditions like voltages or temperature, in calibration objects, which are stored in the Condition and Calibration Database (CCDB). They can then be accessed later, including during asynchronous stages and during physics analysis.
- All the compressed STFs that belong to the same TF are shipped from the FLPs to a given EPN for aggregation (TF building).
- The synchronous part of the reconstruction will be finished on the EPN farm[4]. The main objective of the synchronous processing is the reduction of the data rate, especially from the TPC, which accounts for most of the raw data volume. This is

[4]In general, synchronous data processing is performed on CPU cores in parallel with the GPU processing.

achieved by performing clustering, full track reconstruction and removing background hits from the data. The compressed data are aggregated into so-called compressed time frames (CTFs) and written to a semi-permanent disk buffer.

- After this synchronous stage comes the asynchronous stage, where data reconstruction and final calibrations using the CCDB-stored objects are done on EPNs and on the GRID environment. The final outputs are the Analysis Object Data (AOD), kept on permanent disk storage. These objects contain the information on the reconstructed tracks left by the particles in the detectors. The following physics analysis all exploit these produced objects.

2.2.3 Data taking performances in early Run 3

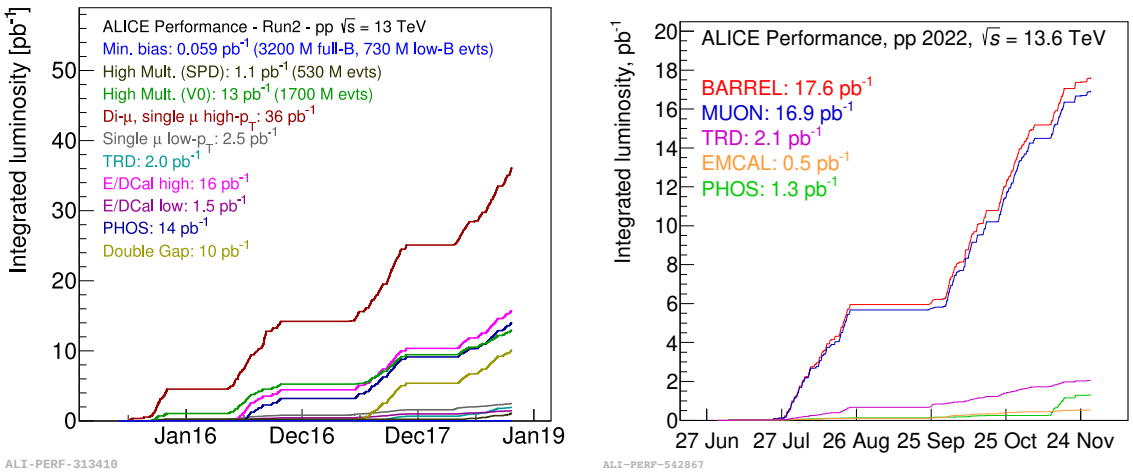

Figure 2.10: (Left) Integrated luminosity for various triggers in pp collisions at $\sqrt{s} = 13\,\mathrm{TeV}$ during Run 2, (right) Integrated luminosity for pp collisions at $\sqrt{s} = 13.6\,\mathrm{TeV}$ taken in 2022.

The continuous readout architecture of Run 3 aims at precise measurements in the open heavy-flavour or low mass dilepton sector. Since these processes do not exhibit signatures that can easily be discriminated by hardware triggers, they can only be satisfactorily collected with a zero bias (Minimum Bias) interaction trigger, i.e. corresponding to an event with at least an inelastic collision. During the beginning of Run 3, in 2022, pp data was recorded mostly at $500\,\mathrm{kHz}$ interaction rate. The integrated luminosity during this period is displayed on Fig. 2.10 (right), which can be compared to the one accumulated during the whole duration of Run 2 (left). The EMCAL detector is still operating in legacy triggered mode as the readout electronics were not upgraded, which explains the lower collected luminosity compared to the Muon and Barrel detectors. As can be seen, the Muon integrated luminosity sampled by the continuous mode in 2022 already amounts to almost half of the dimuon triggered luminosity of Run 2, and more than 6 times the low-p_{T} muon luminosity (recorded with a specific and down-scaled trigger in Run 2 due to bandwidth limitations of the old data acquisition system).

Chapter 3

Muon reconstruction with the Muon Forward Tracker

Among the different detector upgrades installed during LS2 is the Muon Forward Tracker (MFT). It is a Silicon tracking detector designed to add secondary vertexing capabilities to the Muon spectrometer. With this new detector, ALICE will gain access to physics cases. In the first section of this chapter (Sec. 3.1), a brief overview of these new physics cases is given. Next, in Sec. 3.2, is a general presentation of the detector and its reconstruction strategy. The third section is a summary of my personal contribution to the MFT project (Sec. 3.3). Finally, the last section is dedicated to the track matching between the MFT and the Muon spectrometer (Sec. 3.4).

3.1 Physics motivation

The Muon spectrometer allows for measurements at forward rapidities, such as the study of the open heavy-flavours and quarkonium yields, flow and polarization. In addition, it is also possible to study low mass vector mesons, to assess the modification of their spectral function in heavy-ion collisions. However, due to the multiple scattering in the front absorber, the origin of muons is not determined with good precision. Therefore, muons produced e.g. by the decay of charmonia cannot be distinguished from those produced by pion and kaon decays, thus introducing background. Another consequence is that only inclusive measurements are possible with the Muon spectrometer, which does not resolve the collision vertex. Hence, prompt and non-prompt J/ψ measurements as the muons produced from semileptonic decay of charm and beauty can not be disentangled. Furthermore, the multiple scatterings lead to a reduced angular resolution, thus the resonances have a limited invariant mass resolution, in particular at low masses (ω and ϕ mesons). Indeed, the invariant mass of a dimuon is computed as a function of the opening angle θ between the momentum of the two muons:

$$M_{\mu^-\mu^+} = \sqrt{2p_{\mu^-}p_{\mu^+}(1-\cos\theta)} \approx \sqrt{p_{\mu^-}p_{\mu^+}}\theta \tag{3.1}$$

where p_{μ^-} and p_{μ^+} are the magnitude of the momenta of the muon and anti-muon. In Eq. 3.1, we neglect the muon mass, and consider only a small opening angle θ. From this consideration, one sees that the mass resolution is sensitive to both the momentum resolution and the angular resolution.

The MFT upgrade has been proposed, with the goal of providing secondary vertexing capability to the Muon spectrometer. This is done by measuring the positions of muon tracks in layers located much closer to the interaction point than the Muon chambers, upstream of the hadronic absorber. The production vertex of muons can then be determined by extrapolating the tracks formed by the combination of the MFT and the Muon spectrometer, towards the interaction point.

By overcoming this limitation of the Muon spectrometer, mainly due to the presence of the front absorber, the MFT extends the physics program of ALICE in the forward rapidity region. This region is of particular interest, since particles with large absolute pseudorapidities carry a large longitudinal momenta, due to the relativistic boost. This allows to track particles down to p_{T} values smaller than at mid-rapdity, since the bending of particles in a magnetic field is sensitive to the total momentum of the particle. Some of the physics studies that will be amenable with the MFT upgrade are:

- Quarkonium: the MFT will allow for the separation of prompt and non-prompt components to charmonia cross sections. For the $\psi(2\,\mathrm{S})$, a better extraction of the signal is expected, thanks to the background rejection capability of the MFT.
- Heavy-flavour: the MFT will allow for the rejection of background muons coming from pions and kaons decays. This will improve the studies of open heavy flavor hadrons, see [136]. In particular, measurements of open charm will be feasible down to low transverse momentum. In addition, making use of the separation of prompt and non-prompt J/ψ, the measurement of open-beauty hadrons will also be achievable down to low transverse momentum through the $B \to J/\psi + X$ channels.
- B_c: a special case of interest among the $B \to J/\psi + X$ channels is the $B_c \to J/\psi + \mu$. The MFT will allow to reconstruct the 3-prong vertices of this decay, thus measuring the B_c particle at forward rapidities in Pb–Pb. This particle is of great interest for the understanding of regeneration mechanisms. It has been measured in Pb–Pb by the CMS collaboration [137], but only down to $p_{\mathrm{T}} > 6\,\mathrm{GeV}/c$, thus missing the lower p_{T} region where the regeneration mechanism should be the most effective. The measurement of this particle at forward rapidity, with the background rejection allowed by the MFT, will make this region accessible.
- Low-mass dimuons: with the improved resolution on the dimuon opening angle and the background reduction, an enhanced mass resolution is expected for all resonances. In particular, the resolution of low mass resonances (e.g. ω and ϕ) is expected to improve by a factor ~ 4 compared to Run 2, see [136]. The study of these resonances is of prime importance regarding the broadening of the associated spectral functions, due to the expected restoration of chiral symmetry in the QGP phase.

In summary, the Muon spectrometer together with the MFT extends the central barrel pseudo-rapidity $|\eta| < 0.9$ to the forward region $-3.6 < \eta < -2.5$. This acceptance, and measurement capability down to zero transverse momentum, makes ALICE a powerful and unique experiment at the LHC.

3.2 Presentation of the detector

3.2.1 The ALPIDE chip

The most central Pb–Pb collisions can produce up to 10,000 charged tracks, which form a high multiplicity environment. In such conditions, the sensors must have a very small spatial resolution (about $5\,\mu\mathrm{m}$) and a high granularity to distinguish tracks close to the interaction point. In addition, the material budget must be as low as attainable to avoid as much deviation as possible due to multiple scattering of the charged tracks with the material. Furthermore, the readout of the MFT must be able to withstand Run 3 collision rates of $50\,\mathrm{kHz}$ in Pb–Pb and $500\,\mathrm{kHz}$ in pp collisions. In terms of resistance to radiation damage, the sensor should also be able to maintain appropriate performance until it has endured the full integrated luminosity of pp and Pb–Pb collisions targeted in the Run 3 physics program. Finally, the power consumption of the sensors has to be as low as possible to lighten the cooling infrastructure, which can increase the material budget in some parts of the detector.

In order to fulfill the requirement of a high spatial resolution for good track reconstruction performance in the high multiplicity environment of central Pb–Pb collisions, a new semiconductor pixel chip was designed, the ALice PIxel DEtector (ALPIDE) [138]. Since the particle hit density on the MFT layers closest to the beam pipe is of the same order of magnitude ($650\,\mathrm{khit\,s^{-1}\,cm^{-2}}$) as the particle hit density in the ITS2 inner layers, the same silicon pixel chip is used for MFT and ITS2 inner layers.

In a semiconductor, electrons in the conduction band are separated from the valence band by a small energy gap, and can easily move under an electric field. In particular, for silicon, electron-hole pairs are easily created by thermal excitation. By introducing impurities into the silicon crystal lattice, one can produce silicon either doped with electron acceptor atoms, the p-type, or with electron donor atoms, the n-type silicon. A p-n junction is obtained by joining a p-type with a n-type silicon. Because of the different concentrations of electrons and holes in the two types, bringing them in contact sets off a diffusion of electrons towards the p-type region and holes into the n-type region. A surplus of negative charge in the p-type region (positive charge in the n-type region) is created, which generates an electric field counteracting the diffusion. A potential barrier is therefore generated between the two space charge densities, and at equilibrium, the contact region is devoid of charge carriers, forming a so-called depleted region. Additionally, an external voltage can be applied to a p-n junction. If the junction is submitted to a reverse bias voltage (also called back bias), with the positive source connected to the n-type side and negative to the p-type side, the depletion volume becomes wider when increasing the reverse bias voltage.

ALPIDE sensors use the CMOS Monolithic Active Pixel Sensor (MAPS) technology [139, 140]. MAPS allows to combine the sensitive layer and the readout electronics in the same silicon die. The chosen technology is the $0.18\,\mu\mathrm{m}$ CMOS imaging process by TowerJazz. Each chip measures $15\,\mathrm{mm} \times 30\,\mathrm{mm}$. The total thickness of the ALPIDE used in MFT is $50\,\mu\mathrm{m}$. A high resistivity ($> 1\mathrm{k}\Omega \cdot \mathrm{cm}$) epitaxial layer ($25\,\mu\mathrm{m}$ thick) is used as the sensitive

volume of the detector for the ionising particle, with a n-well diode working as a charge collection unit. This is illustrated in Fig. 3.1. When a charged particle crosses the epitaxial layer, it generates electron-hole pairs along its path.The total amount of available charge created by a minimum ionising particle traversing this layer thickness is of the order of a thousand electrons [141]. The electrons first move by thermal diffusion within the epitaxial layer only, due to two potential barriers acting as shielding; the first is between the lightly doped epitaxial layer and the heavily doped p-wells[1] covering it, and the second is at the interface with the underlying highly p-doped substrate.The electrons then reach the depletion volume, where they drift towards the collection diode. A typical collection time is of the order of 100 ns. At that point, the diode generates a signal PIX_IN (Fig. 3.2) at the input of the front-end electronics. The charge collection speed and efficiency can be improved by enlarging the depletion volume. This volume can be enlarged in chip operation by applying a back bias voltage between the collection electrode and the substrate. Heavily irradiated ALPIDE prototype sensors were subjected to test beams, and demonstrated to keep the required functioning performance for non-ionizing doses corresponding to ten times the fluence expected over the ITS2 detector lifetime [134].

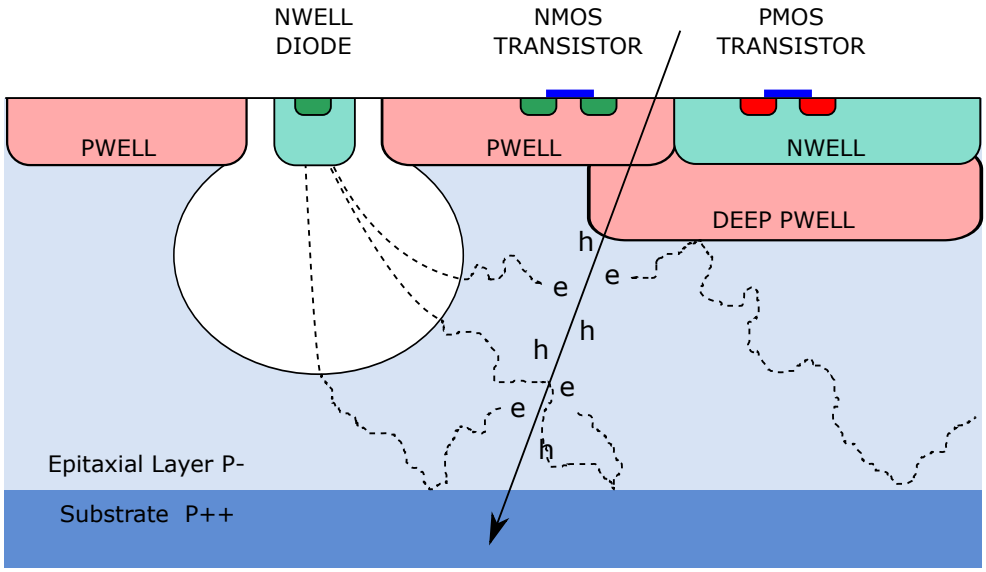

Figure 3.1: Schematic cross section of a MAPS single pixel cell [121].

Each chip is composed of a 512 rows x 1024 columns pixels matrix. These pixels are connected to a readout circuitry organised in a double column pattern, as shown on Fig. 3.3. Its role is to propagate the addresses of the fired pixels to the digital part of the chip. Each pixel cell contains a collecting diode, a front-end amplifying and shaping stage (with $\sim 2\,\mu$s characteristic peaking time of the output signal), a discriminator and a digital section. The digital section includes three hit storage registers (Multi Event Buffer), a pixel masking register and pulsing logic.

[1]The p-wells are shielding the readout circuitry. In particular, the deep p-well prevents the n-well from competing with the collection diode.

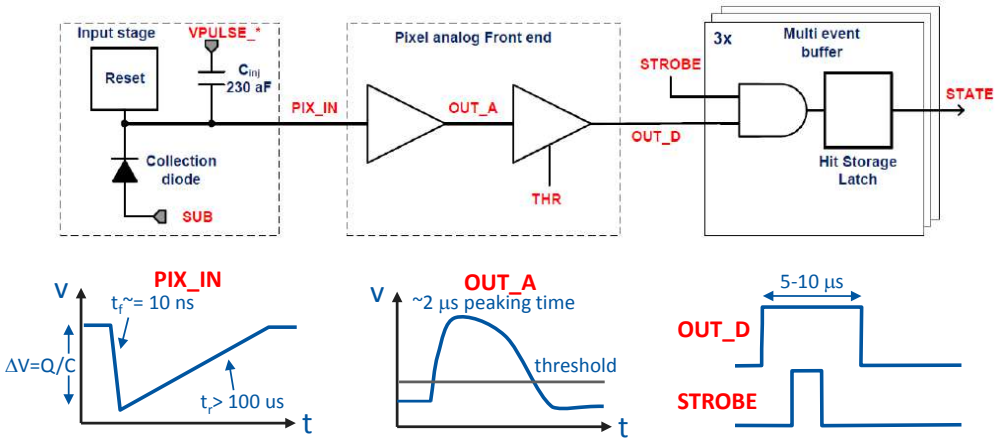

Figure 3.2: Block diagram of the ALPIDE pixel cell [138].

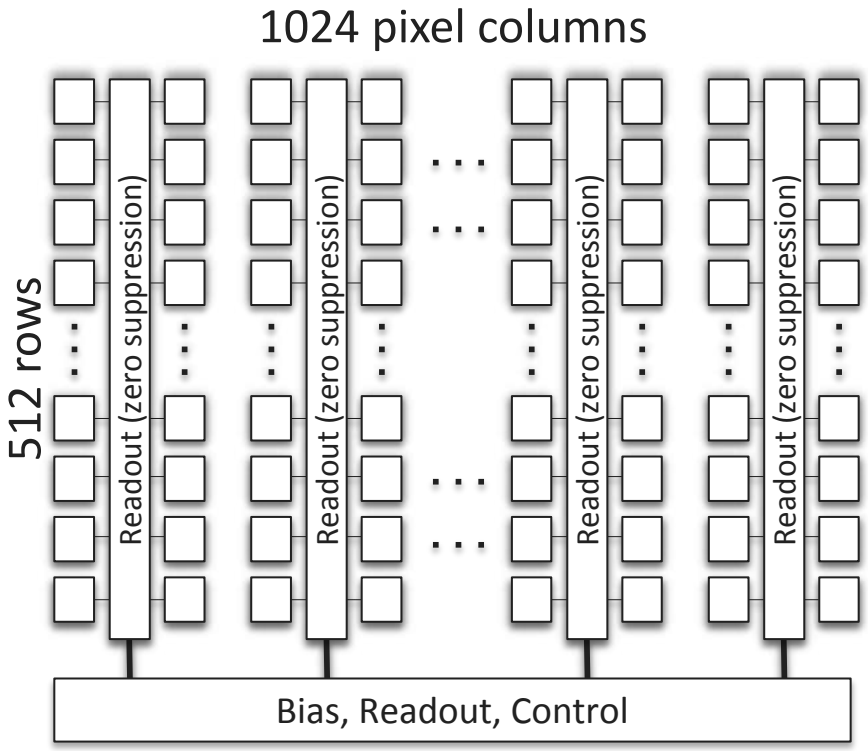

Figure 3.3: General architecture of the ALPIDE chip [134].

A common threshold voltage is applied to all the pixels of the matrix. When the amplitude of the signal is above the threshold, the discriminator outputs an OUT_D hit signal. The storage of the discriminated hits in the registers is controlled by a STROBE signal applied to the full matrix: a pixel hit is stored into one of three registers only if a STROBE pulse is received by a selected cell, while the frontend output is above the threshold voltage [142, 138]. The generation of the internal STROBE signals is the result of an external trigger received by the ALPIDE.The duration of the STROBE pulses is programmable (with a duration expressed in number of BC clock) and is called a Readout Frame (ROF). For the MFT, the ALPIDE pixel sensors usually open the readout frames at a rate close to $202\,\mathrm{kHz}$ in pp collisions (18 ROFs of 198 BC per LHC orbit), or $45\,\mathrm{kHz}$ in Pb–Pb collisions (4 ROFs of 891 BC per LHC orbit).

3.2.2 Detector layout

The MFT provides pointing resolution for muons, and vertexing capability at forward rapidity by matching the tracks reconstructed in the Muon arm to those reconstructed in the MFT. This approach allows for a pointing resolution of muon tracks down to about $100\,\mu\mathrm{m}$ according to the Technical Design Report [136]. The MFT is located $50\,\mathrm{cm}$ from the interaction point, between the interaction point and the front absorber, and surrounds the beam pipe at the closest possible distance. The layout is shown on Fig. 3.4. It provides charged particle tracking in the pseudorapidity interval $-3.6 < \eta < -2.45$. The acceptance is constrained by the size of the beam pipe, and by the volume and position of other detectors, such as ITS or FToC, and their support structures.

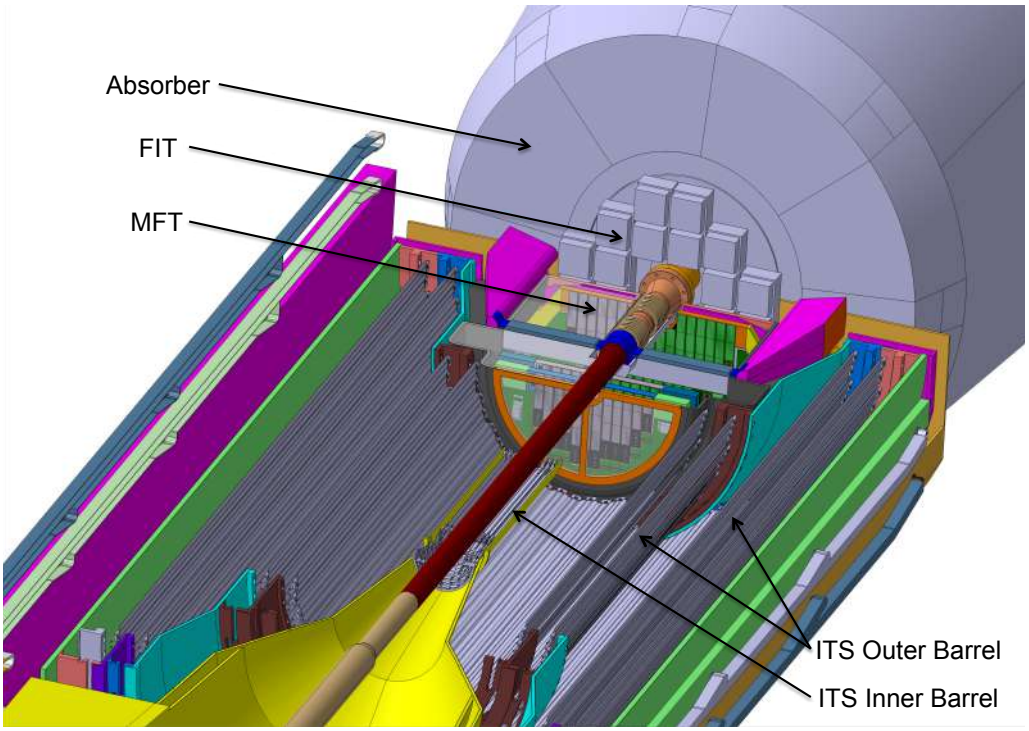

Figure 3.4: Layout of the MFT detector in ALICE [66].

To facilitate the installation of the detector around the beam pipe, the structure of the MFT is divided into two halves, labeled h0 (bottom half) and h1 (top half), which are then assembled together, as illustrated in Fig. 3.5. It is also segmented into five disks, labeled d0 to d4. d0 is the closest to the Interaction Point (IP). Each disk is subdivided into two half-disks (top and bottom one), corresponding to the upper (h1) and lower (h0) half of the MFT. Half-disks have the same global design and Half-Disk-0 and Half-Disk-1 are identical. Each half-disk has two detection planes, one on the front (f0) and one on the back side (f1). The overlap between sensors of the back and front planes ensures the hermeticity of the half-disk: 50% of charged particles will hit both planes of the disk. A total of 936 ALPIDE sensors are distributed and arranged in detection modules called ladders. The ladders are thin structural elements that hold the silicon pixel sensors and ensure electrical links between the sensors, the readout electronics and the power supply. There are

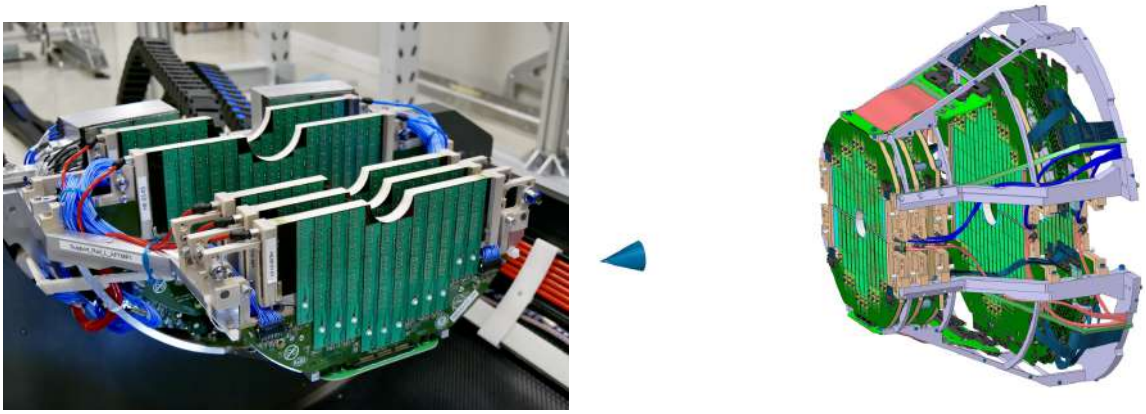

Figure 3.5: (Left) Fully assembled bottom half of the MFT [134], (right) A Schematic view of the full MFT detector [136].

280 ladders, which consist of Flexible Printed Circuits (FPCs) in aluminium connecting between 2 and 5 sensors, depending on the length. Each side of a half-disk, called a "face", contains between 24 and 34 ladders, and is divided into four zones, each of 3 to 5 ladders. Their assembly is illustrated on Fig. 3.6. The faces of the half-disk are separated by a volume which includes water pipes ensuring cooling of the ladders, which contributes to the material budget of the disks. Additional water cooling pipes are used to cool the DC-DC converters outside the acceptance.

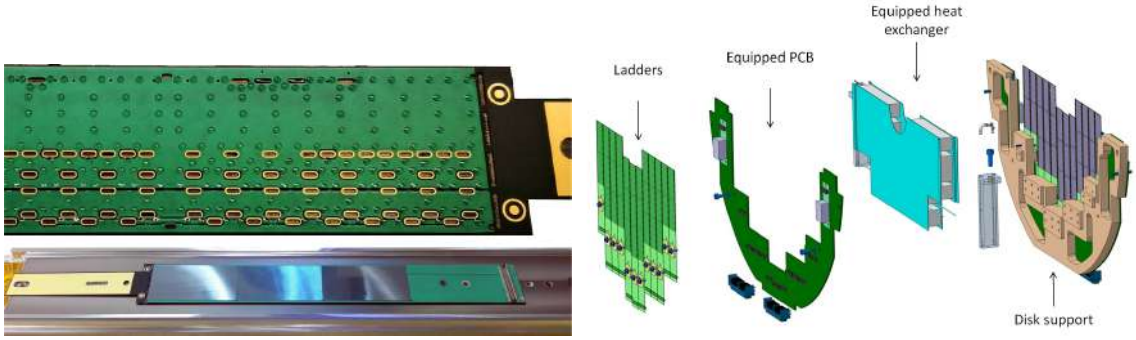

Figure 3.6: (Left) Back and front sides of an assembled ladder, (right) Detailed view of the assembly of a MFT half-disk [134].

The disks´ diameters increase with the distance from the interaction point. In order to power the ALPIDE sensors, three different supplies are requested: digital, analog and back-bias. The powering and power-consumption monitoring of all the half-disks of the detector are managed by a board, called Power Supply Unit (PSU). The MFT detector, composed of 80 zones, is controlled by a total of 4 PSUs for the powering and 80 Readout Units (RUs) for the readout. The disks and the PSU are watercooled and air ventilation is used to ensure temperature homogeneity inside the confined area where the MFT is installed. The half-disks and PSUs are fixed on supports called half-cones, themselves fixed on half-barrels. Powering and cooling services are running along the half-barrels whereas the

readout cables are guided along the front absorber to be connected to the RUs located at the end of this absorber.

3.2.3 Readout

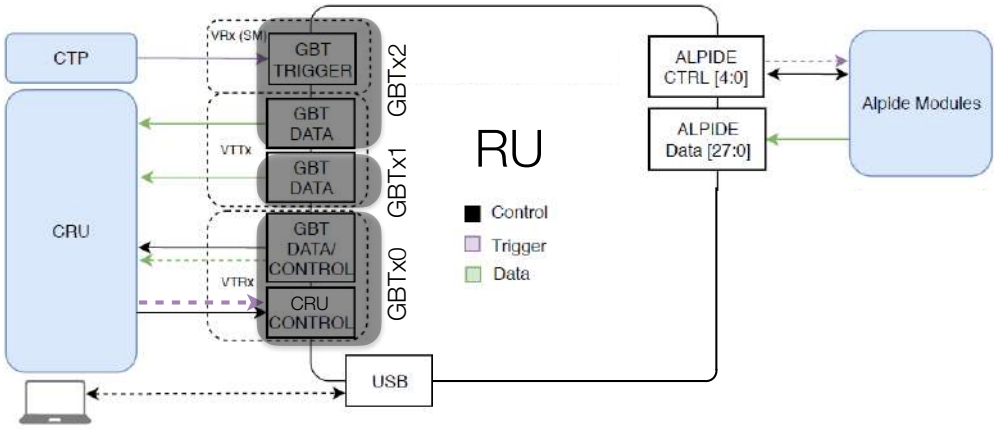

Figure 3.7: Block diagram of MFT Readout Unit card interface [143].

The readout system connects to the ALPIDE data, control, and clock lines. This connection is made by $\sim 8\,\mathrm{m}$ long copper cables that link the readout system to the half-disk PCBs where the ladders are plugged. The readout system receives timing information from the Local Trigger Unit (LTU) dedicated to the MFT, and which is the relay of the Central Trigger Processor (CTP) of ALICE. This ensures the synchronisation of the sensors across the full MFT and with the other detectors in ALICE. The readout system collects, encodes and delivers the raw output data from the sensors to the Common Readout Units (CRUs), housed in FLPs, through optical fibers. As the data throughput of the sensors is not homogeneous over the whole MFT (the sensors closer to the beam pipe have a higher occupancy), a Pb–Pb central Monte-Carlo event was used to select which zones of the MFT should be connected to which CRU, in order to level the load across the CRUs. Each zone is attributed to a Readout Unit card (RU), which collects the ALPIDE data as well as handles the control and clock to the ALPIDE modules. There is a total of 80 readout units for the whole detector. A block diagram of an MFT RU interface is shown on Fig. 3.7.

The readout units include a Field Programmable Gate Array (FPGA) chip, which is used to concentrate the $1.28\,\mathrm{Gb/s}$ data links from four sensors into one $4.96\,\mathrm{Gb/s}$ link. It also runs the main firmware that manages the readout process. In addition, the GBTx (Giga-Bit Transceiver optical link), a radiation tolerant chip, provides the simultaneous transfer of readout data, timing and trigger signals as well as slow control and monitoring data.

The GBTx chips on the RU cards plug into versatile modules (VTRx, VTTx and VRx) , as shown on Fig. 3.7, which convert optical and electrical signals. Via optical fibers, these modules send data to the CRUs, receive control instructions from the CRUs, and timing

messages. The source of the messages is the CTP, through the LTU, connected to the RU via a GBTx link.

3.2.4 Clusterization

The raw data coming from the FLPs of the detector are decoded into so-called "digits". These are an easily readable format in which the addresses (row, column) of all the fired pixels are listed, in each recorded Readout Frame (ROF) for all functioning sensor. The timestamp of all the digits in a given ROF will be the same. Hence, the ROF can be understood as the time resolution of this detector. As we saw in Sec. 3.2.1, for MFT (and ITS2), the ROF size is equal to the strobe length, chosen to be 198 BC in pp collisions, i.e. $\sim 5\mu$s. The next step is to process the decoded digits stored in these ROFs, in the "clusterization" step.

This procedure groups adjacent fired pixels to form a "cluster". Adjacent pixels are either pixels with common sides or corners. These clusters are later used to infer the kinematic properties of the particle which crossed the detector. Hence, each cluster should correspond to the passage of a particle through a considered detection element. The number of fired pixels which compose a cluster left by a charged track depends on the charge sharing between the pixels on a sensor, i.e. charge diffusion between neighboring pixels, which is a property of the chip. In addition, it can depend on the incidence angle of the track with respect to the detection element: a particle hitting a detection plane perpendicularly will fire only one or very few pixels. On the contrary, a track hitting close to parallel to the detection plane will fire many pixels.

For each cluster, space-point coordinates and associated uncertainties are then calculated and passed to the subsequent track-finding procedure. The clustering is performed for each sensor independently from others and can be executed in parallel. The cluster space-point coordinates are stored in the local frame of a sensor. The origin of this frame is the geometrical centre of a sensor. Using a transformation matrix associated with each sensor, these coordinates can be converted to the global ALICE frame or to the tracking frame of the sensor.

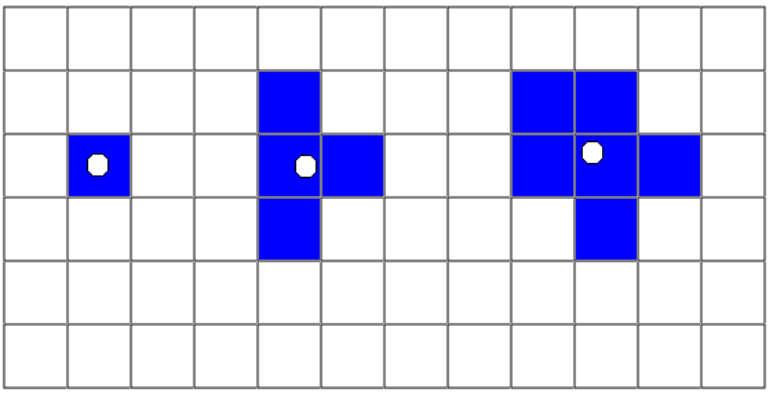

Figure 3.8: Illustration of different cluster patterns, formed by contiguous fired pixels. The white circles show the position of the center of gravity associated with each cluster.

The decoding algorithm, as well as the following clusterization step, both assume that the information about the fired pixels is ordered in row and column numbers. This in particular allows to perform the clusterization without storing the full matrix of the sensor in memory, keeping instead only temporary structures corresponding to the candidates for unfinished clusters. On the arrival of new fired pixel data (row or column), the algorithm checks if it matches the "adjacent" definition for cluster candidates left unfinished from the processing of current and previous rows. If this turns out to be the case, the corresponding cluster candidate is updated with the new pixel information. Otherwise, the unfinished cluster is considered as a new cluster candidate.

Whenever a new row is detected (or when the data from the next sensor arrives), all cluster candidates that were not updated during the processing of the previous row are converted to final clusters and stored. The conversion to a final cluster consists of calculating the center of gravity of its constituent pixels, accounting for the possible shift of the collecting diode from the geometrical centre of the pixels.

To further improve the computing efficiency, cluster dictionaries are used in the reconstruction. To each cluster shape, i.e. topology, a unique ID is attributed in the dictionary. The distribution of the topology-IDs is highly non-uniform, as illustrated by Fig. 3.9. The entries in the dictionaries contain information which is common to the clusters with the same topology:

- numbered of fired pixels,
- bounding box of the cluster, i.e. the smallest rectangle including all fired pixels,
- frequency of appearance of the topology,
- position of the Centre Of Gravity (COG) with respect to the bottom left corner pixel of the bounding box,
- uncertainty associated with the position of the hit point.

The use of such dictionaries avoids recomputing and saving redundantly the information of a given cluster, such as the COG or the position uncertainty. These information are of prime importance for the tracking step of the reconstruction, where the position and its associated error of each cluster are used to compute the track parameters, in a process known as Kalman filter [144, 145, 146], which will be presented in the next subsection (Sec. 3.2.5). Hence, saving the properties beforehand in a dictionary can gain computing efficiency, especially for cluster topologies which are very common. In the dictionary, the entries are sorted with respect to decreasing frequency.

On the other hand, rare topologies, i.e. with a frequency below a threshold defined a priori, do not have their own entries in the dictionaries, but are grouped together with topologies of similar dimensions, according to the dimensions of their bounding box. They are called "group" topologies. These rare topologies are always inside the group identified by the smallest completely filled box able to contain the topology, i.e. their filled bounding box.

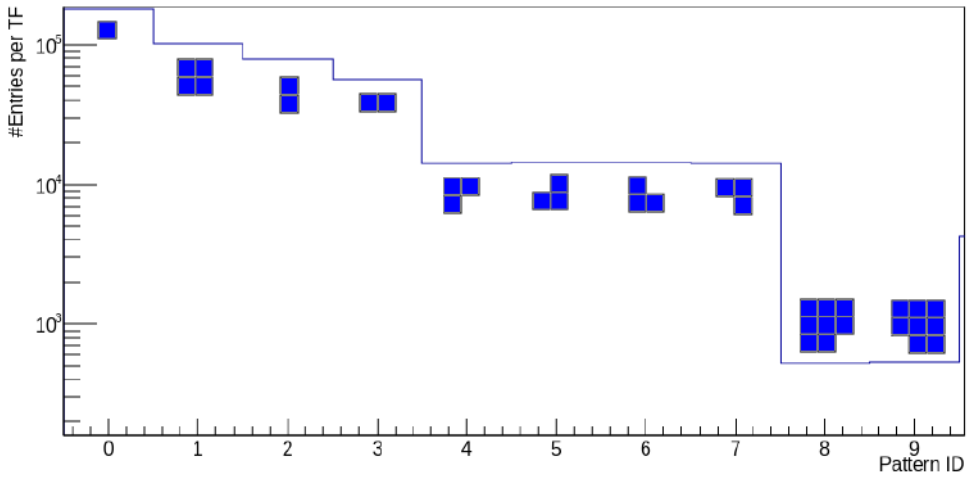

Figure 3.9: Distribution of cluster pattern ID, with the corresponding patterns, in June 2023 pp data.

3.2.5 Track reconstruction

The step following clusterization is track reconstruction. In this procedure, the collected clusters are attached to a track candidate, then used to compute the kinematic parameters of the track corresponding to the particle which left the said clusters in the detector. These parameters are chosen according to a precise track model. This model should be the most appropriate one given the various forces acting on the tracks. In the case of forward tracks, the data model is a helix model along the z direction, due to the solenoid magnetic field. In this track model, the parameters of a track are:

$$\vec{s} = \left(x, y, \phi, \tan\lambda, \frac{q}{p_{\mathrm{T}}} \right)$$

These parameters are defined with respect to a given (x, y) plane at a precise z position to which the track has been propagated. These parameters are illustrated in Fig. 3.10. Then, x and y are the coordinates of tracks in this propagation plane, ϕ the azimuthal angle, indicating the p_{T} direction, q the particle charge and λ the complementary polar angle, such as $\lambda = \frac{\pi}{2} - \theta$.

In the helix model, a track with a given set of 5 parameters at a z_0 location can be propagated to another z position with the transformation:

$$\begin{bmatrix} x \\ y \\ z \end{bmatrix} = \begin{bmatrix} x_0 - \frac{H_z}{(q/p_{t0})k}\sin(\phi_0)\cos(\theta) + \frac{H_z}{(q/p_0)k}\sin(\phi_0) + \frac{\cos(\phi_0)}{(q/p_0)k}\sin(\theta) \\ y_0 + \frac{H_z}{(q/p_{t0})k}\cos(\phi_0)\cos(\theta) - \frac{H_z}{(q/p_{i0})k}\cos(\phi_0) + \frac{\sin(\phi_0)}{(q/p_{i0})k}\sin(\theta) \\ \Delta z + z_0 \end{bmatrix},$$

where $k = 0.3\,|B_z|\,, H_z = \frac{B_z}{|B_z|}$ and $\theta = -\frac{(q/p_{t0})\Delta z k}{\tan\lambda_0}$. The helical track model is especially well suited to describe the path of low momentum particles in the MFT.

Two different steps are required to perform the forward track reconstruction with the MFT: track finding and track fitting.

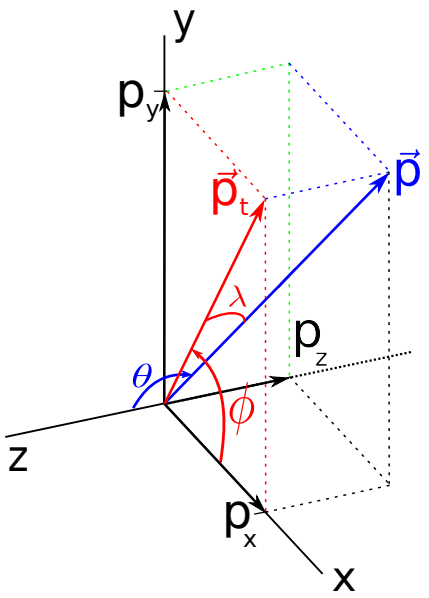

Figure 3.10: Track parameters θ, λ and q/p_{T} in the MFT coordinate system. The λ parameter is negative for tracks moving towards the MFT.

Track finding

The first one is track finding. This procedure combines clusters in the different detection layers of the MFT which have a high chance to originate from the same charged particle track going through the detector, to form a track candidate which will then be fitted in the second step. Two methods are deployed for the track finding: the Cellular Automaton (CA) and the Linear Track Finder (LTF) algorithms [136]. In practice, the LTF is executed first. Then the remaining unused clusters will be left to the CA algorithm.

The CA is used for tracks with low momentum, whose path will be more affected by the multiple scattering in the material of the MFT disks. The CA algorithm builds a track by following and linking step by step segments of tracks formed by two consecutive disks. The starting segment is composed of two clusters found on the first and the second disk, which are the closest to the interaction point. The cluster of the second disk is then used to form the next segment, by pairing with a cluster on the third disk, and so on and so forth. A track candidate is found when it is composed of 4 segments. To reduce the combinatorics, a cut is applied on the relative angle between each segment belonging to a track candidate.

In the LTF algorithm, the tracks formed by particles going through the MFT are assumed to be close to straight lines. Each cluster in a given layer can be associated with compatible clusters in other layers in a given search radius projected to these other layers. The information on the vertex position is used in order to minimize the search radius and thus the number of compatible clusters in other layers for a given cluster. The algorithm unfolds as follows: for a given cluster in the first (or the second) MFT layer, we search for compatible clusters in the last (or the penultimate) layer. This builds a set of seeds for track

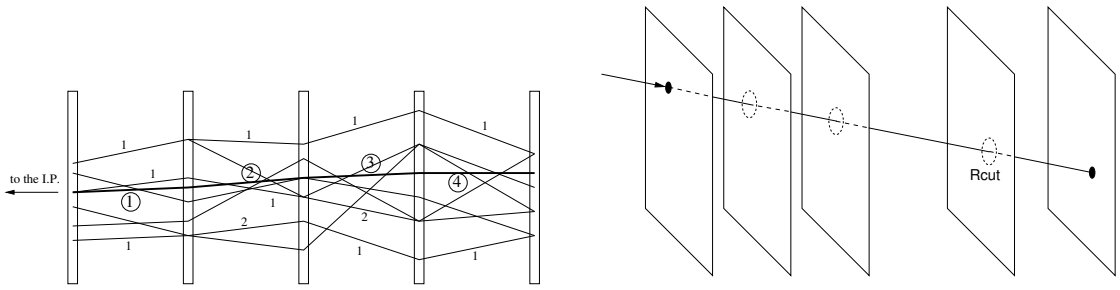

Figure 3.11: Illustration of the two different track finding algorithms used by the MFT: the Cellular automaton (left) and the Linear Track Finder (right) [136].

candidates, approximated as straight lines defined by these two clusters. For each track seed, the algorithm then looks for compatible clusters within each intermediate layer. It selects the first cluster found closest to the current track seed. These track candidates are then saved for further processing only if 5 or more compatible clusters were found for this track seed, and these clusters are distributed on at least 4 different disks out of the 5 of the MFT detector.

The use of the LTF method is justified because the ALICE solenoid only has a residual magnetic field in the acceptance of the MFT. Compared to the CA, the LTF algorithm reduces the computing time, as the cluster combinatorics is smaller for LTF than for CA. However, the track finding efficiency of the LTF algorithm can be limited by the multiple scatterings of particles passing through the material of the MFT disks. In particular, the LTF does not have good efficiency for low momentum and large pseudo-rapidity particles (furthest from the beam pipe), as the track curvature from the residual magnetic field of the solenoid can become prohibitive for the linear track approximation.

Track fitting

The second step of track reconstruction is track fitting. When a track is found, the fitting is performed using a Kalman filter in order to extract the kinematic parameters of the track.

The Kalman filter [144, 145, 146] is an algorithm used to estimate the parameters of a dynamical system, given a set of measurements and their corresponding errors. It uses an iterative procedure where past measurements and a new measurement are combined using their respective covariances to provide an optimal estimate of the true state of the system. In the case of MFT track fitting, the different steps of the algorithm are the following:

1. Initialization: The parameters of a given track are initialized using the coordinates of two clusters in the first two layers of the MFT that were found by the track finder algorithm, and the error covariance matrix is initialized as diagonal. These values represent the initial estimate of the track parameters.

2. Prediction: This seed track is then propagated to the last MFT layer, the furthest from the interaction point. This propagation takes into account the multiple scat-

tering in the material of the MFT disks. This is done by adding corrections to the covariance matrix of the track and then extrapolating the track to the new layer, taking these new covariances into account. The corrections to the covariance are:

$$\sigma_{\phi} = \frac{0.0136\,\mathrm{GeV}/c}{p}\frac{x}{X_0}\frac{1}{\sin\lambda}\frac{1}{\cos^2\lambda} \tag{3.2}$$

$$\sigma_{\tan\lambda} = \frac{0.0136\,\mathrm{GeV}/c}{p}\frac{x}{X_0}\frac{1}{\sin\lambda}\frac{1}{\cos^4\lambda} \tag{3.3}$$

$$\sigma_{q/p_{\mathrm{T}}} = \frac{0.0136\,\mathrm{GeV}/c}{p}\frac{x}{X_0}\frac{1}{\sin\lambda}\tan^2\lambda(q/p_{\mathrm{T}})^2 \tag{3.4}$$

where x/X_0 is the fraction of the radiation length which the extrapolated track traverses. The extrapolation then updates both the parameters and covariances of the track.

3. Measurement Update: The predicted position of the propagated track is then compared to the real position of the cluster of the track in the considered layer. Then a "Kalman gain" is computed, which determines the relative weight of the measurement (i.e. the cluster position) and the prediction (i.e. the propagated track position) in the updated state estimate. Finally, the track parameters and covariance matrix are updated using the Kalman gain and the residual of the position.

4. Repeat: The last two steps (prediction, measurement update) are then repeated for each available cluster previously assigned to the track by the track finder algorithm. At each iteration, this process allows to refine the estimate of the parameters and their uncertainties, based on both the dynamic model (the track model and the propagation with multiple scattering corrections) and the measurements (the actual cluster positions). The procedure is iterated until the last cluster of the track, closest to the interaction point, is reached. Therefore, the Kalman propagation is done inward for the MFT tracks.

After the track reconstruction is done, track matching is then required in order to extract global muon tracks, which are the tracks matched between MFT, MCH, and MID detectors, as will be detailed in Sec. 3.4.

3.3 Contributions to the MFT project

3.3.1 Noise masking

The evolution of the response of an ALPIDE pixel as a function of the value of the injected charge is known as an S-curve. Ideally, if the injected charge is less than the threshold, the pixel should never fire. For values of injected charges larger than the threshold, the number of registered hits should always be equal to the number of injections. In reality, a pixel has a slight non-zero response below the threshold. This non-ideal behavior is due to the noise of the pixel, which can vary in time independently for the different pixels.

Pixel noise can be due to several sources. It can have contributions from the pixel circuitry, such as the pixel reset mechanism, or readout transistors. For high illumination of the pixel, it can also be due to leakage currents in the p-n junction, which come from the thermal excitation of electrons and holes in the depletion volume of the sensor around the collection diode. These different contributions can vary in time and due to the experimental conditions. Hence, it is of prime importance to monitor the response of pixels as a function of time, identify the ones which have a high probability of firing irrespective of the threshold and produce "fake" hits, thus interfering with the measurements, and mask these pixels. For these purposes, the MFT operations require a "noise scan" between each physics fill of the LHC. My task in the MFT group was to develop the software that handles these noise scans, for the new software environment of ALICE, O^2.

The purpose of the noise scan is to evaluate, for each sensor, the fraction of the data taken that has a high probability of being solely due to "noisy" pixels, i.e. firing in the absence of any ionising particles. These noisy pixels can degrade the performance of the tracking of the detector, in particular by generating "fake" clusters which will be automatically included in the combinatorial association of clusters in the tracking algorithm. In addition, this noise can also consume part of the bandwidth in the readout chain and render it less efficient. The purpose of a noise scan is thus to identify noisy pixels to be able to mask them and prevent these caveats.

In practice, during a noise scan, we count the number of hits recorded by each pixel of the detector during an acquisition without any external source such as beam, or charge injection, for a fixed number of strobes, or readout frames. Cosmic rays also contribute to such kinds of acquisition and cannot be avoided, but they have a known and steady rate. The identity of all the noisy pixels found by the scan is put in a list, together with their number of registered hits. Such an object is called a "noise map". This map can later be used to mask the noisiest pixels if needed, in order to reduce the fake-hit rate.

A pixel has a certain probability of firing over a given period of time. This probability can be estimated with a noise scan by dividing the number of hits registered by this pixel by a given number of strobes sent to the sensors. Pixels which have a high firing probability can be considered as noisy since they exhibit an increased probability of producing a hit in comparison to the rest of the pixels.

In order to monitor the noise level of the detector, a threshold must be applied to this firing probability. This is known as a probability threshold, t, which must be applied to the recorded noisy pixels. A threshold value of t means that we register as noisy only the pixels which fired more than $t \times N_{\mathrm{strobes}}$ during the acquisition, where N_{strobes} is the total number of strobes sent during the noise scan. This allows to only keep track of the noisiest pixels, which fired many times during the length of the acquisition, thus rejecting pixels which fire very sporadically, e.g. initiated by cosmic particles.

Indeed, we can reject pixels with a low firing probability, less then t, from the list of noisy pixels as they can still be normally operated most of the time. In addition, their rejection allows to greatly reduce the number of registered pixels, thus reducing the computing and

storage requirements of a noise scan. The determination of this noise threshold level t is hence a trade-off between the efficiency of the noise masking and the efficiency of the tracking which we want to preserve. The usual value considered for this threshold, both for MFT and ITS, is $t = 10^{-5}$. The number of strobes sent to the sensors during a noise scan must thus be set so that we gather enough statistics to locate as many noisy pixels as possible with the desired probability threshold t. The minimum number of strobes needed to reach threshold t is computed as:

$$N_{\text{strobes}} = 1.1 \times \left\lceil \frac{1 + \frac{1}{t}}{\epsilon^2} \right\rceil \tag{3.5}$$

where ϵ is the relative statistical error wanted by the user. If this desired error is small, then a large number of strobes will be needed to ensure that we miss as few noisy pixels as possible.

The default value set in O^2 is $\epsilon = 20\%$. Hence, the default number of strobes used in a noise scan is $N_{\text{strobes}} = 2\,750\,028$. In a noise scan, the strobe frequency is set in the readout configuration to $67.34\,\text{kHz}$, i.e. one strobe every $14.85\,\mu\text{s}$. Hence, the total duration of a noise scan is ~ 40 seconds.

3.3.2 Noise scan procedure

The noise level of the detector can worsen due to the intrinsic noise of the power supplied to the sensors. It can also be influenced by the threshold at which the chip operates: a decrease of the threshold will also mechanically increase the fake-hit rate. As these conditions can vary in time, the noise map of the detector must be updated as often as possible to keep track of the evolution of the noise levels across the different sensors. It was decided for MFT, that a new noise scan would take place at the end of each physics fill of the LHC.

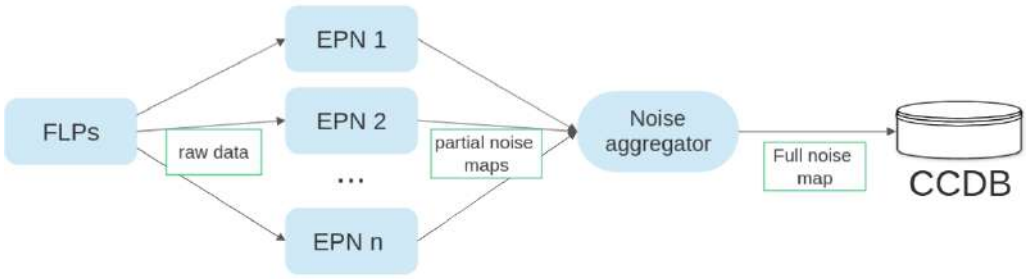

Figure 3.12: Schematic illustration of the chain of different components used in a noise scan acquisition.

The architecture that was decided for noise scans is shown on Fig. 3.12. First, the raw data arrive from the sensors to the 5 FLPs of the MFT, where they are first processed. They are then directed to a certain number of EPNs, fixed by the operator, which decode the raw data into either "digits" or "clusters". This decoded information is then transmitted to a very specific EPN labeled "noise aggregator" which collects all the digits (or clusters)

sent by the different allocated EPNs. This aggregator uses these data to count the number of registered hits for each pixel of the detector. It then applies a probability threshold to the fired pixels, the value of which is fixed to $t = 10^{-5}$, and stores the ones passing through this selection into a "noise map" object. This map is a list of noisy pixels above the probability threshold, together with the recorded number of hits for each pixel. The noise map is eventually stored in the ALICE CCDB, along with the timestamp at which the object is written in the database. This allows to easily access the different noise maps which are stored and compare them for different timestamps. I implemented in O^2 the workflow chain starting from the raw data in the output of the FLP, all the way to the storage in CCDB.

After a beam dump, the detector must be configured for noise scan, through readout configuration commands. These commands specify in particular the used strobe frequency, which is usually set to $67\,\mathrm{kHz}$, sent by the LTU. Next, an Experiment Control System (ECS) environment must be used to deploy the O^2 workflows illustrated on Fig. 3.12 and actually start the noise scan run. This environment also specifies the number of EPNs to allocate for the decoding of the raw data, which is usually set to 30. Once the run has started, with the default configuration of the strobe frequency, the FLP data rate is observed to be $\sim 1.95\,\mathrm{Gbit/s}$. When the programmed number of strobes has been reached, the complete noise map is finalized and directly stored on CCDB. This noise map can then be used in the next physics acquisition runs in two ways. First, it can be used in the reconstruction, during the decoding of raw data and the production of clusters. In this reconstruction, whether it is online (synchronous) or offline (asynchronous), the pixels listed in the latest noise map in the CCDB will be excluded from the processing chain. Second, pixels can also be directly masked at the readout level, i.e. during the acquisition itself, before even reaching the reconstruction step. This is done by using a script which downloads this latest noise map and deploys it on all 5 MFT FLPs, and then uses the Readout Units to send specific instructions to the identified sensors so they enable the mask bit for their listed noisy pixels before the start of the physics run. These two masking strategies have different drawbacks: some pixels can have defects which prevent them from being properly masked at the readout stage. This was observed to be the case for a few number (less than 10) among the noisiest pixels. In addition, as time goes on in a physics run, the sensors accumulate radiation doses. The latches in the sensor circuitry which allow to mask pixels will have an increasingly high probability of experiencing a Single Event Upset. This means that the programmed state for the masked pixels has a growing probability of being reverted if the run continues for a long enough time without refreshing the noise mask pattern configuration. On the other hand, the masking in the reconstruction always automatically uses the latest noise map object that is stored in CCDB. If this latest map is corrupted, e.g. due to any data acquisition problem or some other issues, the masking at the reconstruction level may be compromised. Hence, the two masking options are often used conjointly.

3.3.3 Noise scan results

Figure 3.13 (left) shows the evolution of the total number of noisy pixels in the detector at different dates that I randomly selected for illustration purposes, starting from the

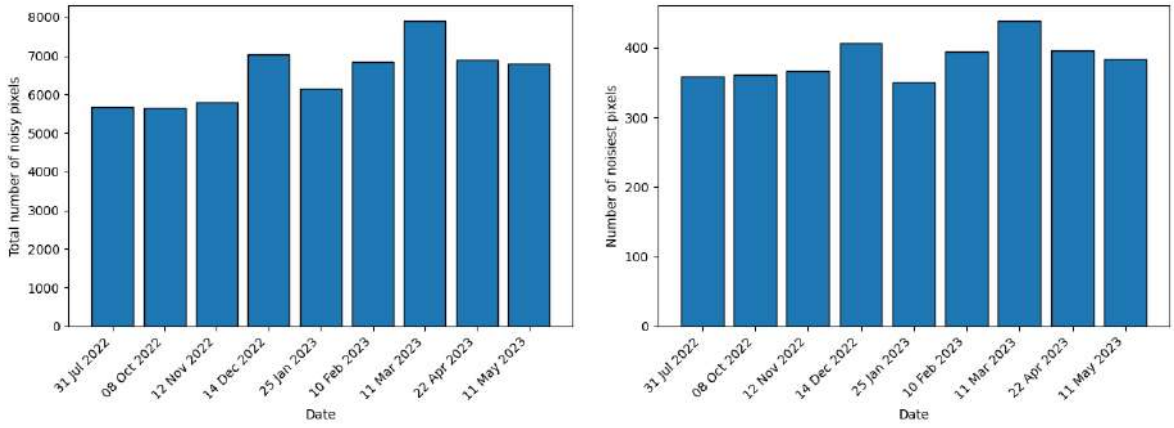

Figure 3.13: (Left) Total number of noisy pixels, with probability threshold of $t = 10^{-5}$, and (right) number of noisiest pixels, with $t = 0.1$, in noise maps recorded at different dates between summer 2022 and spring 2023.

summer 2022 to spring 2023. These noisy pixels are the ones which were above the probability threshold of $t = 10^{-5}$. Each date corresponds to a noise scan performed after a physics fill beam dump. One can see that the number of noisy pixels ranges between 5500 and 8000 depending on the considered noise map. A seemingly increasing trend is observed, although there are also large fluctuations, e.g. for the 11 March scan. These kinds of fluctuations can be due to external physics activity, such as light, to which the ALPIDE sensors are sensitive. The exposition to light can occur during the cavern access.

However, the total number of noisy pixels alone is not the most reliable way to estimate the noise of the detector since we count together pixels which could have responded to a few of the sent strobes and those which could have responded to all of the sent strobes. A way to get a more precise idea of the noise level of the noisy pixels is by increasing the probability threshold selection. This is shown on Fig. 3.13 (right) which shows the same noise maps as on (left) but with an applied probability threshold of $t = 0.1$ instead of 10^{-5}. This means that we only count pixels which responded to 10% or more of all the sent strobes. Although we still observe large fluctuations, the number of these "noisiest" pixels is more stable over time than the total number of noisy pixels. Indeed, the relative variation on the right plot of Fig. 3.13 is about 12%, whereas on the left plot it is about 25%. This can be further quantified by checking if the identity of the noisiest pixels changes from map to map. On average, around 30 pixels are different when comparing the noisiest pixels of two different noise maps.

Another way to quantify the noise level of the detector is with a noise occupancy plot. The noise occupancy O_{noise} is assessed as the number of recorded "fake-hits" per strobe per pixel. This represents an average probability over the whole detector for a pixel to fire without the passage of a charged particle. It is thus defined as:

$$O_{\text{noise}} = \frac{N_{\text{hits}}}{N_{\text{pixels}} \cdot N_{\text{strobes}}}$$

where N_{pixels} is the number of presumably active pixels in the detector. This number is calculated by multiplying the number of active sensors by the number of pixels on each sensor, i.e. $N_{\text{pixels}} = N_{\text{sensors}} \times 512 \times 1024$. It is more reliable than the absolute number of pixels, as some zones, ladders or sensors of the detector can be inactive during some periods of time, due to technical issues of powering or configuration. This can artificially decrease the total number of noisy pixels. By dividing the recorded number of hits by the number of pixels in the active sensors, we thus get a better estimate of the noise level of the detector.

We plot on Fig. 3.14 the evolution of the noise occupancy as a function of the number of masked pixels, for the latest recorded noise map as I write these lines, from the 11th of May 2023. For low numbers of masked pixels, the value of the red curve is simply the total noise occupancy of the detector. When we go along the X-axis, we start to mask some of the noisy pixels stored in the considered noise map, starting from the noisiest ones, i.e. the ones with the largest number of recorded hits. Thus, a number of masked pixels equal to 1 means that we mask only the noisiest of all pixels in the noise map, a number of masked pixels equal to 2 means that we mask only the first two noisiest pixels, and so on. Each time, the value of the noise occupancy is recomputed after masking the considered noisy pixels. What one can see on Fig. 3.14 is that the noise occupancy is quite stable for approximately the first 30 masked noisy pixels. This means that the noise occupancy is not dominated by the 30 most noisy pixels, which typically respond to more then 20% of all sent strobes. However, the last two or three thousand noisy pixels, which typically respond only once or twice over the whole noise acquisition, contribute to 4 or 5 orders of magnitude to the noise occupancy. The top and bottom plots of Fig. 3.14 show the noise occupancy evolution for the two halves of the detector, h0 and h1. Although the total number of noisy pixels is different for the two halves, the noise occupancy is of similar order and follows the same evolution with the number of masked pixels.

However, to properly evaluate the noise fluctuations of the detector, studies of the spatial distribution of the noisy pixels, especially the noisiest ones, responding to 10% or more of all triggers, is still to be carried out and is outside the scope of this thesis. Such a study is necessary, as the radiation dose received by the different layers of the detector increases as we get closer to the beam pipe. In addition, it would be very important to monitor if the identity of the noisiest pixels is stable over time.

3.3.4 Large clusters in pilot beam data

The first commissioning physics data was taken during the LHC pilot beam campaign in October 2021, at injection energy ($450\,\text{GeV}$) and $11.2\,\text{kHz}$ interaction rate. During this pilot beam, I participated to the qualification of the data taken with the MFT. In particular, we noticed that some clusters had an unexpectedly large number of pixels, spanning for some of them over more then 30 columns and/or rows. These "large clusters" were observed by both the MFT and ITS2 detectors. Such large clusters correspond to rare topologies, in the clusterization methodology that was outlined in section 3.2.4.

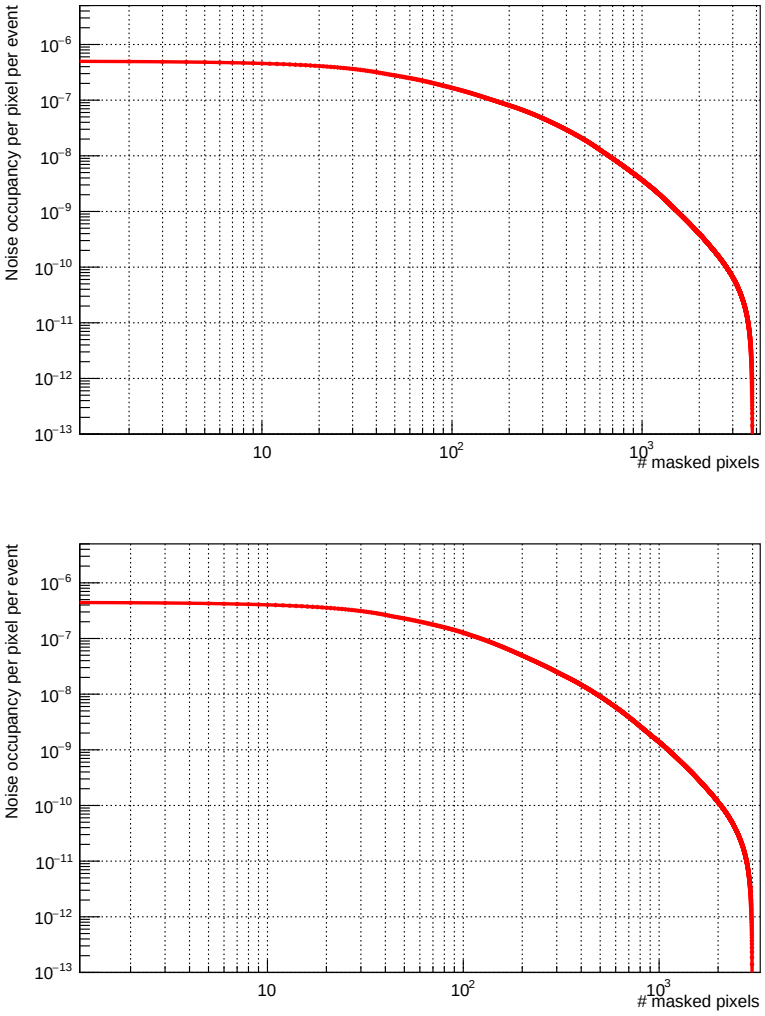

Figure 3.14: Noise occupancy plots from a noise map recorded on May 11th 2023, for h0 (top) and h1 (bottom). The Y-axis represents the number of recorded fake hits divided by the total number of active pixels divided by the number of strobes. The X-axis is the number of masked pixels, starting by masking the noisiest pixels on the left, then gradually masking fewer and fewer noisy pixels, going further to the right of the axis.

My work focused on the understanding of the origin of such large clusters, in particular to investigate if they could be spurious or if they could be truly related to the physics beam. A few runs taken during this pilot beam are shown on Fig. 3.15 which shows the beam intensity as a function of time. In particular, one can notice that run 505582 was taken at high beam intensity, at the beginning of the second fill shown on the figure, whereas run 505600 was taken at the end of the same fill, such that the average beam intensity is lower. The run 505548 was taken during the first fill and lasted almost until its dump. It started a few tens of minutes after the start of the fill, such that the average beam intensity lies in between the values for the two other runs, 505582 and 505600. I then monitored in these runs the evolution of the number of "large" clusters as a function of time. I took as a definition of a "large" cluster, one which has a span in row or column larger than 30 pixels.

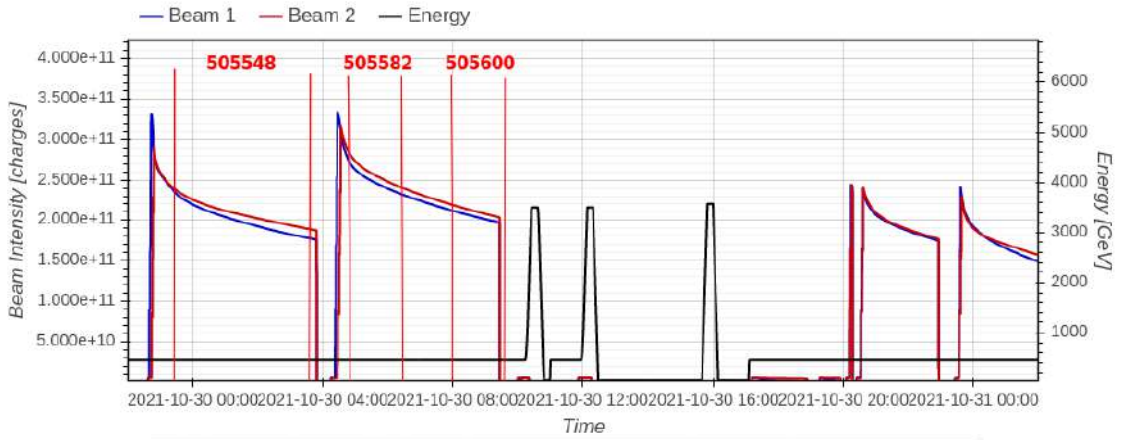

Figure 3.15: Beam intensity as a function of time during the pp October 2021 pilot beam in ALICE, at $900\,\mathrm{GeV}$ injection energy. Three runs are highlighted in the first two fills of the pilot beam.

As shown on Fig. 3.16, the number of large clusters per time bin scales the same way as average beam intensity for three previously mentioned runs: 505582 has the largest clusters (blue), ignoring the last incomplete time bin, followed by run 505548 (black), then by run 505600 (red). The other runs shown on Fig. 3.16 were taken later on and also follow the same scaling behavior with beam intensity. In addition, one notices that the number of large clusters decreases with time, and that this decrease is most notable for run 505582, out of the three runs we focused on. This is again compatible with a scaling with beam intensity, as this particular run was started closest to the beginning of the fill. Indeed, the drop in beam intensity is most pronounced at the beginning of each fill, and then softens as the run progresses.

Finally, the spatial distribution of large clusters in the different chips of the MFT was studied. Such distributions are shown on Fig. 3.17, which displays the number of large clusters per chip in both halves of the first layer of the MFT, integrated over the whole 505582 run. One notices a radial dependence of the number of large clusters per chip; the chips closer to the beam pipe registered a greater number of large clusters than the chips located on the periphery of the acceptance.

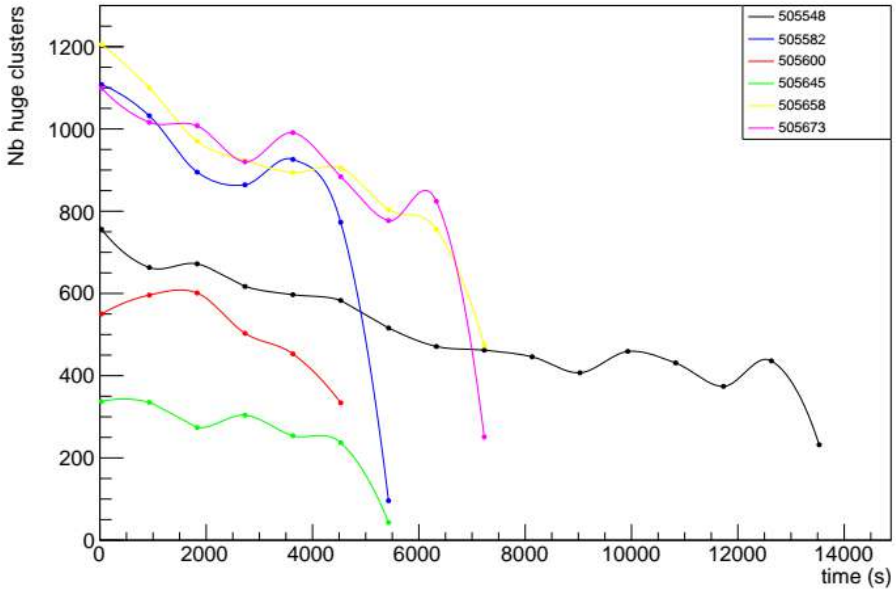

Figure 3.16: Total number of large clusters (row or column span > 30 pixels) observed in the MFT as a function of time, in bins of 14 minutes. Six different runs which took place during the 2021 pilot beam are shown.

These three observations, namely scaling with average beam intensity, scaling with beam intensity as a function of time, and spatial distribution in the detector acceptance, lead us to the conclusion that large clusters are physically induced, i.e. they are produced as a result of physics beam activity.

Examples of large clusters seen in MFT sensors during the 2021 pilot runs are shown on Fig. 3.18. Most of the observed large clusters can be classified into two groups according to their general aspect: thin elongated clusters, like the ones shown on the right plot of Fig. 3.18, or smaller fat "blobs", shown on the left plot of the same Fig. 3.18. Although the shapes are not exactly equivalent, a similar classification was established by ITS2 for their observed large clusters, see Fig. 3.19. Using Monte Carlo simulations, they managed to attribute these different shapes to different physical phenomena. The "blob" clusters correspond to hadronic interactions of particles with the surrounding materials, whereas so-called delta-rays, secondary electrons with high energy that can produce further ionization, are the origin of the thin elongated shapes. It was found by both ITS2 and MFT that delta-rays contributions are dominant at low cluster size (20 < size < 40), while hadronic inelastic scatterings are dominant at large cluster size (size > 40).

At the time of this investigation, a software bug prevented me from going further in the comprehension of these large clusters. Indeed, I spotted large clusters which were registered in the processing chain as disconnected shapes. It was found that this was due to errors issued in the sensor readout chain; due to some malfunction[2], the output of the readout data can be unordered in double columns. As we mentioned earlier, the clusteri-

[2]The presence of too many large clusters can lead to abnormal operating conditions e.g. due to bandwidth limitation

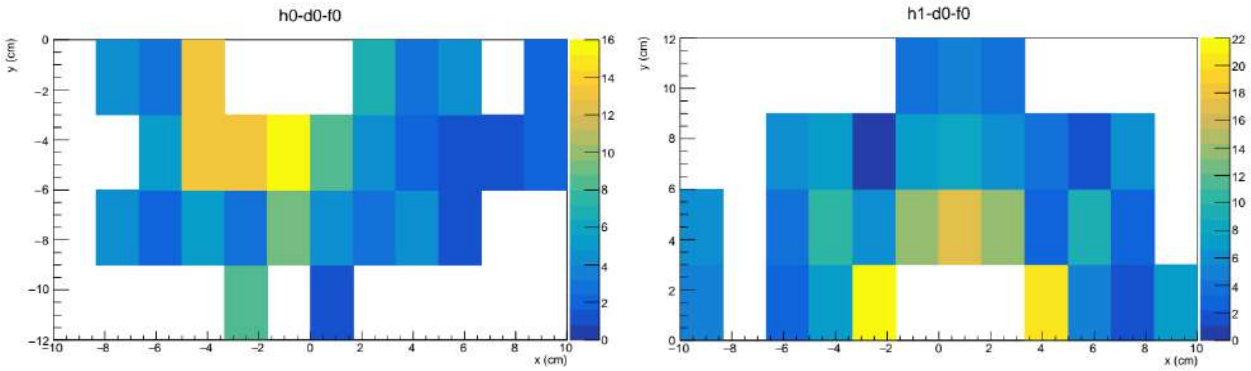

Figure 3.17: Spatial distribution of large clusters (row or column span > 30 pixels) in the two halves of the first MFT layer, (left) h0-d0-f0 and (right) h1-d0-f0. The colors show the count of large clusters per chip recorded during the run 505582 of the October 2021 pilot beam.

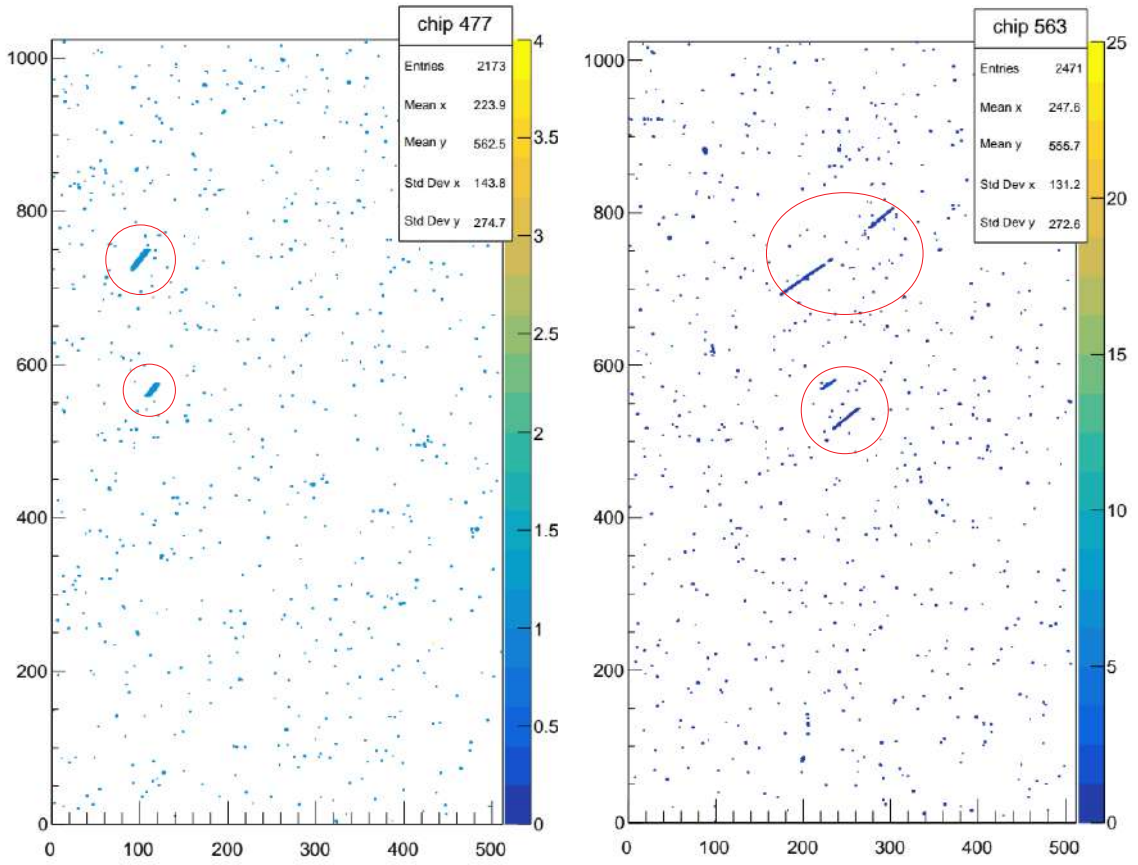

Figure 3.18: Illustration of different large cluster topologies seen in two different chips, (left) 477 and (right) 563, during run 505582.

zation algorithm is based on a presupposed ordering of the data read from the sensors in terms of rows and columns. A misordering of double column numbering caused the clusterization algorithm to form non-continuous cluster patterns. My work allowed to spot this issue and the decoding algorithm was later corrected to handle such situations.

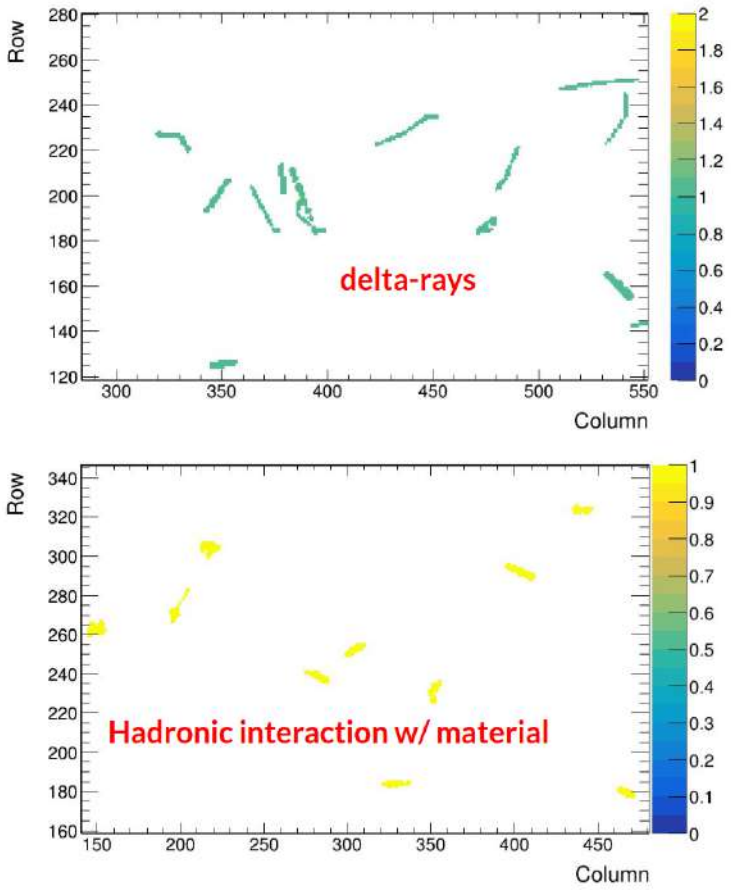

Figure 3.19: Illustration of the two different large cluster topologies classified by ITS. Comparison with Monte Carlo simulations allowed to attribute them to (top) delta rays and (bottom) hadronic interactions [147].

When studying the spatial distribution of large clusters in each chip, it was observed that a high concentration of large clusters was appearing in a zone located near the half of the chips in the column numbering, spanning all rows. This is shown on Fig. 3.20. On this plot, I superimpose the large clusters of all chips that belong to the ho half of the MFT. The concentration is seen only for large clusters, for which I still take the definition of having a row or column span greater than 30. The origin of this was not fully understood. A possible explanation for this concentration of large clusters would be a difference in the substrate material of the sensor near the half of the sensor, shown on Fig. 3.21.

Further checks would be needed to understand the origin of this distribution of large clusters. First, it would be interesting to monitor the evolution of these distributions with the interaction rate, in particular comparing the occurrence of large clusters in $500\,\mathrm{kHz}$

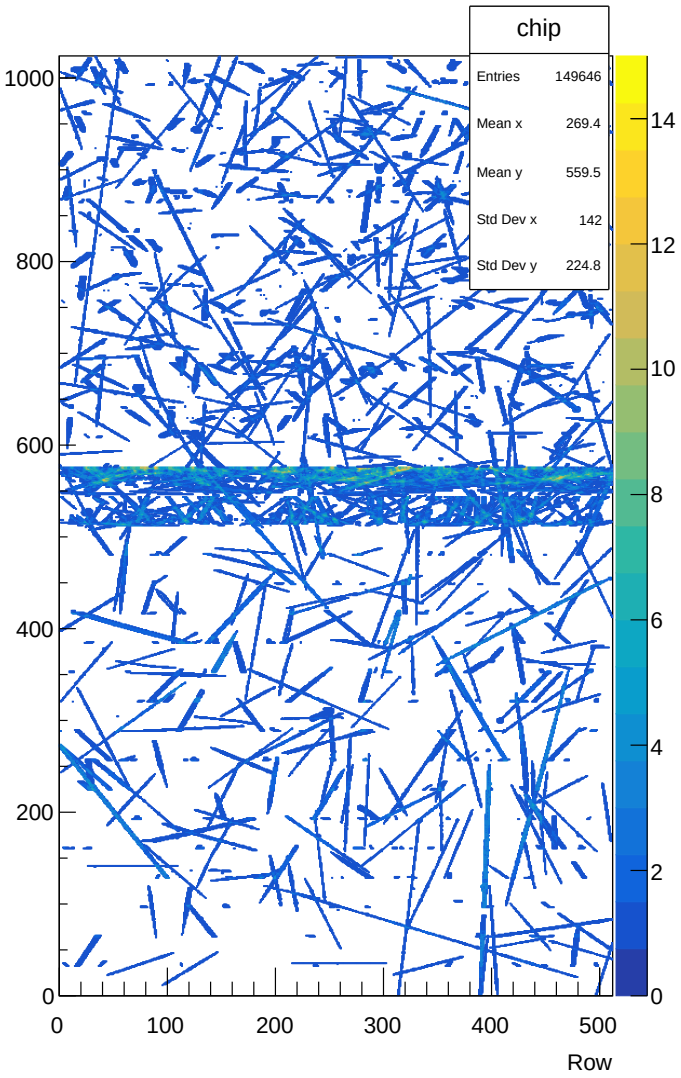

Figure 3.20: Large clusters observed in the whole run 505582 in ho superimposed in the same histogram.

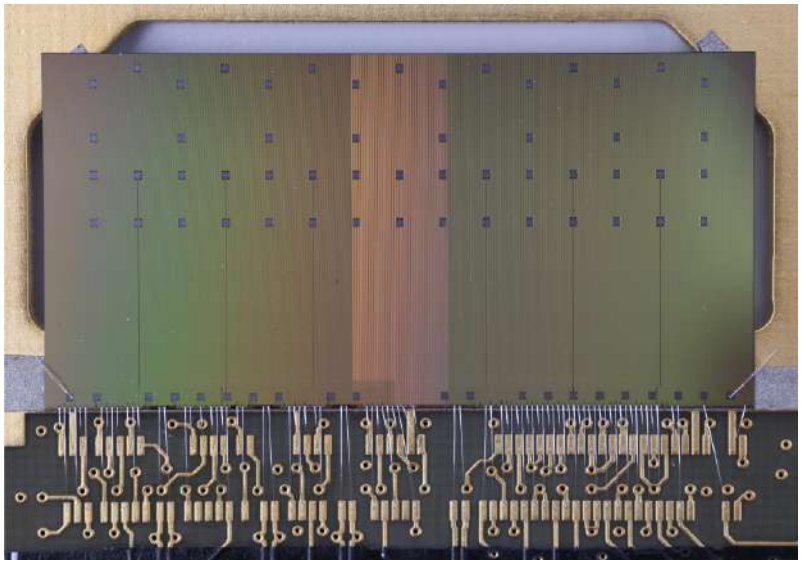

Figure 3.21: Photograph of the ALPIDE chip [134].

runs with lower interaction rate runs, e.g. $10\,\mathrm{kHz}$ runs such as the ones taken in 2022. In addition, a change of the input back-bias voltage, which is currently set to $0\,\mathrm{V}$ in MFT operations, would be useful to study the dependence of the large cluster detection, and check if their concentration in the central zone of the sensors could be affected by the size of the depletion zone. Such studies are outside the scope of this thesis. We note however, that these large clusters have a negligible impact on the detector's tracking performance. Indeed, in the 2021 pilot beam, I monitored the number of reconstructed tracks which used large clusters. It was ranging from 0.015% to 0.05% depending on the considered run. Hence, in the following, we can safely neglect the contribution of these large clusters.

3.4 Matching with the Muon arm

To carry out an analysis using muons, the MFT tracks reconstructed as described in the past sections must be matched to tracks reconstructed using the detectors of the Muon arm: the MCH and the MID. The nomenclature chosen for the different types of detector tracks at forward rapidities is illustrated on Fig. 3.22: a Muon track is a matched track between the MCH and the MID detectors, and a Global muon track is a track matched between the MFT, MCH and MID detectors.

First, the MCH reconstructed tracks are matched with the identification response of the MID [134]. This matching takes as input the lists of MCH ROFs, MCH tracks, MID ROFs and MID tracks, and has two steps. The first one is a matching using the timestamp of the tracks. Indeed, thanks to the very accurate time resolution of the MID detector, the MID ROFs have a duration of 1 BC (~ 25 ns). On the other hand, the MCH ROFs are usually a few BCs long, typically around 4 BCs. Hence, the first step is to find all the MID ROFs compatible with a given MCH ROF. In a second step, the matching is refined using the spatial position of the tracks: the MID track is the most compatible spatially with the MCH track and is kept as the matched MID track. This compatibility is estimated using a χ^2

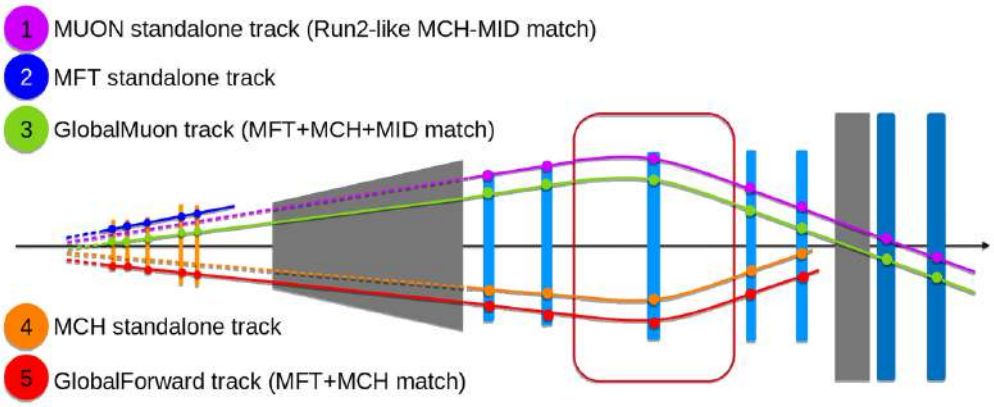

Figure 3.22: Nomenclature of the different types of tracks at forward rapidities in the MFT and the Muon arm [149].

score, which is required to be lower than a given threshold.

Once matched MCH-MID tracks are constructed, they are extrapolated to a given plane so that they can further be matched with MFT tracks. By default, the matching plane is at the z-position $z = -77.5$ cm, which is close to the last layer of the MFT, the one furthest from the interaction point. Therefore, to be able to match an MFT track with a Muon track, the latter must be propagated to this matching plane, through the thick hadronic absorber.

A propagation method is implemented in O^2 which takes into account both energy loss and multiple scattering corrections for the propagation of Muon tracks through this absorber. The energy loss is estimated using the Bethe-Bloch formula:

$$E_{\text{loss}} = L \cdot \rho \cdot m_K \cdot \frac{Z}{A} \cdot \frac{1}{\beta^2} \cdot \left(\frac{1}{2} \ln \left(\frac{4 m_e^2 \beta^4 \gamma^4}{m_I^2} \right) - \beta^2 - \frac{\delta}{2} \right) \tag{3.6}$$

where L is the path length in a given portion of the absorber, ρ, Z/A and m_I are respectively the density, the atomic number divided by the mass number, and the minimum excitation energy for the material in the considered portion of the absorber. $m_K = 3.07 \cdot 10^{-2}\,\text{GeV}\,\text{cm}^2/\text{g}$, m_e is the electron mass, and δ^2 is the density correction term. This energy loss is then added up through the whole propagation of the Muon track through the different materials of the absorber, and is used to correct the total momentum of the track, as well as the associated variance.

The multiple scattering is accounted for by updating the covariance matrix of the track, similarly to what was shown earlier for the propagation of MFT tracks through the MFT material in the Kalman filter.

Once both Muon and MFT tracks are propagated to the matching plane, similarly to the MCH-MID matching, a first selection based on timing is applied. In current operations, the MFT ROFs have a size of 198 BC ($\sim 5\mu$s), which is much larger than the ROF size of Muon

tracks (typically 1 BC). For a given Muon track, the corresponding ROF is retrieved and all compatible MFT ROFs are listed. All the MFT tracks belonging to these ROFs are then flagged as time-compatible with the Muon track. The next step is to use the parameter values of tracks to find the best candidate.

In the case of pp collisions, the best candidate is found based on a χ^2 score. This score is calculated between the Muon and the MFT candidate tracks. The Muon-MFT pair with minimum χ^2 score is selected as a matched Global muon track. The χ^2 is computed as:

$$\chi^2 = P^T \times C^{-1} \times P \tag{3.7}$$

with the residuals of parameters P given with the 5×1 vector as:

$$P = \begin{pmatrix} x_{MFT} - x_{MCH} \\ y_{MFT} - y_{MCH} \\ \phi_{MFT} - \phi_{MCH} \\ \tan\lambda_{MFT} - \tan\lambda_{MCH} \\ \left(\frac{q}{p_{\mathrm{T}}}\right)_{MFT} - \left(\frac{q}{p_{\mathrm{T}}}\right)_{MCH} \end{pmatrix}$$

and the covariance residuals C described by a diagonal 5×5 matrix with the diagonal elements equal to the difference between the MFT and Muon diagonal covariance elements.

Once a good match is found between an MFT track and a Muon track, a Global muon track is constructed. This is done by using a Kalman filter, following the same basic steps as the ones used in the MFT track fitting. The only difference is that in the "Initialization" step, the parameters of the initial track are the ones of the Muon track propagated to the matching plane. The following steps are similar; in each iteration one adds an additional MFT cluster in a new layer to the track, and updates the parameters of the global track using the position and errors of this new cluster, together with the extrapolation of the track to this layer.

In pp collisions, the method used for the MFT-Muon matching is the χ^2 method outlined above. In this method, a cut on the χ^2 values of the matched global muon tracks is necessary to reject the ones which were not matched properly. This means that the MFT and Muon tracks which were paired together do not correspond to the same particle. This is known as a "fake match". These fakes can come from background muons in a given event, a charged hadron which left a track in the MFT and then decayed into a muon on its way to the muon chambers, or are due to inefficiencies of the χ^2 matching method. Hence, the purity of the matching must be estimated, to understand how many fake matches contaminate our sample. This purity is increased by applying a selection on the χ^2 matching score. However, such selection can cause inefficiencies in the reconstruction, if the selection in too tight. The control of inefficiency and purity, and thus the determination of the optimal χ^2 cut, are crucial steps in any muon analysis using the MFT with pp collision data.

Since the methods to evaluate the efficiency and purity of this MFT-Muon matching were not finalized as I write these lines, a basic template fit method was used to estimate

the purity and efficiency of different χ^2 cuts. The procedure for this method is the following: a Monte Carlo simulation is used to provide the shape of the χ^2 distribution of global muon tracks. For this, a simulation based on minimum-bias (MB) events with injected prompt J/ψ signal is used, with one J/ψ injected in each event, as will be detailed in Sec.4.2. A Monte Carlo label is constructed in this simulation to determine if, for a reconstructed global muon track, both matched MFT and Muon tracks correspond to the same MC particle. This flag thus allows us to distinguish the "fake matches" from the "true matches".

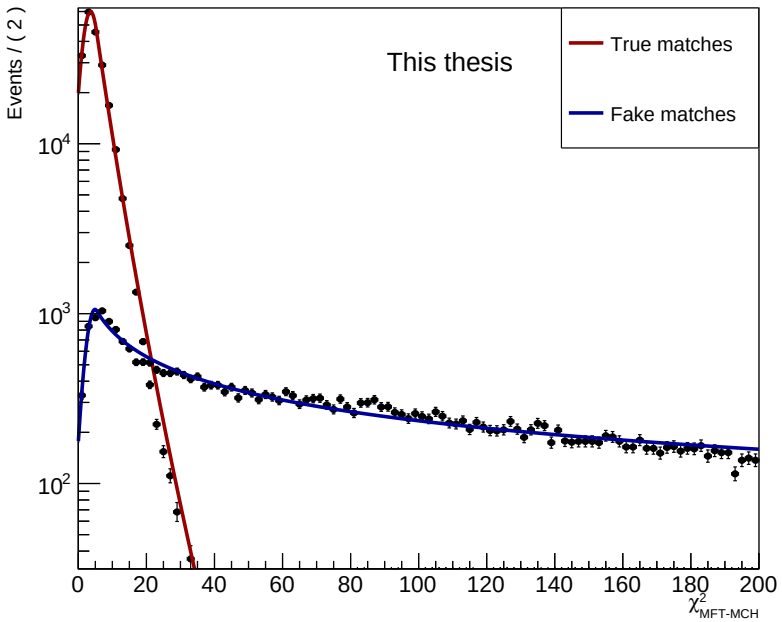

Figure 3.23: Distribution of χ^2 of the matching between MFT and Muon, under the J/ψ peak, in a Monte-Carlo simulation with injected prompt J/ψ. The fake and true matches are separated using MC labels and their respective distributions are fitted with Crystal Ball.

Using this flag, I extracted the matching $\chi^2_{\mathrm{MFT-Muon}}$ distribution of the fake and true matches separately, which are shown on Fig. 3.23. These two distributions are restricted to the invariant mass range $3 < M < 3.2\,\mathrm{GeV}/c^2$, i.e. under the J/ψ peak. They are then fitted using single-sided Crystal ball functions [148]. Next, we want to fit the $\chi^2_{\mathrm{MFT-Muon}}$ distribution observed in the data, in the same invariant mass range, using the sum of two similar functions. To do this, a Roofit model is composed as the sum of two single-sided Crystal ball functions, where the ratio between the means and the ratio between the standard deviations are fixed to the values extracted from the Monte Carlo fits. In addition, the tail parameter of the Crystal ball function corresponding to the background component is extracted by fitting the distribution in the range $\chi^2_{\mathrm{MFT-Muon}} > 100$. All other parameters are left free in the fit.

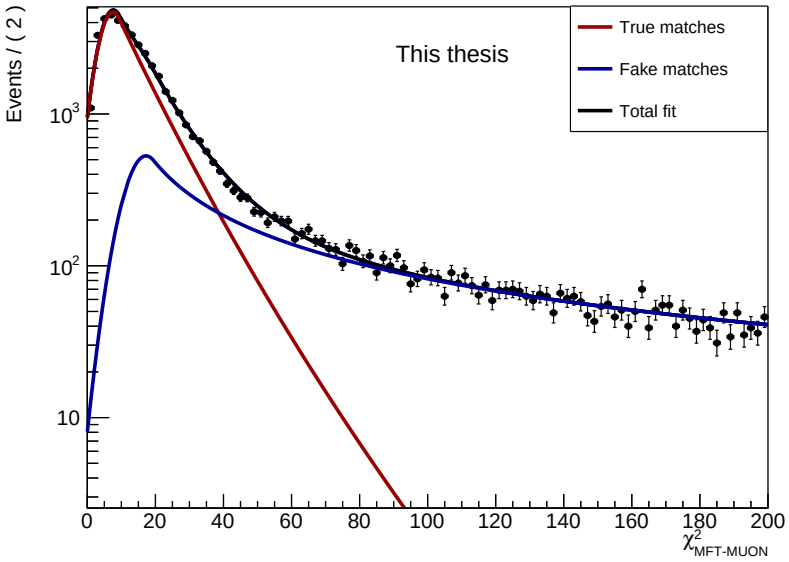

Figure 3.24: Distribution of χ^2 of the matching between MFT and Muon, under the J/ψ peak, in the LHC220 period of the 2022 pp data. The distribution if fitted using the sum of the Crystal Ball function which aim to estimate the fake and true matches distributions.

Matching χ^2 cut	Purity	Efficiency
50	99.2 %	84.6 %
40	96.6 %	85.4 %
30	91.7 %	87.1 %

Table 3.1: Values of purity and efficiency for different selections on $\chi^2_{\text{MFT}-\text{Muon}}$, computed from a fit to the data LHC220 of Run3.

This simple method allows to estimate the shapes of the $\chi^2_{\text{MFT}-\text{Muon}}$ distribution of the data, for both the true and fake matches separately, shown on Fig. 3.24. One can then apply a $\chi^2_{\text{MFT}-\text{Muon}}$ cut on this composite model and estimate the values of purity and efficiency achieved with such as cut: the purity is the number of true matches divided by the the total number of matches below the selected $\chi^2_{\text{MFT}-\text{Muon}}$, and the efficiency is the number of true matches below the selected $\chi^2_{\text{MFT}-\text{Muon}}$ divided by the total number of true matches. These values are listed in the table 3.1.

In the following, a value of 40 for the matching $\chi^2_{\text{MFT}-\text{Muon}}$ cut will be used, as a trade-off between optimized purity and efficiency. However, the method outlined above is only meant to give a rough estimate, while waiting for more robust methods to be fully developed. In particular, the most crucial part is to correctly estimate the position, height and width of the fake-match peak, which is not fully reliable in this method as it was estimated with MC simulations. Indeed, a possible source of discrepancy between the data and MC is the missing relative alignment between the MFT and Muon spectrometer in the data, in both space and time. Hence, the impact of the variation of this cut will be an important

input for the estimation of systematic uncertainties in future studies. Other data-driven methods are currently being developed to estimate the shape of the fake-matches distribution in the collected data; in particular, a method based on the association between MFT and Muon tracks belonging to different events is currently being studied. Another lead is a method where MFT and Muon tracks are associated only if they carry opposite electric charges.

However, a high track multiplicity is expected in Pb–Pb collisions in the MFT (around 2000 charged primary particles), and hence in the matching plane. This can result in a considerable number of fake matches, compared to the situation in pp collisions, and severely limit the performance of the χ^2 method. Indeed, studies were conducted using MC simulations to compare the performance of this method in pp and Pb–Pb collisions. It was found that for selection of $\chi^2_{\mathrm{MFT-Muon}} < 20$, in pp this method could achieve a signal efficiency of $\sim 99\%$ and a purity of $\sim 98\%$. The difference with the values of purity and efficiency quoted above in the case of data is due to missing relative alignment between the MFT and the Muon spectrometer, both spatially and in time. However, in Pb–Pb the same cut produces an efficiency of $\sim 99\%$ but a purity of about 60% only [149]. Thus, in Pb–Pb, other methods than the matching $\chi^2_{\mathrm{MFT-Muon}}$ method must be used. In particular, techniques based on Neural Networks are currently under development in preparation for the Pb–Pb data taking scheduled at the end of the year 2023. Studies of performance of these methods in MC simulations using TensorFlow and the MultiLayer Perceptron packages show that an efficiency greater than 97 % and a purity greater than 91 % are achievable in the environment expected for Pb–Pb collisions, integrated in centrality [149].

3.5 Summary and outlook

The MFT is a new detector installed in ALICE for Run 3. It aims at providing secondary vertexing capabilities to the Muon spectrometer by enabling tracking measurement in front of the absorber, closer to the interaction point. This is of particular importance to separate the prompt and non-prompt contributions to J/ψ production in heavy-ion collisions. To this end, a matching must be performed between the tracks found within the two detectors. For pp collisions, this is done using a χ^2 score selection based matching. The MFT is a silicon pixel detector with a high spatial resolution provided by the ALPIDE sensors. However, the pixels of the silicon chips can suffer from random noise. In order to provide adequate performance in track reconstruction, such noisy pixels must be removed from the clusters to be considered during the reconstruction. One of my contributions was the implementation in the software environment of ALICE, of the workflow responsible for the noise scan. This is a specific type of acquisition during which a list of all the noisy pixels is recorded, which can be later used for masking at both readout and reconstruction stages. The evolution of the number of noisy pixels as a function of time was shown, as well as noise occupancy plots. In particular, the number of the noisiest pixels, i.e. the one responding in more than 10% of all strobes is stable since the beginning of Run 3. However, additional studies are needed, in particular to monitor how the spatial distribution of the noisy pixels in the detector evolves as a function of time. I also studied the distribution of abnormally large clusters, which were first observed during the 2021 pilot beam. It was found that these clusters are produced due to physics activity linked to the beam intensity. Moreover, a non-uniform distribution of these large clusters in the ALPIDE sensors was observed for MFT. More recent studies using the Run 3 data are needed to further monitor the distribution of these large clusters, and to understand their non-uniform distribution in the MFT chips. Finally, I conducted a first study to estimate the efficiency and purity of the χ^2 score matching between the tracks in the MFT and Muon arm in the 2022 pp data of Run 3. More robust methods are currently under development to improve the estimated distribution of the wrongly matched tracks. For the Pb–Pb data taking, programmed at the end of the year 2023, alternative methods for the MFT-Muon matching will be used, based on machine learning techniques.

Chapter 4

Analysis of Prompt-Non-prompt J/ψ separation

This chapter presents a first study of the separation of prompt and non-prompt J/ψ using data recorded by ALICE in proton-proton collisions in 2022, exploiting the secondary vertexing performance of the MFT. The achievement of this separation in proton-proton will also provide a baseline to pursue a similar analysis using Pb–Pb data which will be recorded by ALICE in October 2023. As will be discussed, the study that I present in this chapter is preliminary and additional work is still needed in particular to handle the resolution performance at low transverse momentum.

4.1 Pseudo-proper decay length

Non-prompt J/ψ production originates from the decay of b hadrons. These hadrons have a lifetime of $\tau_B \sim 1.5$ ps, which corresponds to a decay length of $c\tau_B \approx 450\,\mu\mathrm{m}$. The distance between the Primary Vertex (PV), corresponding to the interaction point, and the Secondary $\mu^+\mu^-$ Vertex (SV), corresponding to the decay point of the J/ψ, is measured to access the topology of the J/ψ decay, and eventually separate the prompt and non-prompt components. In particular, the non-prompt is identified by the measurement of a SV displaced from the PV of the corresponding collision, whereas in the case of prompt, the SV is indistinguishable from the PV.

From the distance between the measured PV and SV, a variable must be constructed to estimate the lifetime of the hadrons which traveled from the PV to the SV. In order to achieve this goal, one must take into account, in the laboratory's reference system, the Lorentz boost factor $\gamma = \frac{E}{m}$, where E and m are respectively the energy and mass of the intermediate hadron. Due to this boost, the measured distance travelled before the decay of a particle corresponds to $L = \beta c\gamma\tau_B$, with $\beta = \frac{v}{c}$. As $\gamma = \frac{E}{m} = \frac{m_T}{m}\cosh(y) > \cosh(y)$, at forward rapidities (with $2.5 < |y| < 3.6$), the result is $\gamma > 6.1$. In the studied ultra-relativistic collisions, as $\beta \approx 1$, the measured distance at $|y| > 2.5$ corresponds to $L = \beta c\gamma\tau > 3\,\mathrm{mm}$.

From these consideration, we construct the following variable known as pseudo-proper time of the J/ψ, noted $\tau_{J/\psi}$:

$$\tau_{J/\psi} = \frac{|\vec{L}| M_{J/\psi}}{p} = \frac{|\vec{L}|}{\beta_{J/\psi}\gamma_{J/\psi}c} \tag{4.1}$$

with p the momentum, $M_{J/\psi}$ the invariant mass, and $\vec{L}$ the longitudinal decay length, such as:

$$\vec{L} = \vec{r}_{PV} - \vec{r}_{SV} \tag{4.2}$$

The numbers $\beta_{J/\psi}$ and $\gamma_{J/\psi}$ correspond to the kinematics of the J/ψ candidate, and not to the ones of the intermediate b-hadron. Hence, this pseudo-proper time variable is not exactly equal to the decay lifetime of the b-hadron τ_B, but is considered as an approximation of this quantity. A projection of the longitudinal component of the pseudo-proper time is studied to achieve the separation of prompt and non-prompt J/ψ. Indeed, because of the longitudinal boost of the system provided by the forward rapidity, the longitudinal dimension is much more sensitive to the decay length of particles than the transverse dimension. Hence, only the longitudinal pseudo-proper time is considered, which simplifies the calculations. It is defined as:

$$t_z = \frac{L_z M_{J/\psi}}{p_z} = \frac{(z_{PV} - z_{SV})\, M_{J/\psi}}{p_z} \tag{4.3}$$

At forward rapidities, the Lorentz boost effect acts mainly on the z-direction, thus this longitudinal pseudo-proper time t_z is the most discriminating variable to select non-prompt decays. Finally, we will often refer to the longitudinal pseudo-proper decay length $\ell_{J/\psi}$, which is simply related to the pseudo-proper time t_z by $\ell_{J/\psi} = c \cdot t_z$.

4.2 Muon simulations in Run 3

Monte Carlo (MC) simulations are used in different steps of the analysis, in particular to evaluate acceptance and efficiencies of the various detectors, as well as to evaluate the efficiency of the matching between MFT and Muon. In such MC productions, the simulation of the detector response from generated particle events follows three steps [135].

First, one generates the primary particles and their decays to a given final state using an event generator, for instance PYTHIA8 [150]. Next, the decay products are passed to a transport software which simulates the interaction with the material of the geometry, in particular the one of the relevant detectors and support structure, like GEANT4 [151]. It also records the passage of charged particles through the different active elements of the detectors and their energy deposits, called hits. Here, the detector response must be provided to make the simulation as realistic as possible. Finally, the hit information are converted into electronic signals in the detector readout, producing the so-called "digits" that we mentioned in the previous chapters. These digits can then be reconstructed following the same chain as the offline reconstruction of data. In the case of MFT, this corresponds to the steps of clusterization and tracking.

The MC productions that were used for this analysis are simulations of Minimum Bias (MB) PYTHIA8 events in which J/ψs were injected. These simulations are mainly for efficiency studies and do not contain a realistic abundance of signal in a single event: we artificially inject signals on top of Minimum Bias events as for efficiency and resolution studies in Run 1/2. In particular, two different types of simulations were produced: one containing injected prompt J/ψ's and the other non-prompt J/ψ's. In addition, they are based on two different approaches to inject J/ψ signal in the MB event. In the prompt simulation, the J/ψ particles are generated according to a parametric shapes of transverse momentum and pseudo-rapidity which were extracted in Run 2 ALICE results. In the non-prompt simulation, the PYTHIA8 generator is configured such that a generated b-hadron (B^+, B^0 or B_s^0) is embedded in the MB background PYTHIA event. Any generated b-hadron is forced to decay into a J/ψ. Then, a trigger function is used to select only generated events in which at least one of the decay products of the J/ψ reaches the desired acceptance, in our case, at forward rapidities. In both cases, the decays of J/ψ into dimuons and the decay of the b-hadrons are carried out by the EVTGEN package [152] interfaced with pythia. It uses the PHOTOS model [153] to deal with the influence of radiative decays ($\mathrm{J}/\psi \to \mu^+\mu^-\gamma$).

4.3 Track-collision association

A crucial point of this analysis is the association between the muon tracks and the primary vertex, and its associated collision, from which they originate. Indeed, if two muons coming from the decay of a J/ψ are associated with the "wrong" collision, i.e. a collision which is not the one that produced this particle, the distance between the reconstructed secondary vertex and the primary vertex of this "wrong" collision will not represent the true decay legnth of this J/ψ.

In the Run 3 of ALICE, the third data taking sequence at the LHC which started in June 2022, the association between collisions and tracks is done using the timing information of the different detectors which participate in their reconstruction. In the case of collisions, they are first reconstructed using a primary vertexing algorithm which uses the spatial information from the charged particle tracks reconstructed by the detectors in the central barrel. Each of these detectors assigns a timestamp to the tracks that they reconstruct, and a timing error which represents its timing resolution. A timestamp is associated to the reconstructed primary vertex using the timestamps of all the tracks contributing to this vertex, as a weighted average. The most important detector contributing to the timestamp calculation of the primary vertex is the TOF detector, thanks to its very good time resolution (better than $50\,\mathrm{ps}$).

Regarding muons, the timestamp is given by the MID detector which also provides a very good time resolution of order 1 Bunch Crossing (~ 25 ns). Provided the muon segments in the MID, MCH and MFT subdetectors are accurately matched together, this time resolution is the best within the global muon track and it is complemented by the MFT detector, which has a poorer time resolution (the size of the MFT readout frame is of 198 BC) but provides a good position and thus secondary vertexing performance. Thus,

Parameters	Ambiguous tracks	Orphan tracks	Associated tracks
$n = 4$, Margin=$500\,\mathrm{ns}$	69 %	5 %	26 %
$n = 4$, Margin=0	51 %	9 %	40 %
$n = 3$, Margin=0	42 %	12 %	46 %

Table 4.1: Proportion of ambiguous, orphan, and non-ambiguous associated global muons for different parameters of the track-collision association tool, from the dataset LHC22o pass4. These fractions were obtained without any additional cuts on the single muon tracks or on the vertices.

the matching between all the forward detectors of ALICE is essential to exploit their full potential.

Once the timing information of tracks and collisions is determined, it is used in a track-collision association algorithm. I contributed to the development of this algorithm for the case of forward tracks. It is currently a process which is applied after the production of AODs, and with parameters that can be customized by the analyser. This association algorithm, based on time compatibility, is illustrated on Fig. 4.1. This algorithm computes for each object (track or vertex) a time window using the information produced by the reconstruction. Each track for which the time window overlaps the one of a vertex will be associated with this vertex and the corresponding collision. The time windows are computed using two elements: the timing error of the object, which is computed during the reconstruction and reflects the time resolution of the detectors, and a safety time margin which can be added. This safety margin is added to account for the fact that some detectors are not perfectly aligned in time with respect to each other, which can lead to some bias in the association.

However, as is illustrated on Fig. 4.1, time windows which are large can lead to the occurrence of so-called "ambiguous" tracks. These are tracks which are compatible in time with more than one collision vertex. Such tracks must be rejected from the analyses that require collision-vertex association, since we cannot determine which one of the compatible vertices corresponds to the collisions from which the track originated, and thus the pseudo-proper time of the candidates cannot be properly determined. But if the time windows are too small, some tracks can also be left without any compatible collisions. These are called "orphan" tracks. The size of the time windows must thus be optimized to minimize both the number of orphan tracks and ambiguous tracks.

The two parameters that one can adjust to optimize the association are the time margin and the confidence interval for time error. Indeed, the "time error" range shown on Fig. 4.1 is computed as $t_0 \pm (n \times \sigma)$, where t_0 is the timestamp of the object, σ is the time resolution of the detector, and n is an integer. This last parameter can be adjusted if needed in the algorithm to reduce the time window of the objects.

Although a detailed study of the impact of the variation of these parameters on the performance of the association is still to be done, a first study points to the fact that in the case of global muons, thanks to the good time resolution of the MID and the existing

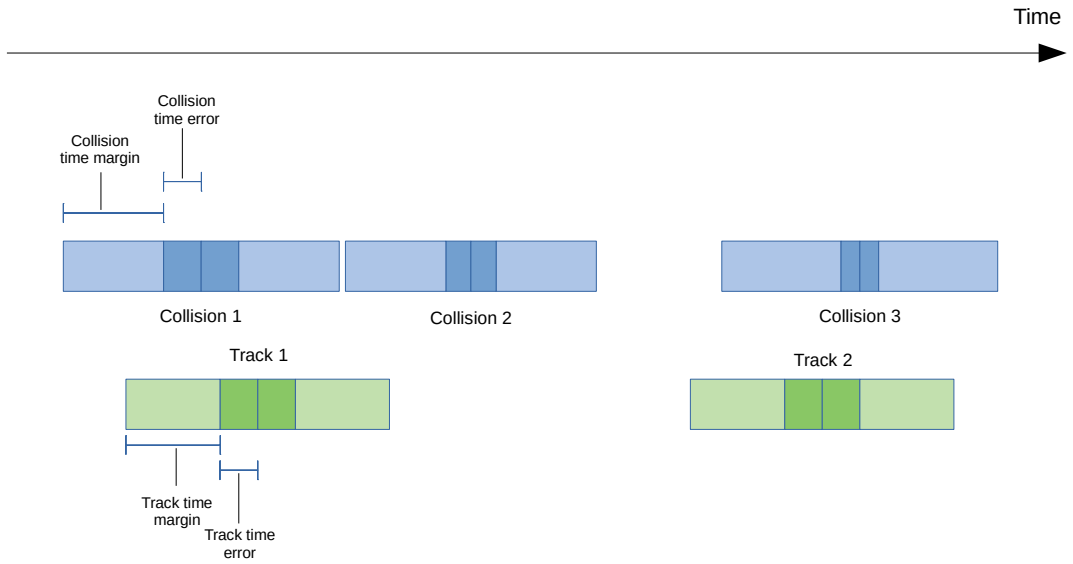

Figure 4.1: Illustration of the time structure of collisions and tracks in Run 3. The time margin added to the tracks and collisions make Track 1 compatible with both Collisions 1 and 2 in the figure, and thus is an ambiguous track. Track 2 is still unambiguously associated to Collision 3.

time alignment between the MID and the central barrel detectors, the time margins can be removed for both tracks and collisions, and the n parameter can be set to $n = 3$ without creating too many orphan tracks as to compromise the analysis, as can be seen on Table.4.1. Although a significant fraction of ambiguous tracks remains even with this restricted time range, these choices will be used in the following study.

4.4 Secondary Vertexing

Once the global muons are reconstructed, they are then grouped in pairs in order to produce dimuons, i.e. J/ψ candidates. This pairing is done event-by-event, meaning that we only pair unlike-sign muons associated with the same collision. This is known as same-event pairing. In this procedure, muon tracks which are paired together are extrapolated towards the interaction region, in order to reconstruct a possible common vertex from which both tracks originate. This procedure is done using the *FwdDCAFitter* class [149] of O^2, which calculates the point of closest approach (PCA) between the two tracks, illustrated on Fig.4.2.

The algorithm for this task takes n tracks as input. First, a starting seed for the vertex is defined. It is computed by minimizing the distance between the input tracks on the (x, y) plane. Then, starting from this seed, the best possible vertex position is determined by a $3\mathrm{D}$ χ^2 minimization, using an iterative Newton-Raphson minimization. This χ^2, which will be noted χ^2_{PCA} in the following, quantifies the quality of the reconstructed secondary vertex; the higher the probability of the tracks crossing, the lower the χ^2_{PCA} score. The convergence is reached when the relative change between the last two cal-

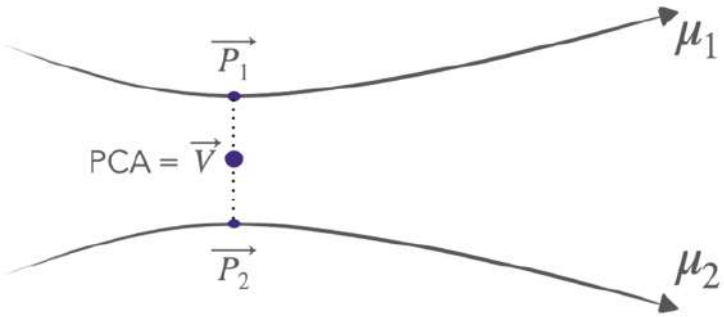

Figure 4.2: Illustration of the definition of the Point of Closest Approach (PCA) between two tracks [149].

culated χ^2_{PCA} scores is smaller than a determined percentage. A maximum number of iterations is allowed to find this convergence status (currently 60 by default), to avoid infinite loops. These parameters were optimized during the development of this algorithm by Rita Sadek [149].

4.5 Data selection

In this study, the dataset $LHC22o$ was used. This corresponds to approximately one month of data-taking at $500\,\mathrm{kHz}$ interaction rate. This period was selected because of the relatively large statistics it collected; indeed, it amounts to $\sim 6.5 \cdot 10^{11}$ inelastic events, which corresponds to $\sim 64\%$ of the whole statistics collected in the 2022 pp runs (reported in section 2.2.3). It is also a period for which the quality of the detector status, especially for MFT, was carefully checked. The latest version available of this reconstruction was used, which was finalized in May 2022. From this dataset, muon tracks and dimuon candidates are extracted based on the following selection criteria:

Single muon selection

- The muon track must be a Global muon, i.e. matched between the MFT, MCH and MID detectors.
- The pseudorapidity η of the muon must fall within the MFT acceptance $-3.6 < \eta < -2.5$ (see Fig.4.3, right).
- A cut of $p_{\mathrm{T}} > 0.5\,\mathrm{GeV}/c$ on the transverse momentum of the single global muon tracks is applied (see Fig.4.3, left).
- A cut on the χ^2 of the matching between MFT and Muon is applied: $\chi^2_{\mathrm{MFT-Muon}} < 40$.

Two additional selection criteria were kept from the Run 2 analysis:

- The radial distance of the muon track to the beam axis at the end of the absorber must satisfy $17.6\,\mathrm{cm} < R_{\mathrm{abs}} < 89.5\,\mathrm{cm}$. This cut ensures that muons emitted at small angles, i.e. those that have crossed a significant fraction of the thick beam

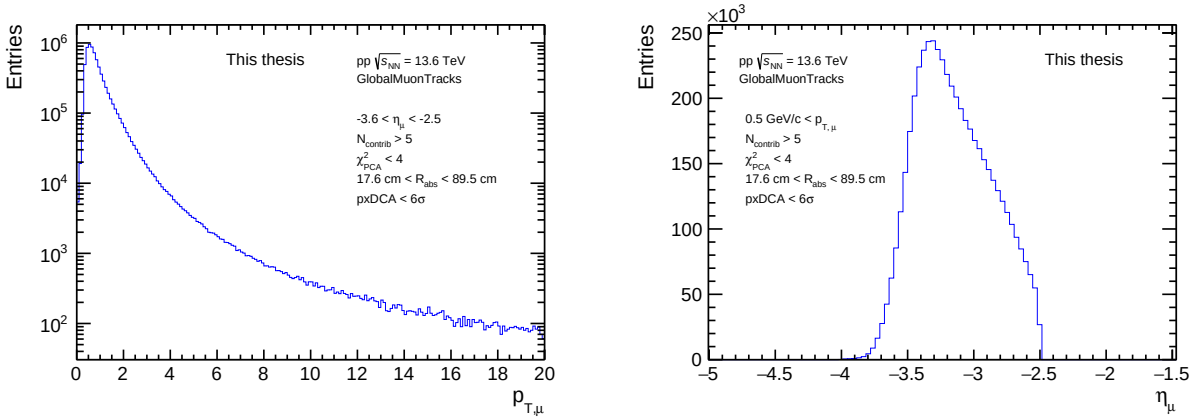

Figure 4.3: (Left) Transverse momentum distribution of muons tracks, (Right) pseudo-rapidity distribution of muon tracks. The selection cuts are applied except for the one of the displayed parameter.

shield, are rejected. Indeed, such tracks are significantly affected by multiple Coulomb scattering, which results in a poor mass resolution of the corresponding dimuon pair.

- A cut on the total momentum $p \times \mathrm{DCA}$ is applied, where DCA is the distance of closest approach, defined as the distance in the transverse plane between the interaction vertex and the extrapolated muon track. The cut is fixed at $p \times \mathrm{DCA} < 6\sigma$, meaning less than six times the standard deviation of the $p \times \mathrm{DCA}$ distribution. This standard deviation varies with the transverse momentum of the muon track. This $p \times \mathrm{DCA}$ variable takes into account both the muon momentum and the transverse distance covered by the particle during its propagation. It enables us to reject fake tracks reconstructed in the spectrometer, beam-gas interactions taking place in the same time interval as the beam-beam collisions, as well as part of the pion and kaon noise [154].

Dimuon selection

- The selected dimuon candidates must be composed of two muon of opposite charges (i.e. a muon and an anti-muon).
- The rapidity y of the dimuon must fall within the spectrometer acceptance $-3.6 < y < -2.5$.
- The χ^2_{PCA} variable, which quantifies the quality of the reconstructed secondary vertices, is restricted using a cut $\chi^2_{\mathrm{PCA}} < 4$. This value was chosen as it was the one which decreased the tails of the pseudo-proper decay length resolution distribution, which will be shown in the following section, while preserving sufficient statistics. However, this cut has an efficiency of $\sim 50\%$ in the invariant mass range $2.95 < M_{\mu\mu} < 3.2$. This points to the fact that the quality of the reconstructed secondary vertices is not fully under control. An alternative would be to use the

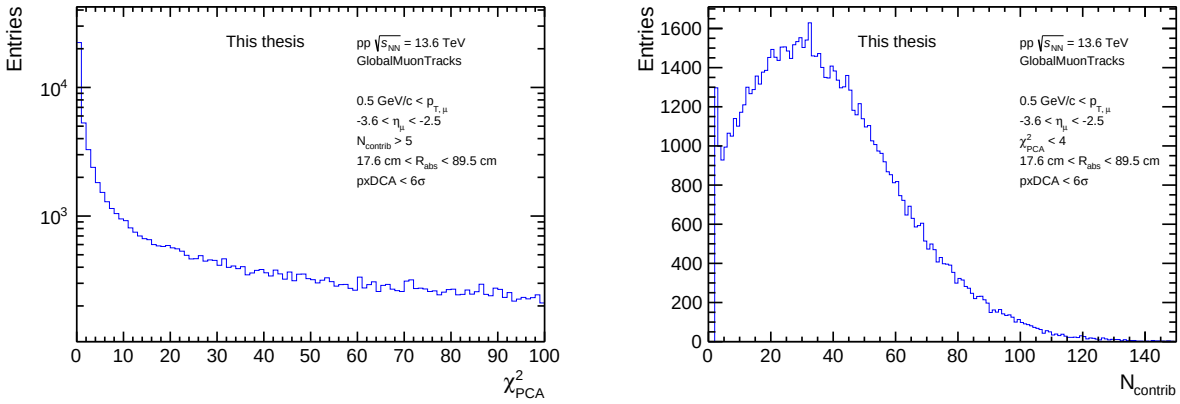

Figure 4.4: (Left) χ^2_{PCA} distribution of selected dimuon candidates , (Right) distribution of the number of contributors to the primary vertices assoicated with the selected dimuon candidates. The selection cuts are applied except for the one of the displayed parameter, and only the candidates in the invariant mass range $2.95 < M_{\mu\mu} < 3.2$.

KFParticle package [155] instead of the *FWDCAFitter* to carry out the secondary vertexing procedure.

- A cut on the number N_{contrib} of central barrel tracks contributing to each reconstructed primary vertex is applied. Such selection ensures the good quality of the primary vertices used in the analysis. Similarly to the χ^2_{PCA}, the value of this cut was chosen to decrease the tails of the resolution distribution, at $N_{\mathrm{contrib}} > 5$. The efficiency for this cut is roughly $\sim 80\%$ for dimuon candidates in the invariant mass range $2.95 < M_{\mu\mu} < 3.2$.

4.6 Signal extraction

In order to separate the prompt and non-prompt J/ψ contributions, a statistical separation following the longitudinal pseudo-proper decay length $\ell_{J/\psi}$ distribution is used.

In this statistical method, the signal extraction is based on a two-dimensional unbinned maximum likelihood fit (2D fits) of the dimuon $(\mu^+\mu^-)$ invariant mass and the longitudinal pseudo-proper decay length $\ell_{J/\psi} = c\tau_z$ distributions for each dimuon p_{T} or rapidity range considered. In this procedure, a Probability Density Function $F\left(\ell_{J/\psi}, M_{\mu\mu}\right)$ is fitted to the data, simultaneously on these two variables. The fraction of non-prompt J/ψ mesons f_B is a free parameter in this fit. In addition, for both mass and pseudo-proper decay length, J/ψ signal and background components are present in the data. Thus, in both dimensions, signal as well as background components must be included in the Probability Density Function to properly fit the data. The functional form of the Probability Density function $F\left(\ell_{J/\psi}, M_{\mu\mu}\right)$ used in the 2D fit is given by:

$$F\left(\ell_{J/\psi}, M_{\mu\mu}\right) = N_{\mathrm{Sig}} \cdot F_{\mathrm{Sig}}\left(\ell_{J/\psi}\right) \cdot M_{\mathrm{Sig}}\left(M_{\mu\mu}\right) + N_{\mathrm{Bkg}} \cdot F_{\mathrm{Bkg}}\left(\ell_{J/\psi}\right) \cdot M_{\mathrm{Bkg}}\left(M_{\mu\mu}\right) \quad (4.4)$$

where N_{Sig} is the number of signal dimuons (i.e. prompt and non-prompt J/ψ candidates), N_{Bkg} is the number of background dimuons, $F_{\mathrm{Sig}}\left(\ell_{J/\psi}\right)$ and $M_{\mathrm{Sig}}\left(M_{\mu\mu}\right)$ are the

functional forms that describe the shape of the signal, respectively in the pseudo-proper decay length $\ell_{J/\psi}$ and invariant mass dimensions. $F_{\mathrm{Bkg}}\left(\ell_{J/\psi}\right)$ and $M_{\mathrm{Bkg}}\left(M_{\mu\mu}\right)$ are the functional forms that describe the shape of the background, in the $\ell_{J/\psi}$ and invariant mass dimensions,respectively.

The functional shape of the signal for the $\ell_{J/\psi}$ variable, $F_{\mathrm{Sig}}\left(\ell_{J/\psi}\right)$, will in the end be the one which allows to separate the prompt and non-prompt components of the J/ψ signal. Indeed, for prompt J/ψ, the true pseudo-proper decay length is zero, as the reconstructed common secondary vertex of the two muon tracks coincides with the primary vertex. Thus, the functional shape of true $\ell_{J/\psi}$ for the prompt J/ψ signal distribution is a delta distribution $\delta(0)$. For the non-prompt J/ψ signal, the true $\ell_{J/\psi}$ distribution follows an exponential representing the lifetime of the b-hadrons from which the non-prompt J/ψ originated. These two different shapes can be used to separate the prompt and non-prompt contributions to the total signal shape $F_{\mathrm{Sig}}\left(\ell_{J/\psi}\right)$. However, in experimental setups, detectors have finite spatial and vertexing resolutions. Thus, the measured distribution of prompt J/ψ will not be the true $\delta(0)$ distribution, but will be smeared by a function representing the resolution of the detector, in our case, of the MFT. The exponential distribution for the non-prompt J/ψ is also smeared by the same function.

The measured $\ell_{J/\psi}$ is thus different from the true pseudo-proper decay length, which will be noted $\ell^{\mathrm{true}}_{J/\psi}$ in the following. The $\ell_{J/\psi}$ signal and background shapes, $F_{\mathrm{Sig,Bkg}}\left(\ell_{J/\psi}\right)$, are given by:

$$F_{\mathrm{Sig,Bkg}}\left(\ell_{J/\psi}\right) = F^{\mathrm{true}}_{\mathrm{Sig,Bkg}}\left(\ell^{\mathrm{true}}_{J/\psi}\right) \otimes R\left(\ell_{J/\psi} - \ell^{\mathrm{true}}_{J/\psi}\right) \tag{4.5}$$

In Eq. 4.5, the $R\left(\ell_{J/\psi} - \ell^{\mathrm{true}}_{J/\psi}\right)$ function is the resolution function. As explained, for the prompt J/ψ, we have $\ell^{\mathrm{true}}_{J/\psi} = 0$. Consequently, $F^{\mathrm{prompt}}_{\mathrm{Sig}}\left(\ell_{J/\psi}\right) = R\left(\ell_{J/\psi}\right)$. This means that the resolution function can be determined with the prompt J/ψ, extracted from the data, or estimated from MC simulations. This resolution function is convoluted with the true distributions for signal and background $F^{\mathrm{true}}_{\mathrm{Sig}}\left(\ell^{\mathrm{true}}_{J/\psi}\right)$ and $F^{\mathrm{true}}_{\mathrm{Bkg}}\left(\ell^{\mathrm{true}}_{J/\psi}\right)$ to obtain the measured $F_{\mathrm{Sig,Bkg}}\left(\ell_{J/\psi}\right)$ distributions, used in Eq. 4.4, that include detector resolution effects.

As motivated above, the $F^{\mathrm{true}}_{\mathrm{Sig}}\left(\ell^{\mathrm{true}}_{J/\psi}\right)$ distribution is given by the sum of prompt and non-prompt components:

$$F^{\mathrm{true}}_{\mathrm{Sig}}\left(\ell^{\mathrm{true}}_{J/\psi}\right) = f_B F^{\mathrm{true}}_{\mathrm{Nonprompt}}\left(\ell^{\mathrm{true}}_{J/\psi}\right) + (1 - f_B) F^{\mathrm{true}}_{\mathrm{Prompt}}\left(\ell^{\mathrm{true}}_{J/\psi}\right), \tag{4.6}$$

where f_B is the fraction of non-prompt J/ψ. By definition, $F^{\mathrm{true}}_{\mathrm{Prompt}}\left(\ell^{\mathrm{true}}_{J/\psi}\right)$ is the delta distribution $\delta(0)$, while $F^{\mathrm{true}}_{\mathrm{Nonprompt}}\left(\ell^{\mathrm{true}}_{J/\psi}\right)$ is an exponential decay. Finally, the function $F^{\mathrm{true}}_{\mathrm{Bkg}}\left(\ell_{J/\psi}\right)$ is determined from fits on the data background $\ell_{J/\psi}$ distributions.

In the following, the procedure to extract the signal from the 2D fit of the Probability Density Function $F\left(\ell_{J/\psi}, M_{\mu\mu}\right)$ expressed in Eq. 4.4 is to first fit the functional shapes of

the mass for signal and background $M_{\mathrm{Sig,Bkg}}\left(M_{\mu\mu}\right)$. This is done by fitting the full one-dimensional invariant mass distribution with the sum of carefully chosen signal and background functions. Next, the resolution function is determined from the data distribution of $\ell_{J/\psi}$. In addition, the exponential of the $F^{\mathrm{true}}_{\mathrm{Nonprompt}}\left(\ell^{\mathrm{true}}_{J/\psi}\right)$ function is initialized using values extracted from MC non-prompt simulations. Then, the parameters which will be determined by the 2D fit are the f_B fraction, N_{Sig} and N_{Bkg}.

4.6.1 Invariant mass fit

In this section, the procedure to obtain the $M_{\mathrm{Sig}}\left(M_{\mu\mu}\right)$ and $M_{\mathrm{Bkg}}\left(M_{\mu\mu}\right)$ invariant mass parameterizations is explained. The inclusive J/ψ yield, i.e. combined prompt and non-prompt, is extracted separately by fitting the one-dimensional invariant $\mu^+\mu^-$mass spectra. These fits are unbinned maximum likelihood fits, performed using the RooFit package [156]. The invariant mass fits are done in the region $2.6 < m_{\mu^+\mu^-} < 3.5\,\mathrm{GeV}/c^2$. In this range, the invariant mass spectrum of unlike-sign dimuons is composed of a peak, centered around $\mathrm{m}_{\mu\mu} \approx 3.097\,\mathrm{GeV}/c^2$, corresponding to the J/ψ in the dimuon channel. In addition to this peak, pairs of uncorrelated muons form a continuous invariant mass distribution called the combinatorial background. These pairs are the products of decays of kaons and pions, as well as semi-leptonic decays of open heavy-flavor hadrons.

To fit the J/ψ signal peak, a double-sided Crystal Ball function $g_{\mathrm{CB2}}(m)$ is used [148]. It combines a Gaussian core and power-law tails on both sides of the peak. The left and right tails respectively have exponents n and n_2. Two additional parameters, α and α_2, define the transition between the Gaussian and the power-law functions. The high-mass tail is attributed to multiple Coulomb scattering in the front absorber and momentum resolution. The low-mass tail is due to the impact of the NLO QED-process $J/\psi \to \mu^+\mu^- + \gamma$. The mean of the Gaussian core is denoted m_0 while the standard deviation is labelled as σ. The function is thus defined as:

$$g_{\mathrm{CB2}}(m) = N \begin{cases} \exp\left(\frac{-(m-m_0)^2}{2\sigma^2}\right) & \text{for } \frac{(m-m_0)}{\sigma} \in [-\alpha, \alpha_2] \\ A\left(B - \frac{(m-m_0)}{\sigma}\right)^{-n} & \text{for } \frac{(m-m_0)}{\sigma} \leq -\alpha \\ C\left(D + \frac{(m-m_0)}{\sigma}\right)^{-n_2} & \text{for } \frac{(m-m_0)}{\sigma} \geq -\alpha_2 \end{cases}$$

where N is a normalization factor, and with:

$$\begin{aligned} A &= \left(\frac{n}{|\alpha|}\right)^n \exp\left(-\frac{|\alpha|^2}{2}\right), \\ B &= \frac{n}{|\alpha|} - |\alpha|\,, \\ C &= \left(\frac{n_2}{|\alpha_2|}\right)^{n_2} \exp\left(-\frac{|\alpha_2|^2}{2}\right), \\ D &= \frac{n_2}{|\alpha_2|} - |\alpha_2| \end{aligned}$$

In addition, an exponential function (thus with a single parameter) is used for the background component of the invariant mass fit. The result of one of these fits is shown on Fig. 4.5 in the $3 < p_{\mathrm{T}} < 4\,\mathrm{GeV}/c$ bin.

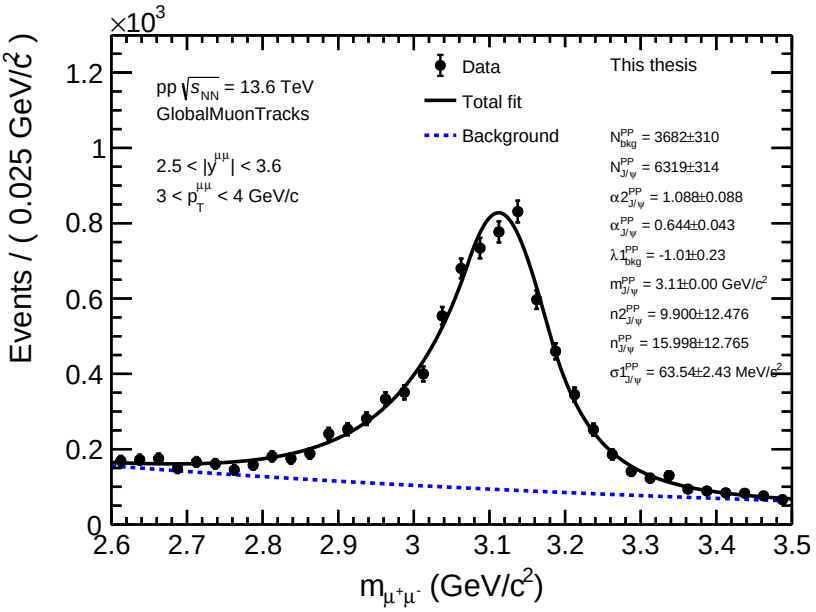

Figure 4.5: Example of an invariant mass fit, with a double Crystal Ball function and an exponential function describing respectively the signal and background components. The fit is shown in the dimuon transverse momentum range $3 < p_{\mathrm{T}} < 4\,\mathrm{GeV}/c$. The parameters of the fitted functions are displayed on the right-hand side of the figure.

In such fits, the tail parameters of the Crystal Ball function are usually fixed to values extracted from MC simulations, while the mean and width of the gaussian core are left free. Thus, similar fits are performed using the MC simulations mentioned in a previous section, in the same bin as the data, but removing the background component of the invariant mass spectrum, thus fitting only the signal shape. However, fixing the set of tail parameters (n,n_2,α,α_2) in the data to the ones extracted from the background-free MC simulation did not lead to a stable convergence of the fits. This discrepancy is attributed to the fact that the current MC simulations were not yet realistic; for instance, there was no residual misalignment included, the readout characteristics of the MFT were not identical between MC and the data, and the modeling of the hadronic absorber is not fully realistic[1]. Thus, instead of fixing the tail parameters to the MC ones, they are just initialized to the MC values, then left free to vary during the fit. Indeed, as can be seen by comparing Fig. 4.5 and Fig. 4.6, the resulting tail parameters after the fit from data and MC are not in good agreement, especially regarding the n and n_2 exponents.

4.6.2 Resolution fit

The previous fit on invariant mass did not need to distinguish between prompt and non-prompt J/ψ. However, to extract the resolution function $R\left(\ell_{J/\psi}\right)$ in Eq. 4.5, only the prompt component of the $\ell_{J/\psi}$ distribution must be considered. Thus, first the background and signal contributions must be disentangled from the distribution, then the

[1]In addition to these known lacking points, other sources of discrepancy, which should not be related to the ones cited here, are still under investigation, see the next subsection.

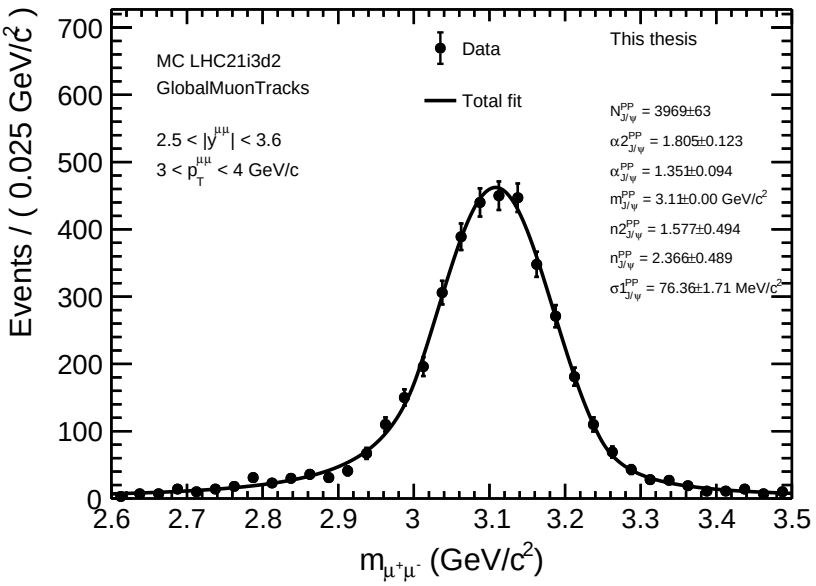

Figure 4.6: Invariant mass fit of an MC simulation, selecting only the J/ψ signal and fitting it with a double Crystal Ball, the dimuon transverse momentum range $3 < p_{\mathrm{T}} < 4\,\mathrm{GeV}/c$. The values of the parameters after the fit are displayed on the right-hand side of the figure and show different values than the ones in Fig. 4.5.

prompt component must be extracted from this signal.

For the first step, to separate the signal and background contributions, we use the so-called *sPlot* technique [157]. It applies to a data sample of events described by a multi-dimensional space of discriminating variables, where there are several sources of events (i.e. signal and background, prompt and non-prompt particles...). The basic concept of the *sPlot* technique consists of constructing the so-called *sWeights* of the different categories of events, using the fit information on a discriminating variable. Then, the data sample can be weighted according to a given category of events, and plot the dataset for another variable. In our specific case, we want to separate signal and background in the $\ell_{J/\psi}$ distribution, so the discriminating variable is $M_{\mu\mu}$. The *sWeights* of signal and background can be constructed from the mass Probability Density functions extracted in the previous subsection.

$$ {}_s\mathcal{W}_{\mathrm{sig}}\left(M_{\mu\mu}\right) = \frac{V_{\mathrm{sig,bkg}} \cdot M_{bkg}\left(M_{\mu\mu}\right) + V_{\mathrm{sig,sig}} \cdot M_{\mathrm{sig}}\left(M_{\mu\mu}\right)}{N_{\mathrm{bkg}} \cdot M_{\mathrm{bkg}}\left(M_{\mu\mu}\right) + N_{\mathrm{sig}} \cdot M_{\mathrm{sig}}\left(M_{\mu\mu}\right)} $$

$$ {}_s\mathcal{W}_{\mathrm{bkg}}\left(M_{\mu\mu}\right) = \frac{V_{\mathrm{bkg,bkg}} \cdot M_{\mathrm{bkg}}\left(M_{\mu\mu}\right) + V_{\mathrm{bkg,sig}} \cdot M_{\mathrm{sig}}\left(M_{\mu\mu}\right)}{N_{\mathrm{bkg}} \cdot M_{\mathrm{bkg}}\left(M_{\mu\mu}\right) + N_{\mathrm{sig}} \cdot M_{\mathrm{sig}}\left(M_{\mu\mu}\right)} $$

where $M_{\mathrm{sig,bkg}}\left(M_{\mu\mu}\right)$ are the signal and background PDFs, $N_{\mathrm{sig,bkg}}$ are the yields of each component and $V_{i,j}$ is the covariance matrix of the i^{th} and j^{th} sources of events ($i, j =$ signal and background).

Once the signal and background components are separated using the *sPlot* technique, the $\ell_{J/\psi}$ distribution for prompt J/ψ can be obtained. For this, we use a data driven

method, which assumes that the negative tail in the signal $\ell_{J/\psi}$ distribution is mostly due to prompt J/ψ affected by resolution. The events from this negative tail are, therefore, used to determine the resolution. The resulting distribution can be described by the weighted sum of several different functions. One of them describes most of the "core" region, while the others take the tail components. Different combinations of functions were tested: a single gaussian function, a weighted sum of two gaussian functions, a weighted sum of three gaussian functions, and a weighted sum of two gaussian functions and a double-sided exponential of the form $\exp(-\lambda|x|)$. This last combination gave the best results in terms of χ^2 of the fits. Indeed, the double-sided exponential manages to capture the tails of the distributions, which are attributed to residual primary or secondary vertices having bad quality.

$$R\left(\ell_{J/\psi}\right) = [f_{\mathrm{res}} \cdot \mathrm{Gauss}(\ell_{J/\psi}, \sigma_1, l_0) + (1 - f_{\mathrm{res}}) \\ \cdot [f2_{\mathrm{res}} \cdot \mathrm{Gauss}(\ell_{J/\psi}\sigma_2, l_0) + (1 - f2_{\mathrm{res}}) \cdot \exp(-\lambda|\ell_{J/\psi} - l_0|)]]$$

where the f_{res} and $f2_{\mathrm{res}}$ are the relative weights of the individual functions on the total resolution function. The Gaussian components have separated sigmas σ_1 and σ_2. The three components of the total probability density function are allowed to be shifted by a mean of l_0. An example of resolution fit in data with these functions is given on Fig. 4.7.

As can be seen in this figure, the mean value of the distributions is shifted from zero towards positive values. This feature points to uncorrected relative spatial positions of the MFT, responsible for the secondary vertexing resolution, with respect to the ITS2, responsible for the primary vertexing resolution, as their relative positions are wrongly assumed to be the ones provided by the ideal ALICE geometry. This is known as the relative spatial misalignement between MFT and ITS2. Thus a shift is observed in all the $\ell_{J/\psi}$ resolution fits, ranging from $l_0 = 30\,\mu\mathrm{m}$ in the $2 < p_{\mathrm{T}} < 3\,\mathrm{GeV}/c$ bin, to $l_0 = 10\,\mu\mathrm{m}$ in the $10 < p_{\mathrm{T}} < 30\,\mathrm{GeV}/c$. The dashed lines on Fig. 4.7 represent the fitting range. In order to fit only the left part of the distribution where the prompt component is dominant, this fitting range must be shifted for each fit to match the appropriate mean of the distribution.

In principle, the resolution function could be also be extracted from MC simulation. Indeed, the signal can be selected in the prompt MC production, and then fitted with the same functions introduced before to extract the resolution function. This procedure would allow to proceed with this extraction by fitting the $\ell_{J\psi}$ signal distribution over the whole range instead of just the left side of the distribution. However, the MC simulations in their current status do not take into account any residual misalignment, and in particular, the relative misalignment between MFT and ITS2 is not accounted for. Hence the MC distributions are centered at $\ell_{J/\psi} = 0$, as can be seen on Fig. 4.8. In addition, this figure shows that the tails of the distributions are not fully reproduced by the MC simulation. Thus, our choice was to use the data-driven method outlined above to extract the resolution.

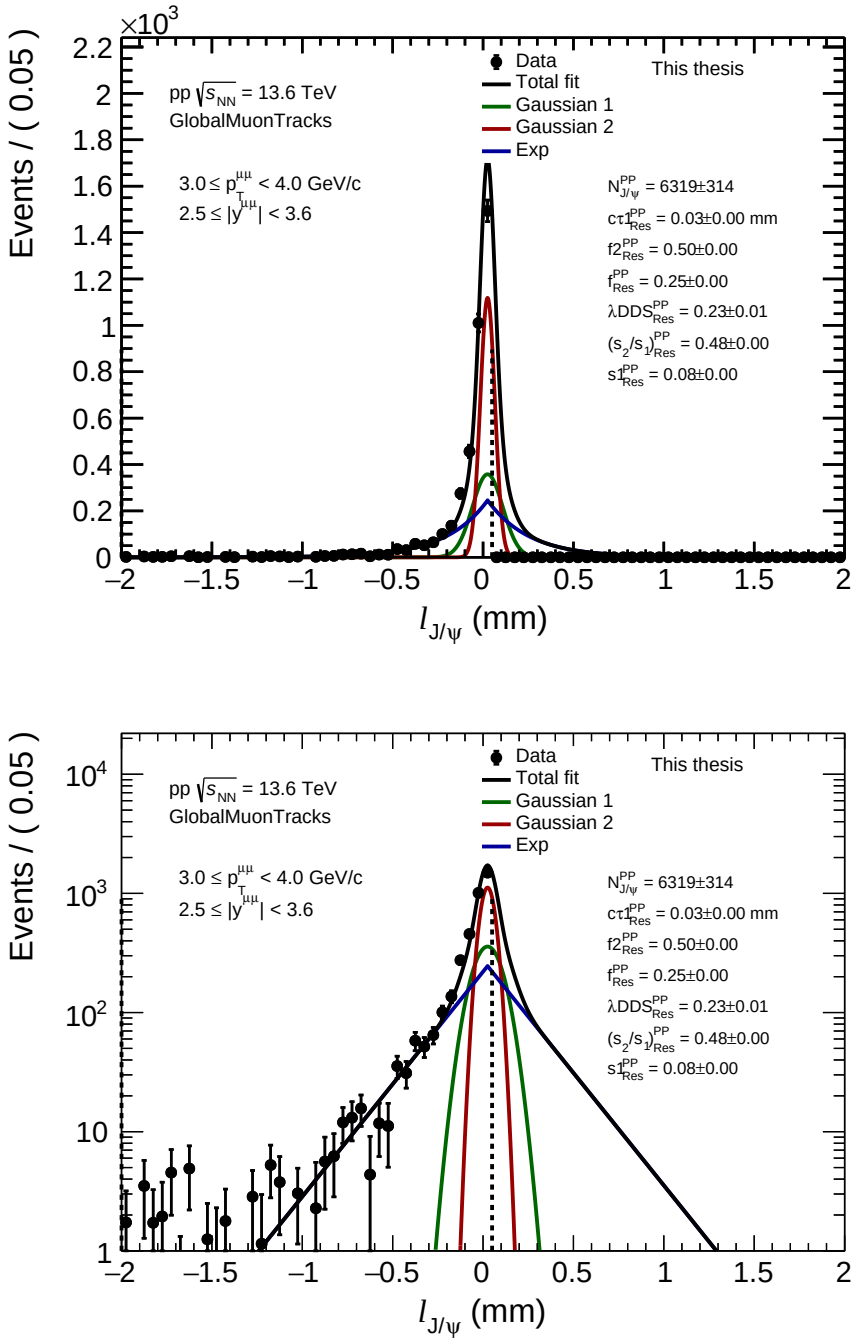

Figure 4.7: Example of a $\ell_{J/\psi}$ resolution fit, (top) in linear scale and (bottom) log scale. The distribution is extracted using the *sPlot* technique. Its mean is shifted from zero due to a residual detector misalignment. Only the left side of the distribution is fitted, as emphasized by the dashed lines. The fit is shown in the dimuon transverse momentum range $3 < p_{\mathrm{T}} < 4\,\mathrm{GeV}/c$.

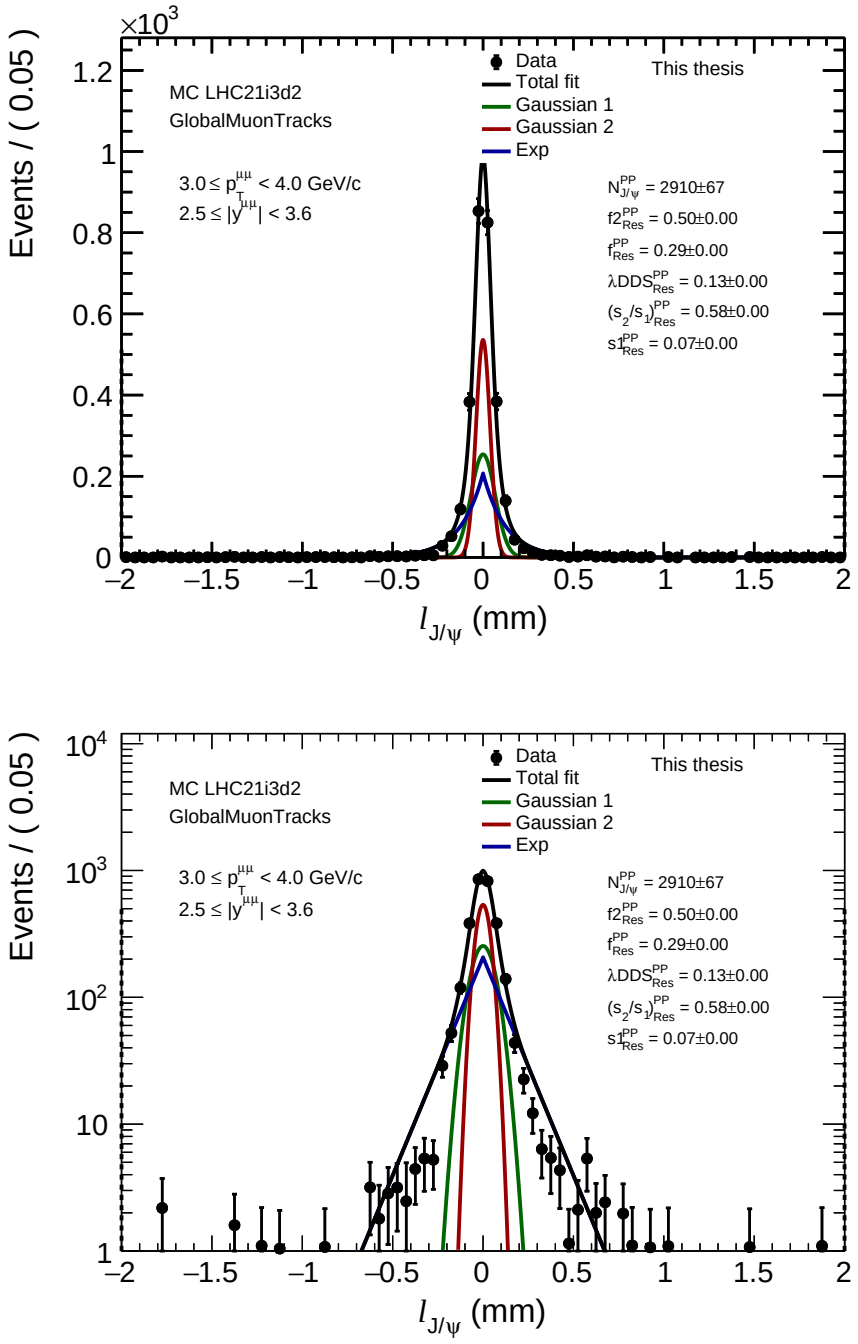

Figure 4.8: $\ell_{J/\psi}$ resolution fit on a MC simulation containing prompt J/ψ, (top) in linear scale and (bottom) log scale. Only the J/ψ signal is selected from the simulation. The fit is shown in the dimuon transverse momentum range $3 < p_{\mathrm{T}} < 4\,\mathrm{GeV}/c$.

4.6.3 Background fit

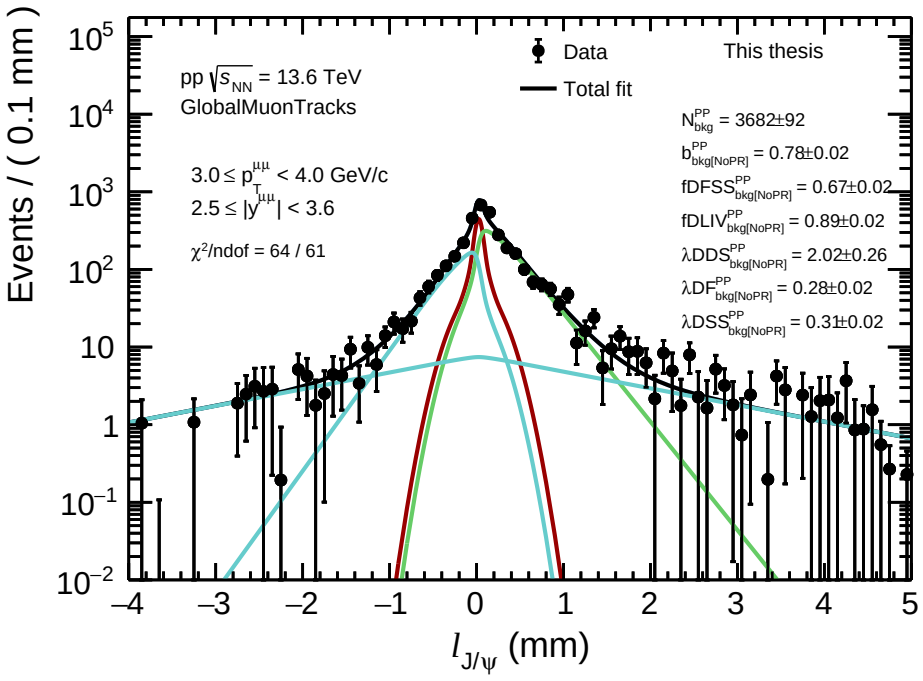

Figure 4.9: Example of a $\ell_{J/\psi}$ background fit. The distribution is extracted using the *sPlot* technique. The fit is shown in the dimuon transverse momentum range $3 < p_{\mathrm{T}} < 4\,\mathrm{GeV}/c$.

The next step is to fit the background $\ell_{J/\psi}$ distribution, $F_{\mathrm{Bkg}}^{\mathrm{true}}\left(\ell_{J/\psi}^{\mathrm{true}}\right)$, in Eq. 4.6. Just like in the previous section for the extraction of signal distribution for the resolution fit, the *sPlot* technique is applied to the full $\ell_{J/\psi}$ in order to determine the background distribution. The total background Probability density function $F_{\mathrm{Bkg}}^{\mathrm{true}}\left(\ell_{J/\psi}^{\mathrm{true}}\right)$ is described by a combination of different functions. The one which gives the best fitting χ^2 is a combination of a single-sided decay function $\exp\left(-\lambda x\right)$, a flipped single-sided decay $\exp\left(\lambda x\right)$, a double-sided decay functions $\exp\left(-\lambda|x|\right)$, and finally a delta distribution. Hence, the total background probability density is parametrized as:

$$
\begin{aligned}
F_{Bkg}^{\mathrm{true}}\left(\ell_{J/\psi}^{\mathrm{true}}\right) = & b_{\mathrm{bkg}} \cdot \Big[f_{\mathrm{DLIV}} \cdot \Big(f_{\mathrm{DFSS}} \cdot e^{-|\lambda_{\mathrm{DSS}}|\ell_{J/\psi}^{\mathrm{true}}} \\
& + (1 - f_{\mathrm{DFSS}}) \cdot e^{|\lambda_{\mathrm{DF}}| \cdot \ell_{J/\psi}^{\mathrm{true}}} \Big) + (1 - f_{\mathrm{DLIV}}) \cdot e^{-\left|\lambda_{\mathrm{DDS}} \cdot \ell_{J/\psi}^{\mathrm{true}}\right|} \Big] \\
& + (1 - b_{\mathrm{bkg}}) \cdot \delta\left(\ell_{J/\psi}^{\mathrm{true}}\right)
\end{aligned}
$$

where b_{bkg} is a fit parameter which quantifies the importance of the delta distribution component of the total distribution with respect to the other components, f_{DLIV} quantifies the importance of the decay exponential with respect to the single-sided exponential

functions, and f_{DFSS} quantifies the importance of the flipped to the unflipped single decay functions. $\lambda_{\mathrm{DDS}}, \lambda_{\mathrm{DSS}}, \lambda_{\mathrm{DF}}$ are the parameters of the double-sided, signle-sided and flipped exponential functions, respectively. This full function is convoluted with the resolution function, as in Eq. 4.5, to fit the background reconstructed $\ell_{J/\psi}$ distributions in data. All the resolution parameters are fixed to those obtained in data fits in the previous sub-section. An example of these background $\ell_{J/\psi}$ fits can be seen in Fig. 4.9.

4.6.4 Total 2D fit

The previous fits allow to constrain the various components which intervene in the total two-dimensional Probability Distribution Functions $F\left(\ell_{J/\psi}, M_{\mu\mu}\right)$ in Eq. 4.4. Then the 2D fit on the invariant mass and pseudo-proper decay length can be put in place:

- From the invariant mass fit, the parameters of signal and background functional shapes parameters are fixed. The number $N_{J/\psi}$ of J/ψ and the number of background candidates N_{bkg} are left free.
- From the fit of the left side of the $\ell_{J/\psi}$ signal, i.e. the resolution function is extracted, and its parameters are fixed.
- From the fit of the $\ell_{J/\psi}$ background distributions, the background shape of the distribution is fixed.
- The parameter of the exponential in the $F^{\mathrm{true}}_{\mathrm{Nonprompt}}\left(\ell^{\mathrm{true}}_{J/\psi}\right)$ Probability density function is initialized to the value of the slope of the $\ell^{\mathrm{true}}_{J/\psi}$ distribution from the nonprompt MC simulation, but is then left free in the fit.

The f_B fraction ($b_{J/\psi}$ in the plots) is a free parameter in the 2D fit. An example of the invariant mass and $\ell_{J/\psi}$ projections of the fit are shown on Fig. 4.10.

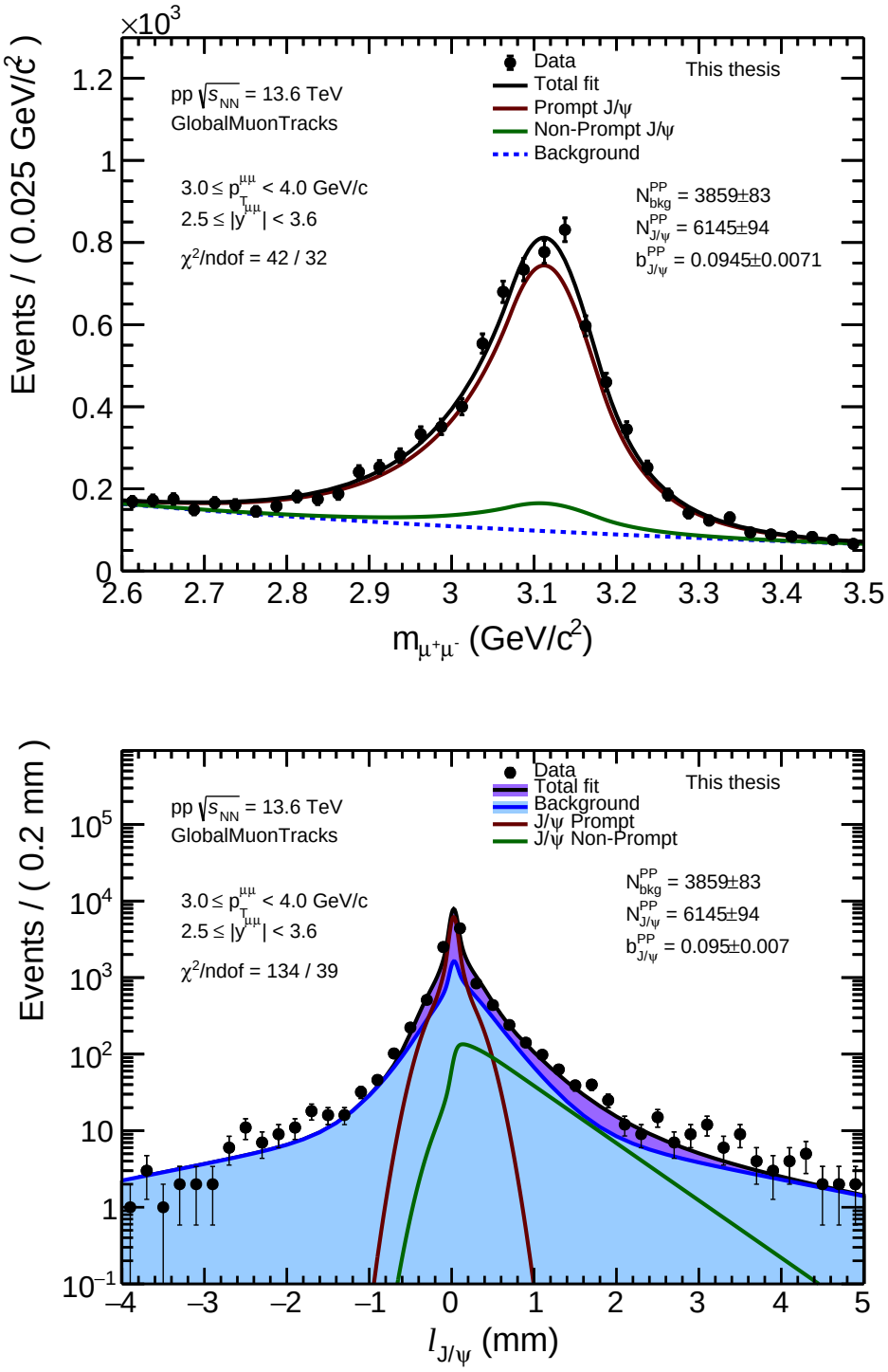

Figure 4.10: Example of results of the 2D fit in the dimuon transverse momentum range $3 < p_{\mathrm{T}} < 4\,\mathrm{GeV}/c$. Projections in (top) invariant mass and (bottom) longitudinal pseudo-proper decay length are displayed. The blue curves show the background component fit, the red curve is the prompt J/ψ component, while the green curve is the non-prompt J/ψ component.

4.7 Preliminary results

The previous 2D fits allow to extract the raw fraction f_B of the non-prompt J/ψ contribution to the inclusive cross section, where only the statistical uncertainties are plotted. The extracted values are plotted on Fig. 4.11 in different p_{T} bins. The raw fraction has an overall rising trend. It goes between $\sim 9\%$ to $\sim 11\%$ between $2 < p_{\mathrm{T}} < 6\,\mathrm{GeV}/c$, and goes up to $\sim 30\%$ in the $10 < p_{\mathrm{T}} < 30\,\mathrm{GeV}/c$ bin.

However, this raw quantity needs to be corrected for the different acceptance$\times$efficiencies for prompt and non-prompt J/ψ, averaged in the p_{T} range where the measurement is performed. The fraction of non-prompt J/ψ corrected for these effects, $f_{\mathrm{B}}^{\mathrm{corr}}$, is obtained as:

$$f_{\mathrm{B}}^{\mathrm{corr}} = \left(1 + \frac{1 - f_{\mathrm{B}}}{f_{\mathrm{B}}} \times \frac{\langle A \times \varepsilon \rangle_{\mathrm{B}}}{\langle A \times \varepsilon \rangle_{\mathrm{prompt}}}\right)^{-1} \tag{4.7}$$

where $\langle A \times \varepsilon \rangle_{\mathrm{prompt}}$ and $\langle A \times \varepsilon \rangle_{\mathrm{B}}$ represent the average acceptance-times-efficiency values for prompt and non-prompt J/ψ, respectively, in the considered p_{T} interval. Indeed, in principle prompt and non-prompt J/ψ can have different acceptance times efficiency $(A \times \varepsilon)$ values. This can happen because the $A \times \varepsilon$ depends on the p_{T} of the J/ψ and prompt and non-prompt J/ψ have different p_{T} distributions within the considered p_{T} range. Indeed, the non-prompt J/ψ has a p_{T} spectrum which is harder than the one of prompt J/ψ.

A previous analysis in ALICE at midrapidity for prompt-to-non-prompt separation at $13\,\mathrm{TeV}$ [158] computed the ratio $\langle A \times \varepsilon \rangle_{\mathrm{B}} / \langle A \times \varepsilon \rangle_{\mathrm{prompt}}$, using realistic p_{T} shapes extracted from data or from FONLL calculations. This ratio was evaluated to range between 1 and 0.97 in the $1 < p_{\mathrm{T}} < 15\,\mathrm{GeV}/c$ range. It was found that such corrections are expected to affect the extracted raw fraction by a few percent only.

The extracted raw fraction shown in Fig. 4.11 can be compared to values obtained by the LHCb collaboration at forward rapidities [159], neglecting the Acceptance-Efficiency correction mentioned above. The values reported by LHCb are written in Tab. 4.2.

$p_{\mathrm{T}}[\mathrm{GeV}/c]$	$2.5 < y < 3$	$3 < y < 3.5$
$2 - 3$	12.6 ± 0.2	12.5 ± 0.2
$3 - 4$	14.2 ± 0.2	13.9 ± 0.2
$4 - 5$	17.0 ± 0.3	15.3 ± 0.3
$5 - 6$	18.2 ± 0.3	16.9 ± 0.3
$6 - 7$	21.1 ± 0.4	19.7 ± 0.5
$7 - 8$	23.0 ± 0.6	21.3 ± 0.6
$8 - 9$	25.6 ± 0.8	23.7 ± 0.8
$9 - 10$	26.3 ± 1.0	27.2 ± 1.1
$10 - 11$	31.5 ± 1.3	30.9 ± 1.4
$11 - 12$	33.3 ± 1.6	28.1 ± 1.8
$12 - 13$	36.5 ± 2.1	33.3 ± 2.2
$13 - 14$	37.3 ± 2.3	33.4 ± 2.8

Table 4.2: The fraction of non-prompt J/ψ (in %) in bins of transverse momentum and rapidity, measured by LHCb in $13\,\mathrm{TeV}$ pp collisions [159].

The values reported in Tab.4.2 are larger than the ones shown on Fig. 4.11 in the range $3 < p_{\mathrm{T}} < 6$, suggesting that the 2D-fit and especially the resolution extraction are not yet fully under control in this study. The values at larger dimuon transverse momentum, in particular in the $6 < p_{\mathrm{T}} < 10$ and $10 < p_{\mathrm{T}}$ bins, are in better agreement with the LHCb measurement, with values of $\sim 20\%$ and $\sim 30\%$ respectively.

These values are smaller than the one measured in [158] in ALICE at midrapidity. This reflects the observation that the fraction of non-prompt J/ψ decreases with increasing rapidity. This was observed e.g. in [160] and [159].

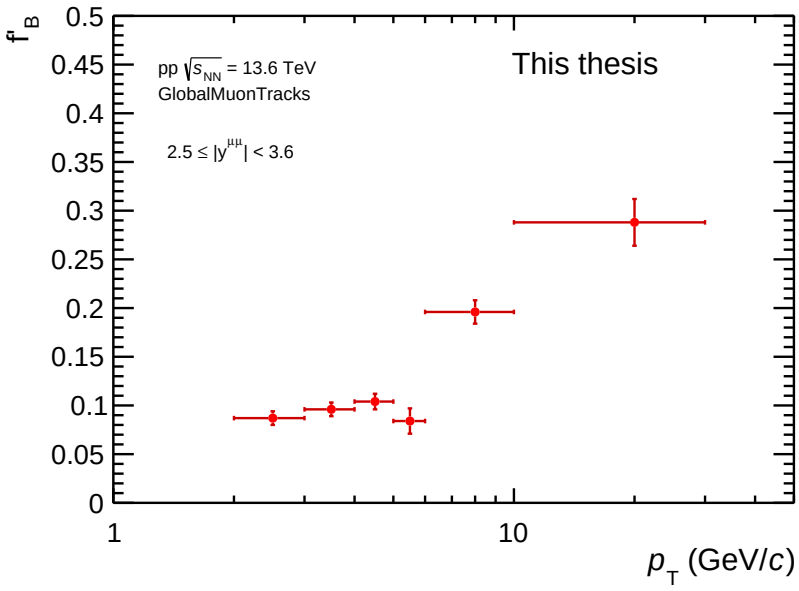

Figure 4.11: Raw fraction of the non-prompt J/ψ component to the inclusive yield, extracted from the bidimensional fit procedure outlined above. The displayed error bars corresponds only to the statistical uncertainty of the fit.

4.8 Towards full analysis

The preliminary results presented in Fig. 4.11 exclude the lowest transverse momentum bin $0 < p_{\mathrm{T}} < 2\,\mathrm{GeV}/c$. Indeed, in the fourth pass of the reconstruction of the 2022 data, used in this preliminary analysis, the $\ell_{J/\psi}$ resolution is strongly degraded compared to previous reconstruction passes. This extracted resolution is shown on Fig. 4.12. The core gaussian of the combined functional shapes, labelled Gaussian 1 on the figure, has a width of $\sigma \sim 110\,\mu\mathrm{m}$, and the Gaussian 2 has a width of $\sigma \sim 380\,\mu\mathrm{m}$. This resolution is too wide to proceed to a reliable statistical separation of the prompt and non-prompt contributions. The cause for this important degradation of the low-p_{T} resolution is still under investigation.

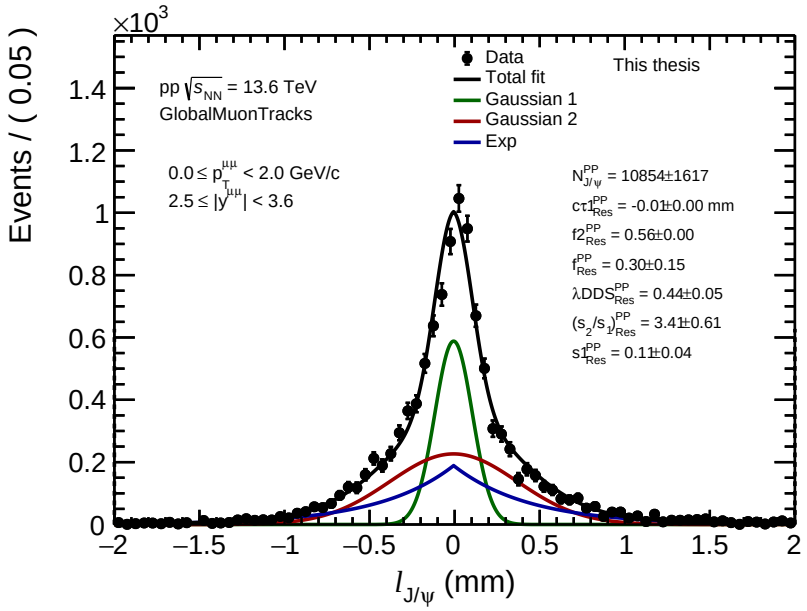

Figure 4.12: $\ell_{J/\psi}$ resolution fit in the dimuon transverse momentum range $0 < p_{\mathrm{T}} < 2\,\mathrm{GeV}/c$. The resolution is strongly degraded in this bin.

We now review the different steps which are necessary in order to pursue this preliminary study into a full analysis.

- First, only a single period of data taking was used in this study, representing about 64% of the luminosity available for the 2022 data-taking. A complete analysis would require the use all of the collected pp statistics.

- A more precise determination of the efficiency and purity for the matching $\chi^2_{\mathrm{MFT-Muon}}$ cut is required, instead of the fit method presented in previous sections. This would allow to determine the optimal selection value, and better control the efficiency and purity of the sample of J/ψ candidates which we collect. As explained in Sec.3.4, different methods, such as track rotation or wrong-sign matching, are currently in development to this end.

- More realistic simulations are needed to check the validity of the invariant mass signal functional shapes, and to check the resolution extracted from the left side of the $\ell_{J/\psi}$ distribution.

- A relative time alignment is still required between some detectors, in particular between the MFT and the central barrel detectors. Once such an alignment is achieved, a more precise study of the optimal parameters for the track-collision association shall follow.

- The estimated uncertainty on the $\ell_{J/\psi}$ variable was not taken into account in this preliminary study, as some issues with their computation still remain in the current status of the O^2 framework. A more thorough analysis should take them into account in the bidimensional fit.

The different sources of systematic uncertainty related to the bidimensional fitting procedure that should be taken into account in a full study are the following:

- Variation of the signal and background shapes. The NA60 function could be used for the signal shape, while the Variable Width Gaussian could be used for the background [148].
- Variation of the fitting range for the invariant mass.
- Use the $\ell_{J/\psi}$ resolution from prompt MC instead of data.
- Instead of relying on the *sPlot* method to extract the background distribution of $\ell_{J/\psi}$, an alternative is to use the side bands of the invariant mass distribution
- Similarly to analyses carried out by LHCb [159], an additional component taking into account residual wrong PV-SV association could be added to the $\ell_{J/\psi}$ distribution in the bidimensional fit.
- Instead of parametrizing the non-prompt component of the signal $\ell_{J/\psi}$ distribution with an exponential for which the parameter is initialized from a fit to the ideal MC simulation, which is then convolved with the extracted resolution, a template could be extracted from a realistic MC simulation.

4.9 Summary and Outlook

In the preliminary study presented in this chapter, we exploited proton-proton data recorded by ALICE during a single period in 2022, using the latest available version of the reconstruction, which was finalized in May 2022. The goal of this study is to assess to what extent a separation between the prompt J/ψ, originating from the primary vertex, and the non-prompt J/ψ produced at a displaced vertex, can be achieved using this data. To achieve this evaluation, two important aspects must be controlled: the association between the muon tracks and the primary vertices, and the reconstruction of the secondary vertices. Indeed, the separation between the prompt and non-prompt components of the inclusive J/ψ yield relies on the computation of the longitudinal pseudo-proper decay length, noted $\ell_{J/\psi}$, which is an estimate of the travelled length of the possible hadron before it decayed into a J/ψ state. The computation of this variable crucially depends on the distance between the primary vertex and the reconstructed secondary vertex. It is thus of prime importance to correctly compute the secondary vertex and to associate it with the right primary vertex.

I developed a tool to handle the track-vertex association, which allows to tune different parameters to decrease the number of ambiguous tracks reconstructed, i.e. tracks which are compatible in time with multiple primary vertices. The secondary vertexing software tool was already implemented. Using a statistical procedure known as a bidimensional fit, I extracted a raw fraction of non-prompt J/ψ in the inclusive yield in different bins of dimuon transverse momentum. This procedure exploits both the invariant mass, to separate the J/ψ signal from the background, and the $\ell_{J/\psi}$ distribution to separate the prompt and non-prompt components. Despite the missing acceptance and efficiency corrections, this preliminary result is compatible within statistical uncertainties with measurements at forward rapidity made by the LHCb collaboration at $13\,\mathrm{TeV}$ in the transverse momentum region above $6\,\mathrm{GeV}/c$. In the range $3 < p_\mathrm{T} < 6\,\mathrm{GeV}/c$, the extracted raw fraction is smaller than in the LHCb measurement, considering only the statistical uncertainties in the current study. In such analysis, a good resolution in the $\ell_{J/\psi}$ distribution is mandatory to achieve a precise separation. It was found that in the lowest p_T region, using the latest reconstruction of the data, the resolution does not permit to carry out the separation in this range, although it was significantly better in a previous version of the reconstruction. This issue is still under investigation. However, the good agreement found in the higher p_T bins leads us to believe that we are on the right track towards a measurement over the full momentum range. This status is already encouraging provided the several open points that need to be understood prior to a publication. In addition, it should be noted that for the upcoming Pb–Pb runs, the interaction will be much smaller ($50\,\mathrm{kHz}$ instead of the $500\,\mathrm{kHz}$ in proton-proton), which will limit the uncertainties of the track-vertex association. Besides understanding the reasons for the degradation of the resolution, other steps are required to achieve a full analysis result, such as using the full available statistics, optimizing the selection cuts used in the data selection, in particular to achieve better purity and efficiency of the MFT-Muon matching, exploiting more realistic simulations than the ones currently available, or performing a time alignment between the MFT and the Muon spectrometer. Finally, systematic uncertainties, in particular of the bidimensional fit procedure, should be estimated.

Chapter 5

Probing early times

This chapter is dedicated to a phenomenology study in which I participated during my PhD. It is the fruit of a collaboration with Sören Schlichting and Xiaojian Du from Bielefeld university, Jean-Yves Ollitrault from IPht and Michael Winn and myself from DPhN. The aim of this work was to estimate to what extent can the dilepton spectrum of heavy-ion collisions give information on the early stages of such collisions. During such stages, known as pre-equilibrium, the medium is brought close to thermal equilibrium, and at the end of these stages, the equations of hydrodynamics can be used to describe it. Hence, the description of these instants is essential to achieve an understanding of how a fluid-like QGP forms in heavy-ion collisions. In the following, I will often use the term "thermal dileptons" to refer to the spectrum of dileptons emission from the QGP, including the early-stages. In the first section (Sec.5.1), I will first give some features of the hydrodynamic description of the QGP, then give a brief description of the initial state of heavy-ion collisions (Sec.5.1.1), and some models of the early-time evolution of the medium (Sec.5.1.2, 5.1.3). The second section (Sec.5.2) motivates thermal dileptons as probes of heavy-ion collisions, and presents general considerations regarding the ideal spectrum of thermal dileptons and its kinematic scaling. Finally, the last section presents our calculations including the early stages of heavy-ion collisions (Sec.5.3).

5.1 Hydrodynamics and the equilibration puzzle

A major discovery of high energy heavy-ion collisions is that the experimental data is consistent with the formation of a hot QGP behaving as an almost perfect fluid. Indeed, in the 2000's, experiments at RHIC indicated that in head-on Au–Au collisions at $\sqrt{s_{NN}} = 200\,\mathrm{GeV}$, the spectra of produced particles were, to a important level of precision, compatible with the picture of an expanding fluid, described by the equations of hydrodynamics [161, 26, 27, 28, 29]. This was in particular established through the study of transverse momentum dependence of light hadron yields at low-p_{T}, and the study of their elliptic flow coefficient, v_2, defined in Sec.1.5. These results were further confirmed at higher energies in Pb–Pb collisions at the LHC [162].

The hydrodynamic description is based on the assumption of local thermodynamic equilibrium. In a quasi-particle picture, it requires that the mean free path between two collisions, λ_{mfp}, is much shorter than all characteristic scales of the system, which we

denote L. Thus: $\lambda_{\mathrm{mfp}} \ll L$ [163, 164]. Non-ideal hydrodynamic equations, such as the Navier-Stokes equations, include terms which are gradients of the velocity of the fluid. The (non-relativistic) momentum conservation equation of Navier-Stokes reads [165]:

$$\rho\partial_t\mathbf{v} + \rho\mathbf{v}\cdot\nabla\mathbf{v} = -\vec{\nabla}P + \eta\vec{\nabla}^2\cdot\mathbf{v} + \vec{\nabla}\left[\vec{\nabla}\cdot\mathbf{v}\left(\zeta + \frac{2}{3}\eta\right)\right]$$

where ρ is the mass density, $\mathbf{v}$ is the fluid velocity, and $\vec{\nabla}P$ is a pressure gradient. The two last terms, containing velocity gradients, are weighted by coefficients called viscosity coefficients. They characterize the viscous properties of the fluid and are related to the dissipation of energy due to the presence of velocity gradients in the fluid. These are of two types: bulk viscosity ζ and shear viscosity η. For QGP physics, the bulk viscosity is mainly important when the temperature is close to the pseudo-critical temperature T_{pc}, but is small at higher temperatures [166, 167, 168]. We will neglect its role in the following discussions. The shear viscosity η of a system measures its resistance to velocity gradients. More precisely, adjacent layers of the fluid move at different speeds, and a frictional drag force between these layers causes energy to be dissipated. This coefficient is also used to quantify the importance of viscous corrections, the velocity gradient terms, in the hydrodynamic equations. This is encapsulated in the Reynolds number, which is the ratio of the ideal kinetic term of the hydrodynamic equation, over the velocity gradient term. For Navier-Stokes, it is expressed as [165, 36]:

$$\mathrm{Re} = \frac{\rho\|\mathbf{v}\cdot\nabla\mathbf{v}\|}{\eta\|\vec{\nabla}^2\cdot\mathbf{v}\|} = \frac{Rv}{\eta/\rho}$$

where R is the characteristic spatial dimension of the system and v is the characteristic fluid velocity. When $\mathrm{Re} \gg 1$, the flow can be considered as having no viscosity, and the fluid is called "ideal" [36]. For an ultrarelativistic fluid, the mass density ρ must be replaced with $\epsilon + P$, the sum of energy density and pressure of the fluid. For very low baryon chemical potential (which is the case at LHC energies), then $\epsilon + P = sT$, where s is the entropy density of the system and T is its temperature. The Reynolds number is then expressed as: $\mathrm{Re} \sim Rv/(T\cdot\eta/s)$. We see that the relevant parameter to characterize the size of the viscous corrections in a fluid description is the shear viscosity-to-entropy density ratio, η/s.

Collisions at RHIC and LHC create a QGP that behaves as a nearly perfect fluid, meaning with a very low value of shear viscosity-to-entropy density ratio of $\eta/s \approx 1/4\pi$ [164]. This value is a theoretical lower bound inferred from gauge theories at infinite coupling [169, 170]. This "unreasonable" descriptive power of near-ideal hydrodynamics was long believed to be a further indication that the produced medium is quickly brought to thermal equilibrium. However, it was first found in calculations based on strong coupling and holographic computations of hydrodynamic evolution, that this assumption of thermalization, i.e. full local thermal equilibrium, could be too strong [171, 172, 173]. Hence, a crucial question in this view is the condition of emergence of such a locally equilibrated medium from the initial wave functions of the crossing nuclei in heavy-ion collisions. In other words, what are the mechanisms at early times that could lead to a thermalization of the matter produced in heavy-ion collisions. While the understanding of the late stages of heavy-ion collisions, i.e. after thermalization where the fluid description is relevant,

has developed significantly, progress in the theoretical descriptions of the early stages of heavy-ion collisions is relatively recent, and lacks experimental constraints. In the following sections, the different early stages of the system created in heavy-ion collisions are presented, including the initial state produced by the crossing of the two nuclei and the possible equilibration mechanisms.

5.1.1 The initial state

As detailed in the introductory chapter in Sec.1.4, when a proton or nucleus is boosted to high energies, because of time dilation, short-lived configurations containing large numbers of partons live much longer, and dominate the phase space. In particular, at fixed scale Q^2, the gluon parton distribution function grows very rapidly with increasing collision energy s (lower x), see Fig. 5.1. Hence, this many-body configuration of gluons will dominate the initial state of HIC, which will subsequently evolve. Based on unitarity imposed by quantum theory, Froissart has shown that the total cross section for the strong interactions grows at most as fast as $\ln^2(s)$, as $s \to \infty$ [174]. The rapid growth of gluon density at small x seen in data (Fig. 5.1, left), as well as prediction from the linear evolution equation of parton distributions at high energy (known as the BFKL equation, Fig. 5.1, right), suggest asymptotically a growth of the distributions which would exceed the Froissart unitarity [175]. Thus, one expects that this growth should somehow be tamed at asymptotically small x, for instance by mechanisms such as gluon recombination, which is an allowed process due to the non-abelian nature of QCD. This means that the gluon phase space density should reach a maximum, i.e. it should "saturate".

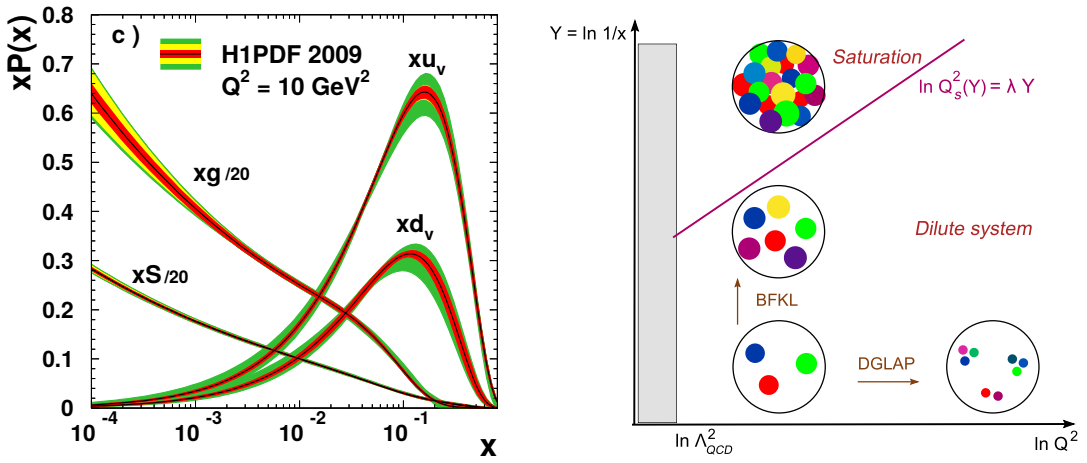

Figure 5.1: (Left) the x-evolution of the gluon, sea quark, and valence quark distributions for $Q^2 = 10\,\mathrm{GeV}^2$ measured at HERA [176]. (Right) QCD evolution of parton densities inside a nucleon according to the probes momentum scale Q^2 and longitudinal momentum fraction x [52]; each colored dot represents a parton with transverse area $1/Q^2$ and longitudinal momentum $k^+ = xP^+$.

This saturation is described by the effective field theory of CGC [52, 175, 177]. At collider energies, the boosted nuclei are ultra-relativistic, with $\gamma_{\mathrm{SPS}} \sim 10 < \gamma_{\mathrm{RHIC}} \sim 100 < \gamma_{\mathrm{LHC}} \sim 2500 - 7000$. The longitudinal size of the colliding nuclei in the centre-of-mass frame is

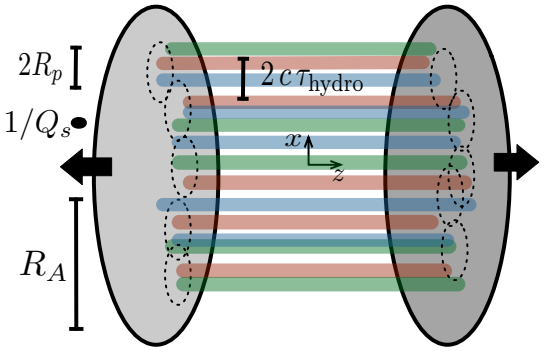

Figure 5.2: (Left) Illustration of the two nuclei as they are passing through each other. Classical longitudinal color fields, rapidly decohere on a scale $\sim Q_s$ [178].

then $L_z \sim 2R/\gamma \sim 10^{-3}\,\mathrm{fm}$. In the CGC theory, these highly contracted incoming nuclei contain a finite density of gluons per transverse area and per unit of rapidity. This density can be expressed as $(dN/dy)/\pi R_A^2$, and grows with collision energy until it reaches the maximal phase space density of order $1/\alpha_s$. This corresponds to the emergence of a saturation momentum scale, known as the saturation momentum Q_s, which is illustrated in the cartoon of Fig. 5.2, and is defined as:

$$Q_s^2 \sim \frac{\alpha_s}{\pi R_A^2}\frac{dN}{dy}$$

The saturation momentum Q_s sets the momentum scale for the transverse momentum of partons in the wave functions of the nucleon. In addition, at this saturation scale, the number of gluons per unit phase space in the initial wave function is large [178]:

$$f_g \sim \frac{1}{\pi Q_s^2 R_A^2}\frac{dN}{dy} \sim \frac{1}{\alpha_s} \gg 1,$$

In this high-occupancy regime, the system can be described classically, i.e. gluons can be modeled as classical chromo-electric and chromo-magnetic fields, similarly to the classical limit of Quantum Electrodynamics (QED), where photons can be described in terms of classical electromagnetic fields. One can then describe the evolution of these highly-packed gluon fields using the non-abelian equivalent of Maxwell's equations, which are known as the classical Yang Mills equations of motion.

A key question in the description of the first instants of the heavy-ion collisions is the strength of interactions between the highly-packed gluons; more precisely, whether the relevant QCD coupling α_s is small or large. In the first case, one can employ perturbative QCD at weak coupling $\alpha_s \to 0$ [32]. The other limit is that of very strong 't Hooft coupling of $\alpha_s N_c \to \infty$ [173]. Both approaches have been explored in the literature. In the following, we will focus on concepts of the weak coupling approach, which have recently seen considerable theoretical developments. According to the CGC picture outlined above, for $Q_s \gg \Lambda_{\rm QCD}$ the coupling constant is small $\alpha_s\,(Q_s) \ll 1$ and the weak-coupling approach should be valid, in the early stages of the system when this saturation momentum is the

relevant scale. However, in experiments, the saturation momentum is $Q_s \sim 1\ \mathrm{GeV}$ at RHIC and $2\ \mathrm{GeV}$ at the LHC [178]. These values are not much larger than Λ_{QCD}, thus the weak coupling approach is not automatically guaranteed, and there could be important corrections in the perturbative expansion.

During the subsequent evolution of the system, the gluon density progressively decreases. At large enough time scales, $\tau \gg 1/Q_s$, the phase space density of gluons is still large, but is now much smaller than $1/\alpha_s\left(Q_s\right)$. In this regime, one can properly interpret gluons as quasi-particles, define gluon phase space distribution, and use kinetic theory to compute the next steps of the evolution. This situation provides the initial conditions for the so-called "bottom-up" thermalization scenario [179], which is a picture of how an equilibrated medium can arise from a far-from-equilibrium initial state in the weak-coupling scenario. Although this picture, is strictly speaking, only valid for asymptotically small coupling, it can still provide valuable insights into the dynamics of the early stages of heavy-ion collision, as this scenario was also shown to be compatible with numerical computations. We will thus give some details of this approach in the following section.

5.1.2 A picture of the first fm/c of HICs

Regardless of the precise configuration of the initial state, insights from hydrodynamic and kinetic models show that the rapid longitudinal expansion of Bjorken flow, which we described in Sec.1.3, puts the system in a state of pressure anisotropy: $P_L \ll P_{\mathrm{T}}$ [180]. The reason for this is that, in the high-energy limit and at early times, the longitudinal expansion scales like $1/\tau$, while it takes a finite time (dependent on the underlying microscopic theory) for interactions between particles to build up significant longitudinal pressure. In other words, at early times, the competition between longitudinal expansion and collisions among constituents is in favor of the expansion, until enough particle interactions can counter it. Hence, in a local rest frame, longitudinal momenta are strongly red-shifted while transverse momenta are largely unaffected at early times. Local particle distributions are thus highly anisotropic in momentum space: particles have a large probability of having kinematics such that $p_{\mathrm{T}} >> p_z$. This anisotropy in momentum space produces the pressure anisotropy $(P_L < p_{\mathrm{T}})$ in hydrodynamic simulations of the early stages of HIC. The expected evolution of this pressure anisotropy is depicted on Fig. 5.3.

The initial phase-space distribution of the system thus has $p_{\mathrm{T}} \sim Q_s$ and $p_L << p_{\mathrm{T}}$. In addition, it is mostly populated by hard gluons (i.e. gluons with momentum $\sim Q_s$). This highly anisotropic initial state provides the starting point for the bottom-up scenario [179], which is a schematic modeling of how thermalization can occur starting from this initial state, in a weakly coupled approach.

During the first phase of bottom-up, the phase space distribution of partons becomes increasingly anisotropic. Indeed, as explained above, at this stage the longitudinal expansion dominates over the interactions among particles. The phase space density of hard gluons decreases as [178]

$$f_{\mathrm{hard}} \sim \frac{1}{\alpha_s} \frac{1}{\left(Q_s \tau\right)^{2/3}},$$

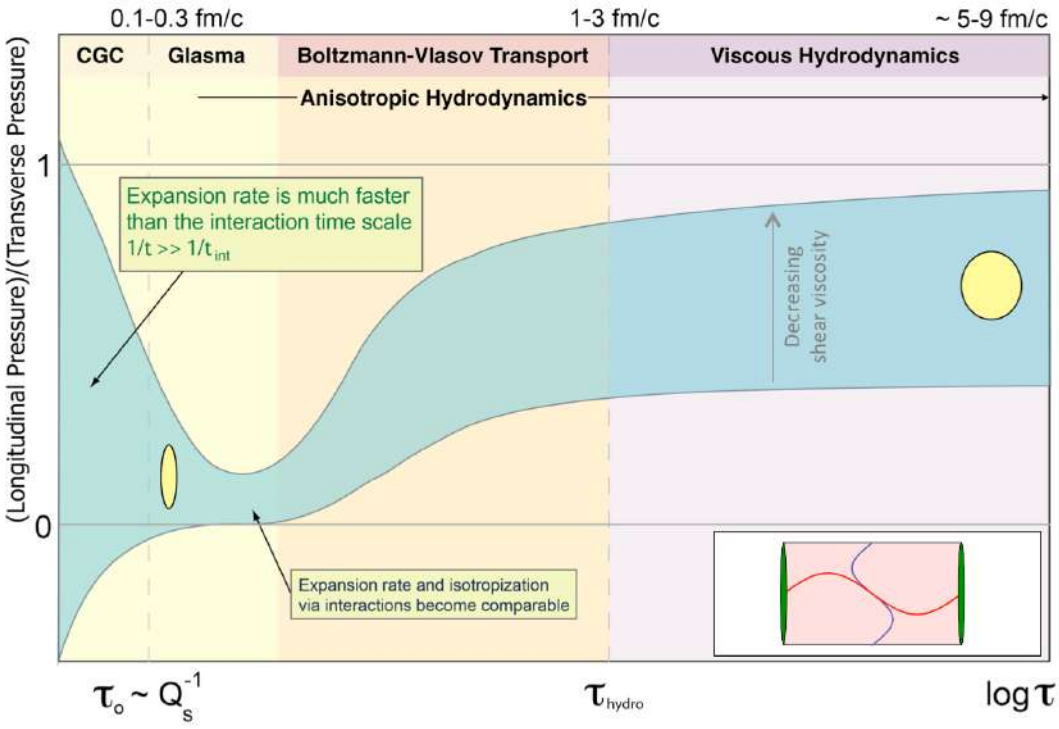

Figure 5.3: Cartoon depicting the temporal evolution of the momentum-space anisotropy evolution in a heavy ion collision at LHC energies. The inset yellow ellipses indicate the shape of the momentum-space distribution with the horizontal direction corresponding to the longitudinal direction [180].

We see that the phase space density becomes of order unity at a time of order $\tau \sim \alpha_s^{-3/2} Q_s^{-1}$, marking the end of this first stage, known as the "over-occupied" stage. It is illustrated on the far-left picture of Fig. 5.4. After this time, hard gluons with $p_{\rm T} \sim Q_s$ are no longer over-occupied, i.e. $f_{\rm hard} \lesssim 1$.

In the second stage of bottom-up, $Q_s\tau \gg \alpha_s^{-3/2}$, medium induced collinear radiation becomes important and increases the number of soft gluons. This is the middle picture of Fig. 5.4. This soft bath will eventually thermalize the hard modes. While this soft bath is being populated by collinear radiation, the phase space density of hard gluons decreases as

$$f_{\rm hard} \sim \frac{1}{\alpha_s^{3/2}} \frac{1}{(Q_s\tau)}$$

At the end of this second stage, $\tau \sim \alpha_s^{-5/2} Q_s^{-1}$, the phase space density of hard gluons scales like: $f_{\rm hard} \sim \alpha_s \ll 1$.

In the last stage of bottom-up, $Q_s\tau \gg \alpha_s^{-5/2}$, the soft bath has equilibrated, and there is a cascade of energy from the hard gluons at scale Q_s to the soft thermalized bath, see right picture of Fig. 5.4. In this final stage, the system reaches isotropy and thermal equilibrium, as the remaining energy from the hard gluons is transferred to the soft bath. Extrapolating this scenario to large coupling, i.e. large values of α_s, the initial occupancy

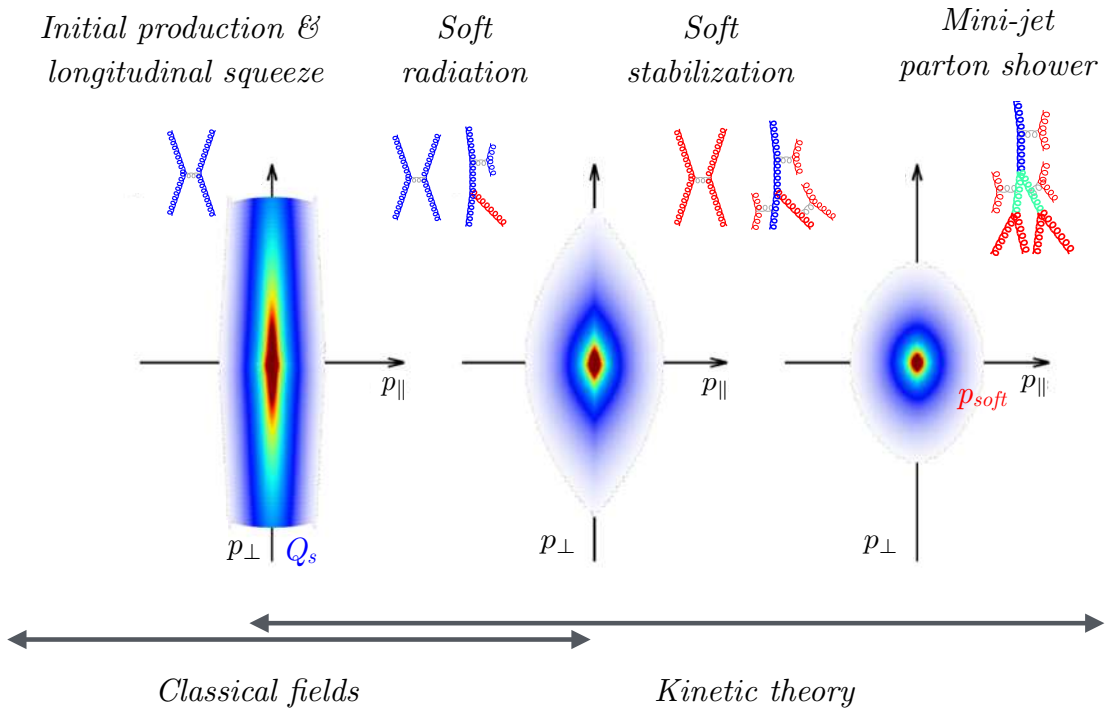

Figure 5.4: Schematic illustration of the bottom-up thermalization showing the evolution of the phase-space distribution of gluons in momentum space based [178].

$f_{\rm hard}$ is already below unity at the first stage, so that the system starts to isotropize almost immediately, and the different stages of the bottom-up scenario are no longer discernible. Hence, we see that this description is mostly relevant in the weak-coupling approach.

5.1.3 Early-time models

We now give a brief summary of different models and approaches which are either weakly or strongly coupled, and which have been employed to describe the early-time dynamics of heavy-ion collisions.

- Glasma [37, 38, 39, 181]: it is a non-equilibrium state of matter, formed at very early times in the collision. It is a state of highly occupied gluons, which strongly interact between themselves. It makes the transition from the Color Glass Condensate to the deposited medium, which will evolve towards a QGP state. Unlike the CGC, this state decays and eventually thermalizes. In this theory, the induced electric and magnetic charges generate flux tubes of chromo-electromagnetic fields that are uniform in rapidity, stretching between the receding nuclei, and which are color-screened on a transverse scale $\geq 1/Q_s$. These "color flux tubes" then decay into the partons which evolve during the rest of the history of the system. The Glasma equations require that, initially, the transverse and longitudinal pressure are respectively $p_{\rm T} = \varepsilon$ and $P_L = -\varepsilon$ where ε is the energy density. Thus, at the earliest times, the pressure in the Glasma is purely transverse, and remarkably the longitudinal pressure is even negative. After initial dynamics, the longitudinal pressure

approaches $\mathcal{P}_L \to 0$ from below. Hence, we see that this description is in line with the expected early-time pressure anisotropy outlined in Sec.5.1.2. This model describes how the bulk of particles is created after the crossing of the two nuclei and makes the link between the initial state provided by CGC and the first stage of the bottom-up scenario.

- QCD kinetics (or Effective Kinetic Theory, EKT) [182, 183, 184, 185]: it is a weakly coupled microscopic model, based on a kinetic equation. It is a leading-order calculation which includes both " $2 \leftrightarrow 2$ elastic processes as well as effective "$1 \leftrightarrow 2$ " collinear inelastic processes. Like any kinetic theory, it is based on a quasi-particle picture, meaning that the considered objects (in our case quarks and gluons) can be viewed as distinguishable point-like entities. This allows to describe their evolution in phase space using distribution functions. The time evolution of these phase space density functions can then be described by the Boltzmann equation for QCD light particles:

$$\left[\partial\tau - \frac{p_z}{\tau}\partial p_z\right] f_a\left(\tau, p_{\mathrm{T}}, p_z\right) = -\, C_a^{2-2}[f]\left(\tau, p_{\mathrm{T}}, p_z\right) - C_a^{1-2}[f]\left(\tau, p_{\mathrm{T}}, p_z\right) \tag{5.1}$$

  where $f = f(p,t)$ represents the phase space density of quasi-particles at time t, and the right-hand term is a spatially-local collision term. It represents the rate at which particles get scattered out of the momentum state p, minus the rate at which they get scattered into this state. The main difficulty is to include all the relevant processes in the collision kernel, so that the Boltzmann equation correctly reflects the desired physics. For QCD kinetics, the so-called AMY framework is exploited [186]. In this approach, the collision kernel is decomposed into two terms : $C_a^{2-2}[f](\vec{p},t)$ is the $2 \leftrightarrow 2$ elastic collision term and $C_a^{1-2}[f](\vec{p},t)$ is the $1 \leftrightarrow 2$ inelastic collision term. All leading order elastic scattering processes between quarks and gluons are taken into account in $\left(C^{2-2}\right)$, and are impacted by in-medium screening of elastic interactions. The inelastic interactions in $\left(C^{1-2}\right)$ are affected by the Landau-Pomeranchuk-Migdal suppression of inelastic rates. The main assumption is that the theory is weakly coupled on the scale of the temperature, $\alpha_s(T) \ll 1$. In addition, it is assumed that all zero-temperature mass scales are negligible and that the phase-space distribution functions have smooth dependencies on momentum. Finally, this effective model is valid on time scales which are large compared to the duration of the scattering processes, which are approximated as instantaneous inside the collision kernel, such that a quasi-particle picture of particles is valid. Hence, it can be viewed as a modeling of the stages succeeding to the Glasma stage, which we call pre-equilibrium.

- Boltzmann Relaxation Time Approximation (RTA) [187, 188, 189]: this approach is similar to QCD kinetics. It is a weakly coupled theory which relies on a microscopic kinetic model, exploiting a Boltzmann balance equation. However, the collision kernel is simplified according to the relaxation time approximation. The equation then takes the form:

$$\left[\partial_\tau - \frac{p_z}{\tau}\partial_{p_z}\right] f(\tau, p_{\mathrm{T}}, p_z) = -\frac{f(\tau, p_{\mathrm{T}}, p_z) - f_{\mathrm{eq}}(p/T)}{\tau_R} \tag{5.2}$$

  $f_{\mathrm{eq}}(p/T)$ depends only on $p = \sqrt{p_{\mathrm{T}}^2 + p_z^2}$ and on an effective temperature $T(\tau)$. This equation makes transparent the competition between the expansion of the

system, which is dictated by the external conditions of the collisions, and the collisions among the plasma constituents, which tend to isotropize the momentum distribution functions. In the absence of the collision term, i.e. for very long relaxation time, the expansion, controlled by the term $-p_z/\tau$ on the left-hand side, leads to a flattened distribution. This is known as "free-streaming". On the other hand, the collision term on the right hand-side drives the distribution towards isotropy, at a rate controlled by the relaxation time τ_R. This approximation is obviously flawed because, in this picture, all quantities, including invariants of motion, relax to their equilibrium values on the scale of τ_R. It also supposes that all the information about the initial far-from-equilibrium state is completely lost due to the scattering processes.

- AdS/CFT [173, 190]: it is a conjecture that relates two different theories: gravity in an Anti-de Sitter space (AdS), and conformal field theory (CFT), which is a category of quantum field theories which are invariant under conformal transformation (a generalization of scale invariance). The AdS/CFT correspondence, also known as the holographic principle, suggests that a strongly interacting conformal field theory in four dimensions can be mapped onto a weakly interacting theory of gravity in higher dimensions in Anti-de Sitter space. In the context of heavy-ion physics, the AdS/CFT correspondence has been used to gain insights into the properties of the QGP, such as its viscosity and energy density, by studying the properties of a weak gravity of superstrings in a 5-dimensional AdS space, which in this correspondence is a dual theory to strongly coupled $\mathrm{N} = 4$ Super Yang-Mills theory. This theory is in some ways similar to QCD (deconfined phase, strongly coupled), but is conformal, which means that there is no running of the coupling and thus, even at very high energy densities, the coupling remains strong.

5.1.4 Different models, a universal attractor

A remarkable feature of the kinetic descriptions of the pre-equilibrium stage of HIC, such as the one mentioned in section 5.1.3, is that with different initial conditions, solutions of the kinetic equations merge as the system approaches isotropy, and converge to the results of viscous hydrodynamics [164, 171, 191]. Indeed, in viscous fluid dynamics, one considers the macroscopic evolution of the energy-momentum tensor $T^{\mu\nu}_{\mathrm{hydro}}(\epsilon, u^\mu, \ldots)$, where ϵ is the energy density and u^μ the local fluid velocity. When the system can be described in terms of quasi-particles, typically for times $\tau \gg 1/Q_s$, the pre-equilibrium evolution of this tensor $T^{\mu\nu}$ can also be calculated from an effective kinetic theory setup, and then matched to a hydrodynamic evolution. Then, the only surviving information used in the fluid evolution are the energy density ϵ and fluid velocity u^μ. All other information about the initial conditions is lost. This is, for instance, a clear property of the Boltzmann RTA outlined in Sec.5.1.3, where there is a loss of information due to the scattering processes.

An even more remarkable feature, is that, for non-vanishing coupling strength ($\alpha_s \geq 0.1$), kinetic simulations indicate that the evolution of the energy-momentum tensor during pre-equilibrium is to a good approximation controlled by a single time scale τ_R, cor-

responding to the equilibrium relaxation rate [191]:

$$\tau_R(\tau) = \frac{4\pi\eta/s}{T_{\rm eff}(\tau)},$$

where η/s is the "shear viscosity-to-entropy density ratio". However, here this parameter is an early-time variable; it is the viscosity used to quantify the deviation from equilibrium. As such, η/s should be viewed in this context as a parameter controlling the relaxation time τ_R, and thus the time scale of applicability of viscous hydrodynamics. In addition, η/s is linked to the strength of the interactions among particles: the stronger these interactions are, the quicker the system will equilibrate.

The fact that the evolution is only controlled by τ_R means that kinetic equilibration becomes approximately independent of η/s once the evolution is plotted as a function of the variable

$$\tilde{w} = \frac{\tau}{\tau_R} = \frac{\tau T_{\rm eff}}{4\pi\eta/s}, \tag{5.3}$$

where the effective temperature off-equilibrium $T_{\rm eff}$ is defined as the fourth root of the energy density $T_{\rm eff} = \left(e/\left(\nu_{\rm eff}\pi^2/30\right)\right)^{1/4}$ (for an ideal gas of quarks and gluons, $\nu_{\rm eff} = 47.5$ and $\nu_{\rm eff} = 16$ for gluons only [36]).

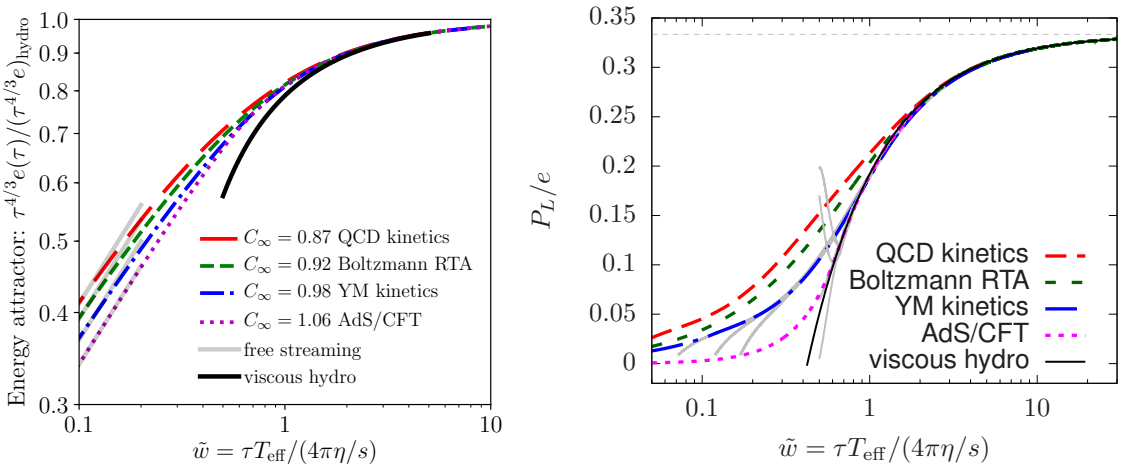

Figure 5.5: Hydrodynamic attractors for pre-equilibrium evolution of the energy density obtained from QCD and Yang Mills kinetic theory, AdS/CFT and Boltzmann RTA, as a function of the scaling variable $\tilde{w}$. (Left) Attractor for energy density, (right) attractor for longitudinal pressure over energy density [191].

This scaling feature is shown on Fig. 5.5, where the evolution of macroscopic variables is plotted for different microscopic descriptions of the pre-equilibrium evolution. Although none of them are expected to be exact models of QCD, in the re-scaled time units $\tilde{w}$, the final stages of QCD equilibration could follow a very similar evolution which eventually matches with the viscous hydrodynamic description. This is known as a "hydrodynamic attractor curve" [191].

This attractor evolution can be plotted for different thermodynamic variables such as energy density or longitudinal pressure over energy density (respectively left and right

Fig. 5.5). We see that these attractors match the asymptotic behavior of viscous hydrodynamics at a time scale $\tau_{\rm hydro} \approx \tau_R(\tau)$, i.e. $\tilde{w} \sim 1$.

It has become common to distinguish the time when hydrodynamics becomes applicable $\tau_{\rm hydro}$ (the so called "hydrodynamization" time) from the time $\tau_{\rm eq}$ when the pressure anisotropy is small and the system can be qualified as near local thermal equilibrium. Due to the rapid longitudinal expansion, the approach towards pressure isotropy $P_L/e \sim 1/3$ occurs only on larger time scales $\tau_{\rm eq} \gg \tau_{\rm hydro}$, see right of Fig. 5.5. Hence, the great success of hydrodynamic descriptions of heavy-ion collisions does not appear to derive from the fact that the system is particularly close to equilibrium throughout most of its space-time evolution, but rather that the range of applicability of hydrodynamics is larger than originally anticipated [192].

Due to this hydrodynamic attractor, the only feature that survives the loss of information is what is imprinted as initial conditions for the later hydrodynamic evolution. One exception are electromagnetic probes. They are sensitive to the full history of the space-time evolution of QCD matter. As such, photons and dileptons are unique tools to access the early stages of heavy-ion collisions. In the following sections we will show to what extent dileptons can be used to investigate these first instants.

5.2 Dilepton production in heavy-ion collisions

Electromagnetic probes are particularly useful to study the hot medium, as they are not subjected to the strong interaction, and thus have very few interactions with quarks and gluons after their creation. This means that the detected spectra of electromagnetic radiation give a good approximation of their production spectra. At Leading Order (LO), they are produced through a process $q\bar{q} \longrightarrow l^- l^+$, when a quark q and an anti-quark $\bar{q}$ annihilate to create a virtual photon, which then decays into a lepton-anti-lepton pair ($l^- l^+$), as illustrated on Fig. 5.6. Compared to photons, dileptons are not massless and thus carry an important extra information which is invariant mass. This is convenient as it is not subjected to blue-shift, caused by the expansion of the medium. One can justify the claim that the interaction of dileptons with the medium is negligible by giving an order of magnitude for the mean free path of a dilepton in a thermal bath of quarks. We estimate the interaction cross section by considering the scattering of an electron off a quark: $\sigma \sim \pi \left(\frac{2q_f \alpha_{\rm EM}}{p}\right)^2 \frac{1}{\theta_{\rm min}^2}$, where q_f is the quark charge which we will take equal to 1/3, $\alpha_{\rm EM} \sim \frac{1}{137}$ is the fine structure constant, and $\theta_{\rm min}$ is the a minimal cut-off angle for the scattering [84]. It can be approximated as $\theta_{\rm min} \sim \frac{m_D}{p}$, where $m_D \sim gT$ is the Debye mass [186]. Then $\sigma \sim \pi \left(\frac{2q_f \alpha_{\rm EM}}{m_D}\right)^2$. For illustration, we take $m_D^2 \sim 0.3\,{\rm GeV}^2$: $\sigma \sim 3{\cdot}10^{-4}\,{\rm GeV}^{-2}$. In addition, the thermal density of quarks in an equilibrated medium is $n \sim \frac{g}{\pi^2} T^3$ where g is the number of degrees of freedom, which for a gas of quarks is $g \sim 24$. We evaluate this density for $T \sim 300\,{\rm MeV}$. Then $n \sim 7 \cdot 10^{-2}\,{\rm GeV}^3$. The mean free path is then evaluated as $\lambda \sim \frac{1}{n\sigma} \sim 12,000\,{\rm fm}$. The typical size of the expanding medium in heavy-ion collisions is $L \sim 10\,{\rm fm}$. Hence $\lambda \gg L$, and the probability of interaction of an electron, and thus of a dilepton, with the thermal medium is of order $1 - \exp(-L/\lambda) \sim 0.08\%$.

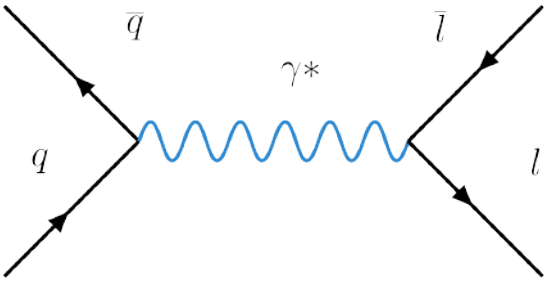

Figure 5.6: Feynman diagram for Leading Order (LO) dilepton production, from $q\overline{q}$ annihilation.

The radiation spectrum of dilepton from a fully equilibrated QCD medium can be calculated with the following formula [193, 194, 195]:

$$\frac{dN_{l+l-}}{d^4xd^4K} = -\frac{\alpha_{EM}^2}{\pi^3 M^2} f_B(k_0, T) \left(\sum_f q_f^2 \right) \frac{1}{3} L(M) \operatorname{Im} \Pi_{EM}{}^{\mu}{}_{\mu}(K, T) \tag{5.4}$$

Here, α_{EM} is the fine structure constant, $\sum_f q_f^2$ is the sum of the squares of the active quark charges (which we will always consider to be u, d and s in the following), $f_B(E,T) = \frac{1}{e^{E/T}-1}$ is the Bose-Einstein distribution. We note x the 4-position of the medium element which emitted the dilepton, K the 4-momentum of the dilepton, E its total energy, $M = K^2$ its invariant mass and T the temperature of the medium.

$L(M)$ is the final-state lepton phase space factor, which is independent of the modeling of the QCD medium, and written:

$$L(M) = \left(1 + \frac{2m^2}{M^2}\right) \left(1 - \frac{4m^2}{M^2}\right)^{1/2} \tag{5.5}$$

where m is the lepton mass, i.e. $m = 511\,\mathrm{keV}$ for electrons and $m = 106\,\mathrm{MeV}$ for muons. We will be mostly interested in the production of dileptons with invariant mass $M > 1\,\mathrm{GeV}$. Hence, $L(M) \sim 1$ to a good approximation.

Finally, $\Pi_{EM}^{\mu\nu}(K,T)$ is the virtual photon self-energy also known as the electromagnetic current-current correlator. It is defined as:

$$\Pi_{EM}^{\mu\nu}(K,T) = \int d^4x e^{iK\cdot x} \Theta(x_0) \langle [j_{EM}^{\mu}(x), j_{EM}^{\nu}(0)] \rangle_T \tag{5.6}$$

where j_{EM}^{μ} is the electromagnetic current of the quark-anti-quark pair which annihilates into a virtual photon, and $\langle ... \rangle_T$ is the finite temperature ensemble average. This current-current correlator encodes the thermal behavior of the quarks represented by the current j_{EM}^{μ}. One can get an intuition for the presence of this term in the rate equation by viewing dilepton production as the linear response of a thermal ensemble of quarks to a small perturbation of its current. The energy dissipation of the system is then given by the imaginary part of the response function (fluctuation-dissipation theorem). In our case, this dissipation takes the form of electromagnetic radiation, and the response function for the current perturbation is the current-current correlator $\Pi_{EM}^{\mu\nu}$.

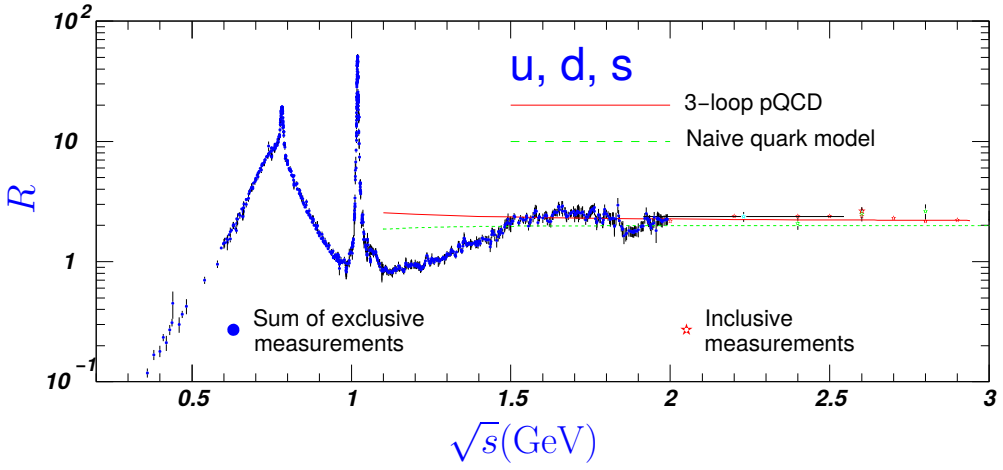

Figure 5.7: Compilation of experimental data for the ratio, R, of cross sections for $e^+e^- \to$ hadrons over $e^+e^- \to \mu^+\mu^-$, as a function of invariant mass $\sqrt{s} = M$ [196].

In the vacuum, the current-current correlator is well known from the e^+e^- annihilation cross section into hadrons, relative to the annihilation into dimuons. Indeed, the ratio between these two cross sections gives [197]:

$$R = \frac{\sigma(e^+e^- \longrightarrow hadrons)}{\sigma(e^+e^- \longrightarrow \mu^+\mu^-)} \propto \frac{\Pi_{EM}^{vac}}{M^2} \tag{5.7}$$

From the plotted invariant mass spectrum on Fig. 5.7, we see that this r atio is constant in the region where $M \geq 1.5\,\mathrm{GeV}$. This is called the Intermediate Mass Region (IMR), whereas the region $M \leq 1.5\,\mathrm{GeV}$ is the Low Mass Region (LMR). The constant behavior in the IMR is interpreted as the signature that the system cannot be described by hadronic degrees of freedom but by partonic ones. Hence, we expect this mass range to be the relevant one to probe radiation from a deconfined medium. In addition, in this region the relations $T \ll M$ and $\alpha_s(M) \ll 1$ are satisfied to a good approximation. This allows to compute the in-medium current-current correlator perturbatively, with corrections in powers of T/M and α_s [197, 198]. At leading order in T/M, it is independent of T, and $\Pi_{EM}^{vac} \sim M^2$, just like in the vacuum case. Then Eq.5.4 shows that the differential production rate of thermal dileptons is simply proportional to the Bose-Einstein distribution.

In the LMR, one can distinguish the spectra associated with meson resonances, to be more precise the ones of the light vector mesons: the ρ, the ω and the ϕ. We have:

$$\mathrm{Im}\,\Pi_{EM} \approx \sum_{V=\rho,\omega,\phi} \frac{m_V^4}{g_V^2}\,\mathrm{Im}\,D_V \tag{5.8}$$

where D_V is the propagator of the meson. So the production is governed by non-perturbative hadronic degrees of freedom (this is called the Vector Dominance Model, or VDM) [197, 199].

5.2.1 Ideal thermal dilepton rate

We start this section by justifying the form of the ideal production rate given in Eq.5.4. The general expression for dilepton production, without the equilibrium requirement, can be written [85]:

$$\frac{dN^{l^+l^-}}{d^4xd^4K} = -\frac{\alpha_{EM}^2}{6\pi^3M^2}L(M)\sum_f q_f^2\Pi_\mu^{\mu,<}(K) \tag{5.9}$$

where $\Pi^{\mu\nu,<}$ is now the Wightman function of the virtual photon:

$$\Pi^{\mu\nu,<}(K) = \int \mathrm{d}^4x \mathrm{e}^{iK\cdot x}\left\langle j_{EM}^\mu(0)j_{EM}^\nu(x)\right\rangle \tag{5.10}$$

The Wightman function measures correlation, whereas the retarded current-current correlator measures causation. In Appendix.A, we derive a general expression at LO for the Wightman function (Eq.5.10), which is used dilepton production rate Eq.5.9, and is valid out of equilibrium:

$$\begin{aligned}\Pi_\mu^{\mu<}(K) = -\frac{N_cK^2}{4\pi^2k}\int \mathrm{d}^3p\frac{1}{p^2}\delta\left(\cos\theta_{pk} - \frac{\left(k^0\right)^2 - 2pk^0 - k^2}{2pk}\right) \\ \times f_q(\mathbf{p}+\mathbf{k})f_{\bar{q}}(-\mathbf{p})\theta\left(k^- < p < k^+\right)\end{aligned} \tag{5.11}$$

where K is the four-momentum of the dilepton, with norm momentum magnitude k and energy k^0 and $\mathbf{p}$ is the momentum of the incoming quark, with norm p, $\cos\theta_{pk}$ is the cosine of the angle between the dilepton momentum and the quark momentum. Finally, f_q and $f_{\bar{q}}$ are the quark and anti-quark distribution functions.

In local thermal equilibrium, the phase-space distributions of quarks and anti-quarks in the medium are isotropic, independent of the direction of partons momenta. Hence, the angular delta function drops out. Then we use the Fermi-Dirac distributions for the quark and antiquark distributions f_q,$f_{\bar{q}}$ and integrate over the momentum p. The result yields:

$$\Pi_\mu^{\mu<}(K)\big|_{eq} = -\frac{N_cK^2}{2\pi}\frac{F(k)}{\exp\left(k^0/T\right)-1} \tag{5.12}$$

And for the production rate:

$$\frac{dN^{l^+l^-}}{d^4xd^4K} = \frac{N_c\alpha_{EM}^2}{12\pi^4}\sum_f q_f^2\frac{F(k)}{\exp\left(k^0/T\right)-1}, \tag{5.13}$$

where

$$F(k) \equiv \frac{2T}{k}\ln\left(\frac{\cosh\left(\frac{k^0+k}{4T}\right)}{\cosh\left(\frac{k^0-k}{4T}\right)}\right) \tag{5.14}$$

In the non-relativistic limit, $k_0 >> T$ and $k_0 >> k$, this factor $F(k)$ is equal to unity, so that the production rate per unit of 4-volume is directly proportional to the Bose-Einstein distribution for the virtual photon, as was shown from Eq.5.4.

This property is not obvious, as we do not expect EM radiation to equilibrate with the strongly interacting medium, given the argument exposed at the beginning of this section. Thus, there is no a priori reason for the rate to follow an equilibrium statistical distribution. Some intuitive explanations are given in Appendix.B.

Equation 5.13 gives a number of dileptons per 4-momentum per unit 4-volume. In a fluid-like picture, it represents how many dileptons of a given 4-momentum will be produced by a single fluid cell of size d^4x. The dilepton spectrum is obtained by integrating this production rate over the space-time evolution of the medium, i.e. we must integrate over all fluid cells of the system. To carry out this integration we make some simplifying assumptions:

- First, as we saw previously, we consider only the Leading-Order contribution to dilepton production, which is simply given by the process $q\bar{q} \longrightarrow l^- l^+$.
- Next, we assume transverse homogeneity. This means that the energy profile in the transverse plane is uniform and that the integration over position in this transverse plane will simply give a constant factor equal to the transverse area of the system: $\int d^2\mathbf{x}_\perp = A_\perp$. As we will see in Sec.5.3.2, this assumption is not necessary but will simplify the expressions.
- Most importantly, we assume Bjorken flow, which we defined in Sec.1.3. It stipulates that the expansion of the system is purely longitudinal, i.e. neglecting any transverse flow, which is a valid approximation at early times. Finally, this assumption also requires that the longitudinal expansion is boost invariant. This means that the velocity of a fluid cell remains unchanged under longitudinal boost.

Under these assumptions, it is natural to trade the time t and longitudinal z coordinates for proper time $\tau \equiv \sqrt{t^2 - z^2}$ and fluid cell rapidity $y_f = \operatorname{artanh}(z/t)$. The space-time volume can be rewritten as $d^4x = d^2\mathbf{x}_\perp \tau d\tau dy_f$, where $\mathbf{x}_\perp$ is the transverse position. In addition, we will note y the rapidity of the dilepton. With these coordinates, the dilepton energy in the fluid cell rest frame is $M_t \cosh(y - y_f)$, where $M_t = \sqrt{k_t^2 + m^2}$ is the transverse mass of the dilepton. The spectrum is then:

$$\frac{dN^{l^+l^-}}{d^4K} = C \int d\mathbf{x}_\perp \int_0^\infty \tau d\tau \int_{-\infty}^{+\infty} dy_f \exp\left(-\frac{M_t \cosh(y - y_f)}{T(\tau)}\right) \tag{5.15}$$

We see that this expression is independent of the dilepton rapidity y: if we boost the system and want to calculate the rate for dileptons of rapidity $y + \delta y$ instead of y, then we can change the integration variable from y_f to $y_f - \delta y$ and get back the same expression. This can be understood as follows: for a given value of the rapidity y of the dilepton, a range of fluid rapidities y_f contributes to the production. Since boost invariance is assumed, if we change the probed dilepton rapidity, the range of contributing fluid rapidities exactly compensates for the change in the production rate.

In addition, we see that Eq.5.15 depends on k_t and M only via the transverse mass. This is a property known as transverse mass scaling. It is independent of the detailed dynamics, and is quite general. It was also seen to approximately hold for hadron spectra, but broken by transverse flow [36]. For dileptons, one expects this scaling to be broken by transverse flow and by next-to-leading order perturbative corrections.

Let us now explicitly carry out the integral in Eq.5.15. We assume that the medium evolution can be described by ideal hydrodynamics. In this case, the system is isotropic ($P_L = p_\mathrm{T}$). To further simplify the calculations, we assume that the system has a conformal equation of state, i.e. the stress-energy tensor is traceless. This implies the following relation between pressure P and energy density: $P = e/3$. The evolution of the energy density in a Bjorken expansion is given by [35, 36]:

$$\partial_\tau e + \frac{e+P}{\tau} = 0 \tag{5.16}$$

which, with the requirement of conformality, becomes:

$$\partial_\tau e = -\frac{4}{3}\frac{e}{\tau} \tag{5.17}$$

By definition, temperature is related to energy density by: $e \propto T^4$. From this, we deduce a simple time scaling of the temperature : $T \propto \tau^{-1/3}$. This gives us the time-dependence of the temperature $T(\tau)$, which we need to carry out the time integration in our production rate. We then obtain:

$$\left(\frac{dN^{l^+l^-}}{d^4K}\right)_{\text{ideal}} = \frac{32N_c\alpha^2\sum_f q_f^2}{\pi^4}\frac{A_\perp\left(\tau T^3\right)^2}{M_t^6} \tag{5.18}$$

which is the M_t^{-6} spectrum obtained by McLerran and Tomeila in their 1986 paper on dilepton production in HIC [193], in the case of ideal hydrodynamics. In this formula, $\tau T^3 = \mathrm{const}$, and we see that the only kinematic is a power law of M_t.

Various publications [195, 200, 201, 202] suggest that measuring the inverse slope of the M_t of dileptons spectrum gives access to the temperature of the medium, in the case of an equilibrated system. From Eq.5.18, the inverse slope is:

$$T_{\text{slope}}\left(M_t\right) \equiv -\left[\frac{d}{dM_t}\ln\left(\frac{dN^{l^+l^-}}{d^4K}\right)\right]^{-1} = \frac{M_t}{6} \tag{5.19}$$

which is independent of the temperature. This is in a way natural, as we integrate from $\tau = 0$ to ∞ (i.e. to the end of the QGP lifetime)[1]. In this calculation, the temperature is asymptotically high at $\tau = 0$ (which is regulated by the rapid exponential fall-off of the rate at high temperature) and decreases with time. Hence, in each transverse mass bin, a large range of temperatures contribute to the spectrum, and the inverse slope only depends on the dilepton kinematics. This is in contrast to other approaches (e.g. in [195]) where the rate is only calculated starting from a time τ_0 where the system is assumed to be in equilibrium, at a temperature T_0. This restores sensitivity to the temperature of the system. This makes sense, as the ideal rate formula is only valid when the system is in equilibrium. However, it assumes that no dileptons are produced before the system is fully equilibrated, and misses the early stages of the collision where the pre-equilibrium dynamic lies. We now tackle this question of early-time contributions in the following section.

[1] In practice, we numerically integrate up-to $\tau = 15\,\mathrm{fm}/c$. Indeed, in the intermediate mass region, the contribution of times latter than $15\,\mathrm{fm}/c$ is negligible in the final dilepton spectrum, as the temperature becomes too small to emit significant radiation at mass $M > 1.5\,\mathrm{GeV}/c$. Hence, we can make the approximation that integrating up-to $\tau \sim 15\,\mathrm{fm}/c$ is equivalent as integrating up-to $\tau \to \infty$.

5.3 Pre-equilibrium dileptons

In this section, we will review a calculation for the contribution to the dilepton spectrum of the early times of heavy-ion collisions, the so-called "pre-equilibrium" stage. This work was conducted in collaboration with Sören Schlichting and Xiaojian Du from Bielefeld university, Jean-Yves Ollitrault from IPht and Michael Winn from DPhN [203, 204]. As previously mentioned, electromagnetic radiation is an ideal probe of the early stages of HIC, as such radiation weakly couples to the strongly interacting medium. The main focus of this study was to investigate how sensitive early dilepton production can be to chemical compositions and equilibration time of the medium in the early stages. It was based on simulations carried out in the QCD kinetic theory framework [182, 185, 205, 206]. My main contributions to this work were on the development of the code, the production of plots and results, and on analytical calculations for the dilepton rate and for the polarization observable which will be presented in Sec.5.3.6.

Dileptons carry an important piece of information which is invariant mass, i.e. the virtuality of the virtual photon which decays into a dilepton. This kinematic quantity is important as it is a Lorentz scalar and is not affected by the expansion of the medium, contrary to the momentum spectrum. Hence, invariant mass spectra are one the main points of our investigations. In addition, we are interested in early-time emission. In HIC, early times corresponds to high production temperature. One can get an intuitive idea of what should be the relevant invariant mass range for early production by first looking at the equilibrium rate. As we saw in Eq.5.13, it is proportional to the Bose-Einstein distribution. It can be approximated by a Boltzmann distribution for virtual photons with high energy $k_0 \gg T$:

$$f_B\left(k_0, T\right) \simeq \exp\left(-\frac{k^0}{T}\right) \tag{5.20}$$

For $M \gg T$, one can also proceed to a non-relativistic expansion:

$$k_0 = \sqrt{M^2 + \vec{k}^2} \simeq M + \frac{\vec{k}^2}{2M} \tag{5.21}$$

With this approximation, one can also approximate $dk_0 = dM$ for fixed $\vec{k}$. Putting these results together, one obtains

$$\frac{dN}{d^4x dM d^3\vec{k}} \propto \exp\left(-\frac{M}{T}\right) \exp\left(-\frac{\vec{k}^2}{2MT}\right) \tag{5.22}$$

up to some dimensionless constant proportional to α_{EM}^2. This can be integrated over $\vec{k}$ and give:

$$\frac{dN}{d^4x dM} \propto (MT)^{3/2} \exp\left(-\frac{M}{T}\right) \tag{5.23}$$

Thus, we see that the production of dileptons at high temperature is exponentially suppressed. As we are interested in early-time, one must look at the highest possible invariant masses to access these high-temperature dileptons, which is intuitive.

Furthermore, as we saw above in Sec.5.2, the current-current correlator for dilepton production is dominated by hadronic resonances below $M = 1 - 1.5\,\mathrm{GeV}/c^2$, and dominated by partonic degrees of freedom above this scale. So the intermediate mass region

of the dilepton spectrum ($1.5 < M < 5\,\mathrm{GeV}/c^2$) is appropriate to probe the early-time dynamics of the medium produced in HIC.

5.3.1 Our calculation

Like in the ideal rate case (Sec.5.2.1), the dilepton rate must be integrated over the space-time history of the system to obtain the yield. We make the same starting assumptions as in the ideal spectrum case in Sec.5.2.1: we assume Bjorken flow, transverse homogeneity, leading-order production, and neglect the transverse expansion of the plasma. Boost invariance implies that the dilepton yield per unit rapidity of the dilepton is equal to the yield per unit rapidity of the fluid. With these assumptions, the space-time integration takes the form:

$$\frac{dN^{l^+l^-}}{dMdy} = A_\perp \int_0^\infty \tau d\tau \, \frac{dN^{l^+l^-}}{d^4xdM}. \tag{5.24}$$

The main difference with the equilibrium case is how the dependence on proper time is modeled. To carry out this time integration, one must determine: the transverse area $A_\perp$, the late time value of the macroscopic variables, the time dependence of macroscopic variables using the attractor curves, and the parametrization of the quark and anti-quark distribution functions f_q and $f_{\bar{q}}$. We now detail each of these steps.

Transverse area $A_\perp$ The dependence on the transverse area $A_\perp$ is of crucial importance. It is evaluated by running a Monte Carlo generator of initial conditions which has been tuned to experimental data, the TRENTO model [207]. This model returns, for each event, an entropy density profile $s(x_T)$, where x_T labels a point in the transverse plane. The transverse area is then estimated as:

$$A_\perp \equiv \frac{\left(\int_{x_T} s(x_T)\right)^2}{\int_{x_T} s(x_T)^2}, \tag{5.25}$$

Note that Eq. (5.25) gives the correct result for a uniform density s_0 within an area A, irrespective of the shape of that area. We eventually average $A_\perp$ over many events in a centrality class. We thus obtain the values $A = 96$, 71, 54, $41\,\mathrm{fm}^2$ for the 0-10%, 10-20%, 20-30%, 30-40% centrality intervals in Pb–Pb collisions [203]. The value which will be used most often in the following corresponds to the 0-5% centrality class:

$$A_\perp \quad = 104\,\mathrm{fm}^2 = 2679\,\mathrm{GeV}^{-2} \tag{5.26}$$

Late time macroscopic variables The time integration will be carried out until the energy density e and entropy density s reach their late-time values. In the case of an ultra-relativistic plasma of quarks and gluons, theses variables can be expressed as a function of the effective temperature as:

$$e(T) = \frac{\pi^2}{30}\nu_{\mathrm{eff}}T^4 \tag{5.27}$$

$$s(T) = \frac{4\pi^2}{90}\nu_{\mathrm{eff}}T^3 \tag{5.28}$$

where $\nu_{\rm eff}$ denotes the effective number of degrees of freedom. The value of this parameter encodes the equation of state which is relevant at the considered temperature. The relation between entropy and energy densities is here $\frac{4}{3}e = Ts$. This is valid if the equation of state is conformal, as can be deduced from the thermodynamic identity $e+P = Ts$. This approximation is valid when the QCD medium is not too close to the pseudo-critical temperature, i.e. for $T \gtrsim 200\,\mathrm{MeV}$, which is adequate for all our early-time estimates.

The evolution of the energy and entropy densities as a function of the proper time τ is then determined by the conservation of entropy. Indeed, the entropy per unit rapidity can be written $dS/dy = A_\perp \tau s(T)$. We assume that at late times, the medium is in local thermal equilibrium. Hence the expansion is isentropic, i.e. no entropy is produced in this late expansion stage. This means that dS/dy is constant at late times. Since $s(T) \propto T^3$, this implies that τT^3 is also constant at late times. This is the same constant that appeared in Eq.5.18 in the case of the ideal spectrum. The value of this constant can be inferred from the measurement of the charged particle multiplicity density $dN_{\rm ch}/dy$, using $dS/dy \simeq (S/N_{\rm ch})\, dN_{\rm ch}/dy$ with $S/N_{\rm ch} = 6.7$ [208]. This quantity τT^3 is constant for $\tau \gg 1\,\mathrm{fm}/c$ but not too late so that we still consider the evolution of a hot QGP, around $T = 200$ to $300\,\mathrm{MeV}$. In this temperature range, we take the equation of state from lattice QCD calculations, which gives $\nu_{\rm eff} \approx 32$ [24, 25]. With this value, we can compute τT^3, which will fix the asymptotic behavior of the evolution of our thermodynamic variables. For Pb–Pb collisions at $\sqrt{s_{\rm NN}} = 5.02\,\mathrm{TeV}$, near midrapidity, in the $0-5\%$ centrality range:

$$\tau T^3 \quad = 8.74\,\mathrm{fm}^{-2} = 0.34\,\mathrm{GeV}^2 \tag{5.29}$$

Fixing time dependence with attractor curves As we saw in Sec.5.1.4, the evolution of the energy density and longitudinal pressure computed in different microscopic simulations with different couplings follows a similar trend towards an attractor curve, when expressed as a function of the scaling variable

$$\tilde{w} = \frac{\tau T_{\rm eff}(\tau)}{4\pi\eta/s}. \tag{5.30}$$

We see that η/s intervenes in the definition of the scaling variable $\tilde{w}$ as a function of time τ. It thus controls the speed of equilibration of the system and is a free parameter in our calculations. We note here that η/s is an early-time parameter, and is different from the shear viscosity discussed e.g. in the context of flow, which is evaluated at much later times. The limit $\tilde{w} \gg 1$ corresponds to $\eta/s \to 0$, which is the ideal hydrodynamic limit. The case $\tilde{w} \ll 1$ corresponds to $\eta/s \to \infty$ which is the limit of free streaming non-interacting particles; the system remains in a longitudinal expansion without ever equilibrating via particle interactions.

The second variable which intervenes in Eq.5.30 is the effective temperature $T_{\rm eff}$. At early times, the system is far from equilibrium and thus there is no temperature with its usual definition. However, one can still define an effective temperature from the energy density by inverting Eq. (5.27):

$$T_{\rm eff}(\tau) \equiv \left(\frac{30}{\pi^2 \nu_{\rm eff}} e(\tau)\right)^{1/4}. \tag{5.31}$$

In this equation, as we are considering pre-equilibrium, we must account for the much higher energy density than in the ideal case. Consequently, we must adapt the equation of state and take an appropriate value for $\nu_{\rm eff}$. The kinetic theory employed for our calculation of energy densities is a weakly coupled theory. Thus it makes sense to consider an equation of state close to the one of a weakly interacting gas of quarks and gluons. So we consider the value $\nu_{\rm eff} = 40$ when computing the early-time effective temperature [24, 182, 209].

The energy attractor $\mathcal{E}(\tilde{w})$ on Fig. 5.5 (left) is expressed as the ratio of the energy density multiplied by $\tau^{4/3}$ to its value at late times, which is a constant. Thus:

$$e(\tau) = \frac{\mathcal{E}(\tilde{w})\ (\tau^{4/3}e)_{\rm hydro}}{\tau^{4/3}} \tag{5.32}$$

$$= \frac{\pi^2}{30}\nu_{\rm eff}(\tau T^3)^{4/3}_{\rm hydro}\frac{\mathcal{E}(\tilde{w})}{\tau^{4/3}}, \tag{5.33}$$

where $(\tau T^3)_{\rm hydro}$ was calculated in Eq.5.29. Similarly, the pressure attractor on Fig. 5.5 (right) is expressed as the ratio of the longitudinal pressure p_L to the energy density e:

$$\frac{p_L(\tau)}{e(\tau)} = \mathcal{P}(\tilde{w}). \tag{5.34}$$

For $\tilde{w} \gtrsim 1$, the evolution of these attractors is well described by viscous hydrodynamics. In the following we will exploit the attractor curves, computed in QCD kinetic theory framework, in order to compute the evolution of macroscopic quantities in the early-time evolution, and separate the hydro production regime defined as $\tilde{w} \gtrsim 1$ and the pre-equilibrium production regime $\tilde{w} \lesssim 1$.

Parametrization of the quark distribution functions The general (i.e. out-of-equilibrium) dilepton rate expression in Eq.5.9 involves the Wightman function (Eq.5.11) which depends on the phase-space distribution of quarks and anti-quarks, f_q and $f_{\bar{q}}$. To carry out our calculation, we must determine the time evolution of these distributions. We cannot simply use a thermal Fermi-Dirac distribution since we want to include the early times of the collision, where the system is far from equilibrium. Instead, we use a parameterization known as the Strickland-Romatschke form, inherited from anisotropic hydrodynamics [180, 210]. This framework was designed to extend hydrodynamic and kinetic calculations to regions of phase space which are far from momentum isotropy, which, as we saw in Sec.5.1.2, is a characteristic of the early stages. In addition, models such as Glasma (see Sec.5.1.3) predict a early stage system which is dominated by gluons, i.e. quarks are underpopulated with respect to gluons. We include this relative suppression of quarks/anti-quarks with respect to gluons during the pre-equilibrium stage. In this approach, the quark and anti-quark distributions are parameterized as:

$$f_{q/\bar{q}}(\tau) \quad = \quad q(\tau) f_{FD}\left(\frac{\sqrt{p_{\rm T}^2 + \xi^2(\tau)p_z^2}}{\Lambda(\tau)}\right) \tag{5.35}$$

where the anisotropy parameter $\xi(\tau) \geq 1$ characterizes the momentum space anisotropy. $0 \leq q(\tau) \leq 1$ accounts for the relative suppression of quark/anti-quarks and $\Lambda(\tau)$ denotes an effective transverse temperature. Finally, f_{FD} is the Fermi-Dirac distribution.

Next, we constrain the values of $\xi(\tau)$, $\Lambda(\tau)$ and $q(\tau)$ by requiring that the energy density and longitudinal pressure obtained using this parametrization match those given by the corresponding attractor curves in Eq.5.32 and Eq.5.34.

Explicit integration gives the following results for the contributions of quarks and gluons to the energy density and longitudinal pressure:

$$e^{(q)}(\tau) = q(\tau) e^{(q)}_{\rm eq}(\Lambda(\tau))\, C(\xi(\tau))\,, \tag{5.36}$$

$$e^{(g)}(\tau) = e^{(g)}_{\rm eq}(\Lambda(\tau))\, C(\xi(\tau))\,, \tag{5.37}$$

$$p^{(q)}_L(\tau) = q(\tau) e^{(q)}_{\rm eq}(\Lambda(\tau))\, S(\xi(\tau)) \tag{5.38}$$

$$p^{(g)}_L(\tau) = e^{(g)}_{\rm eq}(\Lambda(\tau))\, S(\xi(\tau)), \tag{5.39}$$

where

$$C(\xi) = \frac{1}{2}\left[\frac{1}{\xi^2} + \frac{\arctan\sqrt{\xi^2-1}}{\sqrt{\xi^2-1}}\right] \tag{5.40}$$

$$S(\xi) = \frac{1}{2}\left[\frac{1}{\xi^2-\xi^4} + \frac{\arctan\sqrt{\xi^2-1}}{(\xi^2-1)^{3/2}}\right] \tag{5.41}$$

and $e^{(q)}_{\rm eq}(T) = \frac{7\pi^2}{240}\nu_q T^4$ and $e^{(g)}_{\rm eq}(T) = \frac{\pi^2}{30}\nu_g T^4$ correspond to the equilibrium energy densities of quarks and gluons, with the corresponding effective degrees of freedom ν_q and ν_g.

The longitudinal pressure over energy ratio depends only on the anisotropy parameter ξ:

$$\mathcal{P}(\tilde{w}) = \frac{p^{(q)}_L(\tau) + p^{(g)}_L(\tau)}{e^{(q)}(\tau) + e^{(g)}(\tau)} = \frac{S(\xi)}{C(\xi)}. \tag{5.42}$$

Hence, one can directly obtain the value of ξ as a function of $\tilde{w}$ from the pressure attractor curve $\mathcal{P}(\tilde{w})$.

The quark suppression factor $q(\tau)$ is given by the ratio between quark and gluon energy densities, with an appropriate weight to account for the different degrees of freedom. The $\tilde{w}$ dependence is computed with the QCD kinetic theory calculation [206]:

$$q(\tau) = \frac{e^{\rm eq}_g}{e^{\rm eq}_q}\frac{e_q}{e_g}(\tilde{w}). \tag{5.43}$$

This parameter depends on the microscopic theory employed, contrary to the evolution of the energy density and longitudinal pressure, which are given by the attractor properties as mentioned above.

Finally, the effective transverse temperature $\Lambda(\tau)$ is obtained by matching the total energy density $e(\tau)$ obtained from the energy attractor $\mathcal{E}(\tilde{w})$ to the one obtained from

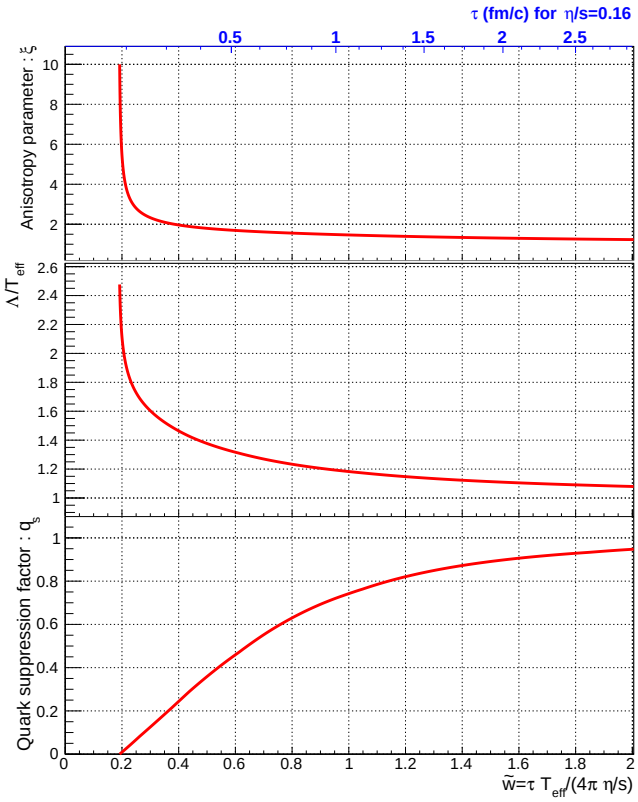

Figure 5.8: (Top) Anisotropy parameters ξ as a function of $\tilde{w}$, (Middle) $\Lambda/T_{\rm eff}$ as a function of $\tilde{w}$, (Bottom) quark suppression factor as a function of $\tilde{w}$.

the anisotropic distribution calculation, with Eqs. (5.36). From this procedure we deduce the relation:

$$\frac{\Lambda(\tau)}{T_{\rm eff}(\tau)} = \left(\frac{\frac{7}{8}\nu_q + \nu_g}{\left[\frac{7}{8}\nu_q q(\tilde{w}) + \nu_g\right] C(\xi(\tilde{w}))} \right)^{1/4} . \tag{5.44}$$

Figure 5.8 displays the variation of ξ, q, and $\Lambda/T_{\rm eff}$, defined by Eqs. (5.42), (5.43) and (5.44), as a function of the scaling variable $\tilde{w}$. The proper time is then related to $\tilde{w}$ using Eq. (5.30).

5.3.2 Yield results for central Pb–Pb collisions

Now that we know how to compute the parameters of our out-of-equilibrium distributions, we can numerically carry out the integration in the yield formula Eq.5.24 to get the dilepton spectrum. In the following we will keep the late-time entropy density fixed to $\tau T^3 \approx 8.74\,\mathrm{fm}/c^{-2}$, which corresponds to the 0-5% centrality bin for Pb–Pb collisions as $\sqrt{s_{NN}} = 5.02\,\mathrm{TeV}$. We show the invariant mass spectrum which results from this calculation on Fig. 5.9. We display the variation of the dilepton yield as a function of mass, for two values of the early-time shear viscosity-to-entropy ratio, $\eta/s = 0.16$ on the top plot and $\eta/s = 0.32$ on the bottom plot. The η/s value for QCD, in the temperature range spanned by the early evolution, is expected to lie in this range [211]. We also show on the same figure the impact of quark suppression at early times (full line curves) compared to

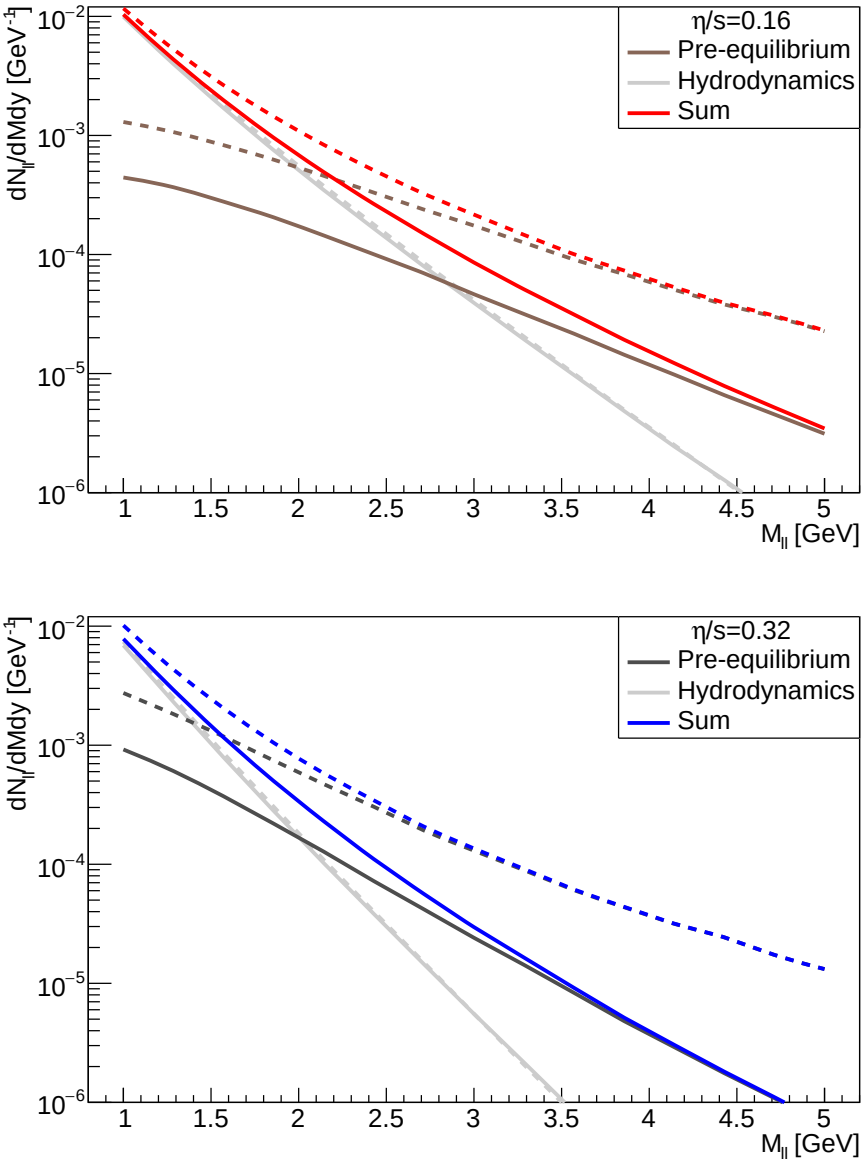

Figure 5.9: Dilepton production yields $dN_{ll}/dMdY$ in the $0-5\%$ most central $5.02\,\mathrm{TeV}$ Pb–Pb collisions at forward rapidity $y=2$. Red (left panel) and blue (right panel) curves show the results including (full lines) and not including (dashed lines) the quark suppression factor, for shear viscosity $\eta/s=0.16, 0.32$ in the left and right panels. We also show separately the contributions (see text) from the pre-equilibrium phase (dark grey) and hydrodynamic phase (light grey).

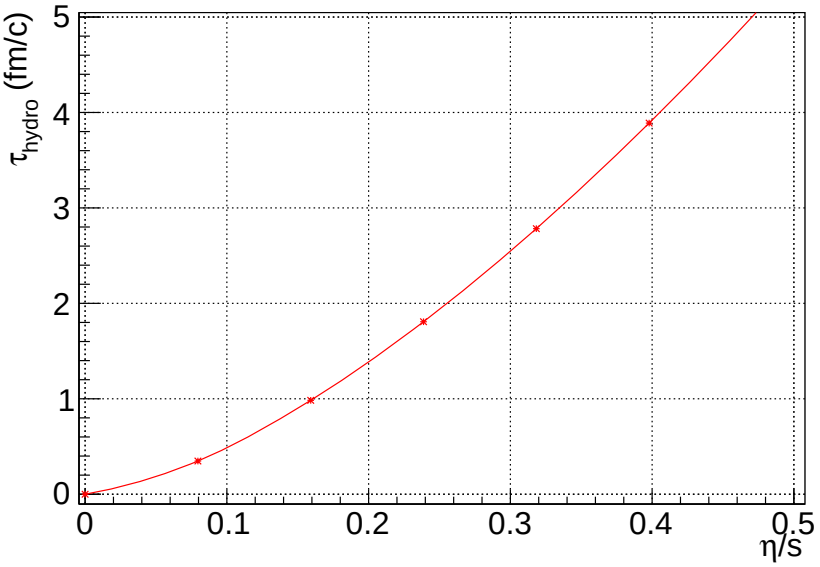

Figure 5.10: Time of applicability of hydrodynamics $\tau_{\rm hydro}$ computed with the condition $\tilde{w}(\tau_{\rm hydro}) = 1$, as a function of the shear viscosity-to-entropy ratio η/s.

the case where chemical equilibrium is achieved from the start of the evolution (dashed lines).

The system is described by viscous hydrodynamics for $\tilde{w} \gtrsim 1$. We define τ_{hydro} by $\tilde{w}(\tau_{hydro}) = 1$ and we define the contribution from the pre-equilibrium by the contributions at times $\tau < \tau_{hydro}$ and the hydrodynamic contribution by $\tau > \tau_{hydro}$. One should note that $\tilde{w} = 1$ does not imply that the pressure is isotropic: the longitudinal pressure attractor in Fig.5.34 shows that $P_L/e\ (\tilde{w} = 1) \approx 0.2$, which still deviates from isotropy. According to the definition of the scaling variable $\tilde{w}$, Eq.5.30, the value of τ_{hydro} depends on the early-time shear viscosity η/s. This dependency is displayed on Fig. 5.10. For $\eta/s = 0.16$, we have $\tau_{hydro} \approx 1\,\mathrm{fm}/c$ while for $\eta/s = 0.32$, $\tau_{hydro} \approx 3\,\mathrm{fm}/c$. The time scale of applicability can thus be quite late in the evolution depending on η/s, i.e. on the strength of the coupling at early times.

When comparing the top and bottom graphs of Fig. 5.9, we see that the total dilepton yield is higher for $\eta/s = 0.16$ than for $\eta/s = 0.32$. Indeed, if we lower the viscosity, the strength of interactions between particles is larger, and the system approaches the hydrodynamic regime faster. Energy density decreases faster in the hydrodynamic regime than in the pre-equilibrium, as illustrated on Fig. 5.11. This fast decrease in the hydrodynamic regime is due to the work done by the system to sustain its longitudinal pressure while suffering from the strong longitudinal expansion. This work is larger in the hydro regime, where the longitudinal pressure is large, than in pre-equilibrium. For fixed charged-particle multiplicity $dN_{\rm ch}/d\eta$, lower viscosity thus implies higher initial energy density, and higher effective transverse temperature throughout the out-of-equilibrium evolution. Higher temperature in turn implies larger dilepton yields. This explains the

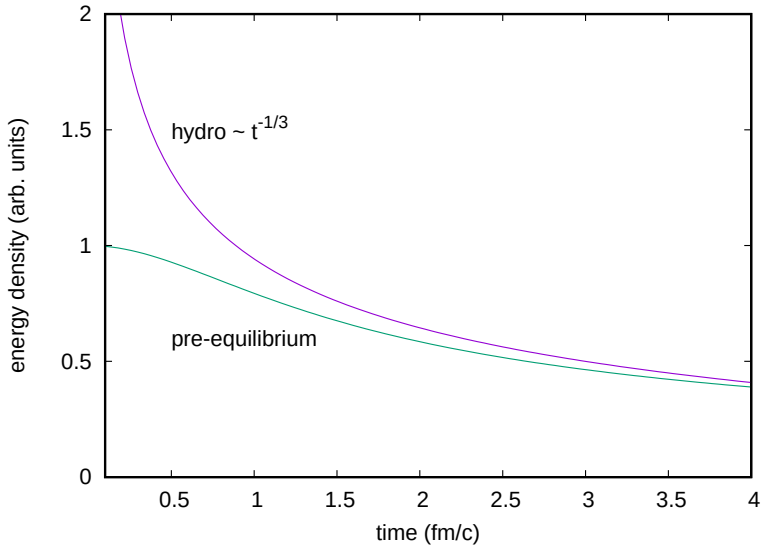

Figure 5.11: Illustration of the different time evolution of energy density between the hydrodynamic regime (in purple) and the pre-equilibrium regime (in green). The fall-off is steeper in the first case because of the larger longitudinal pressure (see text). The energy densities at late times are equalized for the two regimes, and we see as a consequence a larger energy density at t=0 in the case of hydrodynamics than in the case of pre-equilibrium.

dependence on η/s shown in Fig. 5.9.

The hydrodynamic contribution dominates at low invariant mass. It has little sensitivity to quark suppression, but a sizeable sensitivity to η/s. The pre-equilibrium contribution is strongly sensitive to both η/s and quark suppression, and it dominates at high invariant mass. If one takes into account the quark suppression, the crossing point between pre-equilibrium and hydrodynamic emission is $M \sim 2.7\,\mathrm{GeV}$ for $\eta/s = 0.16$ and $M \sim 2\,\mathrm{GeV}$ for $\eta/s = 0.32$. If one does not take into account quark suppression, these crossing points are lowered to $M \sim 2\,\mathrm{GeV}$ and $M \sim 1.5\,\mathrm{GeV}$.

One should note that quark suppression decreases the dilepton yield by a large factor for $M \gtrsim 3\,\mathrm{GeV}$. Hence, the modelling of the chemical equilibration process is crucial in order to interpret the high-mass dilepton spectrum.

Figure 5.12 displays the total dilepton yield as a function of the collision centrality. Different centralities correspond to variations of the charged particle multiplicity $dN_{\mathrm{ch}}/d\eta$ and of the transverse area $A_{\perp}$, resulting in different values of $(\tau T^3)_{hydro}$. The variation of the dilepton yield with centrality is stronger than that of the hadron multiplicity $dN_{\mathrm{ch}}/d\eta$. Indeed, in the hydrodynamic regime, one expects the dilepton yield to scale typically like the space-time volume, which is proportional to $(dN_{\mathrm{ch}}/d\eta)^{4/3}$ [204]. This scaling explains the centrality dependence at low invariant mass M, since low invariant masses originate from the hydrodynamic phase. For larger values of M, the centrality dependence is even stronger. The reason is that τ_{hydro} is smaller in more central collisions. Faster equilibration implies higher initial temperatures as explained above, and this enhances dilepton

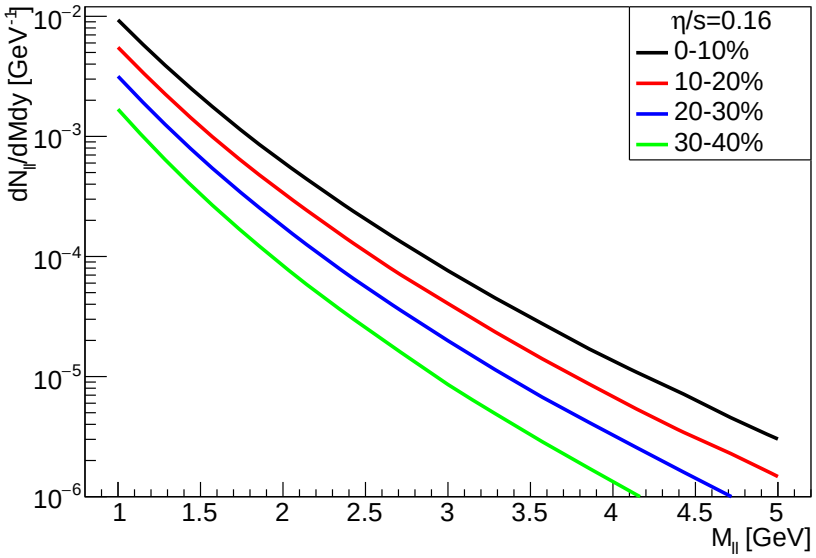

Figure 5.12: Centrality dependence of the dilepton production yields $dN_{ll}/dMdY$ in $5.02\,\mathrm{TeV}$ Pb–Pb collisions at forward rapidity $y = 2$ for shear viscosity $\eta/s = 0.16$ (with quark suppression). Different centrality classes 0-10% (black), 10-20% (red), 20-30% (blue) and 30-40% (green) show are larger at suppression of dilepton production at high invariant masses.

production in the pre-equilibrium phase.

5.3.3 Checking our assumptions

Let us now go through some of the assumptions we made. First, our calculation assumes a simple longitudinal expansion of medium. We do not attempt a full calculation of the evolution, like done by Strickland *et al.* in the anisotropic hydrodynamic framework [212, 213, 214, 215]. However, with the same settings (same initial time, η/s, centrality, p_{T} range, hadron multiplicity, and neglecting quark suppression), our result for $dN/dMdy$ has the same dependence on M, with a scaling factor between the calculations of about 1.7 (shown on Fig. 5.13). We attribute this difference to the detailed evolution simulated in [214].

Second, we assumed in the computation of $(\tau T^3)_{hydro}$ an equation of state based on lattice QCD, at lower temperature then the one used to define the effective temperature. This seems reasonable to us, since this value is only constant at later times. However some papers [182, 191, 208] compute this entropy density, which is then matched to charged particle multiplicity $dN_{\mathrm{ch}}/d\eta$, using a high temperature equation of state, which translates into values of the ν_{eff} and S/N_{ch} parameters different from the ones we used in our calculation: $\nu_{\mathrm{eff}} = 40$ and $S/N_{\mathrm{ch}} = 7.5$. A comparison of the total dilepton yields using different values for these parameters is shown on Fig. 5.14. We see that there is less than a factor 1.5 between the central values of the results for these two sets of parameters, the yield calculated with $\nu_{\mathrm{eff}} = 40$ being larger than the one for $\nu_{\mathrm{eff}} = 32$.

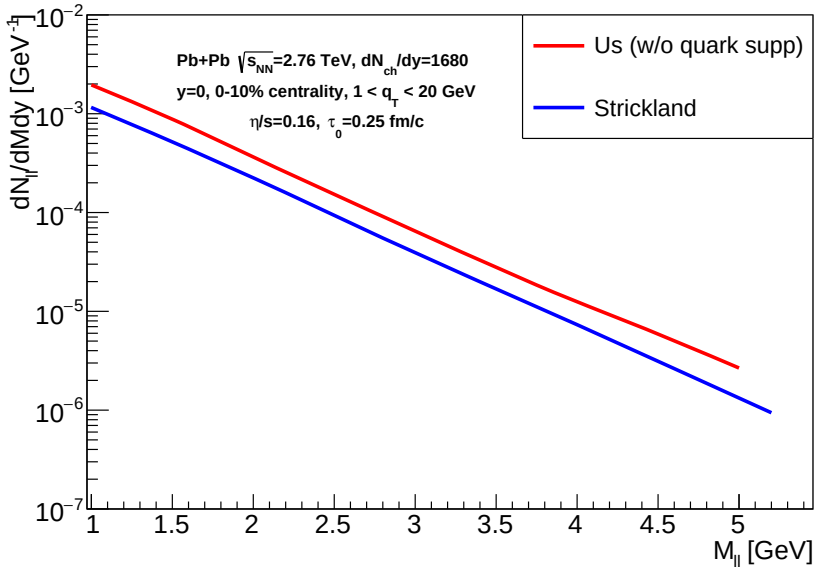

Figure 5.13: Comparison of our calculation for central Pb–Pb collisions at $\sqrt{s_{NN}} = 2.76\,\mathrm{TeV}$ at midrapidity, with the results of [214], with the same fixed parameters.

Third, we assumed that the temperature/energy density profile in the transverse plane is homogeneous. This is a simplification, since the medium should be hotter at the center of the profile and cooler on the edges, towards the freeze-out hyper-surface. In addition, realistic simulations include hot spots in the energy density profile [216, 217, 218, 219], which are localized areas where the temperature is higher than average. These hot spots are event-by-event fluctuations. Since more high-mass dileptons are emitted from high temperatures, we expect that our calculation, which does not include hot spots, underestimates the dilepton yield for large invariant mass. In order to evaluate this effect quantitatively, we have carried out a calculation in which we replace the uniform profile with a fluctuating initial state profile. In this model, the initial energy deposition in the collision between the two nuclei is calculated using k_T-factorization [220, 221] to get the density of gluons in the transverse plane per unit rapidity:

$$\frac{\mathrm{d}N_g}{\mathrm{d}^2x_T\mathrm{d}^2p_\mathrm{T}\mathrm{d}y} = \frac{g^2N_c}{4\pi^5p_\mathrm{T}^2(N_c^2-1)}\int\frac{\mathrm{d}^2k_T}{(2\pi)^2}\Phi_1\left(\vec{x_T}+\frac{\vec{b}}{2},\vec{k_T}\right)\Phi_2\left(\vec{x_T}-\frac{\vec{b}}{2},\vec{p_\mathrm{T}}-\vec{k_T}\right) \quad (5.45)$$

for gluons with transverse momentum p_T, produced per unit rapidity y, at transverse position $\vec{x_T}$. Here g is the strong coupling, $N_c = 3$ the number of colors, $\vec{b}$ the impact parameter of the nucleus-nucleus collision, and $\Phi_{1/2}(\vec{x_T},\vec{k_T})$ the unintegrated gluon distribution of nucleus 1 or 2.

The energy density at each point in the transverse plane is computed from the gluon density:

$$(e\tau)_0 = \int \mathrm{d}^2p_T|p_\mathrm{T}|\frac{\mathrm{d}N_g}{\mathrm{d}^2x_T\mathrm{d}^2p_\mathrm{T}\,\mathrm{d}y} \quad (5.46)$$

The unintegrated gluon distributions are parametrized using a nucleus saturation

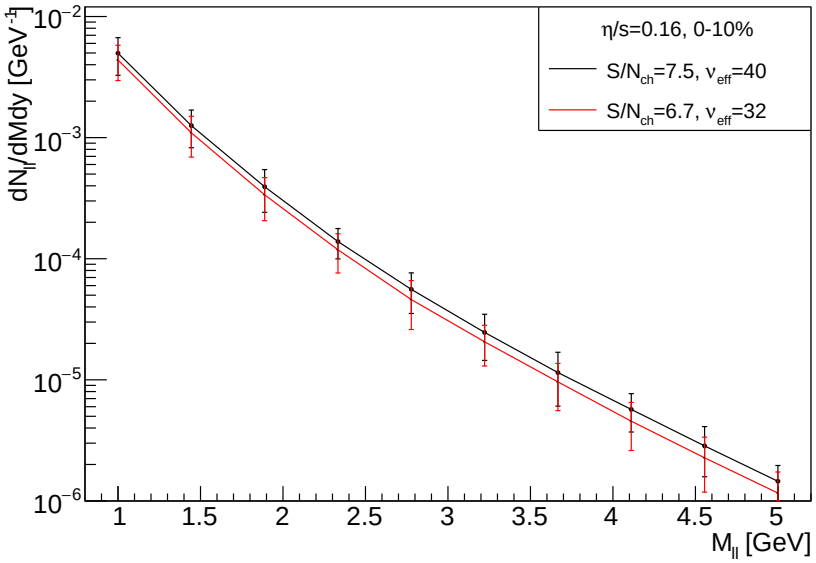

Figure 5.14: Comparison of the results of our calculation for two different sets of the shear viscosity-to-entropy ratio η/s and the effective number of degrees of freedom ν_{eff}. The displayed error bars are statistical uncertainties from the used Monte Carlo integration in our calculation.

scale $Q_{s,1/2}$ with the Golec-Biernat and Wüsthoff (GBW) model [222]. With this parametrization, the initial energy density is computed [223]:

$$(e(\vec{x_T})\tau)_0 = \frac{N_c^2 - 1}{4g^2 N_c \sqrt{\pi}} \frac{Q_{s,1}^2 Q_{s,2}^2}{\left(Q_{s,1}^2 + Q_{s,2}^2\right)^{5/2}} \left[2Q_{s,1}^4 + 7Q_{s,1}^2 Q_{s,2}^2 + 2Q_{s,2}^4\right] \tag{5.47}$$

This initial energy density is then used to compute the energy density at late times, at different positions $(\vec{x_T})$ in the transverse plane:

$$(e(\vec{x_T})\tau^{\frac{4}{3}})_{\text{hydro}} \propto \left(4\pi\frac{\eta}{s}\right)^{\frac{4}{9}} \left(\frac{\pi^2}{30}\nu_{\text{eff}}\right)^{-\frac{8}{9}} (e(\vec{x_T})\tau)_0^{8/9} \tag{5.48}$$

which is then used to compute the time evolution of energy density in Eq.5.32. We then follow the same procedure outlined above to get the dilepton spectrum, the only difference being that the energy density, and thus temperature, now depends on transverse position $(\vec{x_T})$. The nucleus saturation scale is parametrized as:

$$Q_{s,1/2}^2(x, \vec{x_T}) = \sigma_0 T_{1/2}(\vec{x_T}) Q_{s,0}^2 x^{-\lambda}(1-x)^{\delta} \tag{5.49}$$

The nuclear thickness function $T_{1/2}(\vec{x_T})$ is evaluated with a MC Glauber sampling of nucleon positions inside each nucleus. Finally, σ_0, $Q_{s,0}$, λ and δ are tuned so that the model fits the charged-particle multiplicity measured by ALICE for Pb–Pb collisions, in different centrality classes [56]. An example of a resulting initial energy density profile is shown on Fig.5.15. As this model requires an important number of parameters, we only consider it as a way to evaluate the importance of event-by-event fluctuations in the initial energy

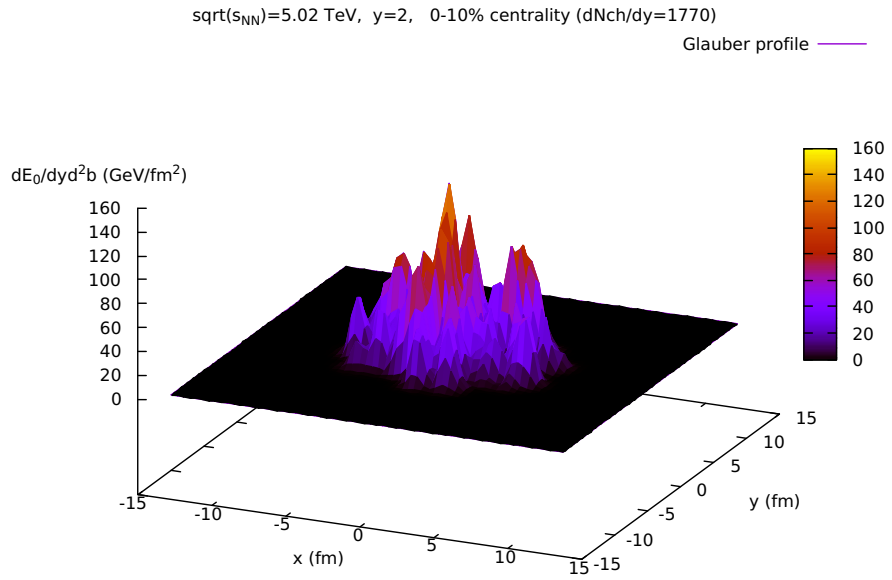

Figure 5.15: Example of a transverse profile of energy density computed in the CGC-Glauber model described in [223], for a single $0-10\%$ central Pb–Pb event at $\sqrt{s_{\mathrm{NN}}} = 5.02\,\mathrm{TeV}$.

density profile. It thus provides a theoretical uncertainty for our simple dilepton spectrum calculation using a homogeneous profile, which has $dN_{ch}/d\eta$ and $A_\perp$ as its two geometric parameters.

As shown on Fig. 5.16, our homogeneous calculation gives similar results as the k_{T}-Glauber model for the $0-10\%$ centrality class. For other classes, starting from the $10-20\%$ centrality class, there is still a good agreement for $M \sim 1\,\mathrm{GeV}$, but our calculation underestimates the yield by a factor $1.5-2$ for $M = 5\,\mathrm{GeV}$. Indeed, the increase of the dilepton yield for large M, due to fluctuations, is larger for more peripheral collisions. Hence, our initial calculation with a uniform energy density profile can be viewed as a conservative estimate at high mass.

Finally, we also compared our calculation with another work on pre-equilibrium contribution to dilepton production, by Churchill *et al.* [224, 225], which found dilepton rates orders of magnitude smaller.

The main difference is that they use an initial momentum distribution of gluons:

$$f_g\left(t_0, p\right) = f_0 \theta\left(1 - \frac{\sqrt{p_\perp^2 + p_z^2 \xi^2}}{Q_s}\right) \tag{5.50}$$

where Q_s is the saturation scale. This form is inspired by CGC theory and is used in some kinetic descriptions for the thermalization of systems of weakly coupled gluons [226, 227]. This means that there are initially no gluons with momentum larger than $\sim 2\,\mathrm{GeV}/c$ at LHC energies. High mass dileptons are produced by the annihilation of a high-momentum

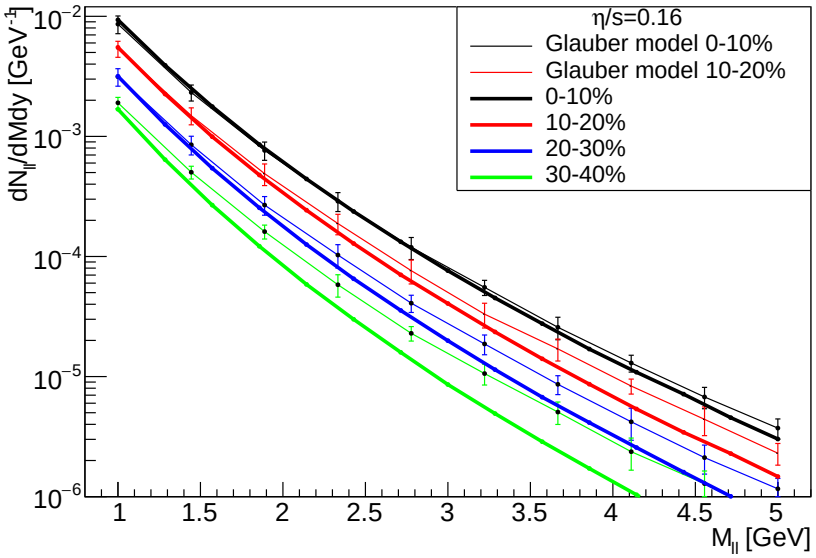

Figure 5.16: A comparison of the dilepton invariant mass yields for different centrality classes, between the k_{T}-Glauber model [223] and our homogeneous profile calculation [203, 204], for Pb–Pb collisions at $\sqrt{s_{\mathrm{NN}}} = 5.02\,\mathrm{TeV}$, with a fixed shear viscosity-to-entropy ratio $\eta/s = 0.16$. The displayed error bars are statistical uncertainties from the used Monte Carlo integration in our calculation.

quark and a high-momentum anti-quark, which are themselves produced by high-momentum gluons. In our calculation, we used results of a QCD kinetic simulation to estimate the quark and gluon energy density, matched to our parametrization. The initial gluon distribution used in this QCD kinetic calculation is of the form [205]:

$$f_g\left(\tau_0, p_{\mathrm{T}}, p_L\right) = f_g^0 \frac{Q_0}{\sqrt{p_{\mathrm{T}}^2 + \xi_0^2 p_L^2}} e^{-\frac{2\left(p_{\mathrm{T}}^2 + \xi_0^2 p_L^2\right)}{3Q_0^2}} \tag{5.51}$$

where Q_0 is proportional to Q_s and ξ_0 is an initial anisotropy parameter. This parametrization has a less abrupt decrease of high-momentum partons than the one in Eq.5.50; there are more high-momentum gluons and thus larger production of high mass dileptons. This parametrization is motivated by similar forms which are also used in the context of CGC, in particular in the McLerran-Venugopalan (MV) model [228, 229, 230] or the GBW model [222], where the phase space distribution of small-x color charges is assumed to be Gaussian. From this, we conclude that it is essential to model as realistically as possible the tail of the initial gluon distribution, and that it represents a large source of uncertainty.

The last caveat of our model is the absence of higher order corrections in perturbation theory. Indeed, at LO, only the quark-anti-quark annihilation process contributes to dilepton production. However, at NLO, virtual corrections arise and an additional diagram opens the phase space for radiation via Compton-scattering (see Fig. 5.17). We did not attempt the calculation at NLO. This is a calculation which has yet to be fully undertaken in the literature in the far-from-equilibrium case.

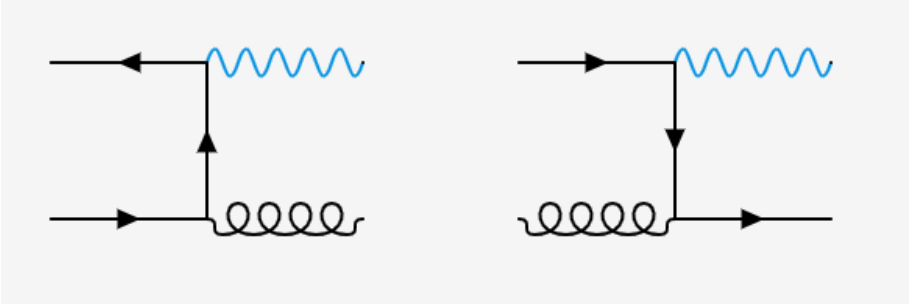

Figure 5.17: Feynman diagrams of next-leading order quark-anti-quark annihilation (left) and Compton scattering (right) which contribute at NLO to dilepton production.

5.3.4 Backgrounds and their suppression

The measurement of pre-equilibrium and thermal dileptons supposes that the signal directly emitted from the QGP can be separated from a background of radiation coming from other sources.

As we have established, we are interested in high mass dileptons, typically with $M > 1.5\,\mathrm{GeV}$. In this region, besides the large J/ψ peak around $M \simeq 3.1\,\mathrm{GeV}$ and the $\psi(2S)$ peak at $M \simeq 3.7\,\mathrm{GeV}$, are semileptonic decays of heavy quark hadrons [231], and Drell-Yan (DY) production in the initial state [232]. Indeed, at LHC energies and at large invariant masses, Drell-Yan production is expected to become important and eventually dominate the mass spectrum of dileptons. This type of production also comes from the quark-anti-quark annihilation, but in this case, the quark and the anti-quark come from the initial wave functions of two colliding nucleons, as shown on Fig. 5.19.

Since this type of dilepton production originates from the same process as pre-equilibrium dileptons, it is difficult to discriminate the two sources. Hence, to a first approximation, Drell-Yan dileptons can be considered as an irreducible background for the measurement of pre-equilibrium dileptons, and define an upper bound on the mass below which thermal and pre-equilibrium dilepton production can be isolated. DY production can be calculated in perturbative QCD using collinear factorization up to next-to-next-to-leading order (NNLO). To establish the feasibility of the measurement of pre-equilibrium and thermal dileptons, we estimated the DY contribution using NLO calculations. In the invariant mass range of interest, the nPDFs used in the collinear calculation are not very well constrained by experimental data, and the scale uncertainties (due to the variation of factorization and renormalization scales) are very large. We perform a calculation using the EPPS nPDFs [54] and the Drell-Yan Turbo software [233], assuming T_{AA} scaling of the cross section [55] in our centrality range of interest. The Drell-Yan calculation is shown in Fig. 5.18, together with our calculation of thermal dileptons. The shaded band corresponds to the independent variation of the factorization and renormalization scales by a factor two. For its upper limit, corresponding to factorization and renormalization scales equal to twice the dilepton mass, we observe that the thermal production dominates the spectrum below a mass $2.7\,\mathrm{GeV}$ ($3.6\,\mathrm{GeV}$) for $\eta/s = 0.32$ ($\eta/s = 0.16$), including quark suppression. Without quark suppression, the thermal production dominates the yield up to masses above $5\,\mathrm{GeV}$.

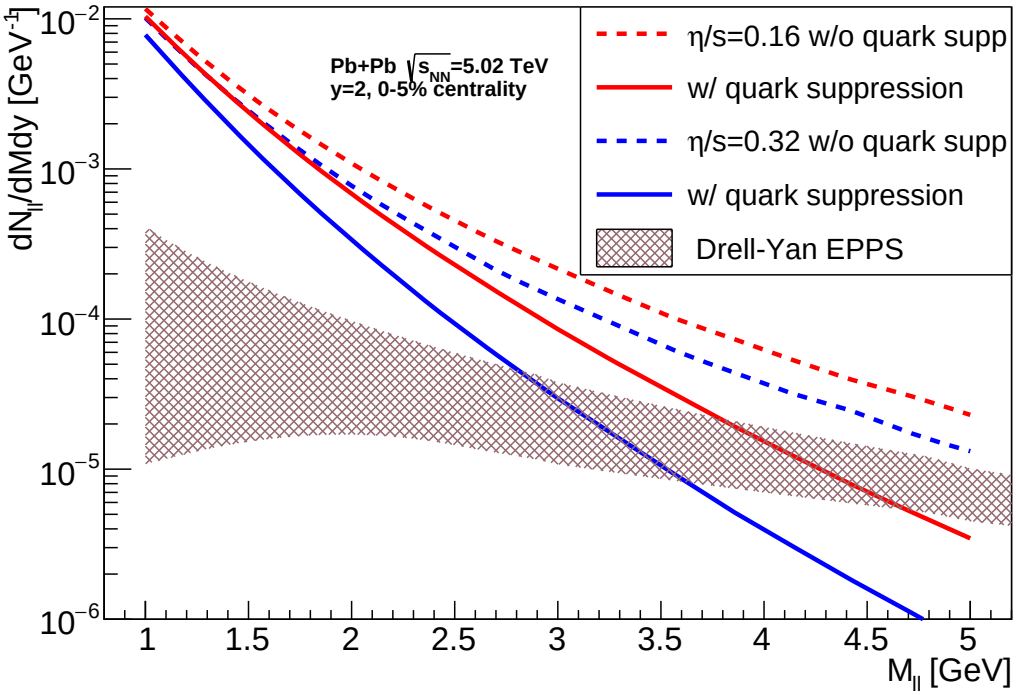

Figure 5.18: Dilepton production yields in the $0-5\%$ most central $5.02\,\mathrm{TeV}$ Pb–Pb collisions at forward rapidity $y=2$ for different values of η/s, with and without quark suppression, compared with the Drell-Yan rate calculated at NLO with EPPS nuclear PDFs.

In addition to DY, at LHC energies, an important source of background is the combinatorial background of the leptons produced by semileptonic decays of heavy hadrons. Indeed, at the LHC, pairs of charm-anti-charm and beauty-anti-beauty quarks are produced abundantly via the strong interaction (about 100 $c\bar{c}$ pairs and 10 $b\bar{b}$ pairs for central Pb–Pb collisions at $\sqrt{s_{NN}}=5.02\,\mathrm{TeV}$). Charm and beauty hadrons have a branching ratio to semileptonic decays of about $\sim 10\%$ [196]. This produces a large number of leptons, and thus an even larger combinatorial background of lepton-antilepton pairs. This dilepton source dominates over the thermal dilepton in the intermediate mass range.

However, charm and beauty hadrons have finite lifetimes and thus finite decay lengths, of order $50-500\,\mu\mathrm{m}$. These decay lengths, together with finite momentum, lead to a displacement of the decay vertex of the hadron with respect to the primary vertex of the collision, where the two colliding nuclei cross in the lab frame. This is in contrast with thermal and DY productions of dileptons, where the decay vertex of the virtual photon is indistinguishable from the primary vertex. In addition to the displacement of these vertices to the primary vertex, the displacement of the lepton with respect to the primary vertex, i.e. the impact parameter of the lepton, can provide an additional handle to reject this source of background. These observables (dilepton secondary vertex and lepton impact parameter) are measurable with silicon vertex detectors, close to the interaction point, similar to the MFT.

The LHCb experiment, originally dedicated to the study of heavy flavors in proton-

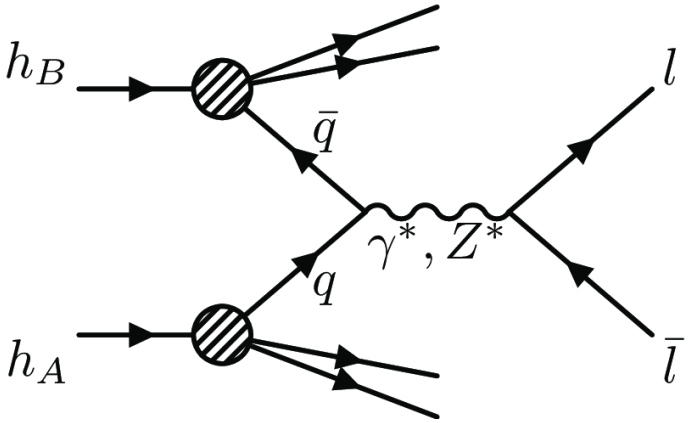

Figure 5.19: Illustration of the Drell-Yan production of dileptons in hadronic collisions [234],

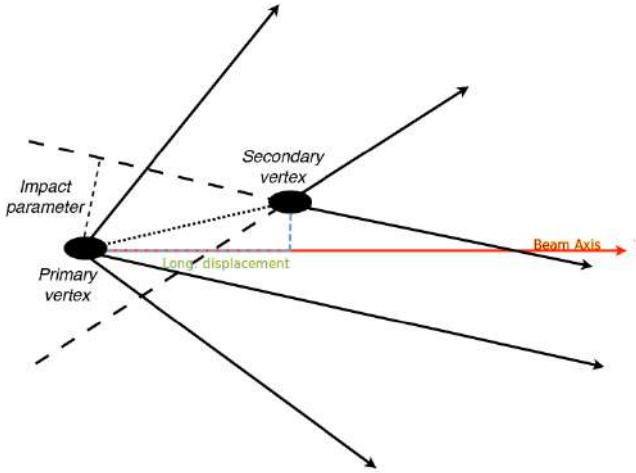

Figure 5.20: Illustration of impact parameter and secondary vertex displacement.

proton collisions, is planning a series of upgrades to be able to exploit heavy-ion collisions [235]. This detector has a vertex detector getting as close as about 5 mm to the vertex, and the forward geometry leads to a longitudinal boost of all particles in acceptance. This boost dilates the displacement of secondary vertices and impact parameters, making them more powerful variables to discriminate between different topologies. These variables are illustrated on Fig. 5.20. I conducted fast simulation studies [236] to evaluate the feasibility of the thermal dilepton measurement with this LHCb setup, to give first estimates of the background rejection that could be achieved in this experiment.

Only the combinatorial background coming from the semileptonic decay of heavy flavors was considered. The variables used for the rejection were the impact parameter of single-track muons with respect to the primary vertex of the interaction, and the longitudinal displacement of the secondary vertex produced by the considered semileptonic decay. Cutting on this last parameter, we assumed that this secondary vertex was correctly identified, which is a strong assumption. Thus, we considered a conservative cut,

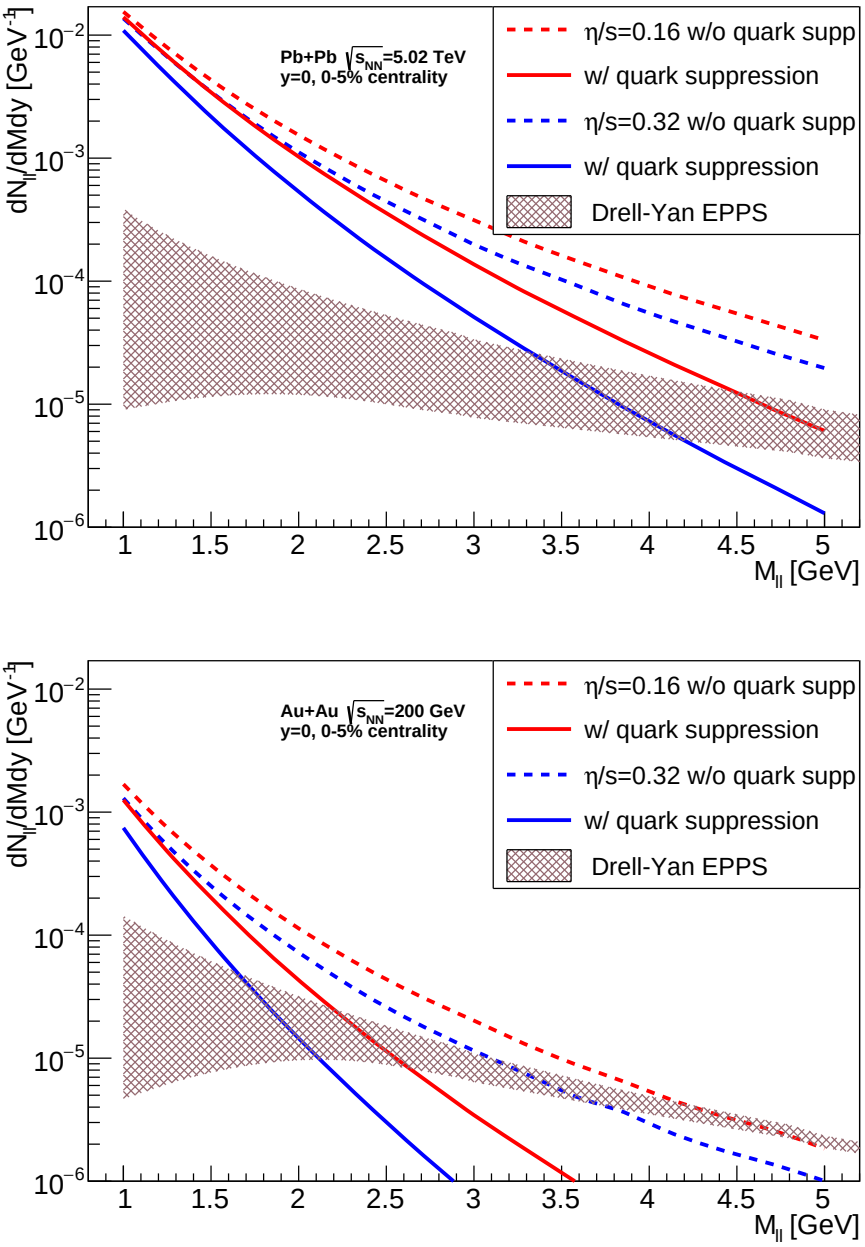

Figure 5.21: Dilepton yields at $y = 0$ for different values of η/s, with and without quark suppression, and Drell-Yan rate calculated at NLO with EPPS pdf, for Pb–Pb at $\sqrt{s_{NN}} = 5.02\,\mathrm{TeV}$ (top) and Au–Au at $\sqrt{s_{NN}} = 200\,\mathrm{GeV}$ (bottom).

rejecting tracks associated with a secondary vertex longitudinally displaced by more than three times the longitudinal vertex resolution expected for LHCb Upgrade. With these assumptions, and varying the cutting parameter on the impact parameter, as well as the nuclear modification factor for charm mesons R_{AA} between 0.5 and 1, we estimated a signal/background from 0.3 up to 1.4 for dimuons in the mass range 1 to $3\,\mathrm{GeV}$.

We also give estimates of dilepton yields for the ALICE experimental setup on Fig. 5.21, at midrapidity, hence giving predictions for the completely new fully silicon-based detector at central rapidity with electron identification, employing a vertex detector with similar performance to LHCb, which is envisioned to be built in the 2030s [237]. Finally, on the same figure, we also provide in the calculation for central Au–Au collisions at the top collision energy of the RHIC ($dN_{ch}/d\eta \simeq 625$ and $A = 100\,\mathrm{fm}/c^2$) compared with Drell-Yan production. We observe that quark suppression has an even larger effect than at the LHC. We also see that Drell-Yan production tends to dominate the yield starting from a much lower mass than at higher energy: thermal dilepton production is smaller than Drell-Yan as soon as M exceeds $2.2\,\mathrm{GeV}/c^2$.

5.3.5 Transverse-mass scaling of QGP dileptons

In this section and in the following one, we give an overview of other observables than invariant mass, which could also bring valuable insights to our understanding of the pre-equilibrium stage.

As we saw previously in Sec.5.2.1, the ideal production rate Eq.5.18 has a feature known as transverse-mass scaling, or M_t-scaling. In this section, we study the impact of pre-equilibrium on this property [204]. Qualitatively, there are two main early-time features which we include in our calculation and which deviate from the ideal spectrum. The first one is momentum anisotropy. In the local rest frame of a fluid cell, the momentum distributions of quarks and gluon are "squeezed" along the longitudinal direction. This means that large transverse momenta are favored over longitudinal momenta. This preference is expected to break M_t-scaling: large values of p_T are favored and hence, at fixed values of M_t, smaller values of the mass M will be favored. The second feature that we include is quark suppression at early times. This is accounted for by the introduction of a quark suppression factor, which is a multiplicative factor in our quark/anti-quark distribution functions. Hence, it is a global suppression factor, independent of kinematics. As such, it should preserve M_t-scaling. We now further investigate these points quantitatively by looking at our results as a function of M_t.

Figure 5.22 displays the M_t spectra of dileptons in central Pb–Pb collisions (closed colored markers) for the two same values of η/s as in the previous sections. The different colors correspond to different fixed values of the mass. As we can see, the different colors do not overlap with each other: at fixed values of M_t, our calculation favors smaller values of the mass. This is the breaking of M_t-scaling which is due to momentum anisotropy. However, this breaking is a modest effect, compared to the overall suppression from the ideal spectrum (black curve), which is due to quark suppression at early times. The dependence of the dilepton yield on the parameters $\eta/s, M_t$ and M is well captured by the

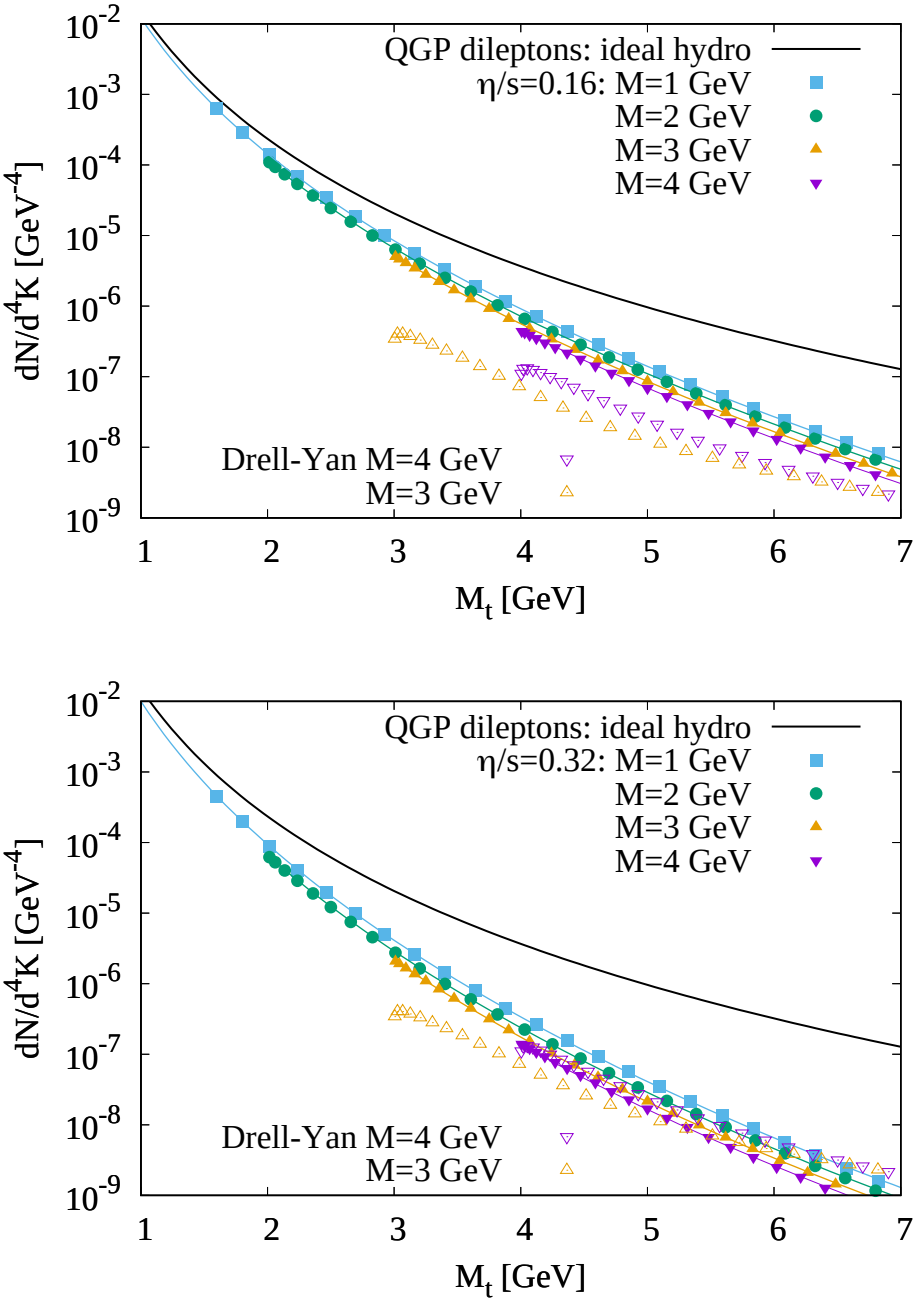

Figure 5.22: Full symbols: Expected dilepton invariant yield per event in $0-5\%$ central Pb–Pb collisions at $\sqrt{s_{\rm NN}} = 5.02\,\mathrm{TeV}$, in the central rapidity window $|y| < 1$, as a function of the transverse mass, for several values of the invariant mass M, and two values of the shear viscosity over entropy ratio, $\eta/s = 0.16$ (top) and $\eta/s = 0.32$ (bottom). The thick line is the McLerran-Toimela spectrum. The thin lines are the global fit of our results. Open symbols: Dilepton yield from the Drell-Yan process. We only plot the central value of the NLO+NLL calculation.

following formula:

$$\frac{dN^{l^+l^-}}{d^4K} \simeq \left(\frac{dN^{l^+l^-}}{d^4K}\right)_{\text{ideal}} \frac{\left(1 + a\frac{\eta}{s}M_t^2/n\right)^{-n}}{\sqrt{1 + b\frac{\eta}{s}M^2}} \tag{5.52}$$

where the first term is the ideal spectrum (given by the McLerran-Toimela expression Eq.5.18). The parameter a quantifies the dependence of the suppression on M_t. The parameter b quantifies the breaking of M_t scaling due to pre-equilibrium dynamics. The parametrization that we choose ensures that the deviations from ideal hydrodynamics are linear in η/s in the limit $\eta/s \to 0$. The parameter n specifies the dependence of pre-equilibrium effects on the Reynolds number (see [204]). The parametrization Eq.5.52 implies that the spectrum is proportional to $1/M$ in the limit of large η/s, thus breaking the M_t scaling.

For each setup of our calculation, i.e., with or without quark suppression taken into account, we have carried out a global fit of all our results for $1.5 < M_t < 7\,\text{GeV}$ using Eq.5.52. Including quark suppression, the best-fit values are $a = 0.61\,\text{GeV}^{-2}$, $b = 1.6\,\text{GeV}^{-2}$, $n = 3.1$. Without quark suppression, they are $a = 0.07\,\text{GeV}^{-2}$, $b = 2.4\,\text{GeV}^{-2}$, $n = 1.2$. We see that the breaking of M_t scaling is larger without quark suppression, resulting in a larger value of b. The parameter a is an order of magnitude smaller without quark suppression, which means that 90% of the pre-equilibrium effects on the M_t spectrum come from chemical equilibration.

The dilepton spectrum is often characterized by an effective temperature T_{slope} [195, 200, 201], defined as the inverse slope of the M_t spectrum Eq.5.53. Similarly to what we saw in Sec.5.2.1 in the ideal case, the T_{slope} extracted from Eq.5.52 still solely depends on M_t, as long as transverse flow can be neglected. In the limit of small η/s, we get:

$$T_{\text{slope}}\left(M_t\right) \simeq \frac{M_t}{6 + 2a\frac{\eta}{s}M_t^2} \tag{5.53}$$

This inverse slope has no dependence on temperature, since we are integrating over the whole space-time history of the medium and hence over all the temperatures that the system achieves during its evolution. However, Eq.5.53 shows that the shear viscosity-over-entropy ratio at early times η/s can be extracted from the inverse slope.

The last effect which breaks M_t scaling is transverse flow. Indeed, for a given M_t, the transverse boost enhances dilepton production for larger transverse momenta of the dilepton, or, equivalently, smaller values of M [238]. We neglected transverse flow in our calculation, therefore we do not quantitatively estimate its effect on the breaking of M_t scaling. However, we can evaluate the robustness of our results regarding this assumption. Transverse flow develops gradually over time and becomes important for $\tau \gtrsim 5\,\text{fm}/c$. If the fraction of the dileptons produced after $5\,\text{fm}/c$ is small, the dilepton yield is likely to have little sensitivity to transverse flow. We have calculated this fraction numerically and found that it only depends on M_t. It is roughly 25% for $M_t = 2\,\text{GeV}$, but only 4% for $M_t = 3\,\text{GeV}$. We conclude that for $M_t \lesssim 2\,\text{GeV}$, sizable corrections from transverse flow are to be expected.

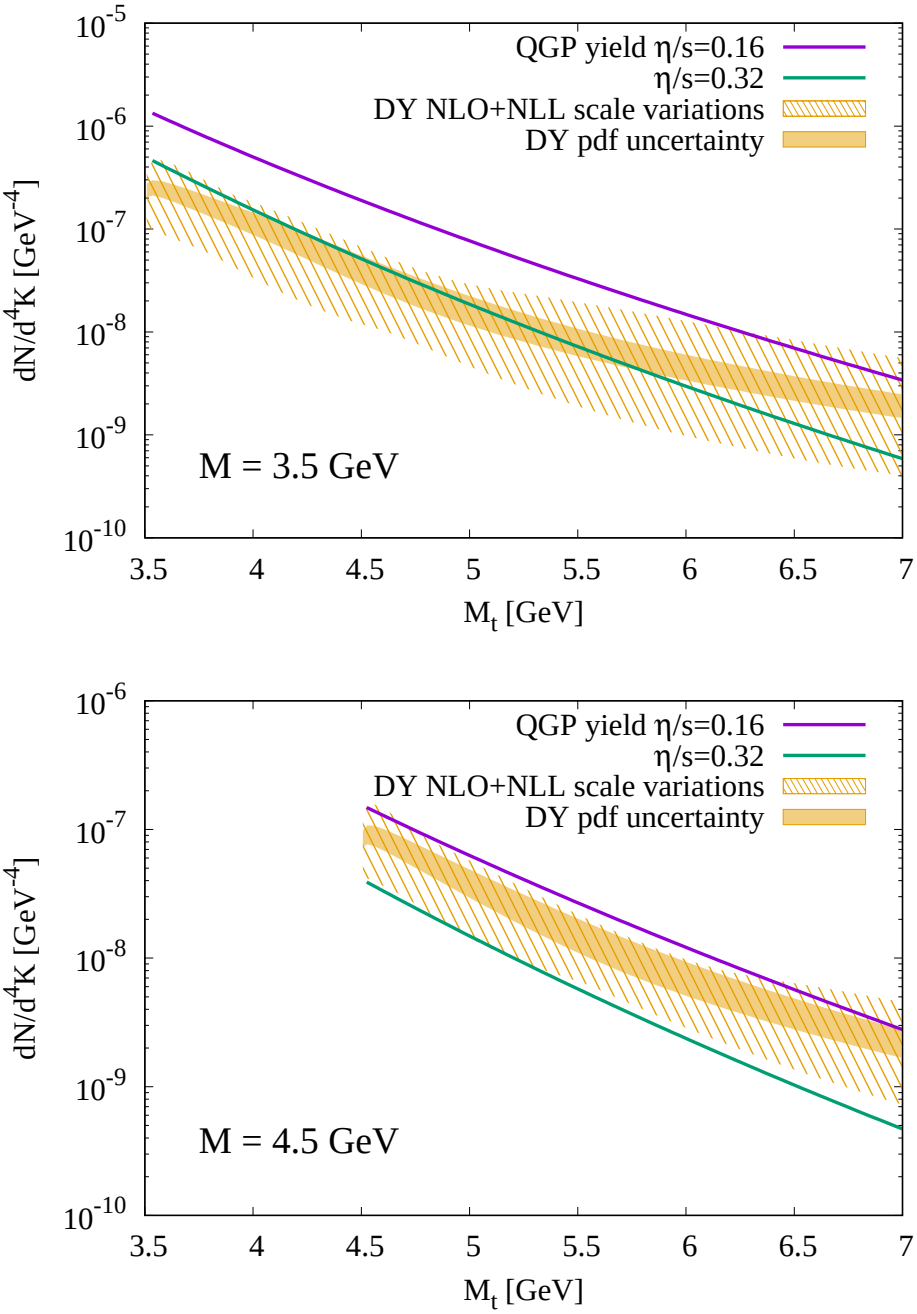

Figure 5.23: Comparison between the dilepton yield from production in the QGP and from the Drell-Yan process for two fixed values of the invariant mass $M = 3.5\,\mathrm{GeV}$ (top) and $M = 4.5\,\mathrm{GeV}$ (bottom). Lines: QGP production with pre-equilibrium dynamics and quark suppression taken into account, for $\eta/s = 0.16$ (upper line) and $\eta/s = 0.32$ (lower line). Dark shaded band: Drell Yan process, with uncertainty from the parton distribution function. Light shaded band: uncertainty on Drell-Yan from the renormalization and factorization scales. Both bands are obtained by taking the envelope of the results obtained by varying the model parameters.

On Fig. 5.22, we again compare our results with the production of dileptons by the Drell-Yan (DY) process using Drell-Yan Turbo [233]. Contrary to our previous DY calculation for the invariant mass spectrum, we now employ a resummation at small transverse momentum at next-to-leading logarithm (NLL) in addition to the NLO part. This is done in order to capture the transverse momentum k_t of the incoming partons more realistically. The uncertainty on the DY spectrum is again obtained by varying the renormalization and factorization scales by a factor two independently. We also take into account the uncertainty on the parton distribution function in the EPPS parametrization [54]. The main difference between thermal and DY dileptons is the normalization, which depends on the invariant mass M. Drell-Yan production is enhanced for larger values of M at a given M_t, contrary to thermal production. The physical explanation is that the momentum of the incoming partons responsible for Drell-Yan production is mostly longitudinal, so that smaller values of the transverse momentum k_t (corresponding to larger values of M at a given M_t) are preferred. The kinematics of thermal production is opposite: in the pre-equilibrium stage, longitudinal momenta are typically smaller than transverse momenta due to early-time anisotropy.

We compare both spectra in Fig. 5.23 for two values of M above the J/ψ peak, and for two values of η/s. We see that thermal production dominates over Drell-Yan for M up to $3.5\,\mathrm{GeV}$, at least for the lowest values of M_t. The precise value of M above which Drell-Yan dominates over thermal production depends on the value of η/s at early times.

Overall, we see that the spectrum dN/d^4K depends mostly on the transverse mass M_t. The underpopulation of quarks at early times results in a steeper M_t spectrum. The viscosity over entropy ratio, which determines the equilibration time of the QGP, can be inferred by measuring the slope of the spectrum. The anisotropy of the momentum distribution at early times breaks transverse mass scaling, by suppressing the production of higher invariant masses M. This is, however, a sub-leading effect compared to the overall suppression from the ideal spectrum due to departure from chemical equilibrium.

5.3.6 Pre-equilibrium dilepton polarization

The final observable which we investigate using our calculation is the angular distribution of single leptons in the final state. To this end, we come back to the dilepton production rate which we now express with an integrand fully differential in both the incoming quarks and the outgoing leptons:

$$\frac{dN}{d^4x d^4K} = \frac{e^4}{K^4}(\sum q_f^2) \int \frac{d^3p_1}{(2\pi)^3(2p_1)} \frac{d^3p_2}{(2\pi)^3(2p_2)} \frac{d^3p_3}{(2\pi)^3(2p_3)} \frac{d^3p_4}{(2\pi)^3(2p_4)} \tag{5.54}$$

$$f_1^q f_2^{\bar{q}} \, (2\pi)^4 \delta^{(4)}(p_1 + p_2 - K) \delta^{(4)}\left(K - p_3 - p_4\right) l_{\mu\nu} \Pi^{\mu\nu} \tag{5.55}$$

where p_1 and p_2 are the 4-momenta of the incoming quarks, and p_3 and p_4 are the ones of the outgoing leptons. The involved squared matrix element $l_{\mu\nu}\Pi^{\mu\nu}$ is defined as:

$$l_{\mu\nu}\Pi^{\mu\nu} \quad = \quad 32 N_c \left[(p_1.p_3)(p_2.p_4) + (p_1.p_4)(p_2.p_3) + (p_1.p_2)m^2\right] \tag{5.56}$$

We now define the relative incoming and outgoing 4-momenta u and v as:

$$u = p_1 - p_2, \quad v = p_3 - p_4 \tag{5.57}$$

These variables are illustrated on the cartoon of Fig. 5.24. The squared matrix element can then be rewritten:

$$l_{\mu\nu}\Pi^{\mu\nu} \quad = \quad 4N_c\left[M^4 + (u\cdot v)^2 + 2(M^2 - v^2)m^2\right] \tag{5.58}$$

where m is the lepton mass. As we did before, we make the approximation $m \approx 0\,\mathrm{GeV}/c^2$, so that:

$$l_{\mu\nu}\Pi^{\mu\nu} \sim 4N_c M^4\left(1 + \frac{(u\cdot v)^2}{M^4}\right) \tag{5.59}$$

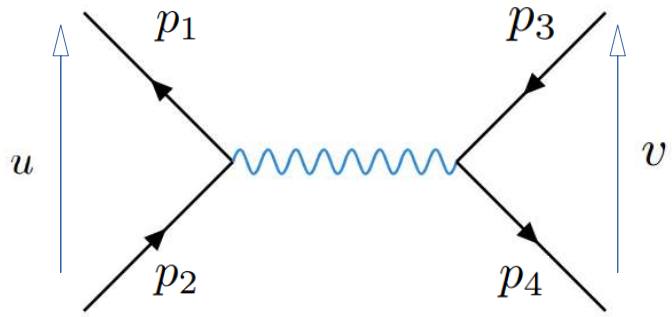

Figure 5.24: Illustration of the relative momentum between the incoming quarks u and the relative momentum between the outgoing leptons v.

We see from Eq.5.59 that the squared matrix element involves the scalar product between the relative incoming momentum $\vec{u}$ and the relative outgoing momentum $\vec{v}$. From this simple consideration, we get the expectation that the outgoing leptons will prefer to be emitted in a plane parallel to the one of the incoming quarks. In particular, if the incoming quarks belong to a plane normal to the longitudinal direction, the beam direction, then the outgoing leptons will be preferably emitted in a parallel plane, i.e. also normal to the longitudinal direction. This is particularly interesting regarding the distinction between pre-equilibrium and Drell-Yen dileptons. Indeed, as we saw in Sec.5.3, pre-equilibrium dileptons are emitted from quarks having mainly transverse momenta in the rest frame of a fluid cell. Hence, the emitted leptons will tend to also have mainly transverse momentum. On the other hand, the incoming quarks involved in the Drell-Yan process have mostly longitudinal momentum, and thus, so will the outgoing leptons. In other words, we expect in the case of pre-equilibrium emission that the production rate will be enhanced for transversely polarized virtual photons, while for Drell-Yan, it will be enhanced for longitudinally polarized virtual photons.

To try to quantify this effect, we look at an observable which is commonly used in polarization measurement; we go to the rest frame of the emitted dilepton and consider the angle θ between the positive lepton and the longitudinal direction, which is the beam direction. This is illustrated on the cartoon Fig. 5.25.

In experimental physics, this is known as the measurement of $\cos\theta^*$ in the Collin-Sopper frame [239]. In this frame, the quantization axis, i.e. the axis with respect to which

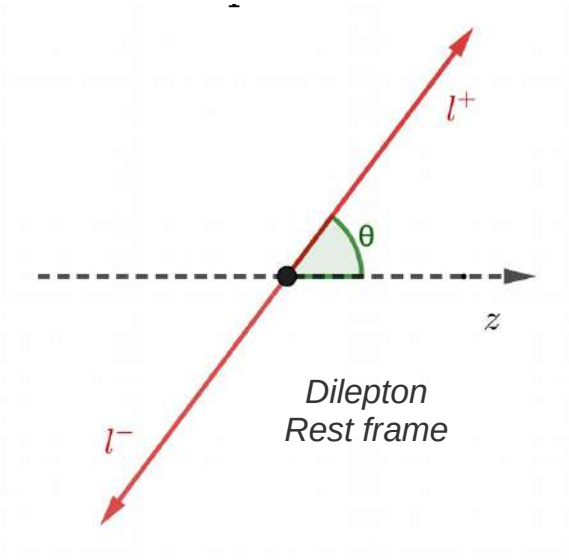

Figure 5.25: Illustration of the polarization angle θ in the dilepton rest frame.

we measure the angular distribution of leptons, is taken as the bisector between the two colliding beam directions. Indeed, in experimental setups, the two colliding beams are not perfectly aligned, so that the bisector is a sort of "mean" direction for the beam. In the ideal setup of our calculation, we assumed that the two beams were perfectly parallel, so that the bisector between the two colliding beams is just the longitudinal direction.

We start by considering the unintegrated production rate, dN/d^4xd^4K, i.e. the production rate of a single fluid cell at a given position and at a given time. We plot this rate as a function $\cos(\theta)$. The result is shown on Fig. 5.26. For illustration, the production rate is evaluated at $y = 0$ and $\tau = 0.2\,\mathrm{fm}/c$, which is a time at which there are enough quarks to start to significantly produce dileptons. The position of the fluid cell in the transverse plane is not important, since we assume a transversely homogeneous system. To get an idea of the effects of pre-equilibrium dynamics, we plot the calculated rate for different fixed values of the anisotropy parameter ξ. As we saw in Sec.5.3, a large value of ξ corresponds to quark distributions which are "squeezed" along the longitudinal direction, which is the case at early times. A value of $\xi = 1$ corresponds to momentum isotropy, which is the case of the ideal spectrum, i.e. for a fully thermalized medium.

As we can see on Fig. 5.26, the angular distribution exhibits a remarkable sensitivity to ξ, i.e. to momentum anisotropy. The thermalized case $\xi = 1$ corresponds to a flat line, which means that there is no preferred direction for the emission of the single leptons. However, for $\xi \gg 1$, the distribution shows a $1 - \cos(\theta)^2$ behavior, the peak at $\cos(\theta) = 0$ being more prominent the larger the parameter ξ is chosen to be. Hence, we see that this observable gives direct access to the momentum anisotropy at early times in heavy-ion collisions.

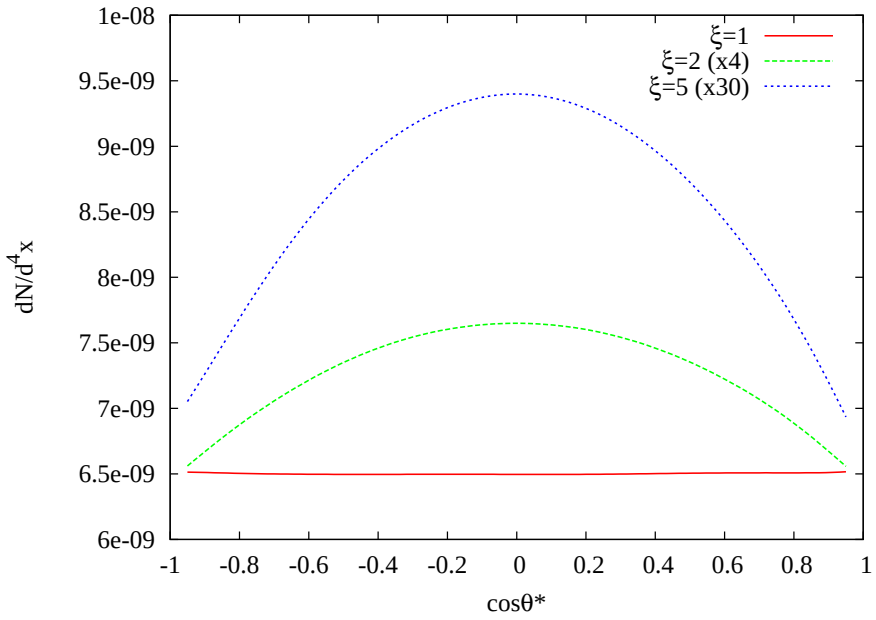

Figure 5.26: Distribution of $\cos(\theta)$ for production rate of thermal dileptons, for different values of the momentum anisotropy parameter ξ. The curve corresponding to $\xi = 1$ represents the equilibrium situation, i.e. full momentum isotropy. The plotted rates for $\xi = 2, 5$ and scaled to be more visible.

We now integrate the production rate over the space-time history of the system, considering the same assumptions as in previous sections 5.3.1 and 5.3.5. The results for $dN/dyd\cos(\theta)$ are shown on Fig. 5.27, in two different mass bins, at midrapidity for $0-5\%$ central Pb–Pb collisions. In this calculation, we considered $\eta/s = 0.16$. We also show a NLO Drell-Yan calculation for comparison. We see that our expectation is confirmed by the calculation: Drell-Yan and pre-equilibrium dileptons have opposite behaviors regarding this angular distribution. The Drell-Yan distribution peaks at $\cos(\theta) = \pm 1$ whereas the pre-equilibrium distribution peaks at $\cos(\theta) = 0$. In addition, the magnitude of the effect for the pre-equilibrium distribution, i.e. how much it deviates from a flat line, changes according to the considered mass bins. In particular, in the mass bin $2.5 < M < 3\,\mathrm{GeV}/c^2$ (Fig. 5.27, left), the magnitude of the variation of the rate in the angular spectrum is of order $\sim 16\%$. However, in the mass bin $4.5 < M < 5\,\mathrm{GeV}/c^2$ the effect is of order $\sim 30\%$. We thus see that the magnitude of the effect is larger in the higher invariant mass bins, i.e. $M \geq 4\,\mathrm{GeV}/c^2$. Incidentally, it is also in this mass range that Drell-Yan emission is expected to dominate over the pre-equilibrium emission. Hence, this angular distribution would be a good handle to disentangle the two contributions at high mass, possibly extending the available invariant mass range to measure pre-equilibrium dileptons. In addition, we see that the increase in magnitude of this polarization effect with mass indicates that we are probing more and more anisotropic quark distributions. This is intuitive, since as we saw previously, the higher the mass, the earlier the production time, and thus the more anisotropic the probed distribution is. Hence, the measurement of this observable as a function of mass would provide the first direct measure of plasma anisotropy as a function of time.

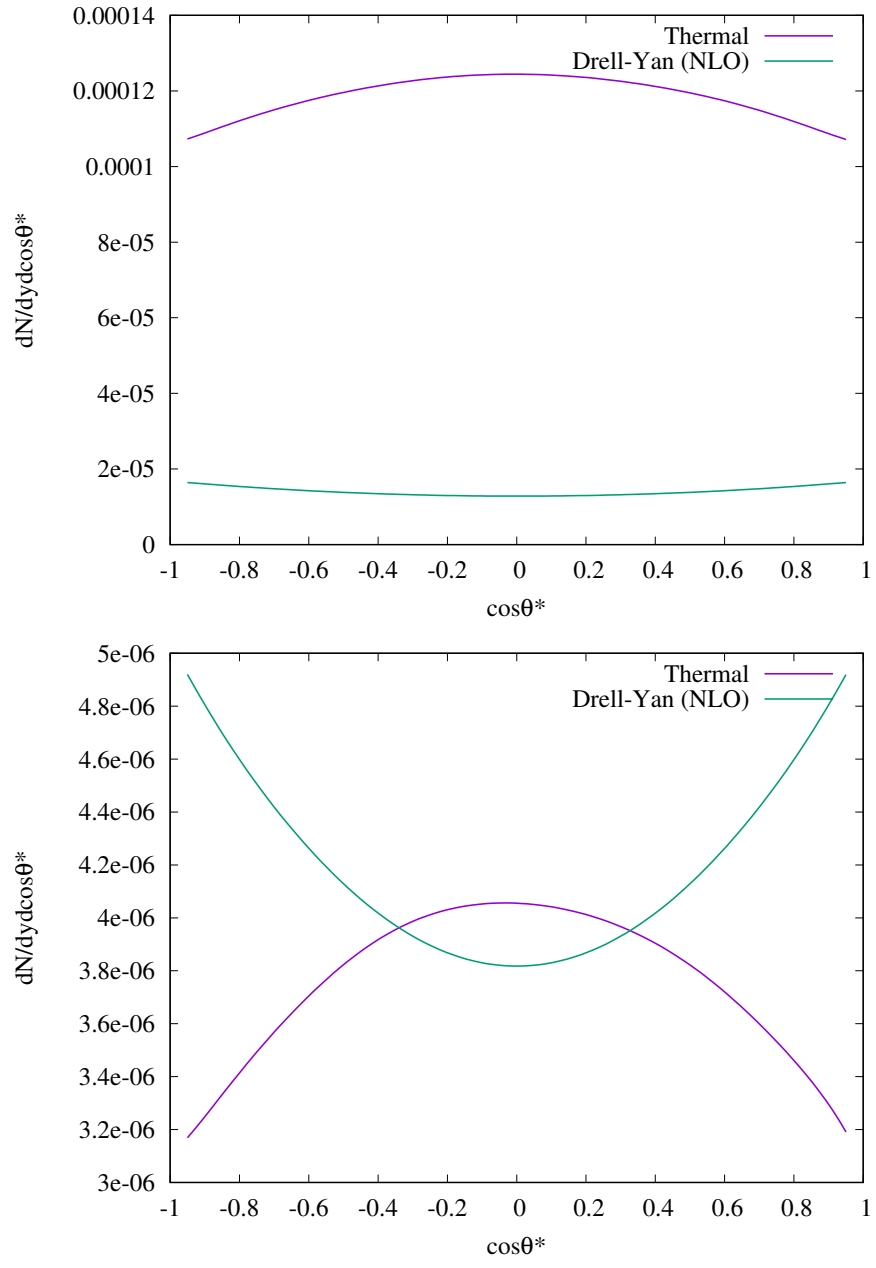

Figure 5.27: Distribution of $\cos(\theta)$ for the thermal dilepton yield and Drell-Yan calculated at NLO, (top) in the $2.5 < M < 3\,\mathrm{GeV}$ invariant mass bin and (bottom) in the $4.5 < M < 5\,\mathrm{GeV}/c^2$.

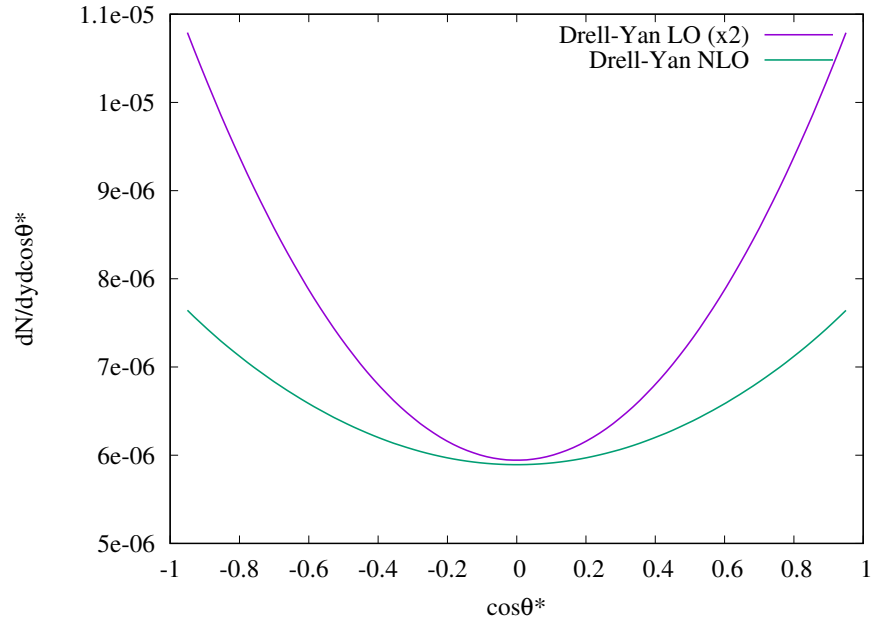

Figure 5.28: Distribution of $\cos(\theta)$ for Drell-Yan production in the $4.5 < M < 5\,\mathrm{GeV}/c^2$, comparing the shapes of the computations at LO and NLO.

One of the main caveats of our approach, as for the other considered observables, is the fact that we only consider a leading-order calculation for the pre-equilibrium and thermal contributions. At next-to-leading order (NLO), other real diagrams must be included, namely Compton scattering and NLO quark-anti-quark annihilation, as well as virtual corrections and interference with the LO amplitude (see Fig. 5.17). These diagrams are included in the NLO Drell-Yan calculation [233] which we compared to our thermal yield throughout this chapter. At LO, the incoming quarks in the Drell-Yan process are purely longitudinal, and the additional diagrams at NLO open the phase space for radiations carrying a non-vanishing transverse momentum. On Fig. 5.28, we compare the resulting angular distributions from LO and NLO Drell-Yan calculations, in the mass bin $4 < M < 5\,\mathrm{GeV}/c^2$. We see that the NLO contribution, which is at most a factor 2 larger than the LO, mitigates the polarization effect, due to the additional outgoing partons in the NLO diagrams. However, the qualitative behavior remains the same: the contribution peaks at $\cos(\theta) = \pm 1$. Indeed, the $\cos\theta$ observable in the Collin-Sopper frame is precisely designed to minimize the impact of transverse radiation [240]. Although this is only a qualitative argument and the two processes have different kinematics, we consider this comparison as an indication that our conclusions regarding this angular distribution observable remains valid. Namely, that it would provide a handle to disentangle Drell-Yan and pre-equilibrium emission at high mass, as well as give direct access to plasma anisotropy as a function of time.

5.4 Summary and outlook

Dilepton production in ultrarelativistic heavy-ion collisions provides valuable information about the early stages of heavy-ion collisions. Indeed, the production of high-mass dileptons occurs at earlier times and probes larger temperatures. In this chapter, we introduced a calculation of dilepton production in such collisions, including the contributions from the pre-equilbirium stage. This stage is characterized by an under-population of quarks with respect to gluons, and by an anisotropy of the quark and gluon distributions in momentum space, favoring large transverse momenta over longitudinal momenta. This calculation is based on a state-of-the-art QCD kinetics model. We found that the yield of intermediate mass dileptons as a function of mass and as a function of transverse mass M_t is sensitive to the chemical equilibration of the medium. In addition, the measurement of the inverse slope of the dilepton spectrum can provide an estimate of the effective viscosity (η/s) at early times, which differs from the viscosity measured through anisotropic flow analysis. In the context of pre-equilibrum, it is a parameter which controls the time scale of applicability of hydrodynamics, known as the hydrodynamization time. This time scale can be much shorter than the time scale of thermalization of the medium, and thus the medium can be modeled using hydrodynamics starting at early times, typically around $1\,\mathrm{fm}/c$. Moreover, the angular distribution of the single leptons which make up pre-equilibrum and thermal dileptons is especially sensitive to the momentum space anisotropy of quarks. We computed the distribution of the angle of leptons to the beam direction in the rest frame of the dilepton. This distribution has opposite behaviors for pre-equilibrum and Drell-Yan emissions. Hence, this distribution can be used as a handle to disentangle the two contributions to the spectrum of dileptons at high mass. In addition, this distribution also provides direct access to the anisotropy of the medium as a function of time. Future heavy-ion experiments, such as LHCb U2 with dimuons and ALICE 3 with dielectrons at the LHC, have the potential to overcome the challenges posed by the large background from semileptonic charm and beauty hadron decays. Detailed simulations of these detector setups and dilepton production in the intermediate mass range are necessary for precise performance assessments and should be considered in the design of the detectors. Finally, improvements can be made to our calculation by considering higher-order diagrams in the dilepton production amplitude, and the computation of dilepton production using a full simulation of the evolution of the medium would provide a better space-time modeling.

Conclusion

In this thesis, two different probes of the matter created in ultrarelatistic heavy-ion collisions were studied: J/ψ, and thermal dileptons.

The suppression or enhancement of J/ψ production in heavy-ion collisions compared to proton-proton collisions provides insights into the properties of the quark-gluon plasma. However, J/ψ can be produced either promptly or non-promptly. Measurement of non-prompt J/ψ provides information on b-hadron production in heavy-ion collisions. The addition of the MFT detector in ALICE for Run 3 allows to extend the separation of prompt and non-prompt J/ψ components to the forward rapidity region of the experiment. The MFT is confronted with challenges related to random noise of the silicon pixels. The control of this noise is of prime importance to ensure the good quality of the data taking. I implemented a workflow in the new software environment of ALICE which is able to monitor the noise level of the detector. Although more detailed studies are needed to evaluate the distribution of noisy pixels in the detector, no dramatic change over time in the global noise level of the detector has been seen since the last year of data taking. Abnormally large clusters, which were first seen in the pilot beam data of 2021, were found to be produced by beam physics. Although their contribution to the reconstructed tracks in the MFT is negligible, their distribution inside the ALPIDE sensors warrants further investigation.

In addition to the performance of the standalone MFT, a crucial point of effort, in view of the prompt-non-prompt J/ψ analysis, is to estimate the efficiency and purity of the matching between the MFT and the Muon spectrometer. I realised first estimates based on MC simulations and data fits, but further improved methods are currently being developed. Preliminary studies utilizing the latest data reconstruction of the 2022 ALICE data demonstrated the separation of prompt and non-prompt J/ψ components in proton-proton collisions, exploiting the vertexing performance of the MFT. Although resolution limitations affect the lowest transverse momentum range in the latest version of the reconstruction, the higher transverse momentum ranges exhibit agreement with other measurements within statistical uncertainties. The additional steps of optimization and error estimations, which are required for more robust results and towards a full analysis, were outlined in this thesis.

The second probe of interest in this thesis, thermal dileptons, was investigated in a phenomenology study. In particular, the impact of including contributions from the pre-equilibrium stage was examined. Intermediate mass dileptons were found to be largely sensitive to this early stage of heavy-ion collisions, such that their study provides valuable insights into the earl-time properties of the QGP. In particular, the invariant and transverse mass spectra of thermal dileptons including these early stages, are sensitive to the

chemical equilibration of the medium, and their inverse slope provides insights into hydrodynamization time of the QGP, i.e. the time scale of the applicability of a fluid description. The high-mass end of the thermal dilepton spectrum is competing with a background contribution from the Drell-Yan process. In addition, it was found that the angular distribution of the single leptons of the thermal dileptons offers a means to differentiate pre-equilibrium and Drell-Yan emission contributions at high mass. Finally, these angluar distributions in different mass ranges provide a direct measurement of the anisotropy of the medium as a function of time. Further developments in this topic should in particular aim at the estimation of the importance of NLO corrections. Future experiments, like LHCb U2 and ALICE 3, hold promise to carry out such challenging measurements but necessitate detailed simulations for performance assessments and detector design.

Bibliography

[1] F. Halzen and A. D. Martin, “QUARKS AND LEPTONS: AN INTRODUCTORY COURSE IN MODERN PARTICLE PHYSICS,”

[2] M. L. Mangano, “Introduction to QCD,”

[3] M. E. Peskin and D. V. Schroeder, “An Introduction to quantum field theory,” Addison-Wesley, 1995, ISBN 978-0-201-50397-5

[4] MissMJ and Cush for Wikimedia Commons, "Standard model of elementary particles", (2019)

[5] R. D. Field, “Applications of Perturbative QCD,” Front. Phys. **77** (1989), 1-366

[6] R. L. Workman *et al.* [Particle Data Group], “Review of Particle Physics,” PTEP **2022** (2022), 083C01 doi:10.1093/ptep/ptac097

[7] M. D. Schwartz, “Quantum Field Theory and the Standard Model,” Cambridge University Press, 2014, ISBN 978-1-107-03473-0, 978-1-107-03473-0

[8] J. Collins, “Foundations of perturbative QCD,” Camb. Monogr. Part. Phys. Nucl. Phys. Cosmol. **32** (2011), 1-624 Cambridge University Press, 2013, ISBN 978-1-107-64525-7, 978-1-107-64525-7, 978-0-521-85533-4, 978-1-139-09782-6

[9] D. J. Gross and F. Wilczek, “Ultraviolet Behavior of Nonabelian Gauge Theories,” Phys. Rev. Lett. **30** (1973), 1343-1346 doi:10.1103/PhysRevLett.30.1343

[10] H. D. Politzer, “Reliable Perturbative Results for Strong Interactions?,” Phys. Rev. Lett. **30** (1973), 1346-1349 doi:10.1103/PhysRevLett.30.1346

[11] V. Koch, “Aspects of chiral symmetry,” Int. J. Mod. Phys. E **6** (1997), 203-250 doi:10.1142/S0218301397000147 [arXiv:nucl-th/9706075 [nucl-th]].

[12] F. Tramontano, “Introduction to perturbative QCD,” CERN Yellow Rep. School Proc. **6** (2019), 43-100 doi:10.23730/CYRSP-2019-006.43

[13] O. Philipsen, “The QCD equation of state from the lattice,” Prog. Part. Nucl. Phys. **70** (2013), 55-107 doi:10.1016/j.ppnp.2012.09.003 [arXiv:1207.5999 [hep-lat]].

[14] P. Braun-Munzinger, V. Koch, T. Schäfer and J. Stachel, “Properties of hot and dense matter from relativistic heavy ion collisions,” Phys. Rept. **621** (2016), 76-126 doi:10.1016/j.physrep.2015.12.003 [arXiv:1510.00442 [nucl-th]].

[15] P. Bedaque and A. W. Steiner, "Sound velocity bound and neutron stars," Phys. Rev. Lett. **114** (2015) no.3, 031103 doi:10.1103/PhysRevLett.114.031103 [arXiv:1408.5116 [nucl-th]].

[16] D. H. Rischke, "The Quark gluon plasma in equilibrium," Prog. Part. Nucl. Phys. **52** (2004), 197-296 doi:10.1016/j.ppnp.2003.09.002 [arXiv:nucl-th/0305030 [nucl-th]].

[17] T. Kojo, "QCD equations of state and speed of sound in neutron stars," AAPPS Bull. **31** (2021) no.1, 11 doi:10.1007/s43673-021-00011-6 [arXiv:2011.10940 [nucl-th]].

[18] R. T. Co, E. Gonzalez and K. Harigaya, "Increasing Temperature toward the Completion of Reheating," JCAP **11** (2020), 038 doi:10.1088/1475-7516/2020/11/038 [arXiv:2007.04328 [astro-ph.CO]].

[19] K. Mukaida and M. Yamada, "Thermalization Process after Inflation and Effective Potential of Scalar Field," JCAP **02** (2016), 003 doi:10.1088/1475-7516/2016/02/003 [arXiv:1506.07661 [hep-ph]].

[20] T. Asaka, D. Grigoriev, V. Kuzmin and M. Shaposhnikov, "Late reheating, hadronic jets and baryogenesis," Phys. Rev. Lett. **92** (2004), 101303 doi:10.1103/PhysRevLett.92.101303 [arXiv:hep-ph/0310100 [hep-ph]].

[21] S. Mukherjee, Quark-matter fireballs hashed out in Protvino, (2012), https://cerncourier.com/a/quark-matter-fireballs-hashed-out-in-protvino/

[22] L. D. McLerran and B. Svetitsky, "Quark Liberation at High Temperature: A Monte Carlo Study of SU(2) Gauge Theory," Phys. Rev. D **24** (1981), 450 doi:10.1103/PhysRevD.24.450

[23] T. Bhattacharya, M. I. Buchoff, N. H. Christ, H. T. Ding, R. Gupta, C. Jung, F. Karsch, Z. Lin, R. D. Mawhinney and G. McGlynn, *et al.* "QCD Phase Transition with Chiral Quarks and Physical Quark Masses," Phys. Rev. Lett. **113** (2014) no.8, 082001 doi:10.1103/PhysRevLett.113.082001 [arXiv:1402.5175 [hep-lat]].

[24] A. Bazavov *et al.* [HotQCD], "Equation of state in (2+1)-flavor QCD," Phys. Rev. D **90** (2014), 094503 doi:10.1103/PhysRevD.90.094503 [arXiv:1407.6387 [hep-lat]].

[25] S. Borsanyi, Z. Fodor, C. Hoelbling, S. D. Katz, S. Krieg and K. K. Szabo, "Full result for the QCD equation of state with 2+1 flavors," Phys. Lett. B **730** (2014), 99-104 doi:10.1016/j.physletb.2014.01.007 [arXiv:1309.5258 [hep-lat]].

[26] K. Adcox *et al.* [PHENIX], "Formation of dense partonic matter in relativistic nucleus-nucleus collisions at RHIC: Experimental evaluation by the PHENIX collaboration," Nucl. Phys. A **757** (2005), 184-283 doi:10.1016/j.nuclphysa.2005.03.086 [arXiv:nucl-ex/0410003 [nucl-ex]].

[27] J. Adams *et al.* [STAR], "Experimental and theoretical challenges in the search for the quark gluon plasma: The STAR Collaboration's critical assessment of the evidence from RHIC collisions," Nucl. Phys. A **757** (2005), 102-183 doi:10.1016/j.nuclphysa.2005.03.085 [arXiv:nucl-ex/0501009 [nucl-ex]].

[28] B. B. Back *et al.* [PHOBOS], "The PHOBOS perspective on discoveries at RHIC," Nucl. Phys. A **757** (2005), 28-101 doi:10.1016/j.nuclphysa.2005.03.084 [arXiv:nucl-ex/0410022 [nucl-ex]].

[29] I. Arsene *et al.* [BRAHMS], "Quark gluon plasma and color glass condensate at RHIC? The Perspective from the BRAHMS experiment," Nucl. Phys. A **757** (2005), 1-27 doi:10.1016/j.nuclphysa.2005.02.130 [arXiv:nucl-ex/0410020 [nucl-ex]].

[30] G. Martinez, "Advances in Quark Gluon Plasma," [arXiv:1304.1452 [nucl-ex]].

[31] B. Betz, "Jet Propagation and Mach-Cone Formation in (3+1)-dimensional Ideal Hydrodynamics," [arXiv:0910.4114 [nucl-th]].

[32] J. Berges, M. P. Heller, A. Mazeliauskas and R. Venugopalan, "QCD thermalization: Ab initio approaches and interdisciplinary connections," Rev. Mod. Phys. **93** (2021) no.3, 035003 doi:10.1103/RevModPhys.93.035003 [arXiv:2005.12299 [hep-th]].

[33] S. Acharya *et al.* [ALICE], "Anisotropic flow of identified particles in Pb-Pb collisions at $\sqrt{s_{\rm NN}} = 5.02$ TeV," JHEP **09** (2018), 006 doi:10.1007/JHEP09(2018)006 [arXiv:1805.04390 [nucl-ex]].

[34] Y. Akiba, A. Angerami, H. Caines, A. Frawley, U. Heinz, B. Jacak, J. Jia, T. Lappi, W. Li and A. Majumder, *et al.* "The Hot QCD White Paper: Exploring the Phases of QCD at RHIC and the LHC," [arXiv:1502.02730 [nucl-ex]].

[35] J. D. Bjorken, "Highly Relativistic Nucleus-Nucleus Collisions: The Central Rapidity Region," Phys. Rev. D **27** (1983), 140-151 doi:10.1103/PhysRevD.27.140

[36] J. Y. Ollitrault, "Relativistic hydrodynamics for heavy-ion collisions," Eur. J. Phys. **29** (2008), 275-302 doi:10.1088/0143-0807/29/2/010 [arXiv:0708.2433 [nucl-th]].

[37] T. Lappi and L. McLerran, "Some features of the glasma," Nucl. Phys. A **772** (2006), 200-212 doi:10.1016/j.nuclphysa.2006.04.001 [arXiv:hep-ph/0602189 [hep-ph]].

[38] A. Kovner, L. D. McLerran and H. Weigert, "Gluon production from nonAbelian Weizsacker-Williams fields in nucleus-nucleus collisions," Phys. Rev. D **52** (1995), 6231-6237 doi:10.1103/PhysRevD.52.6231 [arXiv:hep-ph/9502289 [hep-ph]].

[39] A. Kovner, L. D. McLerran and H. Weigert, "Gluon production at high transverse momentum in the McLerran-Venugopalan model of nuclear structure functions," Phys. Rev. D **52** (1995), 3809-3814 doi:10.1103/PhysRevD.52.3809 [arXiv:hep-ph/9505320 [hep-ph]].

[40] J. Feltesse, "Introduction to deep inelastic scattering: Past and present," doi:10.3204/DESY-PROC-2012-02/6

[41] R. K. Ellis and W. J. Stirling, "QCD and collider physics," FERMILAB-CONF-90-164-T.

[42] J. D. Bjorken, "Asymptotic Sum Rules at Infinite Momentum," Phys. Rev. **179** (1969), 1547-1553 doi:10.1103/PhysRev.179.1547

[43] V. N. Gribov and L. N. Lipatov, "Deep inelastic e p scattering in perturbation theory," Sov. J. Nucl. Phys. **15** (1972), 438-450 IPTI-381-71.

[44] Y. L. Dokshitzer, "Calculation of the Structure Functions for Deep Inelastic Scattering and e+ e- Annihilation by Perturbation Theory in Quantum Chromodynamics.," Sov. Phys. JETP **46** (1977), 641-653

[45] G. Altarelli and G. Parisi, "Asymptotic Freedom in Parton Language," Nucl. Phys. B **126** (1977), 298-318 doi:10.1016/0550-3213(77)90384-4

[46] L. Del Debbio, "Parton distributions in the LHC era," EPJ Web Conf. **175** (2018), 01006 doi:10.1051/epjconf/201817501006

[47] A. Rothkopf, "Heavy Quarkonium in Extreme Conditions," Phys. Rept. **858** (2020), 1-117 doi:10.1016/j.physrep.2020.02.006 [arXiv:1912.02253 [hep-ph]].

[48] J. J. Ethier and E. R. Nocera, "Parton Distributions in Nucleons and Nuclei," Ann. Rev. Nucl. Part. Sci. **70** (2020), 43-76 doi:10.1146/annurev-nucl-011720-042725 [arXiv:2001.07722 [hep-ph]].

[49] L. Apolinário, Y. J. Lee and M. Winn, "Heavy quarks and jets as probes of the QGP," Prog. Part. Nucl. Phys. **127** (2022), 103990 doi:10.1016/j.ppnp.2022.103990 [arXiv:2203.16352 [hep-ph]].

[50] Kollar, M. Top-Quark and Top-Squark Production at Hadron Colliders at Electroweak NLO. (2007,1)

[51] N. Armesto, "Nuclear shadowing," J. Phys. G **32** (2006), R367-R394 doi:10.1088/0954-3899/32/11/R01 [arXiv:hep-ph/0604108 [hep-ph]].

[52] F. Gelis, E. Iancu, J. Jalilian-Marian and R. Venugopalan, "The Color Glass Condensate," Ann. Rev. Nucl. Part. Sci. **60** (2010), 463-489 doi:10.1146/annurev.nucl.010909.083629 [arXiv:1002.0333 [hep-ph]].

[53] B. Schmookler *et al.* [CLAS], "Modified structure of protons and neutrons in correlated pairs," Nature **566** (2019) no.7744, 354-358 doi:10.1038/s41586-019-0925-9 [arXiv:2004.12065 [nucl-ex]].

[54] K. J. Eskola, P. Paakkinen, H. Paukkunen and C. A. Salgado, "EPPS16: Nuclear parton distributions with LHC data," Eur. Phys. J. C **77** (2017) no.3, 163 doi:10.1140/epjc/s10052-017-4725-9 [arXiv:1612.05741 [hep-ph]].

[55] M. L. Miller, K. Reygers, S. J. Sanders and P. Steinberg, "Glauber modeling in high energy nuclear collisions," Ann. Rev. Nucl. Part. Sci. **57** (2007), 205-243 doi:10.1146/annurev.nucl.57.090506.123020 [arXiv:nucl-ex/0701025 [nucl-ex]].

[56] J. Adam *et al.* [ALICE], "Centrality dependence of the pseudorapidity density distribution for charged particles in Pb-Pb collisions at $\sqrt{s_{\rm NN}} = 5.02$ TeV," Phys. Lett. B **772** (2017), 567-577 doi:10.1016/j.physletb.2017.07.017 [arXiv:1612.08966 [nucl-ex]].

[57] J. Y. Ollitrault, "Anisotropy as a signature of transverse collective flow," Phys. Rev. D **46** (1992), 229-245 doi:10.1103/PhysRevD.46.229

[58] R. Pasechnik and M. Šumbera, "Phenomenological Review on Quark-Gluon Plasma: Concepts vs. Observations," Universe **3** (2017) no.1, 7 doi:10.3390/universe3010007 [arXiv:1611.01533 [hep-ph]].

[59] J. D. Bjorken, "Energy Loss of Energetic Partons in Quark - Gluon Plasma: Possible Extinction of High p(t) Jets in Hadron - Hadron Collisions," FERMILAB-PUB-82-059-THY.

[60] N. Brambilla, A. Pineda, J. Soto and A. Vairo, "Potential NRQCD: An Effective theory for heavy quarkonium," Nucl. Phys. B **566** (2000), 275 doi:10.1016/S0550-3213(99)00693-8 [arXiv:hep-ph/9907240 [hep-ph]].

[61] E. Braaten, "Introduction to the NRQCD factorization approach to heavy quarkonium," [arXiv:hep-ph/9702225 [hep-ph]].

[62] J. J. Aubert *et al.* [E598], "Experimental Observation of a Heavy Particle J," Phys. Rev. Lett. **33** (1974), 1404-1406 doi:10.1103/PhysRevLett.33.1404

[63] J. E. Augustin *et al.* [SLAC-SP-017], "Discovery of a Narrow Resonance in e^+e^- Annihilation," Phys. Rev. Lett. **33** (1974), 1406-1408 doi:10.1103/PhysRevLett.33.1406

[64] L. D. Landau, "On the angular momentum of a system of two photons," Dokl. Akad. Nauk SSSR **60** (1948) no.2, 207-209 doi:10.1016/B978-0-08-010586-4.50070-5

[65] Yang, C. Selection Rules for the Dematerialization of a Particle into Two Photons. *Phys. Rev.*. **77**, 242-245 (1950,1), https://link.aps.org/doi/10.1103/PhysRev.77.242

[66] CERN-LHCC-2015-001, A. Technical Design Report for the Muon Forward Tracker. (2015), https://cds.cern.ch/record/1981898

[67] A. Andronic, F. Arleo, R. Arnaldi, A. Beraudo, E. Bruna, D. Caffarri, Z. C. del Valle, J. G. Contreras, T. Dahms and A. Dainese, *et al.* "Heavy-flavour and quarkonium production in the LHC era: from proton–proton to heavy-ion collisions," Eur. Phys. J. C **76** (2016) no.3, 107 doi:10.1140/epjc/s10052-015-3819-5 [arXiv:1506.03981 [nucl-ex]].

[68] J. P. Lansberg, "New Observables in Inclusive Production of Quarkonia," Phys. Rept. **889** (2020), 1-106 doi:10.1016/j.physrep.2020.08.007 [arXiv:1903.09185 [hep-ph]].

[69] C. Quigg, "Realizing the potential of quarkonium," AIP Conf. Proc. **424** (1998) no.1, 173-188 doi:10.1063/1.55117 [arXiv:hep-ph/9707493 [hep-ph]].

[70] Eichten, E., Gottfried, K., Kinoshita, T., Kogut, J., Lane, K. & Yan, T. Spectrum of Charmed Quark-Antiquark Bound States. *Phys. Rev. Lett.*. **34**, 369-372 (1975,2), https://link.aps.org/doi/10.1103/PhysRevLett.34.369

[71] L. Kluberg and H. Satz, "Color Deconfinement and Charmonium Production in Nuclear Collisions," doi:10.1007/978-3-642-01539-7_13 [arXiv:0901.3831 [hep-ph]].

[72] F. Karsch, "Deconfinement and quarkonium suppression," Eur. Phys. J. C **43** (2005), 35-43 doi:10.1140/epjc/s2005-02192-2 [arXiv:hep-lat/0502014 [hep-lat]].

[73] B. A. Thacker and G. P. Lepage, "Heavy quark bound states in lattice QCD," Phys. Rev. D **43** (1991), 196-208 doi:10.1103/PhysRevD.43.196

[74] M. B. Einhorn and S. D. Ellis, "Hadronic Production of the New Resonances: Probing Gluon Distributions," Phys. Rev. D **12** (1975), 2007 doi:10.1103/PhysRevD.12.2007

[75] C. H. Chang, "Hadronic Production of J/ψ Associated With a Gluon," Nucl. Phys. B **172** (1980), 425-434 doi:10.1016/0550-3213(80)90175-3

[76] H. Fritzsch, "Producing Heavy Quark Flavors in Hadronic Collisions: A Test of Quantum Chromodynamics," Phys. Lett. B **67** (1977), 217-221 doi:10.1016/0370-2693(77)90108-3

[77] J. F. Amundson, O. J. P. Eboli, E. M. Gregores and F. Halzen, "Colorless states in perturbative QCD: Charmonium and rapidity gaps," Phys. Lett. B **372** (1996), 127-132 doi:10.1016/0370-2693(96)00035-4 [arXiv:hep-ph/9512248 [hep-ph]].

[78] B. Abelev *et al.* [ALICE], "J/ψ polarization in pp collisions at $\sqrt{s} = 7$ TeV," Phys. Rev. Lett. **108** (2012), 082001 doi:10.1103/PhysRevLett.108.082001 [arXiv:1111.1630 [hep-ex]].

[79] M. Cacciari, M. Greco and P. Nason, "The p(T) spectrum in heavy-flavour hadroproduction," JHEP **9805** (1998) 007 [arXiv:hep-ph/9803400]; M. Cacciari, S. Frixione and P. Nason, "The p(T) spectrum in heavy-flavor photoproduction," JHEP **0103** (2001) 006 [arXiv:hep-ph/0102134].

[80] V. Khachatryan *et al.* [CMS], "Measurement of the total and differential inclusive B^+ hadron cross sections in pp collisions at $\sqrt{s}$ = 13 TeV," Phys. Lett. B **771** (2017), 435-456 doi:10.1016/j.physletb.2017.05.074 [arXiv:1609.00873 [hep-ex]].

[81] R. Aaij *et al.* [LHCb], "Measurement of the b-quark production cross-section in 7 and 13 TeV pp collisions," Phys. Rev. Lett. **118** (2017) no.5, 052002 [erratum: Phys. Rev. Lett. **119** (2017) no.16, 169901] doi:10.1103/PhysRevLett.118.052002 [arXiv:1612.05140 [hep-ex]].

[82] B. Abelev *et al.* [ALICE], "Measurement of prompt J/ψ and beauty hadron production cross sections at midrapidity in pp collisions at $\sqrt{s} = 7$ TeV," JHEP **11** (2012), 065 doi:10.1007/JHEP11(2012)065 [arXiv:1205.5880 [hep-ex]].

[83] T. Matsui and H. Satz, "J/ψ Suppression by Quark-Gluon Plasma Formation," Phys. Lett. B **178** (1986), 416-422 doi:10.1016/0370-2693(86)91404-8

[84] J. D. Jackson, "Classical Electrodynamics," Wiley, 1998, ISBN 978-0-471-30932-1

[85] M. L. Bellac, "Thermal Field Theory," Cambridge University Press, 2011, ISBN 978-0-511-88506-8, 978-0-521-65477-7 doi:10.1017/CBO9780511721700

[86] A. Mocsy, P. Petreczky and M. Strickland, "Quarkonia in the Quark Gluon Plasma," Int. J. Mod. Phys. A **28** (2013), 1340012 doi:10.1142/S0217751X13400125 [arXiv:1302.2180 [hep-ph]].

[87] A. Mocsy, "Potential Models for Quarkonia," Eur. Phys. J. C **61** (2009), 705-710 doi:10.1140/epjc/s10052-008-0847-4 [arXiv:0811.0337 [hep-ph]].

[88] L. Grandchamp and R. Rapp, "Thermal versus direct J / Psi production in ultrarelativistic heavy ion collisions," Phys. Lett. B **523** (2001), 60-66 doi:10.1016/S0370-2693(01)01311-9 [arXiv:hep-ph/0103124 [hep-ph]].

[89] X. Zhao and R. Rapp, "Charmonium in Medium: From Correlators to Experiment," Phys. Rev. C **82** (2010), 064905 doi:10.1103/PhysRevC.82.064905 [arXiv:1008.5328 [hep-ph]].

[90] O. Kaczmarek, "Screening at finite temperature and density," PoS **CPOD07** (2007), 043 doi:10.22323/1.047.0043 [arXiv:0710.0498 [hep-lat]].

[91] P. Petreczky and K. Petrov, "Free energy of a static quark anti-quark pair and the renormalized Polyakov loop in three flavor QCD," Phys. Rev. D **70** (2004), 054503 doi:10.1103/PhysRevD.70.054503 [arXiv:hep-lat/0405009 [hep-lat]].

[92] A. Tumasyan *et al.* [CMS], "Fragmentation of jets containing a prompt J/ψ meson in PbPb and pp collisions at $\sqrt{s_{\mathrm{NN}}} = 5.02$ TeV," Phys. Lett. B **825** (2022), 136842 doi:10.1016/j.physletb.2021.136842 [arXiv:2106.13235 [hep-ex]].

[93] S. Acharya *et al.* [ALICE], "J/ψ elliptic and triangular flow in Pb-Pb collisions at $\sqrt{s_{\mathrm{NN}}}$ = 5.02 TeV," JHEP **10** (2020), 141 doi:10.1007/JHEP10(2020)141 [arXiv:2005.14518 [nucl-ex]].

[94] B. B. Abelev *et al.* [ALICE], "Centrality, rapidity and transverse momentum dependence of J/ψ suppression in Pb-Pb collisions at $\sqrt{s_{\mathrm{NN}}}$=2.76 TeV," Phys. Lett. B **734** (2014), 314-327 doi:10.1016/j.physletb.2014.05.064 [arXiv:1311.0214 [nucl-ex]].

[95] R. L. Thews, M. Schroedter and J. Rafelski, "Enhanced J/ψ production in deconfined quark matter," Phys. Rev. C **63** (2001), 054905 doi:10.1103/PhysRevC.63.054905 [arXiv:hep-ph/0007323 [hep-ph]].

[96] P. Braun-Munzinger and J. Stachel, "(Non)thermal aspects of charmonium production and a new look at J / psi suppression," Phys. Lett. B **490** (2000), 196-202 doi:10.1016/S0370-2693(00)00991-6 [arXiv:nucl-th/0007059 [nucl-th]].

[97] A. Andronic, P. Braun-Munzinger, K. Redlich and J. Stachel, "Decoding the phase structure of QCD via particle production at high energy," Nature **561** (2018) no.7723, 321-330 doi:10.1038/s41586-018-0491-6 [arXiv:1710.09425 [nucl-th]].

[98] P. Braun-Munzinger and J. Stachel, "The quest for the quark-gluon plasma," Nature **448** (2007), 302-309 doi:10.1038/nature06080

[99] R. Rapp and X. Du, "Theoretical Perspective on Quarkonia from SPS via RHIC to LHC," Nucl. Phys. A **967** (2017), 216-224 doi:10.1016/j.nuclphysa.2017.05.097 [arXiv:1704.07923 [hep-ph]].

[100] S. Acharya *et al.* [ALICE], "Measurements of inclusive J/ψ production at midrapidity and forward rapidity in Pb$-$Pb collisions at $\sqrt{s_{\mathrm{NN}}}$ = 5.02 TeV," [arXiv:2303.13361 [nucl-ex]].

[101] X. Du and R. Rapp, "Sequential Regeneration of Charmonia in Heavy-Ion Collisions," Nucl. Phys. A **943** (2015), 147-158 doi:10.1016/j.nuclphysa.2015.09.006 [arXiv:1504.00670 [hep-ph]].

[102] K. Zhou, N. Xu, Z. Xu and P. Zhuang, "Medium effects on charmonium production at ultrarelativistic energies available at the CERN Large Hadron Collider," Phys. Rev. C **89** (2014) no.5, 054911 doi:10.1103/PhysRevC.89.054911 [arXiv:1401.5845 [nucl-th]].

[103] M. He, B. Wu and R. Rapp, "Collectivity of J/ψ Mesons in Heavy-Ion Collisions," Phys. Rev. Lett. **128** (2022) no.16, 162301 doi:10.1103/PhysRevLett.128.162301 [arXiv:2111.13528 [nucl-th]].

[104] H. Hushnud [ALICE], "Overview of quarkonium production with ALICE at the LHC," [arXiv:2208.14757 [nucl-ex]].

[105] [ALICE], "$\psi(2S)$ suppression in Pb-Pb collisions at the LHC," [arXiv:2210.08893 [nucl-ex]].

[106] B. Alessandro *et al.* [NA50], "Charmonium production and nuclear absorption in p-A interactions at 450-GeV," Eur. Phys. J. C **33** (2004), 31-40 doi:10.1140/epjc/s2003-01539-y

[107] F. Arleo and S. Peigne, "Heavy-quarkonium suppression in p-A collisions from parton energy loss in cold QCD matter," JHEP **03** (2013), 122 doi:10.1007/JHEP03(2013)122 [arXiv:1212.0434 [hep-ph]].

[108] E. G. Ferreiro, F. Fleuret, J. P. Lansberg and A. Rakotozafindrabe, "Impact of the Nuclear Modification of the Gluon Densities on J/ψ production in pPb collisions at $\sqrt{s_{NN}} = 5$ TeV," Phys. Rev. C **88** (2013) no.4, 047901 doi:10.1103/PhysRevC.88.047901 [arXiv:1305.4569 [hep-ph]].

[109] Evans, L. & Bryant, P. LHC Machine. *Journal Of Instrumentation*. **3**, S08001 (2008,8)

[110] M. Vretenar, J. Vollaire, R. Scrivens, C. Rossi, F. Roncarolo, S. Ramberger, U. Raich, B. Puccio, D. Nisbet and R. Mompo, *et al.* "Linac4 design report," CERN, 2020, ISBN 978-92-9083-579-0, 978-92-9083-580-6 doi:10.23731/CYRM-2020-006

[111] K. H. Reich, "The CERN Proton Synchrotron Booster," IEEE Trans. Nucl. Sci. **16** (1969), 959-961 doi:10.1109/TNS.1969.4325414

[112] W. Fischer and J. M. Jowett, "Ion Colliders," Rev. Accel. Sci. Tech. **7** (2014), 49-76 doi:10.1142/S1793626814300047

[113] Esma Mobs. "The CERN Accelerator Complex". In: Open-Pho-Accel-2016-009, Open-Pho-a (2018).

[114] R. Steerenberg and HCPSS2020, "Course on Accelerator Physics for CERN-Fermilab Summer School HCPSS2020." https://indico.fnal.gov/event/43762/, August 2020.

[115] G. Aad *et al.* [ATLAS], "The ATLAS Experiment at the CERN Large Hadron Collider," JINST **3** (2008), S08003 doi:10.1088/1748-0221/3/08/S08003

[116] S. Chatrchyan *et al.* [CMS], "The CMS Experiment at the CERN LHC," JINST **3** (2008), S08004 doi:10.1088/1748-0221/3/08/S08004

[117] A. A. Alves, Jr. *et al.* [LHCb], "The LHCb Detector at the LHC," JINST **3** (2008), S08005 doi:10.1088/1748-0221/3/08/S08005

[118] G. Apollinari, O. Brüning, T. Nakamoto and L. Rossi, "High Luminosity Large Hadron Collider HL-LHC," CERN Yellow Rep. (2015) no.5, 1-19 doi:10.5170/CERN-2015-005.1 [arXiv:1705.08830 [physics.acc-ph]].

[119] K. Aamodt *et al.* [ALICE], "The ALICE experiment at the CERN LHC," JINST **3** (2008), S08002 doi:10.1088/1748-0221/3/08/S08002

[120] Arturo Tauro. "ALICE Schematics". General Photo. May 2017

[121] B. Abelev *et al.* [ALICE], "Technical Design Report for the Upgrade of the ALICE Inner Tracking System," J. Phys. G **41** (2014), 087002 doi:10.1088/0954-3899/41/8/087002

[122] C. Lippmann [ALICE], "Upgrade of the ALICE Time Projection Chamber," CERN-LHCC-2013-020.

[123] A. Akindinov, A. Alici, A. Agostinelli, P. Antonioli, S. Arcelli, M. Basile, F. Bellini, G. Cara Romeo, L. Cifarelli and F. Cindolo, *et al.* "Performance of the ALICE Time-Of-Flight detector at the LHC," Eur. Phys. J. Plus **128** (2013), 44 doi:10.1140/epjp/i2013-13044-x

[124] S. Acharya *et al.* [ALICE], "The ALICE Transition Radiation Detector: construction, operation, and performance," Nucl. Instrum. Meth. A **881** (2018), 88-127 doi:10.1016/j.nima.2017.09.028 [arXiv:1709.02743 [physics.ins-det]].

[125] P. Cortese *et al.* [ALICE], "ALICE electromagnetic calorimeter technical design report," CERN-LHCC-2008-014.

[126] G. Dellacasa *et al.* [ALICE], "ALICE technical design report of the photon spectrometer (PHOS)," CERN-LHCC-99-04.

[127] G. Volpe [ALICE], "The High Momentum Particle IDentification (HMPID) detector PID performance and its contribution to the ALICE physics program," Nucl. Instrum. Meth. A **876** (2017), 133-136 doi:10.1016/j.nima.2017.02.037

[128] A. I. Maevskaya [ALICE], "Fast Interaction Trigger for the upgrade of the ALICE experiment at CERN: design and performance," EPJ Web Conf. **204** (2019), 11003 doi:10.1051/epjconf/201920411003 [arXiv:1812.00594 [physics.ins-det]].

[129] G. Dellacasa *et al.* [ALICE], "ALICE technical design report of the zero degree calorimeter (ZDC)," CERN-LHCC-99-05.

[130] C. Finck [ALICE Muon Spectrometer], "The muon spectrometer of the ALICE," J. Phys. Conf. Ser. **50** (2006), 397-401 doi:10.1088/1742-6596/50/1/056

[131] Maevskaya, A., the ALICE collaboration. ALICE FIT Data Processing and Performance during LHC Run 3. Phys. Atom. Nuclei 84, 579–584 (2021). https://doi.org/10.1134/S1063778821040189

[132] A Addendum of the Letter of Intent for the upgrade of the ALICE experiment : The Muon Forward Tracker. (CERN,2013), https://cds.cern.ch/record/1592659

[133] B. B. Abelev *et al.* [ALICE], "Performance of the ALICE Experiment at the CERN LHC," Int. J. Mod. Phys. A **29** (2014), 1430044 doi:10.1142/S0217751X14300440 [arXiv:1402.4476 [nucl-ex]].

[134] [ALICE], "ALICE upgrades during the LHC Long Shutdown 2," [arXiv:2302.01238 [physics.ins-det]].

[135] P. Buncic, M. Krzewicki and P. Vande Vyvre, “Technical Design Report for the Upgrade of the Online-Offline Computing System,” CERN-LHCC-2015-006.

[136] CERN-LHCC-2015-001. Technical Design Report for the Muon Forward Tracker. (2015), https://cds.cern.ch/record/1981898

[137] A. Tumasyan *et al.* [CMS], “Observation of the B_c^+ Meson in Pb-Pb and pp Collisions at $\sqrt{s_{NN}}$=5.02 TeV and Measurement of its Nuclear Modification Factor,” Phys. Rev. Lett. **128** (2022) no.25, 252301 doi:10.1103/PhysRevLett.128.252301 [arXiv:2201.02659 [hep-ex]].

[138] ALICE ITS ALPIDE development team, ALPIDE Operations Manual. (2016), https://sunba2.ba.infn.it/MOSAIC/ALICE-ITS/Documents/ALPIDE-operations-manual-version-0_3.pdf, Version: 0.3

[139] S. Senyukov, J. Baudot, A. Besson, G. Claus, L. Cousin, A. Dorokhov, W. Dulinski, M. Goffe, C. Hu-Guo and M. Winter, “Charged particle detection performances of CMOS pixel sensors produced in a 0.18νm process with a high resistivity epitaxial layer,” Nucl. Instrum. Meth. A **730** (2013), 115-118 doi:10.1016/j.nima.2013.03.017 [arXiv:1301.0515 [physics.ins-det]].

[140] Ballin, J. et al. Monolithic Active Pixel Sensors (MAPS) in a Quadruple Well Technology for Nearly 100

[141] Reidt, F. Studies for the ALICE Inner Tracking System Upgrade. (2016), https://cds.cern.ch/record/2151986, Presented 28 Apr 2016

[142] ALICE MFT Operation Webpage, "MFT Readout", https://alice-mft-operation.docs.cern.ch/Introduction

[143] A. Rakotozafindrabe. MFT WP6 meeting. (2020), https://indico.cern.ch/event/951676/

[144] Peter Hansen, "Track reconstruction, Lecture notes", Nordic detector course, (2015)

[145] A. Strandlie and R. Fruhwirth, “Track and vertex reconstruction: From classical to adaptive methods,” Rev. Mod. Phys. **82** (2010), 1419-1458 doi:10.1103/RevModPhys.82.1419

[146] X. Ai, H. M. Gray, A. Salzburger and N. Styles, “A non-linear Kalman filter for track parameters estimation in high energy physics,” Nucl. Instrum. Meth. A **1049** (2023), 168041 doi:10.1016/j.nima.2023.168041 [arXiv:2112.09470 [physics.ins-det]].

[147] Francesco Mazzaschi, Stefano Politano, "Update on cluster size in pilot beam data", ITS WP2, https://indico.cern.ch/event/1180360/, Presented on 12 July 2022

[148] [ALICE], “Quarkonium signal extraction in ALICE,” ALICE-PUBLIC-2015-006.

[149] Sadek Finot, R. MFT commissioning and preparation for Run 3 data analysis with ALICE (LHC, CERN). (Ecole nationale supérieure Mines-Télécom Atlantique,2022,10), https://theses.hal.science/tel-04008085

[150] T. Sjostrand, S. Mrenna and P. Z. Skands, "A Brief Introduction to PYTHIA 8.1," Comput. Phys. Commun. **178** (2008), 852-867 doi:10.1016/j.cpc.2008.01.036 [arXiv:0710.3820 [hep-ph]].

[151] S. Agostinelli *et al.* [GEANT4], "GEANT4–a simulation toolkit," Nucl. Instrum. Meth. A **506** (2003), 250-303 doi:10.1016/S0168-9002(03)01368-8

[152] D. J. Lange, Nucl. Instrum. Meth. A **462** (2001), 152-155 doi:10.1016/S0168-9002(01)00089-4

[153] P. Golonka and Z. Was, Eur. Phys. J. C **45** (2006), 97-107 doi:10.1140/epjc/s2005-02396-4 [arXiv:hep-ph/0506026 [hep-ph]].

[154] Massacrier, L. La physique des (di)muons dans ALICE au LHC : analyse en collisions pp ($\sqrt{s}$ = 7 TeV) et Pb-Pb ($\sqrt{s_{NN}}$ = 2.76 TeV) des résonances de basses masses (ρ, ω, Φ) et étude d'un trajectographe en pixels de Silicium dans l'ouverture du spectromètre. (Université Claude Bernard - Lyon I,2011,10), https://theses.hal.science/tel-00800827

[155] S. Gorbunov and I. Kisel, "Reconstruction of decayed particles based on the Kalman Filter", CBM-SOFT-note-2007-003, 7 May 2007

[156] W. Verkerke and D. P. Kirkby, eConf **C0303241** (2003), MOLT007 [arXiv:physics/0306116 [physics]].

[157] M. Pivk and F. R. Le Diberder, "SPlot: A Statistical tool to unfold data distributions," Nucl. Instrum. Meth. A **555** (2005), 356-369 doi:10.1016/j.nima.2005.08.106 [arXiv:physics/0402083 [physics.data-an]].

[158] S. Acharya *et al.* [ALICE], "Prompt and non-prompt J/ψ production cross sections at midrapidity in proton-proton collisions at $\sqrt{\mathrm{s}}$ = 5.02 and 13 TeV," JHEP **03** (2022), 190 doi:10.1007/JHEP03(2022)190 [arXiv:2108.02523 [nucl-ex]].

[159] R. Aaij *et al.* [LHCb], "Measurement of forward J/ψ production cross-sections in pp collisions at $\sqrt{s} = 13$ TeV," JHEP **10** (2015), 172 [erratum: JHEP **05** (2017), 063] doi:10.1007/JHEP10(2015)172 [arXiv:1509.00771 [hep-ex]].

[160] R. Aaij *et al.* [LHCb], "Measurement of J/ψ production in pp collisions at $\sqrt{s} = 7\,\mathrm{TeV}$," Eur. Phys. J. C **71** (2011), 1645 doi:10.1140/epjc/s10052-011-1645-y [arXiv:1103.0423 [hep-ex]].

[161] K. H. Ackermann *et al.* [STAR], "Elliptic flow in Au + Au collisions at (S(NN))**(1/2) = 130 GeV," Phys. Rev. Lett. **86** (2001), 402-407 doi:10.1103/PhysRevLett.86.402 [arXiv:nucl-ex/0009011 [nucl-ex]].

[162] B. Muller, J. Schukraft and B. Wyslouch, "First Results from Pb–Pb collisions at the LHC," Ann. Rev. Nucl. Part. Sci. **62** (2012), 361-386 doi:10.1146/annurev-nucl-102711-094910 [arXiv:1202.3233 [hep-ex]].

[163] Belen'kji, S. & Landau, L. Hydrodynamic theory of multiple production of particles. *Il Nuovo Cimento (1955-1965)*. **3**, 15-31 (1956,1), https://doi.org/10.1007/BF02745507

[164] P. Romatschke and U. Romatschke, "Relativistic Fluid Dynamics In and Out of Equilibrium," Cambridge University Press, 2019, ISBN 978-1-108-48368-1, 978-1-108-75002-8 doi:10.1017/9781108651998 [arXiv:1712.05815 [nucl-th]].

[165] Landau, L. & Lifshitz, E. Fluid Mechanics, Second Edition: Volume 6 (Course of Theoretical Physics). (Butterworth-Heinemann,1987,1), http://www.worldcat.org/isbn/0750627670

[166] P. B. Arnold, C. Dogan and G. D. Moore, "The Bulk Viscosity of High-Temperature QCD," Phys. Rev. D **74** (2006), 085021 doi:10.1103/PhysRevD.74.085021 [arXiv:hep-ph/0608012 [hep-ph]].

[167] J. S. Moreland, J. E. Bernhard and S. A. Bass, "Bayesian calibration of a hybrid nuclear collision model using p-Pb and Pb-Pb data at energies available at the CERN Large Hadron Collider," Phys. Rev. C **101** (2020) no.2, 024911 doi:10.1103/PhysRevC.101.024911 [arXiv:1808.02106 [nucl-th]].

[168] M. Byres, S. H. Lim, C. McGinn, J. Ouellette and J. L. Nagle, "Bulk viscosity and cavitation in heavy ion collisions," Phys. Rev. C **101** (2020) no.4, 044902 doi:10.1103/PhysRevC.101.044902 [arXiv:1910.12930 [nucl-th]].

[169] P. Kovtun, D. T. Son and A. O. Starinets, "Viscosity in strongly interacting quantum field theories from black hole physics," Phys. Rev. Lett. **94** (2005), 111601 doi:10.1103/PhysRevLett.94.111601 [arXiv:hep-th/0405231 [hep-th]].

[170] D. T. Son and A. O. Starinets, "Viscosity, Black Holes, and Quantum Field Theory," Ann. Rev. Nucl. Part. Sci. **57** (2007), 95-118 doi:10.1146/annurev.nucl.57.090506.123120 [arXiv:0704.0240 [hep-th]].

[171] W. Florkowski, M. P. Heller and M. Spalinski, "New theories of relativistic hydrodynamics in the LHC era," Rept. Prog. Phys. **81** (2018) no.4, 046001 doi:10.1088/1361-6633/aaa091 [arXiv:1707.02282 [hep-ph]].

[172] M. P. Heller, R. A. Janik and P. Witaszczyk, "The characteristics of thermalization of boost-invariant plasma from holography," Phys. Rev. Lett. **108** (2012), 201602 doi:10.1103/PhysRevLett.108.201602 [arXiv:1103.3452 [hep-th]].

[173] P. Romatschke, "Relativistic Fluid Dynamics Far From Local Equilibrium," Phys. Rev. Lett. **120** (2018) no.1, 012301 doi:10.1103/PhysRevLett.120.012301 [arXiv:1704.08699 [hep-th]].

[174] M. Froissart, "Asymptotic behavior and subtractions in the Mandelstam representation," Phys. Rev. **123** (1961), 1053-1057 doi:10.1103/PhysRev.123.1053

[175] E. Iancu and R. Venugopalan, "The Color glass condensate and high-energy scattering in QCD," doi:10.1142/9789812795533_0005 [arXiv:hep-ph/0303204 [hep-ph]].

[176] F. D. Aaron *et al.* [H1], "A Precision Measurement of the Inclusive ep Scattering Cross Section at HERA," Eur. Phys. J. C **64** (2009), 561-587 doi:10.1140/epjc/s10052-009-1169-x [arXiv:0904.3513 [hep-ex]].

[177] L. D. McLerran, "The Color glass condensate and small x physics: Four lectures," Lect. Notes Phys. **583** (2002), 291-334 doi:10.1007/3-540-45792-5_8 [arXiv:hep-ph/0104285 [hep-ph]].

[178] S. Schlichting and D. Teaney, "The First fm/c of Heavy-Ion Collisions," Ann. Rev. Nucl. Part. Sci. **69** (2019), 447-476 doi:10.1146/annurev-nucl-101918-023825 [arXiv:1908.02113 [nucl-th]].

[179] R. Baier, A. H. Mueller, D. Schiff and D. T. Son, "'Bottom up' thermalization in heavy ion collisions," Phys. Lett. B **502** (2001), 51-58 doi:10.1016/S0370-2693(01)00191-5 [arXiv:hep-ph/0009237 [hep-ph]].

[180] M. Strickland, "Anisotropic Hydrodynamics: Three lectures," Acta Phys. Polon. B **45** (2014) no.12, 2355-2394 doi:10.5506/APhysPolB.45.2355 [arXiv:1410.5786 [nucl-th]].

[181] B. Schenke, P. Tribedy and R. Venugopalan, "Fluctuating Glasma initial conditions and flow in heavy ion collisions," Phys. Rev. Lett. **108** (2012), 252301 doi:10.1103/PhysRevLett.108.252301 [arXiv:1202.6646 [nucl-th]].

[182] A. Kurkela, A. Mazeliauskas, J. F. Paquet, S. Schlichting and D. Teaney, "Effective kinetic description of event-by-event pre-equilibrium dynamics in high-energy heavy-ion collisions," Phys. Rev. C **99** (2019) no.3, 034910 doi:10.1103/PhysRevC.99.034910 [arXiv:1805.00961 [hep-ph]].

[183] A. Kurkela, A. Mazeliauskas, J. F. Paquet, S. Schlichting and D. Teaney, "Matching the Nonequilibrium Initial Stage of Heavy Ion Collisions to Hydrodynamics with QCD Kinetic Theory," Phys. Rev. Lett. **122** (2019) no.12, 122302 doi:10.1103/PhysRevLett.122.122302 [arXiv:1805.01604 [hep-ph]].

[184] A. Kurkela and A. Mazeliauskas, "Chemical Equilibration in Hadronic Collisions," Phys. Rev. Lett. **122** (2019), 142301 doi:10.1103/PhysRevLett.122.142301 [arXiv:1811.03040 [hep-ph]].

[185] A. Kurkela and A. Mazeliauskas, "Chemical equilibration in weakly coupled QCD," Phys. Rev. D **99** (2019) no.5, 054018 doi:10.1103/PhysRevD.99.054018 [arXiv:1811.03068 [hep-ph]].

[186] P. B. Arnold, G. D. Moore and L. G. Yaffe, "Effective kinetic theory for high temperature gauge theories," JHEP **01** (2003), 030 doi:10.1088/1126-6708/2003/01/030 [arXiv:hep-ph/0209353 [hep-ph]].

[187] M. P. Heller, A. Kurkela, M. Spaliński and V. Svensson, "Hydrodynamization in kinetic theory: Transient modes and the gradient expansion," Phys. Rev. D **97** (2018) no.9, 091503 doi:10.1103/PhysRevD.97.091503 [arXiv:1609.04803 [nucl-th]].

[188] M. Strickland, J. Noronha and G. Denicol, "Anisotropic nonequilibrium hydrodynamic attractor," Phys. Rev. D **97** (2018) no.3, 036020 doi:10.1103/PhysRevD.97.036020 [arXiv:1709.06644 [nucl-th]].

[189] J. P. Blaizot and L. Yan, "Fluid dynamics of out of equilibrium boost invariant plasmas," Phys. Lett. B **780** (2018), 283-286 doi:10.1016/j.physletb.2018.02.058 [arXiv:1712.03856 [nucl-th]].

[190] J. M. Maldacena, "The Large N limit of superconformal field theories and supergravity," Adv. Theor. Math. Phys. **2** (1998), 231-252 doi:10.4310/ATMP.1998.v2.n2.a1 [arXiv:hep-th/9711200 [hep-th]].

[191] G. Giacalone, A. Mazeliauskas and S. Schlichting, "Hydrodynamic attractors, initial state energy and particle production in relativistic nuclear collisions," Phys. Rev. Lett. **123** (2019) no.26, 262301 doi:10.1103/PhysRevLett.123.262301 [arXiv:1908.02866 [hep-ph]].

[192] P. Romatschke, "Do nuclear collisions create a locally equilibrated quark-gluon plasma?," Eur. Phys. J. C **77** (2017) no.1, 21 doi:10.1140/epjc/s10052-016-4567-x [arXiv:1609.02820 [nucl-th]].

[193] McLerran, L. & Toimela, T. Photon and dilepton emission from the quark-gluon plasma: Some general considerations. *Phys. Rev. D*. **31**, 545-563 (1985,2), https://link.aps.org/doi/10.1103/PhysRevD.31.545

[194] H. A. Weldon, "Reformulation of finite temperature dilepton production," Phys. Rev. D **42** (1990), 2384-2387 doi:10.1103/PhysRevD.42.2384

[195] R. Rapp and H. van Hees, "Thermal Dileptons as Fireball Thermometer and Chronometer," Phys. Lett. B **753** (2016), 586-590 doi:10.1016/j.physletb.2015.12.065 [arXiv:1411.4612 [hep-ph]].

[196] P. A. Zyla *et al.* [Particle Data Group], "Review of Particle Physics," PTEP **2020** (2020) no.8, 083C01 doi:10.1093/ptep/ptaa104

[197] R. Rapp, "Dilepton Spectroscopy of QCD Matter at Collider Energies," Adv. High Energy Phys. **2013** (2013), 148253 doi:10.1155/2013/148253 [arXiv:1304.2309 [hep-ph]].

[198] M. Laine, "Thermal dilepton production from hot QCD," PoS **CPOD2014** (2015), 065 doi:10.22323/1.217.0065 [arXiv:1502.05796 [hep-ph]].

[199] Gale, C. & I. Kapusta, J. Vector dominance model at finite temperature. *Nuclear Physics B*. **357**, 65-89 (1991), https://www.sciencedirect.com/science/article/pii/055032139190459B

[200] R. A. Tripolt, "Electromagnetic and weak probes: theory," Nucl. Phys. A **1005** (2021), 121755 doi:10.1016/j.nuclphysa.2020.121755 [arXiv:2001.11232 [hep-ph]].

[201] R. Arnaldi *et al.* [NA60], "NA60 results on thermal dimuons," Eur. Phys. J. C **61** (2009), 711-720 doi:10.1140/epjc/s10052-009-0878-5 [arXiv:0812.3053 [nucl-ex]].

[202] J. Adamczewski-Musch *et al.* [HADES], "Probing dense baryon-rich matter with virtual photons," Nature Phys. **15** (2019) no.10, 1040-1045 doi:10.1038/s41567-019-0583-8

[203] M. Coquet, X. Du, J. Y. Ollitrault, S. Schlichting and M. Winn, "Intermediate mass dileptons as pre-equilibrium probes in heavy ion collisions," Phys. Lett. B **821** (2021), 136626 doi:10.1016/j.physletb.2021.136626 [arXiv:2104.07622 [nucl-th]].

[204] M. Coquet, X. Du, J. Y. Ollitrault, S. Schlichting and M. Winn, "Transverse mass scaling of dilepton radiation off a quark-gluon plasma," Nucl. Phys. A **1030** (2023), 122579 doi:10.1016/j.nuclphysa.2022.122579 [arXiv:2112.13876 [nucl-th]].

[205] X. Du and S. Schlichting, "Equilibration of the Quark-Gluon Plasma at Finite Net-Baryon Density in QCD Kinetic Theory," Phys. Rev. Lett. **127** (2021) no.12, 122301 doi:10.1103/PhysRevLett.127.122301 [arXiv:2012.09068 [hep-ph]].

[206] X. Du and S. Schlichting, "Equilibration of weakly coupled QCD plasmas," Phys. Rev. D **104** (2021) no.5, 054011 doi:10.1103/PhysRevD.104.054011 [arXiv:2012.09079 [hep-ph]].

[207] J. S. Moreland, J. E. Bernhard and S. A. Bass, "Alternative ansatz to wounded nucleon and binary collision scaling in high-energy nuclear collisions," Phys. Rev. C **92** (2015) no.1, 011901 doi:10.1103/PhysRevC.92.011901 [arXiv:1412.4708 [nucl-th]].

[208] P. Hanus, A. Mazeliauskas and K. Reygers, "Entropy production in pp and Pb-Pb collisions at energies available at the CERN Large Hadron Collider," Phys. Rev. C **100** (2019) no.6, 064903 doi:10.1103/PhysRevC.100.064903 [arXiv:1908.02792 [hep-ph]].

[209] S. Borsanyi, Z. Fodor, J. Guenther, K. H. Kampert, S. D. Katz, T. Kawanai, T. G. Kovacs, S. W. Mages, A. Pasztor and F. Pittler, *et al.* "Calculation of the axion mass based on high-temperature lattice quantum chromodynamics," Nature **539** (2016) no.7627, 69-71 doi:10.1038/nature20115 [arXiv:1606.07494 [hep-lat]].

[210] Romatschke, P. & Strickland, M. Collective modes of an anisotropic quark-gluon plasma. *Phys. Rev. D*. **68**, 036004 (2003,8), https://link.aps.org/doi/10.1103/PhysRevD.68.036004

[211] N. Christiansen, M. Haas, J. M. Pawlowski and N. Strodthoff, "Transport Coefficients in Yang–Mills Theory and QCD," Phys. Rev. Lett. **115** (2015) no.11, 112002 doi:10.1103/PhysRevLett.115.112002 [arXiv:1411.7986 [hep-ph]].

[212] Strickland, M. Thermal photons and dileptons from non-equilibrium quark-gluon plasma. *Physics Letters B*. **331**, 245-250 (1994), https://www.sciencedirect.com/science/article/pii/0370269394910456

[213] R. Ryblewski and M. Strickland, "Dilepton production from the quark-gluon plasma using (3+1)-dimensional anisotropic dissipative hydrodynamics," Phys. Rev. D **92** (2015) no.2, 025026 doi:10.1103/PhysRevD.92.025026 [arXiv:1501.03418 [nucl-th]].

[214] B. S. Kasmaei and M. Strickland, "Dilepton production and elliptic flow from an anisotropic quark-gluon plasma," Phys. Rev. D **99** (2019) no.3, 034015 doi:10.1103/PhysRevD.99.034015 [arXiv:1811.07486 [hep-ph]].

[215] Martinez, M. & Strickland, M. Pre-equilibrium dilepton production from an anisotropic quark-gluon plasma. *Phys. Rev. C*. **78**, 034917 (2008,9), https://link.aps.org/doi/10.1103/PhysRevC.78.034917

[216] J. L. Albacete and A. Soto-Ontoso, "Hot spots and the hollowness of proton–proton interactions at high energies," Phys. Lett. B **770** (2017), 149-153 doi:10.1016/j.physletb.2017.04.055 [arXiv:1605.09176 [hep-ph]].

[217] H. Mäntysaari and B. Schenke, "Evidence of strong proton shape fluctuations from incoherent diffraction," Phys. Rev. Lett. **117** (2016) no.5, 052301 doi:10.1103/PhysRevLett.117.052301 [arXiv:1603.04349 [hep-ph]].

[218] H. Mäntysaari and B. Schenke, "Revealing proton shape fluctuations with incoherent diffraction at high energy," Phys. Rev. D **94** (2016) no.3, 034042 doi:10.1103/PhysRevD.94.034042 [arXiv:1607.01711 [hep-ph]].

[219] S. Demirci, T. Lappi and S. Schlichting, "Hot spots and gluon field fluctuations as causes of eccentricity in small systems," Phys. Rev. D **103** (2021) no.9, 094025 doi:10.1103/PhysRevD.103.094025 [arXiv:2101.03791 [hep-ph]].

[220] T. Lappi and S. Schlichting, "Linearly polarized gluons and axial charge fluctuations in the Glasma," Phys. Rev. D **97** (2018) no.3, 034034 doi:10.1103/PhysRevD.97.034034 [arXiv:1708.08625 [hep-ph]].

[221] J. P. Blaizot, T. Lappi and Y. Mehtar-Tani, "On the gluon spectrum in the glasma," Nucl. Phys. A **846** (2010), 63-82 doi:10.1016/j.nuclphysa.2010.06.009 [arXiv:1005.0955 [hep-ph]].

[222] K. J. Golec-Biernat and M. Wusthoff, "Saturation in diffractive deep inelastic scattering," Phys. Rev. D **60** (1999), 114023 doi:10.1103/PhysRevD.60.114023 [arXiv:hep-ph/9903358 [hep-ph]].

[223] N. Borghini, M. Borrell, N. Feld, H. Roch, S. Schlichting and C. Werthmann, "Statistical analysis of initial-state and final-state response in heavy-ion collisions," Phys. Rev. C **107** (2023) no.3, 034905 doi:10.1103/PhysRevC.107.034905 [arXiv:2209.01176 [hep-ph]].

[224] J. Churchill, L. Yan, S. Jeon and C. Gale, "Emission of electromagnetic radiation from the early stages of relativistic heavy-ion collisions," Phys. Rev. C **103** (2021) no.2, 024904 doi:10.1103/PhysRevC.103.024904 [arXiv:2008.02902 [hep-ph]].

[225] J. Churchill, L. Yan, S. Jeon and C. Gale, "Electromagnetic radiation from the pre-hydrodynamics stage of the quark-gluon plasma," Nucl. Phys. A **1005** (2021), 121946 doi:10.1016/j.nuclphysa.2020.121946 [arXiv:2001.11110 [hep-ph]].

[226] J. P. Blaizot, F. Gelis, J. F. Liao, L. McLerran and R. Venugopalan, "Bose–Einstein Condensation and Thermalization of the Quark Gluon Plasma," Nucl. Phys. A **873** (2012), 68-80 doi:10.1016/j.nuclphysa.2011.10.005 [arXiv:1107.5296 [hep-ph]].

[227] J. P. Blaizot, J. Liao and L. McLerran, "Gluon transport equation in the small angle approximation and the onset of Bose–Einstein condensation," Nucl. Phys. A **931** (2014), 359-364 doi:10.1016/j.nuclphysa.2014.10.012

[228] L. D. McLerran and R. Venugopalan, "Computing quark and gluon distribution functions for very large nuclei," Phys. Rev. D **49** (1994), 2233-2241 doi:10.1103/PhysRevD.49.2233 [arXiv:hep-ph/9309289 [hep-ph]].

[229] L. D. McLerran and R. Venugopalan, "Gluon distribution functions for very large nuclei at small transverse momentum," Phys. Rev. D **49** (1994), 3352-3355 doi:10.1103/PhysRevD.49.3352 [arXiv:hep-ph/9311205 [hep-ph]].

[230] L. D. McLerran and R. Venugopalan, "Green's functions in the color field of a large nucleus," Phys. Rev. D **50** (1994), 2225-2233 doi:10.1103/PhysRevD.50.2225 [arXiv:hep-ph/9402335 [hep-ph]].

[231] T. Song, W. Cassing, P. Moreau and E. Bratkovskaya, "Open charm and dileptons from relativistic heavy-ion collisions," Phys. Rev. C **97** (2018) no.6, 064907 doi:10.1103/PhysRevC.97.064907 [arXiv:1803.02698 [nucl-th]].

[232] S. D. Drell and T. M. Yan, "Massive Lepton Pair Production in Hadron-Hadron Collisions at High-Energies," Phys. Rev. Lett. **25** (1970), 316-320 [erratum: Phys. Rev. Lett. **25** (1970), 902] doi:10.1103/PhysRevLett.25.316

[233] S. Camarda, M. Boonekamp, G. Bozzi, S. Catani, L. Cieri, J. Cuth, G. Ferrera, D. de Florian, A. Glazov and M. Grazzini, *et al.* "DYTurbo: Fast predictions for Drell-Yan processes," Eur. Phys. J. C **80** (2020) no.3, 251 [erratum: Eur. Phys. J. C **80** (2020) no.5, 440] doi:10.1140/epjc/s10052-020-7757-5 [arXiv:1910.07049 [hep-ph]].

[234] Bechtel, F. & Schleper, P. The Underlying Event in Proton-Proton Collisions. (2023,4)

[235] R. Aaij *et al.* [LHCb], "Physics case for an LHCb Upgrade II - Opportunities in flavour physics, and beyond, in the HL-LHC era," [arXiv:1808.08865 [hep-ex]].

[236] G. A. Cowan, D. C. Craik and M. D. Needham, "RapidSim: an application for the fast simulation of heavy-quark hadron decays," Comput. Phys. Commun. **214** (2017), 239-246 doi:10.1016/j.cpc.2017.01.029 [arXiv:1612.07489 [hep-ex]].

[237] D. Adamová, G. Aglieri Rinella, M. Agnello, Z. Ahammed, D. Aleksandrov, A. Alici, A. Alkin, T. Alt, I. Altsybeev and D. Andreou, *et al.* "A next-generation LHC heavy-ion experiment," [arXiv:1902.01211 [physics.ins-det]].

[238] J. Deng, Q. Wang, N. Xu and P. Zhuang, "Dilepton flow and deconfinement phase transition in heavy ion collisions," Phys. Lett. B **701** (2011), 581-586 doi:10.1016/j.physletb.2011.06.027 [arXiv:1009.3091 [nucl-th]].

[239] J. C. Collins and D. E. Soper, "Angular Distribution of Dileptons in High-Energy Hadron Collisions," Phys. Rev. D **16** (1977), 2219 doi:10.1103/PhysRevD.16.2219

[240] Maestre, J. Details on the Collins-Soper reference frame and lepton angular distributions in electroweak vector boson production at hadron colliders. (Centro de Investigaciones Energéticas, Medio Ambientales y Tecnológicas (CIEMAT),2020)

[241] J. Ghiglieri, A. Kurkela, M. Strickland and A. Vuorinen, "Perturbative Thermal QCD: Formalism and Applications," Phys. Rept. **880** (2020), 1-73 doi:10.1016/j.physrep.2020.07.004 [arXiv:2002.10188 [hep-ph]].

[242] Kubo , R. Statistical-Mechanical Theory of Irreversible Processes. I. General Theory and Simple Applications to Magnetic and Conduction Problems. *Journal Of The Physical Society Of Japan*. **12**, 570-586 (1957), https://doi.org/10.1143/JPSJ.12.570

Appendix A

Dilepton production in thermal field theory

A.1 Thermal field theory propagators

In this section we will start by reviewing the basic computation of Leading Order dilepton production. From the Eq.5.9, we need to compute the Wightman function:

$$\Pi^{\mu\nu,<}(K) \tag{A.1}$$

where K is the 4-momentum of the virtual photon. We will compute this function at Leading Order using thermal field theory.

There are two formulations of perturbative thermal field theory: the "real time" and "imaginary time" formalism [85]. These two formulations are equivalent, and the most practical one depends on the observable. In the real-time formalism, we can easily extend the calculation in thermal equilibrium to the out-of-equilibrium case. This approach is also very useful for computing self-energies and particle production rates. We will use this formalism in the following. The disadvantage of the real-time formalism compared to the imaginary time is that there is an apparent doubling of the degrees of freedom of the propagators. This means that when computing a Feynman diagram one must deal with two types of propagators and effectively sum them to get the correct answer. This can make the computation more cumbersome.

When computing a diagram in this formalism, we must assign a label to each vertex, noted 1 or 2. The only rule is that two vertices connected by a propagator must have opposite types. We then must sum all the labeling possibilities. There are four types of propagators linking these 2 types of vertices. They are given by the following expressions for massless fermions [241]:

$$S_{11}(P) = \left\{\frac{i}{P^2+i\epsilon} - (2\pi)\delta(P^2)f_q(p)\right\}\not{P} \tag{A.2}$$

$$S_{12}(P) = 2\pi\not{P}\delta\left(P^2\right)\left\{-f_q(p)\theta\left(p^0\right) + (1-f_{\bar{q}}(-p))\,\theta\left(-p^0\right)\right\} \tag{A.3}$$

$$S_{21}(P) = 2\pi\not{P}\delta\left(P^2\right)\left\{(1-f_q(p))\,\theta\left(p^0\right) - f_{\bar{q}}(-p)\theta\left(-p^0\right)\right\} \tag{A.4}$$

$$S_{22}(P) = \left\{\frac{-i}{P^2-i\epsilon} - (2\pi)\delta(P^2)f_q(p)\right\}\not{P} \tag{A.5}$$

P is the momentum of the propagator, and $\not{P} = P^\mu\gamma_\mu$ where γ_μ are the Dirac matrices. $f_q(p)$ and $f_{\bar{q}}(p)$ are the quark and anti-quark distribution functions. It is important to note that, although we will first consider these distributions to be in equilibrium, i.e. Fermi-Dirac distributions, the real-time formalism also allows to replace them with far-from-equilibrium distributions. This will enable us to extend the calculation to the pre-equilibrium case.

A.2 Leading order calculation

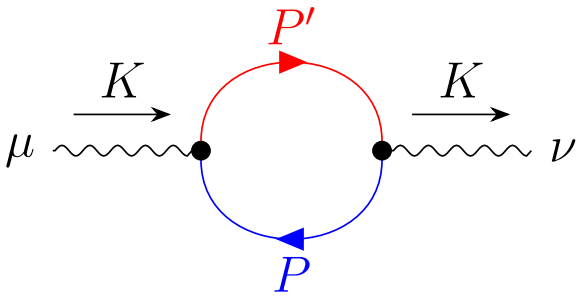

Figure A.1: Leading order diagram of the photon self-energy. It is the starting point of the dilepton production calculation.

We must compute the Wightman function $\Pi^{\mu\nu,<}(K)$, which amounts to the virutal photon self energy in Fig. A.2. As only two vertices are included in this diagram, there are only two labeling possibilities, assigning the label 1 to the vertex of the incoming photon and 2 to the vertex of the outgoing photon, and inversely. In the real-time formalism, the Wightman function $\Pi^{\mu\nu,<}$ corresponds to the first ordering mentioned, and is written $\Pi^{\mu\nu}_{12} = -\Pi^{\mu\nu,<}$. These two labeling possibilities are perfectly equivalent. Thus, we will only compute the diagram where the incoming vertex is 1, and the outgoing vertex is 2. The indices 1 and 2 correspond to the labels of the incoming and outgoing external photon propagators of this diagram, while μ and ν correspond to the polarization indices of the incoming and outgoing photons. Hence, we must compute the product of a 12 propagator (in red) and a 21 propagator (in blue).

We note $q^2 := \sum_f q_f^2$ the sum of the squares of active quark flavors (which in our case will be u, d and s). The Wightman function is given by the integral of the momentum loop in the diagram with these two propagators:

$$\Pi_{12}^{\mu\nu} = N_c \int \frac{d^3p}{(2\pi)^3 2p^0} \int \frac{d^3p'}{(2\pi)^3 2p'^0} (2\pi)^4 \delta\left(K + P - P'\right) \mathrm{Tr}\left[\gamma^\mu S_{12}\left(P'\right) \gamma^\nu S_{21}(P)\right] \quad \text{(A.6)}$$

$$= N_c \int \frac{d^3p}{(2\pi)^3 2p^0} \mathrm{Tr}\left[\gamma^\mu S_{12}(P+K) \gamma^\nu S_{21}(P)\right] \quad \text{(A.7)}$$

$$= (2\pi)^2 N_c \int \frac{d^3p}{(2\pi)^3 2p^0} \left\{-f_q(\mathrm{p}+\mathrm{k})\theta\left(p^0+k^0\right) + (1 - f_{\bar{q}}(-\mathrm{p}-\mathrm{k}))\,\theta\left(-p^0-k^0\right)\right\} \quad \text{(A.8)}$$

$$\times \left\{(1 - f_q(\mathrm{p}))\,\theta\left(p^0\right) - f_{\bar{q}}(-\mathrm{p})\theta\left(-p^0\right)\right\} \delta\left(P^2\right) \delta\left([P+K]^2\right) \mathrm{Tr}\left[\gamma^\mu (\not{P} + \not{K}) \gamma^\nu \not{P}\right]. \quad \text{(A.9)}$$

where p and p' are the momentum of the blue and red propagators respectively. N_c is the number of colors, i.e. $N_c = 3$, p_0 is the energy of the blue propagator, and θ is the Heaviside step function. We now compute the trace of the considered propagators:

$$\mathrm{Tr}\left[\gamma^\mu (\not{P} + \not{K}) \gamma^\nu \not{P}\right] = (P+K)_\alpha P_\beta \,\mathrm{Tr}\left[\gamma^\mu \gamma^\alpha \gamma^\nu \gamma^\beta\right] \quad \text{(A.10)}$$

$$= 4(P+K)_\alpha P_\beta \left[g^{\nu\beta} g^{\mu\alpha} - g^{\alpha\beta} g^{\mu\nu} + g^{\mu\beta} g^{\alpha\nu}\right] \quad \text{(A.11)}$$

$$= 4\left[2P^\mu P^\nu + K^\mu P^\nu + K^\nu P^\mu - P\cdot(P+K) g^{\mu\nu}\right] \quad \text{(A.12)}$$

Therefore we find:

$$\Pi_{12}^{\mu\nu} = 16\pi^2 N_c \int \frac{d^3p}{(2\pi)^3 2p^0} \left\{-f_q(\mathrm{p}+\mathrm{k})\theta\left(p^0+k^0\right) + (1 - f_{\bar{q}}(-\mathrm{p}-\mathrm{k}))\,\theta\left(-p^0-k^0\right)\right\} \quad \text{(A.13)}$$

$$\times \left\{(1 - f_q(\mathrm{p}))\,\theta\left(p^0\right) - f_{\bar{q}}(-\mathrm{p})\theta\left(-p^0\right)\right\} \delta\left(P^2\right) \delta\left([P+K]^2\right) \quad \text{(A.14)}$$

$$\times \left[2P^\mu P^\nu + K^\mu P^\nu + K^\nu P^\mu - P\cdot(P+K) g^{\mu\nu}\right] \quad \text{(A.15)}$$

As shown in Eq.5.9, we will in the end be interested only in the Lorentz contracted quantity $\Pi_\mu^{\mu,<}$. Contracting the Lorentz indices yields :

$$\left[2P^\mu P^\nu + K^\mu P^\nu + K^\nu P^\mu - P\cdot(P+K) g^{\mu\nu}\right] = \left[2P^2 + 2P\cdot K - 4P^2 - 4P\cdot K\right] \quad \text{(A.16)}$$

$$= -2\left[P^2 + P\cdot K\right] \quad \text{(A.17)}$$

And hence :

$$\Pi_{12\ \mu}^{\mu} = -32\pi^2 N_c \int \frac{d^3p}{(2\pi)^3 2p^0} \left\{-f_q(\mathrm{p}+\mathrm{k})\theta\left(p^0+k^0\right) + (1 - f_{\bar{q}}(-\mathrm{p}-\mathrm{k}))\,\theta\left(-p^0-k^0\right)\right\} \quad \text{(A.18)}$$

$$\times \left\{(1 - f_q(\mathrm{p}))\,\theta\left(p^0\right) - f_{\bar{q}}(-\mathrm{p})\theta\left(-p^0\right)\right\} \delta\left(P^2\right) \delta\left([P+K]^2\right) \left[P^2 + P\cdot K\right] \quad \text{(A.19)}$$

As we are considering dilepton production, the photon must be virtual, and thus $K^2 \neq 0$. Furthermore, the $\delta\left(P^2\right)$ factor states that the quarks are on-shell and therefore $P^2 = 0$. Developing the second delta function, $\delta\left([P+K]^2\right)$, we find:

$$(P+K)^2 = P^2 + K^2 + 2P\cdot K = K^2 + 2P\cdot K = \left(k^0\right)^2 - k^2 + 2p^0k^0 - 2pk\cos\theta_{\rm pk}.$$

where k^0 is the energy of the virtual photon, and $\theta_{\rm pk}$ is the angle between the photon momentum and the quark with momentum p. Thus:

$$\delta\left([P+K]^2\right) = \delta\left(\left(k^0\right)^2 - k^2 + 2p^0k^0 - 2pk\cos\theta_{\rm pk}\right) = \delta\left(2pk\cos\theta_{\rm pk} - \left(k^0\right)^2 + k^2 - 2p^0k^0\right) \tag{A.20}$$

$$= \delta\left(2pk\cos\theta_{\rm pk} - \left(k^0\right)^2 + k^2 - 2p^0k^0\right) \tag{A.21}$$

$$= \frac{1}{2pk}\delta\left(\cos\theta_{\rm pk} - \frac{\left(k^0\right)^2 + 2p^0k^0 - k^2}{2pk}\right) \tag{A.22}$$

We now note that dilepton production is only possible when $k^0 - k > 0$ and $k^0 + k > 0$. This corresponds to positive invariant mass and positive energy of the virtual photon. We now confront these conditions with the constraints of the delta function in Eq.A.22.

According to θ functions in the second line of Eq.A.18 and the $\delta\left(P^2\right)$ factor, we must either have $p^0 = p > 0$ or $p^0 = -p < 0$. The constraint in Eq.A.22 can be rewritten:

$$-2pk < (k^0)^2 - k^2 + 2p^0k^0 < 2pk$$

If we assume that $p^0 = p > 0$, then we can write:

$$(k^0)^2 - k^2 + 2pk^0 < 2pk \implies -(k-k^0)(k+k^0) < 2p(k-k^0)$$

We have the condition $k^0 - k > 0$. Thus:

$$-(k+k^0) > 2p > 0$$

Consequently, $k^0 + k < 0$, which violates the second condition needed for dilepton production. We see that if $p^0 = p > 0$, then the two required conditions cannot be satisfied simultaneously. We thus deduce that $p^0 = -p < 0$.

Next, we see from the θ functions in the first line of Eq.A.18, that we must either have $p^0 < -k^0$ or $-k^0 < p^0$. We assume that $p^0 < -k^0$. We can write:

$$2p^0k < (k^0)^2 - k^2 + 2p^0k^0 \implies 2p^0(k-k^0) < (k^0-k)(k^0+k)$$

We have the condition $k^0 - k > 0$. Thus:

$$-2p^0 < (k^0+k) \implies 2k^0 < (k^0+k) \implies k^0 - k < 0$$

This violates the condition for dilepton production: $k^0 - k > 0$. Thus, we must have $-k^0 < p^0 < 0$.

We can now remove the unneeded θ functions in Eq.A.18, and restrict the integration over the momentum p over the range $\frac{k^0-k}{2} < p < \frac{k^0+k}{2}$, given by the established constraints.

$$\Pi_{12}^{\mu} = -32\pi^2 N_c \int \frac{d^3p}{(2\pi)^3 2p^0} \delta\left(P^2\right) \delta\left([P+K]^2\right) [P\cdot K] f_q(\mathrm{p}+\mathrm{k}) \theta\left(p^0+k^0\right) f_{\bar{q}}(-\mathrm{p}) \theta\left(-p^0\right) \tag{A.23}$$

$$= -32\pi^2 N_c \int_{-k^0}^{0} \frac{\mathrm{d}p^0}{(2\pi)^4} \int_{\mathrm{p}} \frac{1}{2p} \delta\left(p^0+p\right) \frac{1}{2pk} \delta\left(\cos\theta_{\mathrm{pk}} - \frac{\left(k^0\right)^2 + 2p^0k^0 - k^2}{2pk}\right) \tag{A.24}$$

$$\times \left[p^0k^0 - \mathrm{p}\cdot\mathrm{k}\right] f_q(\mathrm{p}+\mathrm{k}) f_{\bar{q}}(-\mathrm{p}) \theta\left(k^- < p < k^+\right) \tag{A.25}$$

$$= -\frac{N_c}{2\pi^2 k} \int \mathrm{d}^3p \frac{1}{p^2} \delta\left(\cos\theta_{\mathrm{pk}} - \frac{\left(k^0\right)^2 - 2pk^0 - k^2}{2pk}\right) \theta\left(k^- < p < k^+\right) \tag{A.26}$$

$$\times \left[-pk^0 - pk\cos\theta_{\mathrm{pk}}\right] f_q(\mathrm{p}+\mathrm{k}) f_{\bar{q}}(-\mathrm{p}) \tag{A.27}$$

$$= \frac{N_c K^2}{4\pi^2 k} \int \mathrm{d}^3p \frac{1}{p^2} \delta\left(\cos\theta_{\mathrm{pk}} - \frac{\left(k^0\right)^2 - 2pk^0 - k^2}{2pk}\right) f_q(\mathrm{p}+\mathrm{k}) f_{\bar{q}}(-\mathrm{p}) \theta\left(k^- < p < k^+\right) \tag{A.28}$$

where we used

$$pk^0 + pk\cos\theta_{\mathrm{pk}} = pk^0 + pk\frac{\left(k^0\right)^2 - 2pk^0 - k^2}{2pk} = pk^0 + \frac{1}{2}\left[\left(k^0\right)^2 - k^2\right] - pk^0 = \frac{1}{2}K^2$$

Finally, we get:

$$\Pi_{\mu}^{<\mu} = -\frac{N_{\mathrm{c}} K^2}{4\pi^2 k} \int \mathrm{d}^3p \frac{1}{p^2} \delta\left(\cos\theta_{pk} - \frac{\left(k^0\right)^2 - 2pk^0 - k^2}{2pk}\right) f_q(p+k) f_{\bar{q}}(-p) \theta\left(k^- < p < k^+\right). \tag{A.29}$$

This last expression is the general equation of virtual photon decay into dilepton.

We now compute the leptonic tensor $L^{\mu\nu}(K)$. It describes the production of the lepton pair with invariant mass K from the virtual photon

$$L^{\mu\nu}(K) = \int \frac{d^2p_1}{(2\pi)^3 2E_1} \int \frac{d^2p_2}{(2\pi)^3 2E_2} (2\pi)^4 \delta\left(K - P_1 - P_2\right) l^{\mu\nu}\left(P_1, P_2\right)$$

with $l^{\mu\nu}\left(P_1, P_2\right)$ being the matrix element squared averaged over spins

$$\begin{aligned} l^{\mu\nu}\left(P_1, P_2\right) &= \sum_{s_1, s_2} \bar{u}_{s_1}\left(p_1\right) \gamma^{\mu} v_{s_2}\left(p_2\right) \bar{v}_{s_2}\left(p_2\right) \gamma^{\nu} u_{s_1}\left(p_1\right) \\ &= 4\left[P_1^{\nu} P_2^{\mu\varepsilon} + P_2^{\nu} P_1^{\mu} - \left(P_1\cdot P_2 + m^2\right) g^{\mu\nu}\right]. \end{aligned}$$

such that

$$L_{\mu\nu}(K) = \frac{1}{6\pi}\left(1 + \frac{2m^2}{K^2}\right)\left(1 - \frac{4m^2}{K^2}\right)^{1/2} \theta\left(K^2 - 4m^2\right)\left(K_{\mu}K_{\nu} - K^2 g^{\mu\mu}\right)$$

Since the vector current j^{μ} is conserved, i.e. $\partial_{\mu} j^{\mu} = 0$, the current-current correlator is transverse $Q_{\mu}Q_{\nu}\Pi^{\mu\nu,<}(K) = 0$, and only the second factor in the leptonic tensor contributes. Hence we get :

$$\frac{dN^{l^+l^-}}{d^4x d^4K} = -\frac{\alpha_{em}^2}{6\pi^3 K^2} \underbrace{\left(1 + \frac{2m^2}{K^2}\right)\left(1 - \frac{4m^2}{K^2}\right)^{1/2}}_{=L(K)} \sum_f q_f^2 \Pi_{\mu}^{\mu,<}(K) \tag{A.30}$$

For m equal to the muon mass $m_\mu = 106\,\mathrm{MeV}/c^2$ and invariant masses larger than $M > 1\,\mathrm{GeV}/c^2$, the leptonic phase space factor is close to unity to good approximation.

Appendix B

Why is the ideal dilepton production rate thermal?

As we saw in Eq.5.13, the ideal dilepton production rate can be written:

$$\frac{dN^{l^+l^-}}{d^4xd^4K} = \frac{N_c\alpha^2}{12\pi^4}\sum_f q_f^2 \frac{F(k)}{\exp\left(k^0/T\right)-1}, \tag{B.1}$$

We see that a Bose-Einstein factor appears in this expression. The reason for this weight may not be directly obvious since, in a QGP at thermal equuilibrium, although the quarks and gluons are in equilibrium, the electromagnetic radiation is not. This can be understood in two alternative pictures:

1) First, this can be seen on dimensional grounds. The rate expression can be expressed as

$$\frac{dN^{l^+l^-}}{d^4xd^4K} = \int \frac{d^3p_1}{(2\pi)^3 2p_1}\frac{d^3p_2}{(2\pi)^3 2p_2} f_q\left(x,\mathbf{p}_1\right) f_{\bar{q}}\left(x,\mathbf{p}_2\right)|\mathcal{A}|^2(2\pi)^4\delta^{(4)}\left(P_1+P_2-K\right) \tag{B.2}$$

where $\mathcal{A}$ is the Lorentz-invariant amplitude of the process, which is not modified by the thermal medium, at leading order in perturbation theory. Assuming local thermal equilibrium and $M \gg T$, the distribution of quarks and antiquarks can be considered to follow Boltzmann statistics to a good approximation: $f_q(x,\mathbf{p}) = f_{\bar{q}}(x,\mathbf{p}) = \exp(-p/T)$. The product of the quark and antiquark distributions yields $f_q\left(x,\mathbf{p}_1\right) f_{\tilde{q}}\left(x,\mathbf{p}_2\right) = \exp\left(-k_0/T(x)\right)$, where k_0 is the energy of the virtual photon. We can then move this statistical factor out of the integration:

$$\frac{dN^{l^-l^-}}{d^4xd^4K} = e^{-k^0/T(x)}\int \frac{d^3p_1}{(2\pi)^3 2p_1}\frac{d^3p_2}{(2\pi)^3 2p_2}|\mathcal{A}|^2(2\pi)^4\delta^{(4)}\left(P_1+P_2-K\right)$$

The pre-factor on the right-hand side is the Boltzmann factor corresponding to the dilepton. The rest of the integral must be a Lorentz scalar and has the dimension of energy. The only Lorentz invariant scale is the invariant mass M of the dilepton, hence the integral can only depend on M. This integral must thus be constant. Hence, we see the statistical factor naturally arising from the product of the distribution of the quark and the antiquark, and from energy conservation.

$$\frac{dN^{l^+l^-}}{d^4xd^4K} = C\exp\left(-\frac{k_0}{T(x)}\right),$$

2) From the thermal field theory point of view, this thermal behavior is a direct consequence of the Kubo-Martin-Schwinger (KMS) condition [242]. This condition states that in equilibrium one can relate the different Wightman functions by simple relations. The time-ordered and anti-time-ordered Wightman functions can be related to each other via [85][241]:

$$\Pi^{>}(t) = \Pi^{<}(t + i\beta) \tag{B.3}$$

In momentum space, the above relations take a particularly useful form:

$$\Pi^{>}(\omega) \equiv \int dt e^{i\omega t} D^{>}(t) = e^{\beta\omega}\Pi^{<}(\omega) \tag{B.4}$$

In addition, the imaginary part of the retarded current-current correlator (Eq.5.6) can be expressed in terms of these Wightman functions [85]:

$$\mathrm{Im}\Pi_{EM} \propto \Pi^{>} - \Pi^{<} \tag{B.5}$$

$\Pi^{>}(k)$ can be understood as a decay rate, the rate at which particles leave the initial phase space. On the other hand, $\Pi^{<}(k)$ can be viewed as describing the creation rate. This is the reason for the appearance of this Wightman function in the expression for the production rate Eq.5.9. In vacuum (i.e. $T = 0$), one must have $\Pi^{<}(k) = 0$. However, in a thermally equilibrated medium, the KMS condition Eq.B.3 gives us the relation $\Pi^{>}(k) = e^{\beta k_0}\Pi^{<}(k)$, and hence $\mathrm{Im}\Pi_{EM}(k) \propto -\Pi^{<}(k)(1 - e^{\beta k_0})$. It is $\mathrm{Im}\Pi_{EM}$ which has the simple scaling $\mathrm{Im}\Pi_{EM}(k) \propto M^2$ in the IMR. However, $\mathrm{Im}\Pi_{EM}$ contains both annihilation and creation rates, instead of only the creation rate. The statistical Bose-Einstein factor simply corrects that.

Appendix C

Résumé en français

Chapitre 1: Introduction

La nature comporte quatre forces fondamentales, qui sont la gravitation, l'électro-magnétisme, l'interaction faible et l'interaction forte. Cette dernière est responsable de la cohésion interne des noyaux atomiques. Dans le modèle standard de la physique des particules, l'interaction forte agit sur des particules appelées quarks et gluons. Elle possède une propriété nommée la liberté asymptotique : son intensité, que l'on appelle couplage et note α_s, devient de plus en plus petite à mesure que la distance devient grande ou que l'énergie du processus devient petite, et inversement. Il s'agit d'une propriété remarquable, propre à l'interaction forte. Une autre de ses propriétés est le confinement de couleur. En effet, les quarks, porteurs de charges de couleur, ne sont pas observés dans la nature de manière isolée, mais dans des objets composites neutres en charge couleur. On appelle ces particules composites des hadrons (comme le proton, le pion, ...). La matière qui compose l'essentiel de l'univers est faite de hadrons. Cependant, dans des accélérateurs de particules comme le LHC, dans ce que l'on appelle des collisions d'ions lourds ultra-relativistes, l'environnement créé peut atteindre des températures si élevées que l'interaction entre les quarks devient trop faible pour qu'un état confiné de la matière puisse exister. On assiste alors à une transition vers un état déconfiné où les quarks et les gluons peuvent se propager. On appelle cet état de la matière le plasma de quarks et de gluons (PQG).

Dans ces collisions d'ions lourds, l'évolution du PQG suit plusieurs étapes : aux premiers instants ont lieu des processus "durs". À ce stade, l'état de la matière est très éloigné de l'équilibre thermodynamique. Puis vient une phase nommée pré-équilibre, au cours de laquelle le milieu approche un état proche de l'équilibre thermodynamique. Le comportement du PQG peut alors être remarquablement décrit par la mécanique des fluides. Il s'agit du fluide ayant la plus petite viscosité jamais mesurée. Ensuite, la température décroît, et après un temps d'environ $10\,\mathrm{fm}/c$, les quarks et les gluons redeviennent confinés dans des hadrons sans couleur, ce que l'on nomme l'hadronisation. Du fait de cette courte durée de vie, des observables doivent être judicieusement choisies pour étudier l'évolution du PQG créé dans ces collisions. L'une d'entre elles, dont nous parlerons dans le chapitre 5, est les dileptons thermiques. Une autre est le charmonium. Il s'agit d'états liés de quarks et d'antiquarks lourds appelés des quarks charm (notés $c\bar{c}$). Du fait de cette

masse importante, ces particules ne sont créées que lors des processus durs aux premiers instants de la collision d'ions lourds. De plus, leur durée de vie est suffisamment longue pour qu'elles puissent se propager avant la disparition du PQG et donc interagir avec ce dernier. Ces interactions peuvent briser la liaison entre les deux quarks, et produire une suppression de la production du charmonium, comparé aux collisions entre protons. Cependant, si l'énergie de collision est suffisamment importante pour créer une grande population de quarks charm lors des processus durs, un phénomène de régénération peut intervenir, où un quark charm provenant d'un charmonium qui a été dissocié, s'approche suffisamment dans l'espace des phases d'un antiquark charm provenant de la dissociation d'un autre charmonium, et ainsi forme un nouvel état lié. Cela fut observé en comparant la production de charmonium au LHC (à 5 TeV) par rapport au RHIC (à 200 GeV). Deux visions concurrentes s'attachent à modéliser ces mécanismes : le modèle d'hadronisation statistique et les modèles de transport. Dans la première vision, tous les états liés sont dissociés dans le PQG, y compris les charmonia, et la formation des états liés ne se produit que lors de la phase d'hadronisation. Dans la seconde approche, il y a une dissociation et une formation continuelle de charmonia dans le PQG. La discrimination du modèle le plus à même de décrire les données procurerait une avancée importante dans la compréhension du PQG.

Un état de charmonium abondamment produit dans les collisions est le J/ψ. Il possède une haute probabilité de se désintégrer en une paire de leptons, électron-positon ou muon-antimuon. Cependant, plusieurs processus peuvent aboutir à la production de cet état. La paire $c\bar{c}$ peut être produite au début de la collision, puis s'hadroniser en J/ψ (ou un état excité). On parle alors de J/ψ prompt, car l'endroit où l'on reconstruit le vertex de désintégration de ce J/ψ coïncide avec le point de collision des deux ions lourds, que l'on nomme vertex primaire. Une autre source sont les J/ψ dits non-prompts, qui proviennent de la désintégration faible de hadrons qui contiennent un quark beauty (on parle de hadron b). Ces hadrons b possèdent une grande durée de vie ($\sim 10^{-12}\mathrm{s}$), si bien que leur vertex de désintégration, et donc celui des J/ψ non-prompts produits, est reconstruit comme déplacé dans l'espace par rapport au vertex primaire de la collision. Les études des J/ψ prompt et non-prompt dans les collisions d'ions lourds revêtent chacune un intérêt, la première car elle permet d'étudier les effets de dissociation et régénération des charmonia dans les collisions d'ions lourds, et la seconde car elle permet d'étudier la production de quarks beauty dans ces collisions. Dans le chapitre 4, une analyse préliminaire de la séparation prompt-non-prompt utilisant des données de collisions proton-proton récoltées par l'expérience ALICE en 2022.

Chapitre 2: Dispositif expérimental

Le Large Hadron Collider (LHC) est situé au CERN, proche de la frontière franco-suisse. Il s'agit d'un accélérateur circulaire permettant d'accélérer puis de faire entrer en collision des hadrons tels que des protons ou des noyaux d'ions lourds, typiquement du plomb. Un complexe d'accélérateurs accélère ces hadrons et les injecte dans deux anneaux du LHC (mesurant $27\ \mathrm{km}$ de circonférence), en sens opposés. Cela constitue ce qu'on appelle des faisceaux de particules, collimatés par des aimants et accélérés par des cavités radiofréquences. Les deux faisceaux circulant en sens opposés se croisent à quatre endroits

sur la circonférence de l'accélérateur, nommés des points d'interaction. Quatre expériences distinctes sont construites et récoltent des données autour de ces points : ATLAS, CMS, LHCb et ALICE.

Alors que des expériences comme CMS et ATLAS sont plus généralistes, ALICE (A Large Ion Collider Experiment) est dédiée à l'étude des collisions d'ions lourds et du PQG. Elle est composée de plusieurs sous-détecteurs, séparés en deux catégories : le baril central qui couvre une région de l'espace à mi-rapidité autour du point d'interaction, et le spectromètre à muons, qui couvre une région vers l'avant. Dans le baril central, on retrouve des détecteurs comme l'ITS, qui reconstruit les vertex primaires des collisions, la TPC, un détecteur gazeux permettant de trajectographier les particules chargées qui le traversent et de les identifier, ou encore le TOF qui possède une bonne résolution temporelle. Ces détecteurs sont plongés dans un champ magnétique solénoïdal permettant de mesurer l'impulsion des particules chargées. Dans la région vers l'avant, le spectromètre à muons filtre les particules incidentes avec un absorbeur hadronique, afin de laisser passer principalement des muons. Ensuite, cinq chambres de trajectographie plongées dans un champ magnétique dipolaire permettent de mesurer l'impulsion des particules, suivie de deux chambres d'identification. L'un des facteurs limitants de ce spectromètre est l'absorbeur hadronique, placé entre le point d'interaction et les chambres à muons. En effet, les muons traversant cet absorbeur subissent des diffusions coulombiennes multiples ainsi que des pertes d'énergie. Ceci empêche le spectromètre seul de reconstruire des vertex secondaires de désintégration de particules telles que le J/ψ. Cette capacité est désormais apportée par le MFT, dont des détails sont donnés dans le chapitre 3. De 2018 à 2021, le LHC était arrêté et l'expérience ALICE a pu être améliorée, en vue de la troisième prise de données du LHC appelée Run 3. Ces améliorations permettent notamment à ALICE de faire l'acquisition des données de manière continue, au lieu de déclencher l'acquisition par des triggers physiques comme lors de Runs 1 et 2. De plus, un nouvel environnement logiciel, O^2, a été conçu pour permettre de reconstruire les données de manière synchrone avec la prise de données elle-même, ainsi qu'ultérieurement après des procédures de calibration. Lors de ces phases de reconstruction, le flux de données continu est segmenté par chaque détecteur en blocs temporels appelés Readout Frames (ROF). La taille de ces ROF varie pour les différents détecteurs en fonction de leur résolution temporelle. Ce mode d'acquisition en continu permet de récolter une statistique bien plus importante que lors des précédentes prises de données et ainsi d'étudier des processus rares comme la production de saveur lourde ouverte, ou encore des résonances de basse masse.

Chapitre 3: Reconstruction de muons avec le Muon Forward Tracker

Le Muon Forward Tracker (MFT) est un détecteur installé en 2021 dans l'expérience ALICE, ayant pour but de fournir au spectromètre Muon une capacité de résolution spatiale au niveau du point d'interaction. Ce nouveau détecteur permet d'élargir le champ des observables physiques accessibles dans la région de rapidité à l'avant d'ALICE. En effet, la capacité de vertexing du MFT permet la séparation des contributions prompt et non-prompt de la production inclusive de J/ψ. De plus, l'ajout des plans de détection du MFT

permet d'améliorer la résolution en masse invariante des résonances de basse masse telles que le ω ou le Φ. Finalement, le B_c constitue un cas de physique très intéressant pour le MFT, puisqu'il s'agit d'une particule pour laquelle les effets de régénération dans les collisions à haute énergie devraient être extrêmement importants. La mesure de ces observables sera accessible jusqu'à basse impulsion transverse (p_{T}), puisque dans la région de rapidité à l'avant, toutes les particules détectées subissent un boost de Lorentz dans la direction du faisceau (longitudinale). De plus, ce boost longitudinal produit une dilatation des longueurs, notamment de la distance de désintégration des particules telles que les hadrons b. Cela permet donc une séparation plus claire entre les vertex primaires et secondaires.

Le MFT est un détecteur basé sur une technologie silicium, c'est-à-dire utilisant des puces de semi-conducteurs. Les puces du MFT sont composées d'une matrice de pixels. Chacun contient une diode de collecte de charge, permettant de détecter le passage d'une particule chargée, ainsi qu'une électronique permettant d'enregistrer seulement les signaux dépassant un certain seuil de charge. Les puces sont agencées sur des plaques appelées des échelles, qui sont elles-mêmes regroupées pour former des demi-faces de disque. Ainsi, un disque est composé de deux moitiés, une moitié supérieure et une moitié inférieure, se positionnant au-dessus et en dessous du tube du faisceau. Chaque demi-disque est composé d'une face avant et d'une face arrière. Le MFT, qui est situé à environ 50 cm du point d'interaction, est constitué d'un total de 5 disques. Lors de la reconstruction, les données brutes issues du MFT. Ensuite, vient l'étape de clusterisation qui consiste à regrouper des hits de pixels contigus afin de reconstituer les "tâches", appelées clusters, laissées par le passage d'une particule chargée. Ensuite, vient l'étape de trajectographie, où des clusters reconstruits sur différents plans sont associés pour reformer le chemin laissé par une particule chargée à travers le détecteur.

Les pixels silicium des ALPIDEs subissent un bruit fluctuant, qui peut générer un "faux" signal. Il est donc primordial de contrôler le niveau de bruit du détecteur. Pour cela, j'ai développé un outil permettant d'effectuer un scan de bruit. Ces scans permettent d'enregistrer dans une base de données une liste des pixels ayant un bruit au-delà d'un certain seuil. Cette liste est ensuite utilisée lors de la reconstruction pour masquer les pixels bruyants. Une contribution au bruit lors de ces scans peut néanmoins provenir des rayons cosmiques. Il est donc important de choisir judicieusement le seuil de bruit à appliquer. Depuis le début des collisions proton-proton du Run 3 en juin 2022, le niveau de bruit total du détecteur n'a que peu évolué. En effet, si le nombre total de pixels bruyants peut significativement varier, le nombre de pixels les plus bruyants reste relativement stable, avec une variation enregistrée maximale de l'ordre de 12%. Même si des études détaillées sur la répartition du bruit à l'intérieur du détecteur sont encore à développer, les fluctuations de bruit ne semblent pas rédhibitoires pour la reconstruction des traces MFT. Mon travail a également porté sur l'étude des clusters de tailles anormalement élevées (supérieures à 20 pixels), observés lors du faisceau pilote proton-proton d'octobre 2021. L'étude de leur distribution a permis de déterminer qu'ils provenaient de l'activité physique du faisceau du LHC. En effet, le nombre de ces grands clusters est corrélé avec l'intensité du faisceau. De plus, la densité spatiale de grands clusters dans les plans de détection du MFT diminue avec la distance radiale au tube du faisceau. Ces

observations confirment l'origine physique de la production de ces grands clusters liée à l'activité du faisceau. En revanche, une distribution non-uniforme de ces clusters a également été observée à l'intérieur de chaque puce ALPIDE, et leur origine reste à déterminer.

Un aspect essentiel de l'étude des muons avec le MFT est l'appariement des traces reconstruites dans le MFT avec celles reconstruites dans le spectromètre Muon. Cela signifie associer une trace MFT et une trace Muon laissées par la même particule chargée ayant traversé les deux détecteurs. Cet appariement est appelé le "matching" entre le MFT et le spectromètre Muon. L'algorithme actuellement utilisé pour ce matching dans les collisions proton-proton est un algorithme dit du χ^2, où toutes les combinaisons de traces MFT et Muon compatibles en temps sont essayées, et un score de χ^2 est calculé pour chaque combinaison. Celui-ci est calculé en utilisant la différence des paramètres des traces MFT et Muon. Une coupure sélectionnant la combinaison avec le meilleur χ^2 est ensuite appliquée. Cependant, il est possible que cet algorithme sélectionne la mauvaise combinaison. On appelle ce cas des faux matches. Ainsi, le critère de sélection sur le χ^2 doit être choisi de sorte à minimiser la contamination de faux matches, i.e. maximiser la pureté, tout en conservant le plus de matches corrects, i.e. maximiser l'efficacité. Une première optimisation a été effectuée en utilisant des simulations Monte Carlo pour estimer la forme de la distribution en χ^2 des faux matches et des matches corrects. Cela permet d'avoir une première estimation de la pureté et de l'efficacité de l'échantillon après la sélection en χ^2. Cette méthode a permis de déterminer qu'une sélection de $\chi^2 < 40$ était raisonnable. Cependant, cette méthode reste basée sur des simulations dont la qualité n'est pas assurée. Des méthodes plus robustes sont en cours de développement. De plus, si l'algorithme du χ^2 peut convenir pour la reconstruction des données proton-proton, ses performances sont trop faibles pour permettre son application aux données des collisions Pb–Pb. Des méthodes de matching basées sur le Machine Learning sont actuellement en développement pour ce type de données.

Chapitre 4: Analyse préliminaire de la séparation entre les J/ψ prompts et non-prompts.

Dans ce chapitre, une étude préliminaire de la séparation entre les J/ψ prompt et non-prompt dans les collisions proton-proton est présentée. Cette séparation se base sur une variable appelée longueur de désintégration pseudo-propre des J/ψ et notée $\ell_{J/\psi}$. C'est une approximation de la longueur de désintégration de la potentielle particule mère du J/ψ considéré. Ainsi, cette variable vaut $\ell_{J/\psi} = 0$ dans le cas des J/ψ prompts (avec une résolution infiniment petite), puisque le J/ψ provient directement du vertex primaire. Dans le cas des J/ψ non-prompt, cette variable est une approximation de la longueur de désintégration des hadrons b. Ainsi, les J/ψ prompts peuvent être distingués des J/ψ non-prompt en examinant la valeur de ce paramètre. Pour réaliser cette étude, un échantillon des données récoltées lors des collisions proton-proton de 2022 a été utilisé. À partir de ces données, les muons reconstruits sont associés aux vertex primaires dont ils sont censés provenir. Cette association est basée sur un horodatage des traces muons et des vertex. Une fois cette association réalisée, des paires de combinaisons muon-anti-muon sont effectuées, vertex par vertex. Ces paires forment des candidats J/ψ provenant du

canal $J/\psi \longrightarrow \mu^+\mu^-$. L'association entre les traces muons et le vertex primaire est décisif, car si elle est mauvaise alors la variable $\ell_{J/\psi}$ n'est pas une approximation de la longueur de désintégration des particules mères. J'ai développé un outil permettant d'effectuer cette association, basé sur le temps des traces et des vertex. Dans cet outil, des plages temporelles sont associées à chaque vertex et à chaque trace. La largeur de ces plages prend en compte les résolutions temporelles des détecteurs, ainsi qu'une marge de sécurité qui peut être paramétrisée par l'utilisateur. Une fois l'association entre les muons et les vertex primaires réalisée, et les paires de muons construites, il faut reconstruire les vertex secondaires formés par la désintégration des J/ψ et permettant de calculer la variable $\ell_{J/\psi}$. Ces vertex secondaires sont estimés en propageant les traces muons de chaque paire jusqu'au point minimisant la distance entre les deux traces. Plusieurs critères de qualité sont appliqués aussi bien sur les traces muons simples que sur les paires de muons, les vertex secondaires et les vertex primaires. Ces sélections permettent de limiter la contamination de l'échantillon par du bruit et de s'assurer de la bonne qualité des traces et des vertex reconstruits.

Le signal doit ensuite être extrait de l'échantillon de données en utilisant une méthode statistique de fit bidimensionnel. Pour cela, deux variables sont examinées : la masse invariante M des candidats J/ψ et la longueur de désintégration pseudo-propre $\ell_{J/\psi}$. La masse invariante M permet de séparer parmi les candidats ceux provenant bel et bien d'un signal J/ψ du bruit de fond combinatoire constitué d'autres muons produits dans la collision. La variable $\ell_{J/\psi}$ permet de discriminer parmi le signal J/ψ les composantes prompt et non-prompt. Dans ce fit bidimensionnel, une densité de probabilité en deux dimensions est fittée aux données. Cette densité de probabilité totale est composée d'une fonction décrivant le bruit de fond, d'une composante décrivant le signal prompt et d'une composante décrivant le signal non-prompt. Avant que le fit bidimensionnel lui-même puisse être réalisé, plusieurs paramètres doivent être fixés au préalable. Tout d'abord, les paramètres des fonctions décrivant le signal et le bruit de fond dans le spectre de masse invariante sont fixés par un fit en une dimension sur la masse. Ensuite, la résolution du MFT en $\ell_{J/\psi}$ doit être estimée. Pour cela, on utilise une méthode statistique appelée $sPlot$ qui, à partir du fit en masse invariante réalisé, permet de séparer le signal et du bruit de fond dans la distribution en $\ell_{J/\psi}$. Une fonction est fittée à la partie gauche de cette distribution de signal. En effet, cette partie est dominée par la composante prompt du signal, tandis que la composante non-prompt réside principalement dans la partie droite de la distribution. La distribution en $\ell_{J/\psi}$ du signal prompt permet d'estimer la résolution du détecteur. Ensuite, toujours en utilisant la méthode $sPlot$, la distribution en $\ell_{J/\psi}$ du bruit de fond est sélectionnée, puis elle est fittée avec une nouvelle fonction. Enfin, toutes ces composantes sont réunies dans la densité de probabilité totale : les paramètres de la composante bruit de fond ont été fixés par les fits sur M et $\ell_{J/\psi}$, la composante du signal prompt est un pic représentant la résolution du détecteur, et la composante non-prompt est une fonction exponentielle convoluée à la fonction de résolution, dont l'unique paramètre est initialisé en utilisant une valeur extraite de simulations. On peut alors réaliser le fit bidimensionnel où seule la fraction de la composante non-prompt f_B du signal ainsi que le paramètre de l'exponentielle de cette même composante sont libres. Les résultats obtenus sont encourageants, puisque la fraction f_B est en accord avec de précédentes mesures par LHCb dans les régions à haute impulsion

transverse. En revanche, à plus basse impulsion transverse, la résolution est trop grande pour permettre une extraction robuste de cette fraction. Les causes de cette dégradation sont encore en étude. Enfin, pour aboutir à un résultat final, il faudrait corriger la fraction f_B extraite pour tenir compte de la différence d'efficacité et d'acceptance entre les composantes prompt et non-prompt du signal. De plus, les incertitudes systématiques liées aux fits réalisés restent à évaluer. Néanmoins, ces résultats préliminaires vont dans la bonne direction et ouvrent la voie à une analyse complète dans les collisions Pb–Pb.

Chapitre 5: Sonder les premiers instants du PQG avec les dileptons thermiques

Ce dernier chapitre est consacré à une étude phénoménologique réalisée en collaboration avec Jean-Yves Ollitraul de l'Institut de Physique Théorique du CEA, Sören Schlichting et Xiaojian Du de l'université de Bielefeld, et Michael Winn du département de physique nucléaire du CEA. L'objet de cette étude est les dileptons thermiques, qui sont des paires d'électrons-positrons ou de muons-anti-muons, émis par le PQG sous la forme d'une radiation thermique. Nous avons cherché à déterminer dans quelle mesure leur étude dans les collisions d'ions lourds peut fournir des informations sur les premiers instants du PQG. En effet, le système créé immédiatement après la collision est très éloigné de l'équilibre thermodynamique. On sait cependant que plus tard, le PQG est remarquablement décrit par les équations de la mécanique des fluides. Cette phase de connexion est nommée le pré-équilibre. Plusieurs développements théoriques récents donnent une description effective de cette phase. Ces approches reposent en général sur une hypothèse quant à la valeur du couplage de l'interaction forte α_s lors de cette phase. Certaines approches supposent un couplage faible qui permet de décrire le pré-équilibre en employant une théorie cinétique effective. Une découverte remarquable de ces calculs est que lorsque ceux-ci sont représentés en fonction d'un temps normalisé par une variable que l'on appelle η/s, ils suivent des courbes très proches les unes des autres. Ainsi, les calculs à fort couplage ou faible couplage donnent des résultats très similaires lorsqu'ils sont représentés avec cette normalisation. On parle d'attracteur. Le paramètre η/s intervenant dans la description de l'attracteur quantifie le temps d'applicabilité de la mécanique des fluides. Il est intéressant de remarquer que les divers modèles du pré-équilibre prédisent que le milieu est encore éloigné de l'équilibre thermodynamique lorsque la mécanique des fluides devient applicable. En particulier, la distribution des quarks et des gluons dans l'espace des impulsions est anisotrope, en raison de l'expansion longitudinale du système lors des premiers instants. De plus, l'équilibre chimique entre les quarks et les gluons n'est pas complètement réalisé : en effet, dans l'état initial, les gluons dominent largement le système créé. Ce n'est qu'au cours des interactions et de l'évolution du milieu que des quarks sont produits. Les dileptons sont des sondes intéressantes des propriétés du PQG. En effet, ce sont des rayonnements électromagnétiques qui ont une faible probabilité d'interagir avec le milieu. De plus, ils sont produits durant toute la durée de vie du PQG, ce qui leur permet de sonder différentes phases de son évolution. Enfin, ils ont une masse invariante. Les dileptons ayant une masse invariante $M > 1\ \mathrm{GeV}/c^2$ sont principalement produits par des processus partoniques, i.e. des interactions entre quarks et gluons. C'est donc dans cette région de masse qu'il est pertinent de rechercher les

dileptons thermiques issus de la radiation du PQG déconfiné. On appelle cette région la région de masse intermédiaire. De plus, dans cette région, plus la masse du dilepton est élevée, plus sa température de production est élevée, ce qui correspond a des temps tôt dans l'historique de la collision. Par conséquent, plus on monte en masse dans le spectre de masse intermédiaire des dileptons, plus on remonte dans l'historique de la collision, éventuellement jusqu'au pré-équilibre.

Dans notre calcul, nous prenons en compte la contribution de la phase de pré-équilibre au spectre des dileptons. Nous considérons uniquement le processus de premier ordre, d'annihilation quark-antiquark. Nous avons utilisé un modèle cinétique effectif à bas couplage pour calculer l'évolution de la densité d'énergie. Nous convertissons ensuite cette densité d'énergie en température et calculons le taux de production de dileptons thermiques associé à cette température. Cette approche nous permets d'utiliser le fait que l'évolution de la densité d'énergie suit la courbe attractrice. Ainsi, notre calcul présente une forme de généralité, car les résultats seraient très similaires si la densité d'énergie avait été calculée à l'aide d'un autre modèle de pré-équilibre. De plus, nous prenons en compte dans notre calcul le fait que les distributions des quarks lors de la phase de pré-équilibre sont anisotropes dans l'espace des impulsions, et que les quarks sont sous-représentés par rapport aux gluons dans cette phase. Le seul paramètre libre de notre calcul est η/s.

Les conclusions de cette étude sont les suivantes. La phase de pré-équilibre modifie considérablement le spectre de masse invariante des dileptons thermiques. En particulier, la sous-représentation des quarks, ainsi que le paramètre η/s, influe significativement sur la production à haute masse, par plusieurs ordres de grandeur. La mesure de la pente du spectre de masse invariante, ainsi que celle du spectre de masse transverse, donne accès à la valeur de ce paramètre η/s. Cependant, à haute masse, typiquement pour $M > 4 - 5\ \mathrm{GeV}/c^2$, un bruit de fond appelé le Drell-Yan, provenant des processus durs de l'état initial, domine le spectre de dileptons. En examinant une distribution de polarisation, nous constatons que les dileptons thermiques le Drell-Yan ont des comportements opposés. Cet effet de polarisation est de l'ordre de 20 à $30\ \%$ dans la région de masse $4 < M < 5\ \mathrm{GeV}/c^2$. La séparation de ces deux contributions semble donc envisageable dans cette région. De plus, cette distribution angulaire permet un accès direct à l'anisotropie de la distribution en impulsion des quarks en fonction du temps. Si elle peut être menée à bien, il s'agirait de la première mesure directe de l'anisotropie des premiers instants du PQG. La mesure des dileptons thermiques se confronte à d'importants bruits de fond provenant de la désintégration semi-leptonique de saveurs lourdes. Ceux-ci peuvent être rejetés par des coupures sur le déplacement des vertex secondaires des dileptons par rapport aux vertex primaires. Cependant, cela nécessite une résolution de vertexing très hors de portée des expériences actuelles capables de supporter la multiplicité des collisions d'ions lourds centrales. Des expériences futures telles que ALICE3 ou encore l'upgrade 2 de LHCb, prévues toutes les deux pour l'horizon 2030-2035, devraient fournir de telles performances et ainsi permettre ces mesures.

Acronyms

AdS/CFT: Anti-deSitter/Conformal Field Theory

ALICE: A Large Ion Collider Experiment

ALPIDE: ALice PIxel DEtector

AOD: Analysis Object Data

BC: Bunch Crossing/Bunch Clock

CA: Cellular Automaton

CCDB: Condition and Calibration Database

CEM: Color Evaporation Model

CGC: Color Glass Condensate

CRU : Common Readout Unit

CS: Color Signlet

CTP : Central Trigger Processor

DCS: Detector Control System

DY: Drell-Yan

ECS: Experiment Control System

ECS: Experiment Control System

EKT: Effective Kinetic Theory

EPN: Event Processing Node

FLP : First Level Processor

FONLL: Fixed Order, Next-to-Leading Logarithm.

FPGA: Field Programmable Gate Array

GBTx: Giga-Bit Transceiver optical link

HIC: Heavy-Ion Collisions

IP : Interation Point

ITS: Inner Tracking System

LHC: Large Hadron Collider

LO: Leading Order

lQCD: Lattice QCD

LTF: Linear Track Finder

LTU : Local Trigger Unit

MB: Minimum Bias

MCH: Muon CHambers

MC: Monte Carlo

MFT: Muon Forward Tracker

MID: Muon IDentification

NLO: Next-to-Leading Order

nPDF: nuclear Parton Distribution Function

NRQCD: Non-Relativistic Quantum ChromoDynamics

O^2**:** Online-Offline

PCA: Point of Closest Approach

PDF: Parton Distribution Function

pQCD: perturbative Quantum ChromoDynamics

PV: Primary Vertex

QCD: Quantum ChromoDynamics

QED: Quantum ElectroDynamics

QGP: Quark-Gluon Plasma

RHIC: Relativistic Heavy Ion Collider

ROF: Readout Frame

RTA: Relaxation Time Approximation

RU: Readout Unit

SV: Secondary Vertex

List of Figures

List of Tables